Chemical Impurities and Physical Properties of Polar Ice

DISSERTATION

der Mathematisch-Naturwissenschaftlichen Fakultät
der Eberhard Karls Universität Tübingen
zur Erlangung des Grades eines
Doktors der Naturwissenschaften
(Dr. rer. nat.)

vorgelegt von
JAN EICHLER
aus Cheb / Tschechien

Tübingen
2019

Gedruckt mit Genehmigung der Mathematisch-Naturwissenschaftlichen Fakultät
der Eberhard Karls Universität Tübingen.

Tag der mündlichen Qualifikation:	26. April 2019
Dekan:	Prof. Dr. Wolfgang Rosenstiel
1. Berichterstatter:	Jun.-Prof. Dr. Ilka Weikusat
2. Berichterstatter:	Prof. Dr. Paul D. Bons

EBERHARD KARLS UNIVERSITÄT TÜBINGEN

Mathematisch-Naturwissenschaftliche Fakultät
Geowissenschaften

Chemical Impurities and Physical Properties of Polar Ice

Dissertation
von

Jan EICHLER

Zusammenfassung

Der Grönländische und der Antarktische Eisschild sind die größten Süßwasserreservoirs unseres Planeten. Das darin enthaltene Eis bildete sich über Jahrtausende aus dem Niederschlag und durch natürliche Verdichtung von Schnee, und stellt damit ein einzigartiges Klimaarchiv dar. Die großen Eismassen fließen unter ihrem eigenen Gewicht und verfrachten so Eis vom Landesinneren in die Ozeane. Die Eisdynamik wird mithilfe von numerischen Fließmodellen simuliert, u. a. um den zukünftigen Beitrag von Eisschilden zum Meeresspiegelanstieg zu prognostizieren. Die viskoplastische Verformung von Eis auf der Mikroskala involviert ähnliche Mechanismen wie die Deformation anderer polykristalliner Materialen. Die Scherung einzelner Kristalle wird durch Rekristallisation und Bildung bestimmter Mikrostrukturen begleitet. Daher können Konzepte und Vorgehensweisen der Strukturgeologie auf natürliche Eisproben angewandt werden, um ihren Deformationsstatus und die daran beteiligten Prozesse zu studieren.

Chemische Spurenstoffe im Schnee und Eis setzen sich mit dem Niederschlag ab und spiegeln die Zusammensetzung der in der Atmosphäre enthaltenen Aerosole wider. Als solche spielen sie eine wichtige Rolle für paläoklimatische Rekonstruktionen. Trotz ihrer extrem niedrigen Konzentrationen beeinflussen Spurenstoffe viele physikalischen Eigenschaften von Eis, insbesondere auch das Deformationsvermögen. Konzentrationschwankungen diverser Spurenstoffkomponenten mit der Tiefe korrelieren mit Heterogenitäten im Fließgeschwindigkeitsprofil und scheinen die Bildung von lokalisierten Scherzonen zu begünstigen. Ein besseres Verständnis dieser Zusammenhänge und der dahinterstehenden Mechanismen ist notwendig um den Effekt von Spurenstoffen realistisch in Fließmodelle implementieren zu können.

Die vorgelegte Arbeit befasst sich mit dem Zusammenhang zwischen chemischen Spurenstoffen und physikalischen Eigenschaften von polarem Eis. Eine zentrale Herausforderung ist es zu verstehen, in welcher Form und wo Spurenstoffe in der Eismatrix integriert sind, bzw. wie sie mit ihr während der Deformation und Rekristallisation interagieren. Natürliches Eismaterial aus Eiskernbohrungen wurde mittels einer Kombination verschiedener Methoden zur Mikrostrukturanalyse untersucht. Die Verteilungen und Zusammensetzungen von Spurenstoffen wurden mittels eines konfokalen Kryo-Raman-Mikroskops analysiert. Im Rahmen dieser Arbeit wurden neue Routinen zur Messung und Datenerfassung entwickelt.

Die Ergebnisse zeigen ein komplexes Zusammenspiel zwischen Spurenstoffen, Kristallstruktur und lokalisierter Deformation von Eis. Einerseits verursachen hohe Spurenstoffkonzentrationen höhere Deformationsraten, die von feinkörniger Kristallstruktur begleitet werden. Andererseits wird die Verteilung und möglicherweise Zusammensetzung der Spurenstoffe durch die Deformation des Eises beeinflusst.

Der Anteil dissoziirter Stoffe im Eis konnte nur qualitativ und indirekt durch den Vergleich der Ramananalyise mit den Ergebnissen einer chemischer Analyse von Schmelzwasser geschätzt werden. Die Ramanspektroskopischen Messungen deuten allerdings klar darauf hin, dass mikroskopische Einschlüsse sekundärer Phasen im Eis einen erheblich höheren Anteil bilden, als im flüssigen Wasser. Das Mischen von Spurenstoffen und chemische Reaktionen zwischen ihnen werden durch die Eisdeformation begünstigt. Unser Bild von "Eis als gefrorenes Archiv" könnte durch "Eis als effektiver Reaktor" ersetzt werden, je nachdem welche zeitlichen und räumlichen Spannen gemeint sind. Die darausfolgende Auswirkung auf die chrono-stratigraphische Integrität von Eiskerndaten ist insgesamt jedoch positiv, da die Reaktionsprodukte oft niedrigere Diffusionsraten besitzen. Ein universeller Mechanismus für die Auswirkung von Spurenstoffen auf die Eisdeformation konnte nicht vollständig aufgedekt werden. Vielmehr scheint Deformationslokalisierung als Folge der mechanischen Anisotropie eine intrinsische Eigenschaft von Eis zu sein, die durch die Variation in Spurenstoffkonzentrationen getriggert wird. Viele Fragen hinsichtlich der Form und Wirkung von Spurenstoffen im Eis stehen allerdings noch offen für zukünftige Forschungsprojekte.

EBERHARD KARLS UNIVERSITÄT TÜBINGEN
Mathematisch-Naturwissenschaftliche Fakultät
Geowissenschaften

Chemical Impurities and Physical Properties of Polar Ice

Doctoral Thesis
by

Jan EICHLER

Abstract

The Greenland Ice Sheet and the Antarctic Ice Sheet are the largest reservoirs of freshwater on our planet. They consist of ice which formed over thousands of years out of the precipitation and due to natural densification of snow. As such, polar ice represents a unique archive of the past climate. The large ice masses flow under their own weight causing a transport of ice from the inlands towards the oceans. Numerical flow models are used to simulate the ice dynamics, i. a., in order to project future contributions of the ice sheets to the rising sea level. The viscoplastic deformation of ice on the micro-scale involves similar mechanisms as the deformation of other poly-crystalline materials. The shear of individual crystals is accompanied by recrystallization and the development of characteristic microstructures. Thus, structural-geological concepts and methods can be applied to natural ice samples in order to study their deformation state and active physical processes.

Chemical impurities are deposited in snow and ice during the precipitation and reflect the aerosol composition of the atmosphere. As such they play an important role for the reconstructions of the climate of the past. Despite their extremely low concentrations, impurities influence many physical properties of ice, in particular also the deformation rate. The concentrations of the different impurities vary with depth and these variations are correlated with heterogeneities in the flow-velocity profile. This results in the development of localized shear zones in ice. A better understanding of the mechanisms is necessary in order to implement the effect of impurities into the flow models.

The presented thesis addresses the relationship between the chemical impurities and the physical properties of polar ice. A central challenge of the project is to understand in which form impurities integrate in ice and where they are located in the bulk, respectively how they interact with it during deformation and recrystallization. A combination of methods for the microstructural analysis was applied to natural ice material from ice cores. The distribution and composition of impurities was analyzed using a confocal cryo-Raman microscope. Within the scope of this thesis, new routines for the acquisition and data processing were developed.

The results reveal a complex interplay between impurities, crystal structure and localized deformation in ice. On the one hand, high impurity concentrations cause higher strain rates occurring together with small grain sizes. On the other hand, the deforming ice matrix affects the distribution of impurities and possibly also their chemical composition. The portion of dissociated components in ice could be estimated only qualitatively and through the comparison to the chemical analysis of the meltwater. However, the Raman-spectroscopy data clearly suggest that microscopic inclusions of second phase are present in solid ice in significantly higher concentrations, compared to liquid water. Mixing and chemical reactions of impurities is

promoted through the deforming ice matrix. Our image of “ice as a frozen archive” could be replaced by “ice as an effective reactor”, depending on the spatial scales and time spans referred to. The resulting implication for the chrono-stratigraphic integrity of ice-core records may still be positive, because the reaction products often posses lower diffusion rates. A universal mechanism for the impurity effect on ice deformation could not be identified. The localized deformation seems to be in fact an intrinsic property of ice produced by the mechanical anisotropy and triggered by the varying impurity concentrations. However, many questions regarding the form and effect of impurities in ice remain open for future investigations.

Contents

Contribution to scientific publications

Paper I

Jan Eichler, Ina Kleitz, Maddalena Bayer-Giraldi, Daniela Jansen, Sepp Kipfstuhl, Wataru Shigeyama, Christian Weikusat, and Ilka Weikusat (2017). "Location and distribution of micro-inclusions in the EDML and NEEM ice cores using optical microscopy and in situ Raman spectroscopy." In: *The Cryosphere* 11.3, pp. 1075–1090. DOI: 10.5194/tc-11-1075-2017. URL: https://www.the-cryosphere.net/11/1075/2017/tc-11-1075-2017.pdf

Scientific ideas	**Data generation**	**Analysis and interpretation**	**Paper writing**
Full development of the scientific idea of mapping of micro-inclusions over large areas. Initial idea of impurity imaging by SK and IW.	Measurements and generation of raw data partly with assistance of IK and WS.	All analysis and interpretation with contribution of all co-authors.	All paper writing. Proof-reading and comments by all co-authors.

Paper II

Jan Eichler, Christian Weikusat, Anna Wegner, Birthe Twarloh, Melanie Behrens, Hubertus Fischer, Maria Hörhold, Daniela Jansen, Sepp Kipfstuhl, Urs Ruth, Frank Wilhelms, and Ilka Weikusat (2019). "Impurity Analysis and Microstructure Along the Climatic Transition From MIS 6 Into 5e in the EDML Ice Core Using Cryo-Raman Microscopy." In: *Frontiers in Earth Science* 7. DOI: 10.3389/feart.2019.00020

Scientific ideas	**Data generation**	**Analysis and interpretation**	**Paper writing**
Full development of the scientific idea of acquiring Raman spectra of micro-inclusions using previously created impurity maps. Development of the half-automatic Raman measurements.	Generation of all Raman data with assistance of CW. Ion chromatography data generated by BT. Continuous flow analysis data by AW, MB, HB, MH and UR. Dielectric profiling by FW.	All analysis and interpretation with contribution of all co-authors.	All paper writing. Proof-reading and comments by all co-authors.

Paper III

Florian Steinbach, Ernst-Jan N. Kuiper, Jan Eichler, Paul D. Bons, Martyn R. Drury, Albert Griera, Gill M. Pennock, and Ilka Weikusat (2017). "The Relevance of Grain Dissection for Grain Size Reduction in Polar Ice: Insights from Numerical Models and Ice Core Microstructure Analysis." In: *Frontiers in Earth Science* 5, p. 66. ISSN: 2296-6463. DOI: 10.3389/feart.2017.00066. URL: https://www.frontiersin.org/article/10.3389/feart.2017.00066

Scientific ideas	**Data generation**	**Analysis and interpretation**	**Paper writing**
Discussion and support for FS. Ideas regarding 3D effects in Fabric Analyser images.	Processing of Fabric Analyser data, generation and selection of fabric images.	Analysis and interpretation of ice sample data together with FS and ENK.	Contribution to the paper writing providing text parts and figures related to the Fabric Analyser data.

Paper IV

Ilka Weikusat, Daniela Jansen, Tobias Binder, Jan Eichler, Sérgio H. Faria, Frank Wilhelms, Sepp Kipfstuhl, Simon Sheldon, Heinrich Miller, Dorthe Dahl-Jensen, and Thomas Kleiner (2017b). "Physical analysis of an Antarctic ice core–towards an integration of micro- and macrodynamics of polar ice." In: *Philosophical Transactions of the Royal Society A: Mathematical, Physical and Engineering Sciences* 375.2086, p. 20150347. DOI: 10.1098/rsta.2015.0347. URL: http://doi.org/10.1098/rsta.2015.0347

Scientific ideas	**Data generation**	**Analysis and interpretation**	**Paper writing**
Assistance with development of the main idea by IW, by continued discussion of the EDML dataset.	Contribution to the measurements and processing of the crystal-preferred orientations.	Contribution in form of discussions with IW and DJ regarding grain size and crystal-preferred orientations.	Contribution to paper writing by commenting and proof-reading.

Paper V

Johanna Kerch, Olaf Eisen, Jan Eichler, Tobias Binder, Pascal Bohleber, Johannes Freitag, Paul Bons and Ilka Weikusat (2019). "Short-scale variations in high-resolution crystal-preferred orientation data in an alpine ice core – do we need a new statistical approach?". Submitted to *Journal of Geophysical Research*.

Scientific ideas	**Data generation**	**Analysis and interpretation**	**Paper writing**
Contribution to the scientific idea discussing correlations between grain sizes and lattice orientations.	Contribution to the generation and processing of microstructure data. Assistance and support in the laboratory and during data processing.	Support during analysis of microstructure data.	Contribution to paper writing in form of proof-reading and comments.

Chapter 1

Introduction

This chapter introduces basic concepts and terminology. It is intended for a broader audience not necessarily familiar with the subject of glaciology. However, the scope of this thesis and the complexity of this particular field of research do not always allow for an instructive approach. Interested readers are recommended to resort to the relevant textbooks on the physics of ice by Hobbs (1974), Petrenko and Whitworth (1999), and Cuffey and Paterson (2010).

1.1 Why study ice?

1.1.1 Ice – A Material Full of Curiosities

Ice – the frozen phase of water – is a fascinating medium for multiple reasons. The fact that ice floats on water likely offered a friendly environment for the evolution of life on Earth and its preservation in polar regions and during very cold climatic epochs (e. g., "Snowball Earth", Hoffman, 1998). For a few millions years, during the current 'icehouse' climate, ice sheets – large masses of permanent ice on the poles – have played an important role for the energy budget and climatic stability of our planet (Summerhayes, 2015). For humans, ice represents a practical resource on the one hand (snow and ice as means of transportation, construction, cooling, winter sports, etc.), and an object of struggle on the other hand.

From the physicist's point of view, ice is a material of extraordinary characteristics. Water distinguishes itself from other materials through a long list of anomalous properties – some authors count up to 74 anomalies (Chaplin: *Water Structure and Science*; Brovchenko and Oleinikova, 2008). For the most part, the public is familiar with the density anomalies at the transition between liquid water and ice. During freezing at atmospheric pressure and 0° C, the volume increases by approximately 9% after the water is completely frozen to ice. Hence, ice floats on water – and lakes and oceans freeze from the surface. Water density exhibits a maximum at about 4° C, the density of ice around 70 K ($\approx -203°$ C). Also, the melting, boiling and critical point are unusually high compared to similar compounds (e. g., H_2S). Water thus coexists in the solid, liquid and gaseous phase in nature. Ice is ductile and brittle at the same time even at its melting point and its surface is slippery and sticky at the same time even far below its melting point. Many of the unique characteristics of H_2O can be explained through the nearly tetrahedral shape of the sp^3-hybridized water molecule and its ability to form hydrogen bonds (Petrenko and Whitworth, 1999). Hydrogen bonds are also responsible for the spatial arrangement of water molecules in the ice crystal.

Hexagonal ice (denoted as ice I_h) is the only phase among the 18 (and more) polymorphs of solid H_2O discovered so far (Fuentes-Landete et al., 2015) which is stable under the thermodynamic conditions encountered on the Earth's surface (Bartels-Rausch et al., 2012). An account of its structure has been proposed by Pauling, 1935.

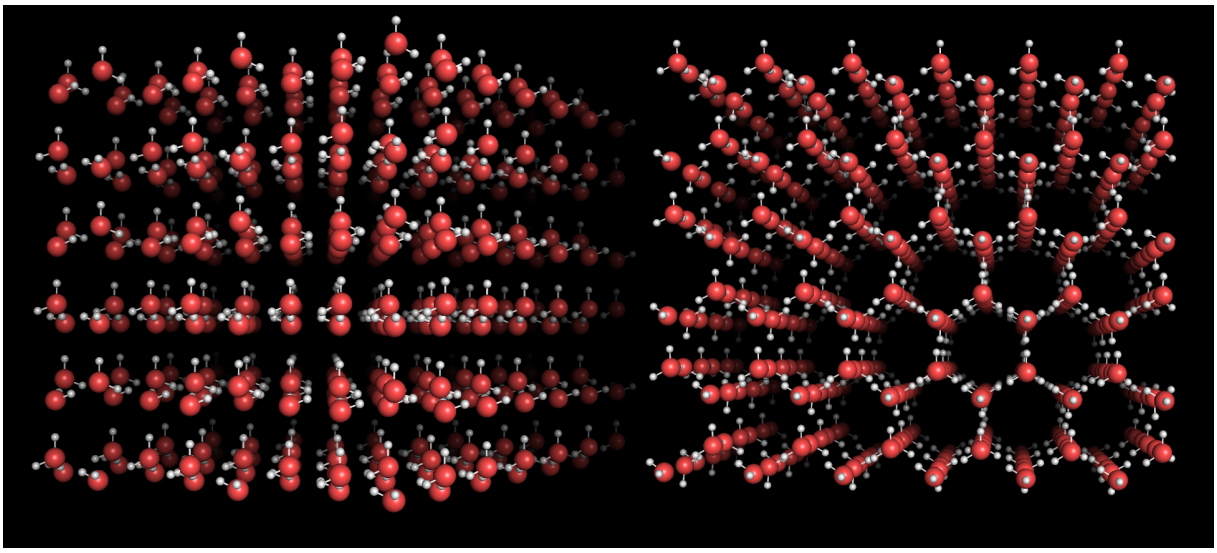

FIGURE 1.1: The structure of ice I_h. Oxygens appear as red spheres, hydrogens in white. Left: View parallel to the basal plane with visible planes of densely packed molecules. Right: View perpendicular to the basal plane. The hexagonal ordering of the water molecules is visible. Plotted using PyMOL.

The arrangement of water molecules in ice I_h follows two simple rules, the Bernal–Fowler rules:

1. each oxygen is covalently bonded to two hydrogens so that the entity of the water molecule is preserved.

2. there is only one hydrogen atom participating in each bond between oxygens (the hydrogen bond).

The lattice structure of ice is identical with the hexagonal form of ZnS (Wurtzite, Petrenko and Whitworth, 1999). The rather large dimensions of the hexagonal-prism-shaped unit cell ($a \approx 4.52$ Å and $c \approx 7.26$ Å, Hobbs, 1974) are responsible for the low density of hexagonal ice. Ice features planes with densely packed molecules, alternating with planes of wide spacing between the molecules (Figure 1.1) These planes are oriented parallel to the basal crystallographic plane (0001) and normal to the main symmetry axis (the c-axis). This structure is the underlying cause for the highly anisotropic behavior of ice which is reflected in its mechanical, electrical, and optical properties (Petrenko and Whitworth, 1999). The basal plane and the c-axis are important measures indicating the direction of this anisotropy. The Bernal–Fowler ice rules do not fully determine the positions of the hydrogens (protons) and a number of different arrangements are possible. Thus, hydrogens in ice do not posses a long-range translational symmetry and the ice I_h lattice is inherently proton-disordered (Petrenko and Whitworth, 1999).

The ice-covered part of the Earth's surface – *the cryosphere* – presently accounts for ca. 20 % of the total surface area of our planet (IPCC, 2013, Table 4.1 therein). 68.7 % of the Earth's fresh water is stored in frozen reservoirs, in particular ice sheets, ice caps, glaciers, sea ice, lake and river ice, and seasonal snow cover (Shiklomanov, 2000). The two present-day ice sheets – the Antarctic Ice Sheet with $25.71 \cdot 10^6$ km^3 and the Greenland Ice Sheet with $2.85 \cdot 10^6$ km^3 – represent by far the largest ice masses with a total sea level equivalent (SLE) of approximately 66 m (IPCC, 2013). Among the manifold scientific goals of ice-sheet research, two main goals can be

distinguished: (I) the reconstruction of past climates and (II) the analysis of the influence of ice sheets on the present climate and the clarification of its role to improve future projections. These differing goals have led to the establishment of two branches of research with different temporal foci. The following two sections comment on these two not completely independent perspectives of glaciology in more detail.

1.1.2 Ice Sheets I: Archives of the Past Atmosphere

Ice sheets, ice caps, and glaciers consist of meteoric ice, i. e., ice that originates from the precipitation of snow. Due to permanent accumulation of fresh snow, older layers are compacted and buried deeper in the snow column. Originally separated snow grains sinter together, forming a solid porous ice–air aggregate, referred to as *firn* (Blackford, 2007; Colbeck, 1983; Fierz et al., 2009; Wilkinson and Ashby, 1975). Further firn compaction causes an increase of density with depth, until pores are gradually closed off and the air remains trapped in separate bubble-like inclusions (Schwander and Stauffer, 1984; Stauffer et al., 1985). Pore close-off occurs at densities around 830 $\mathrm{kg\,m^{-3}}$ and defines the transition zone between firn and ice. The burial depth of the firn–ice transition can vary significantly from site to site, depending on the accumulation rate, temperature, and the thinning rate (Cuffey and Paterson, 2010). However, recent studies have shown that the exact depth of the firn–ice also depends on more complex micro-structural processes occurring during firn densification (Freitag et al., 2013; Hörhold et al., 2012; Schaller et al., 2017).

In geological terms, glacial ice is a sedimentary mono–mineralic rock of very high purity. Depending on the amount of site-specific precipitation, the annual layer thickness can vary from millimeters to up to a meter or more (Cuffey and Paterson, 2010) and it decreases with depth due to progressive thinning by compression and ice-flow divergence. Since all the components – i. e. the ice itself as well as its gas content and other impurities – originate from precipitation, ice sheets represent the most direct archives of the past atmosphere. Analysis of the air trapped inside the ice can directly reveal the history of atmospheric composition, e. g., the concentration of greenhouse gases (CO_2, CH_4, N_2O) over time, etc. (Etheridge et al., 1996; Loulergue et al., 2008; Wolff, 2011). Other palaeo-climatic parameters can be measured in the form of so-called *climate proxies* (Grinsted et al., 2010; Mayewski et al., 2009; Ruth et al., 2008; Schüpbach et al., 2013), i. e., quantities which are linked to certain climatic or atmospheric conditions through more or less complex processes. Probably the most prominent climate proxies obtained from snow and ice are the compositions of stable water isotopes, in particular the $^{18}O/^{16}O$ and D/H ratios (Galewsky et al., 2016). Dansgaard (1953, 1964) discovered that their variations (expressed as $\delta^{18}O$ and δD) are closely linked to atmospheric temperature. Since the first long record was measured on the Camp Century ice core (Dansgaard et al., 1969), stable water isotopes have been established as the basis for global and local temperature reconstructions (Galewsky et al., 2016; Johnsen et al., 2001; Lorius et al., 1979; Vinther et al., 2009). However, the detailed mechanisms of isotopic signal formation (e. g., fractionation during water-vapor transport, precipitation and snow metamorphism) still remain partly unknown and are the object of ongoing investigations (e. g., Ebner et al., 2017; Freitag et al., 2013; Galewsky et al., 2016).

The chronology of climatic signals in ice depends on a number of site-specific factors, in particular total ice thickness, annual layer thickness, thinning rate and flow behavior. Ice in the central regions of Antarctica can reach a thickness of more than 3 km and contain ice which was formed several hundreds of millennia ago. The

deepest part of the EPICA Dome C ice core – the oldest continuous ice-core record so far – provided a stable-water-isotopic signal dated 800 000 years back in the past (EPICA community members, 2004). A new European ice-core project in Antarctica, called "Beyond EPICA – Oldest Ice", is currently taking off with the goal to retrieve a continuous record of the past 1.5 million years (Fischer et al., 2013; Karlsson et al., 2018; Liefferinge et al., 2018; Parrenin et al., 2017; Young et al., 2017).

In palaeo-glaciology, the dating of an ice core – i. e., assigning a time scale to the depth – is a key task for chronological reconstructions of climate records (Blunier and Brook, 2001; Rasmussen et al., 2013; Ruth et al., 2007). However, this task becomes more difficult with increasing depth (ergo with the age of the ice). In shallow depths, a number of complementary dating methods can be combined, such as the counting of individual annual layers (Svensson et al., 2011), the matching of absolute markers ,e. g., referenced volcanic events (Gow and Meese, 2007; Moore et al., 1991; Sigl et al., 2015), or isotopic methods (). In contrast, the dating of deep ice is restricted to only a few absolute markers. The application of thinning models represents the main tool for dating deep ice (Huybrechts et al., 2007; Parrenin et al., 2007; Rasmussen et al., 2013; Veres et al., 2013). Furthermore, ice close to the bedrock is in general subject to increased shearing and deformation which can disturb the original stratigraphy on multiple scales (strain localization, folding and other types disruptions Faria et al., 2010; Hudleston, 2015; NEEM community members, 2013). Thus, a more profound understanding of the ice flow is necessary in order to reliably assess the impact of deformation on the chronology of deep ice and, eventually, design methods for the reconstruction of climate signals even from depths where the stratigraphy has been clearly disrupted.

1.1.3 Ice Sheets II: Their Role in (a Changing) Climate

Ice sheets are in continuous movement driven by their own weight, similar to the flow of a highly viscous fluid under the influence of gravitation (Petrenko and Whitworth, 1999). Ice flows from sites with high altitudes down the slope towards low altitudes (Fig. 1.2). This ice flow causes a mass transport from the central parts of Antarctica and Greenland towards the coastal areas. There, the ice forms outflow glaciers and, eventually, reaches the oceans and transforms into floating ice (ice shelves, icebergs). This process is fed by snow accumulation on the surface in high latitude and altitude regions (accumulation zones) and the progressive transformation of snow into new ice. Hence, the flow of ice is a self-containing part of the Earth's water cycle. Under stable boundary conditions, the accumulation of new snow and the ice loss due to melting and glacier discharge are at equilibrium – zero ice mass balance. However, this is not the case anymore under changing climatic conditions such as a rising global temperature.

During the last decades, the Antarctic Ice Sheet and the Greenland Ice Sheet have been losing mass due to global warming and have contributed to the global sea level rise. The global sea level has been rising at an averaged rate of 3.1 $\mathrm{mm\,yr^{-1}}$ SLE between 1993 and 2018 and has been accelerating about 0.1 $\mathrm{mm\,yr^{-2}}$ over this period (WCRP Global Sea Level Budget Group, 2018). The estimated present contributions to global sea level rise are: 42% ocean thermal expansion, 21% glaciers, 15% Greenland Ice Sheet and 8% Antarctic Ice Sheet. The average ice loss in Greenland over the period 1993–2016 contributed with $\approx$ 0.47 $\mathrm{mm\,yr^{-1}}$ SLE and was accelerating towards $\approx$ 0.75 $\mathrm{mm\,yr^{-1}}$ SLE for the period 2005–2016 (WCRP Global Sea Level Budget Group, 2018). The accelerating trend has been observed also in Antarctica

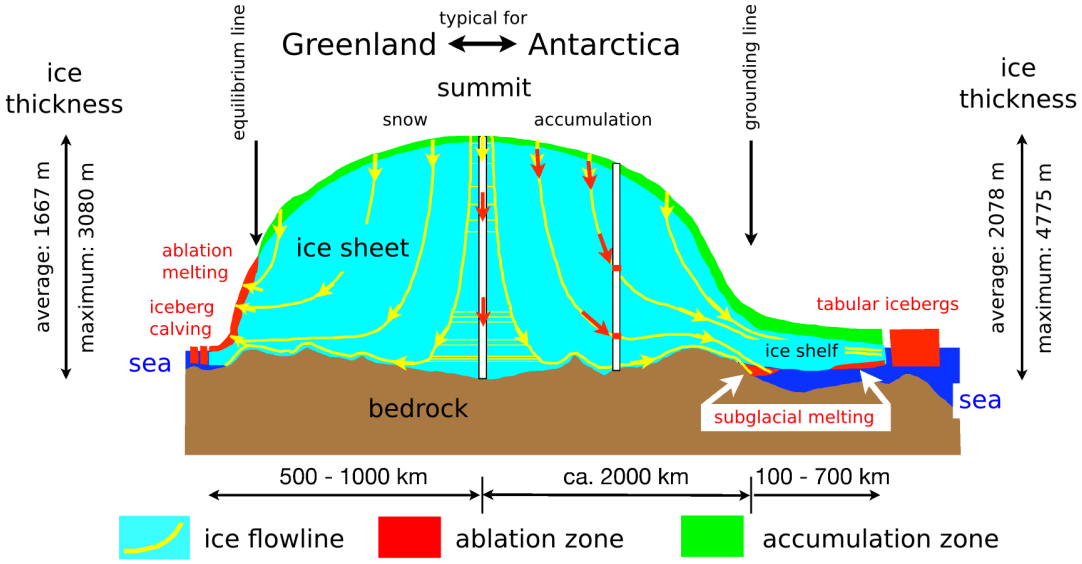

FIGURE 1.2: Cross section of an ice sheet, modified after Oerter (2009). Snow accumulates on the surface of the ice sheet (accumulation zone) and transforms to ice due to compaction and densification. Annual layers are progressively thinned on they way down through the ice column. The flowlines indicate the movement of individual ice particles from the inland towards the ablation zone and the ocean.

where ice loss in recent years reached about ≈ 0.55 mm yr^{-1} SLE. However, in comparison to Greenland, the current Antarctic contribution to the sea level rise is minimal considering the huge amounts of ice stored in Antarctica. Nevertheless, future response of the Antarctic Ice Sheet to further climatic pressure is uncertain. According to the Fifth Assessment Report (AR5) of the Intergovernmental Panel on Climate Change (IPCC, 2013), future contributions of ice sheets represent major uncertainties in projections of global sea level rise. While during the 20th century most meltwater discharge into the oceans was provided by retreating glaciers, future development of the sea level will most likely be determined by the response of ice sheets to changing climate conditions.

Predictions of future ice discharge into the ocean are based on numerical ice sheet models which simulate the development of ice sheets on multiple scales and under different scenarios. Ice sheet models have evolved rapidly over last years parallel to the increase in computational power (Greve and Blatter, 2009). Recent approaches allow to integrate many relevant physical processes (ice flow, ice-bedrock interaction, surface melting, subglacial hydrology, ice-ocean interaction, etc.). However, the physics of ice flow that have been implemented in these models were established six decades ago (Glen's flow law, 1.2.2). This flow law does not always suit recent field and laboratory observations, as explained in more detail further below. In order to improve the flow law and thus the projections of the sea level, a better understanding of mechanisms governing the ice flow is necessary.

1.2 Deformation Macro Scale (Fluid)

While the fast movement of glaciers is to a large extent realized through the gliding of whole ice masses over bedrock, most of the flow in the interior of ice sheets is a product of visco-plastic deformation – *ice creep* (Budd and Jacka, 1989). On large

spatial scales and over long time spans, the behavior of ice is similar to the flow of a highly viscous fluid.

1.2.1 Ice Creep

Creep occurs in most solids under the application of mechanical stress over long time spans. Creep rates generally depend on temperature, exposure time, load, and material properties (Frost and Ashby, 1982; Haasen, 1994; Karato, 2008). The activation energy for ice creep ranges between 60 and 80 kJ mol^{-1} (Mellor and Testa, 1969; Schulson and Duval, 2009). Ice deforms relatively easily compared to other minerals (Hobbs, 1974). A substantial number of laboratory creep experiments have been carried out with the aim to describe the deformation of ice under controlled temperatures and stress–strain configurations (Azuma, 1995; Dahl-Jensen et al., 1997; Journaux et al., 2018; Qi et al., 2018; Weertman, 1973, 1983; Wilson and Zhang, 1994). Deformation tests on artificial polycrystalline ice under constant stresses were initiated by Glen in the 1950s (e. g., Glen, 1952, 1955). The strain (or strain rate) under constant load was recorded as a function of time. The *creep curves* obtained from theses measurements show that the process is characterized by three stages (Budd and Jacka, 1989; Steinemann, 1954; Treverrow et al., 2012). After an initial elastic response, the specimens undergo irreversible plastic deformation (*primary* creep). The strain rate decreases with time as short-range internal stresses build up due to incompatibilities in shapes and orientations of the deforming adjacent grains (Section 1.3.2). After a certain deformation time depending on stress and temperature a minimum strain rate is reached, called the *secondary* creep. Experiments by Jacka (1984) show that independent of load and temperature the minimum strain rate occurs after reaching a total octahedral shear strain of about 0.6 %. Many deformation experiments terminate after reaching the secondary stage of creep, mainly due to time limitations. Perhaps this is the reason why secondary creep is sometimes (incorrectly) referred to as a steady state. However, after some time with progressing deformation, the strain rate starts to increase again and eventually reaches an accelerated (true) steady state. This *tertiary* creep stage (Treverrow et al., 2012) is associated with the onset of dynamic recrystallization (Sect. 1.3.3) and the release of accumulated internal stresses. While in ice sheets the creep has enough time to reach its tertiary state, it can hardly be achieved in laboratory tests under realistic stress–temperature–time constraints.

1.2.2 Glen's Flow Law

In order to derive the 'viscosity' of ice, Glen (1952, 1955) performed creep experiments with different stress magnitudes and recorded strain rates for the secondary creep phase. The results show that the relationship between stress and strain rate is highly non-linear and can be described sufficiently well with an exponential function. This power law has been established as Glen's Flow Law:

$$\dot{\epsilon} = A\,\tau^n \tag{1.1}$$

with the *strain rate* $\dot{\epsilon}$ and the dominant *stress* τ. The *creep factor* A and the *stress exponent* n are fitting parameters to be determined. A can vary across several orders of magnitude (Cuffey and Paterson, 2010, p. 64) depending on other factors and boundary conditions. It can be split into a temperature-independent prefactor

A_0 and a temperature-dependent term of the Arrhenius type:

$$A = A_0 \, \mathrm{e}^{(-Q/RT)} \tag{1.2}$$

with the Kelvin temperature T, the universal gas constant R and the activation energy for creep $Q \approx 60\,\mathrm{kJ\,mol^{-1}}$ (Paterson, 1977). The stress exponent n is assumed to be an ice-specific material constant. The values for n, derived from creep experiments, field data and theoretical considerations range from 1.4 to 4.2 (Gillet-Chaulet et al., 2011; Glen, 1952, 1955; Goldsby et al., 2001; Hooke, 1981) with an average around $n \approx 3$. Although this value has been widely established and implemented in numerical ice-flow models, the universality of $n = 3$ for ice sheets is challenged by an increasing number of studies which propose other stress exponents suitable for different stress configurations, e. g., $n < 2$ at low stresses by Goldsby et al. (2001) or $n = 4$ for the Greenland Ice Sheet by Bons et al. (2018).

1.3 Deformation Micro Scale (Solid)

The description of ice as a highly viscous fluid serves as a first approximation and is relatively useful for an implementation in numerical flow models (Greve and Blatter, 2009; Huybrechts, 2007; Pattyn et al., 2008). However, it is only sufficient on a certain level of abstraction. A number of solid-specific characteristics of ice cannot be easily described by the fluid model. This is illustrated e. g. by the need to include mechanical anisotropy into the flow models (Durand et al., 2007; Martin et al., 2009; Pettit et al., 2007) or the composite flow law suggested by Goldsby et al. (2001). Other solid-specific features not represented in the model are shear localization, folding, the effect of impurities, and grain size. In order to incorporate these features into large-scale ice models, a more detailed understanding of the mechanisms on the micrometer and sub-micrometer scale is necessary.

1.3.1 Single Crystal

As it is the case for metals or other crystalline materials, plastic deformation of ice is realized on the molecular level through the creation of linear lattice discontinuities – *dislocations* – and their propagation through the crystal (Hirth and Tullis, 1992; Read, 1953; Weertman and Weertman, 1992). This so-called *dislocation creep* (Pimienta and Duval, 1987; Shoji and Higashi, 1978) is more effective and energy-efficient than the shifting of whole crystallographic planes against each other, since only a small number of molecular bonds need to be disconnected at once (namely the ones along the dislocation line).

The plasticity of the ice crystal is highly anisotropic. Dislocations in ice glide much easier through the basal plane than through other crystallographic planes (Duval et al., 1983; Nakaya, 1958). As a result, the stress needed to achieve a given strain rate is up to 80 times lower for the shear along the basal plane than for other crystallographic planes (Duval et al., 1983). The slip along the basal plane is therefore called *easy slip*. This anisotropic behavior is comparable to a deck of cards which will easily slide over each other, but hardly deform under compression perpendicular to the slip plane.

1.3.2 Polycrystal

Large ice bodies such as polar ice sheets form polycrystals, i. e., aggregates of many single crystals (grains) with different lattice orientations, shapes, and volumes. Typical grain diameters range from few millimeters to several centimeters. The interfaces between grains are called *grain boundaries* and are characterized by a discontinuity in lattice orientation. Grain boundaries represent planar lattice defects with higher energy and finite interface tension.

The creep of polycrystalline ice involves the deformation of many adjacent grains with different orientations. Grains which are oriented favorably to the shear direction will activate easy slip first (Section 1.3.1). However, their basal slip systems are generally not compatible with the orientations of their neighbors which will block further shearing by easy slip. This results in the development of complex internal stress fields (Ashby and Duval, 1985; Castelnau et al., 2008; Duval et al., 1983, 2010) which govern further deformation on the sub-grain scale. The amount of strain energy stored in the lattice grows with the density of dislocations in the crystal. In creep experiments, this stage is called secondary creep and it is characterized by a minimum in the strain rate (Section 1.2.1). While the main part of the strain is still realized trough the basal slip system, the deformation rate is determined by mechanisms which are able to accommodate intergranular stresses at grain boundaries. Depending on the applied stresses, several accommodating mechanisms have been proposed, such as diffusional flow, grain boundary sliding, dislocation climb (Goldsby et al., 2001) or the activation of dynamic recrystallization (Schulson and Duval, 2009).

1.3.3 Dynamic Recrystallization

When the internal strain energy stored in dislocations reaches a critical level, it can be released by the activation of recrystallization. Recrystallization refers to processes in which the structure of the polycrystal changes over time. This is mainly realized through migration of grain boundaries or through creation of new grains and grain boundaries (Drury and Urai, 1990). Such mechanisms, which are driven by the reduction of internal strain energy are collectively called dynamic recrystallization.

Rotation recrystallization (RRX) refers to a process in which dislocations of the same type arrange themselves in planar configurations which serve as seeds for the creation of new low-angle grain boundaries. These arrangements of dislocations produce a localized lattice distortion called subgrain boundary with a misorientation angle of a few degrees. The parent grain is divided into areas with slightly different orientations – subgrains. This first step of RRX is also referred to as *recovery* or *polygonization* (Alley et al., 1995; De La Chapelle et al., 1998; Passchier and Trouw, 2005; Urai et al., 1986; White, 1977). Its energetic benefit arises from the lower energy of the generated subgrain boundary compared to randomly dispersed dislocations. In continuation, subgrains can progressively rotate and increase the misorientation angles between them so that a regular high-angle grain boundary is formed (Drury and Pennock, 2007). Since RRX involves the splitting of grains, its footprint in the polycrystalline structure is the reduction of the average grain size and the establishment of straight grain boundaries.

Strain-induced grain boundary migration (SIBM) is another recrystallization mechanism which contributes to the reduction of dislocation density by migrating grain boundaries Passchier and Trouw, 2005. The driving force for SIBM is a difference in dislocation density between two adjacent grains across the grain boundary

(Humphreys and Hatherly, 2004). The grain boundary is attracted by the region with a higher density of lattice defects (Means, 1981). After the passage of the grain boundary, the crystal is virtually free of dislocations. The evidences for SIBM being active are highly curved grain boundaries and irregular grain shapes (Jessell, 1986; Passchier and Trouw, 2005).

1.3.4 Crystal-Preferred Orientations (CPO)

Grains in polycrystalline ice under deformation develop a crystal-preferred orientation (CPO)[1]. This is produced by the rotation of deforming crystals as a consequence of deformation mainly through easy dislocation slip. In *uniaxial compression* (pure shear) the c-axis (normal to the basal plane) rotates towards the axis of maximum compression (Alley, 1988; Azuma and Higashi, 1985; Faria et al., 2014c; Gow and Williamson, 1976). As a result, initially randomly oriented grains develop a nearly unimodal preferred orientation of their c-axes which all align in the same direction parallel to the shortening direction (single maximum orientation distribution). A similar effect is produced by simple shear, i. e., the translation of parallel planes relative to each other. With increasing shear strain, the direction of maximum shortening progressively rotates from an initial angle of 45° towards an almost perpendicular orientation to the shear plane (e. g., Alley, 1988; Gow and Williamson, 1976; Jun et al., 2000; Llorens et al., 2016b; Montagnat et al., 2012, 2014; Treverrow et al., 2012). Hence, the c-axes also develop a single maximum CPO in simple shear. In the inverse case of *uniaxial extension*, the c-axes rotate away from the axis of maximum elongation and distribute in a plane normal to it, forming a girdle-type orientation distribution.

The development of CPO has been observed in natural samples from ice cores (Durand et al., 2009; Eichler, 2013; Faria et al., 2014a; Lipenkov et al., 1989; Weikusat et al., 2017b) as well as in laboratory-deformed ice (Jacka and Maccagnan, 1984; Treverrow et al., 2012). The mechanisms of its formation have been extensively studied with the help of computer simulations (Llorens et al., 2016a,b). The gross evolution of CPO with depth in ice cores is consistent with our general understanding of the strain configuration at the usual drilling sites. [2] In shallow depths, the predominant deformation mode is pure shear due to the thinning under the load of new ice layers. The CPO, starting with nearly random (uniform) distribution at the surface, develops with increasing depth towards a single maximum in the vertical direction (e. g., the North Greenland Eemian Ice Drilling (NEEM) ice core: Montagnat et al., 2014). At sites located on an ice divide, an additional component of extensional strain contributes to the CPO, causing the development of a girdle fabric or a mix of girdle and single maximum (e. g., the EPICA[3] Dronning Maud Land (EDML) ice core: see Chapter 8). With increasing depth and decreasing distance to the bedrock, the horizontal shear strain component becomes more dominant and typically drives the development of a strong vertical single maximum CPO in the deeper parts of ice cores.

[1] also referred to as lattice-preferred orientation (LPO), fabric, or texture in relevant literature.

[2] Most deep ice cores are drilled at ice domes or ice divides, i. e., at sites with simple strain configurations and low flow velocities. The East Greenland Ice-Core Project (EGRIP) is an exception.

[3] European Project for Ice Coring in Antarctica

1.3.5 Strain Localization

CPO is associated with mechanical anisotropy on the macroscopic scale (Budd and Jacka, 1989; Gao and Jacka, 1987). Its variations with depth can result in differences in the stress–strain relationship of the deforming ice. For instance, a vertical single maximum produced by vertical compression (pure shear) rotates most of the grains with their slip systems in an unfavorable arrangement for further compression. Pure shear thus causes a *hardening* of the material. In contrast, a vertical single maximum produced by horizontal shear offers a favorable arrangement of the c-axes for further shearing. Thus, simple shear causes the development of *soft* layers for further shearing in the ice column. Variations in mechanical anisotropy can lead to a localization of strain.

Inhomogeneous strain distributions in ice have been observed on multiple scales in the field (Talalay and Hooke, 2007) as well as in laboratory experiments (Golding et al., 2012). Localized shear bands are often correlate with characteristic changes in the CPO, grain size and/or impurity content (see Sections 2.1 and 2.2). However, recent numerical modeling studies of the deformation of polycrystalline ice suggest that strain localization is an intrinsic property of ice (Lebensohn et al., 2009; Llorens et al., 2016a,b; Riese et al., 2019, in review; Steinbach et al., 2016).

1.4 Impurities

In the scope of this thesis, the term ice impurities refers to chemical compounds or other extrinsic materials which originate from the atmosphere and were deposited at the ice-sheet (glacier) surface during or after the accumulation of new snow layers. Material which originates from the interaction with the glacier bedrock is not included in this consideration. Also air bubbles and other gas inclusions are usually treated separately and are not considered impurities in the narrower sense. A very useful review on glaciochemistry was written by Legrand and Mayewski (1997a).

Glacial polar ice is one of the purest materials on the Earth's surface. Mass concentrations of impurities in the Antarctic Ice Sheet vary between 10^{-9} during warm periods and 10^{-6} in the most dusty layers during glacial periods (Faria et al., 2010; Legrand and Mayewski, 1997a). Impurity concentrations in the Greenland Ice Sheet are roughly ten times higher due to its lower distance from continental sources. Ice impurities resemble the composition of aerosols in air masses above the precipitation site. Concentrations of individual impurity components show local and seasonal variations depending on the distance from their sources, transport paths, and types of deposition (Legrand and Mayewski, 1997a). Relevant literature distinguishes between *wet* and *dry* deposition, depending on whether precipitation is involved or not. During wet deposition, hygroscopic aerosols serve as condensation nuclei which, after having accumulated a sufficient amount of water molecules, fall down in the form of ice crystals, snow flakes, or rain drops ("rain out"). On their way down through the air column, occasional collisions with other aerosols result in a further "wash out" of aerosols from the atmosphere. Dry deposition refers to a direct trapping of aerosols out of the moving air due to their collision with the snow surface. The following overview lists major aerosol components found as impurities in polar snow and ice:

- **Mineral dust** in the atmosphere originates mainly from desert regions where large areas of eroded earth-crust material are exposed to blowing winds. Collisions between initially horizontally moving dust particles result

in vertical impulse causing further dispersion of the particles by wind. The size of mineral-dust particles deposited in the ice is typically in the range between hundreds of nanometers and a few micrometers (Wegner et al., 2015). The residence time of larger particles in the atmosphere is too short due to their heavy weight. They are typically deposited closer to their sources before they can reach the polar regions. The Chemical composition of mineral dust reflects the composition of the Earth's crust with Si, Al and Fe being the most abundant elements. Mineral dust also contains a substantial portion of Ca, mainly in the form of Ca-carbonate and Ca-plagioclase.

- **Marine aerosols** are salt particles created through dispersion of seawater droplets into the air, followed by evaporation of the water content. The ionic composition resembles the ionic ratios in seawater with major ions being Cl^-, SO_4^{2-}, Na^+, Mg^{2+}, Ca^{2+} and K^+. NaCl is by far the most abundant salt in marine aerosol(Warneck, 1988).

- **Sulfate** is the most common sulfur-containing aerosol. Chemical analyses of ice cores distinguish between sulfate originating from seasalt ($ss\,SO_4^{2-}$) and non-seasalt sulfate ($nss\,SO_4^{2-}$). The main nss sources are (a) the oxidation of natural or anthropogenic SO_2 in the higher troposphere (major contribution) and (b) marine biogenic sulfate as a product of the oxidation of dimethyl sulfide (DMS, mainly in Antarctica, Kaufmann et al., 2010). Strong temporal peaks in sulfate concentration are caused by volcanic eruptions. They serve as absolute chronological markers for ice core dating (section 1.1.2).

- **Nitrate** is another major acidic impurity. NO_3^- is formed in the troposphere by the oxidation of nitrogen oxides (NO_X). The many possible sources of (NO_X) include soil exhalation, biomass burning, lightning, cosmic radiation, oxidation of N_2O, and dissociation of N_2 (Legrand and Mayewski, 1997a). Although many ice-core records of nitrate exist, the interpretation of concentration variations remains challenging (Röthlisberger et al., 2000b; Wolff, 1995) and is further complicated by the high diffusion rates of NO_3^-, reported by Thibert and Dominé (1998).

- **Ammonium** is another nitrogen-containing aerosol component. It is produced and emitted to the atmosphere during bio-activity. In Greenland Ice Sheet, the ammonium concentration varies with the season and peaks in summer (Legrand and Mayewski, 1997a). NH_3 reacts with acidic aerosols (mainly H_2SO_4 and HNO_3), forming ammonium salts $(NH_4)_2SO_4$ and NH_4NO_3.

- **Black carbon** or soot is a product of an incomplete combustion of organic matter. During the 19th and 20th century, burning of fossil fuels caused an increase of black-carbon concentrations in the atmosphere (Wang et al., 2015). Higher concentrations of black carbon on snow and ice surfaces increase the absorption of solar energy (decrease albedo) and possibly contributed to the warming trend in the 20th century (McConnell et al., 2007).

Ice impurities play a central role in this thesis. Beside their key relevance as climatic proxies, their varying concentrations seem to affect the mechanical properties of ice. Consequently, they trigger inhomogeneities in the flow of ice sheets.

Chapter 2

Motivation and Objectives

The principal motivation for this thesis is elucidated in the first two sections of this chapter. Concrete objectives are defined in the last section (2.3).

2.1 Why is ice-age ice sometimes soft?

The title of a paper by Paterson (1991): "Why is ice-age ice sometimes soft?" expresses the observation reported already in prevous studies (e. g., Fisher and Koerner, 1986), that ice formed during glacial periods often deforms more readily than interglacial ice. Paterson (1991) reviewed the available data of borehole deformation rates at several drilling sites as well as laboratory creep experiments on natural ice samples. He concluded that "ice-age ice" deforms on average 2.5 times faster in simple shear compared to interglacial ice under the same stress and temperature conditions and argued that ice-flow models have to be modified to take in account these effects.

The enhanced creep of glacial ice was attributed to its inherently high impurity content compared to interglacial ice. The impurity concentrations in glacial ice are up to 2–3 orders of magnitude higher than in interglacial ice (Faria et al., 2010; Legrand and Mayewski, 1997b). In search for the responsible mechanism, (Paterson, 1991) reviewed microstructure data – grain sizes and c-axis preferred orientations (CPO) – and found that the high impurity concentration in glacial ice often correlates with a strong near-vertical single maximum CPO and significantly smaller grain sizes. Paterson's conclusions were the following: (1) High impurity concentrations in glacial ice (possibly chloride and sulfate) slow down grain boundary migration and grain growth resulting in reduced grain sizes. (2) Fine grains in simple shear rotate faster and develop strong single maximum CPO. (3) Ice with a pronounced vertical CPO deforms easier in simple shear parallel to the bedrock.

The basis of data grew significantly in the last decades due to the drilling of new ice cores and improvements of the analytical techniques. The efficiency of microstructure measurements grew with the development of fast automatic instruments (Review by Faria et al., 2014c; LASM: Krischke et al., 2015; Fabric Analyser: Peternell et al., 2010; Wilson et al., 2003) and the application of computer-based digital-image-processing algorithms for data analysis (Binder et al., 2013; Eichler, 2013). Thus, the grain size and CPO profiles along the EDML (Antarctica) and NEEM (Greenland) ice cores now exist at much higher spacial resolution and statistical significance than in previous ice cores (see chapter 8 for the EDML ice core and Montagnat et al., 2014 for the NEEM ice core). Recent data confirm correlations between impurity concentration, small grains, strong CPO and enhanced deformation also on smaller scales. Repeated logging of the NEEM borehole has revealed that strong fluctuations of impurity concentrations on the scale of several meters –

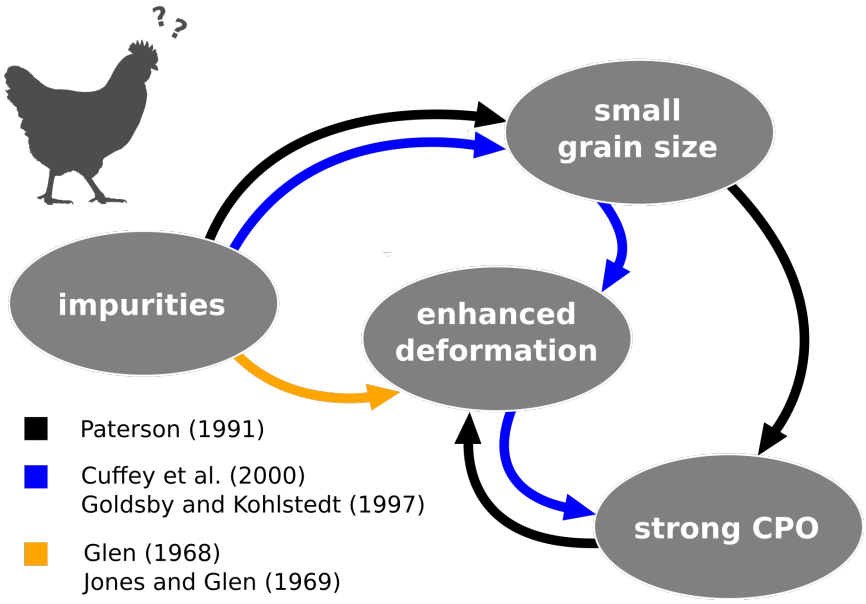

FIGURE 2.1: The chicken or the egg problem: High deformation rate, small grain size and strong CPO often characterize ice with high concentration of impurities. However, to distinguish between the main cause and its effects is not so straight forward. Different causality chains were proposed by Cuffey et al. (2000b), Glen (1968), Goldsby and Kohlstedt (1997b), Jones and Glen (1969), and Paterson (1991).

an effect of Dansgaard–Oeschger events – were reflected in a local reduction of the borehole diameter (Dahl-Jensen, pers. comm.). Also the EDML borehole shows localized deformations which correlate to abrupt changes of impurity concentrations in the ice core (chapter 8).

However, as will be addressed in the next section, the sense of causalities between the correlating observables is not resolved yet. To accomplish this quest is crucial to properly model the effect of impurities on the ice flow.

2.2 The Chicken or the Egg Problem

Paterson (1991) pointed out that enhanced shear deformation which is favored by a strong CPO further strengthens the CPO and keeps the grains small – i. e., there is a positive feedback between strain rate and CPO. In fact, the causality chain hypothesized by Paterson (impurities ⇒ small grains ⇒ strong CPO ⇒ enhanced deformation) is only one of the possibilities and the implication relations between the observables need to be verified one by one. In the classical view for instance, CPO is typically understood as a product of strain (Azuma and Higashi, 1985; Veen and Whillans, 1994). Similarly, finer grain sizes are usually interpreted as a product of higher strain rates (Faria et al., 2014c). Hence, a direct control of the strain rate (impurities ⇒ enhanced deformation) could also produce finer grain sizes and stronger CPO in the affected layers. Indeed, some impurities have been reported to enhance the dislocation activity, which directly controls the creep rate of ice (Glen, 1968; Jones and Glen, 1969; Whitworth et al., 1976). Another causality chain arises from the investigations by Cuffey et al. (2000b), Goldsby and Kohlstedt (1997b), and Goldsby et al. (2001) who found a direct dependence of strain rate on grain size (impurities ⇒ small grains ⇒ enhanced deformation ⇒ strong CPO). According to the authors,

grain-size-sensitive mechanisms such as grain boundary sliding (GBS) or diffusion along grain boundaries would play an important role for the flow of ice.

While the assumption that impurities act as the initial driver for different ice behavior seems to be justified, the relation between an enhanced strain rate and the characteristic microstructure (small grains and strong CPO) brings to mind the dilemma of the chicken or the egg (Fig. 2.1). In principle, the causality chain can only be resolved if concrete mechanisms behind the multiple correlations can be formulated and confirmed. Share the same motivation as Paterson (1991), our strategy is to confine the initial principal question "Why is impurity-rich ice soft?" to a more specific problem: How do different impurities integrate and distribute in ice? Addressing this question would not only help to resolve the causality dilemma stated above, but is also of great relevance for our understanding and interpretation of the palaeo-climatic records in ice.

2.3 How Do Impurities Integrate and Distribute in Ice?

The main objective of this thesis is to answeir the question "How do impurities integrage and distribute in natural ice?". In fact, this problem includes a number of subquestions, in particular: How do impurities interact with grain boundaries? Do grain boundaries and triple junctions contain higher concentrations of some impurities? Which components dissociate in ice and which form a second phase?

Liquid water is a relatively good solvent due to the electric dipole of the water molecule. In contrast, solid ice rejects most extrinsic substances from the crystal (Petrenko and Whitworth, 1999). This is caused by the dimensions and the geometry of the ice I_h lattice as well as the nature of the hydrogen bonds. The relevant theory predicts a few exceptions which – based on their ionic radii – could in principle substitute oxygens in the lattice (F^-, Cl^-) or fill interstitial sites (NH_4^+, Petrenko and Whitworth, 1999). However, most chemical compounds are in general not able to properly incorporate in ice. Thus, they introduce some kind of distortion or local disorder which is associated with an increase of free energy. The amount of energy is defined by the amount of lattice distortion which again depends on the concentration and form of impurities – e. g., individual ions, molecules, clusters or condensed phases (droplets and micro-particles). Furthermore, additional (chemical) effects can occur which can lower the eutectic point and lead to local melting (Bartels-Rausch et al., 2012; Dash et al., 2006).

Being planar lattice defects, grain boundaries also posses a finite energy expressed as interface tension ($\gamma \approx 65$ mJ m^{-2}, Hobbs, 1974). During recrystallization, migrating grain boundaries occasionally cross impurities, so that the lattice-disordered areas merge, resulting in a release of energy. Vice versa, the separation of impurities from a grain boundary requires an extra work. The attraction between grain boundaries and second-phase inclusions is known from material sciences as the *Zener pinning* (in Smith, 1948). The Zener force has a reducing effect on grain boundary migration and grain growth (Humphreys and Hatherly, 2004). Thus grain boundary pinning on dust particles has been suggested as the main grain-size reducing effect of impurities in glacial ice (Fisher and Koerner, 1986). Alley et al., 1986a,b reviewed the Zener theory and concluded that particle concentrations in ice sheets are in general too low to significantly affect normal grain growth. However, dissolved molecules or molecular clusters (nano-particles) are mobile enough to eventually stick to the migrating grain boundary. With time and increasing amount of recrystallization, the concentration of impurities dragged with the migrating grain

boundary would grow causing a decrease of the grain boundary mobility. Thus observations of accumulations of impurities in grain boundaries would be a direct evidence for the grain-size reducing effect of impurities.

Measured data on the distribution and form of impurities in natural ice are rare and difficult to obtain due to the extremely low concentrations which require very sensitive analytical techniques. Among all, the three most suitable tools proved to be: Raman spectroscopy, energy-dispersive X-ray spectroscopy (EDX) and laser ablation inductively coupled plasma mass spectrometry (LA-ICPMS). Wolff and Paren (1984) suggested that acids like HCl, HNO_3 and H_2SO_4 would concentrate at grain boundaries and triple junctions, lowering the eutectic point and forming liquid veins. This hypothesis was supported by Mulvaney et al. (1988) who used EDX to detect sulfur at three triple junctions in ice. Furthermore, Fukazawa et al. (1998b) detected sulfate in one triple junction using Raman spectroscopy. However, other Raman analyses by Ohno et al. (2005, 2006) and Sakurai et al. (2011) found most (or all) sulfates forming salt particles without any correlation with grain boundaries or triple junctions. In contrast, EDX experiments by Baker et al. (2003), Barnes (2003), Barnes et al. (2002), and Cullen and Baker (2001) and Iliescu and Baker (2008) demonstrated traces of sodium, chlorine, and sulfur in filaments which would grow out of grain boundaries after controlled surface sublimation of natural ice samples. Della Lunga et al. (2014) used UV-LA-ICPMS to analyze the spatial distribution of different elements in discrete samples from the glacial part of the NGRIP ice core. No correlation was found between impurities and grain boundaries in cloudy bands. However, the authors observed concentration peaks at grain boundaries in the cleaner parts of the ice. Particulate impurities (micro-inclusions) accumulated along grain boundaries were reported by Durand et al., 2006b who used the dust concentrations to model grain size evolution along the Dome Concordia ice core. However, other studies could not confirm such accumulations of micro-particles along grain boundaries (Faria et al., 2010).

A review of relevant literature shows that the results differ significantly from study to study. The way in which different impurities integrate in ice may in fact depend on various factors, e. g., the sample origin, temperature, deformation and recrystallization state, absolute impurity concentration and relative concentrations between different chemical compounds. In order to assess the questions stated at the beginning of this section, a more complex information is needed. Attaining this information requires a combination of complementary methods across different spatial scales and resolutions.

Chapter 3

Methods

Although quite specific in its object of research, glaciology is a highly multi-disciplinary field of science. Scientists with different backgrounds and expertises collaborate to compose 'the big picture'. Among the many methods applied in glaciology are for example airborne and satellite imagery and remote sensing, ground-penetrating radar and seismics, numerical modeling of ice flow and subglacial hydrology, ice core drilling and related on-site projects (e. g., borehole surveying), analysis of ice cores (gas and impurity content, isotopic composition, physical properties and crystal structure), experiments with laboratory-made ice, and many more. This chapter introduces analytical techniques which were used for the purpose of this thesis.

3.1 Ice Cores

Drilling and analyzing ice cores is an essential part of glaciology since it offers a unique access to real physical samples along the whole depth of an ice sheet. Deep ice core drilling projects are very expensive in terms of logistics, technology, and man power. Usually, it takes several field seasons to reach the base of the ice sheet. High expenses are associated not only with the drilling itself, but also with related programs such as run-up surveying and the localization of the optimal drilling site, as well as with the transport and the storage of recovered ice.

Freshly drilled ice cores are logged on-site during the drilling campaign and divided into longitudinal segments for different purposes following a previously agreed-upon cutting plan. The sample material used during this thesis originates mainly from the segment for the analysis of physical properties (PP), from the two deep ice cores EDML (Antarctica) and NEEM (Greenland).

3.1.1 EDML

The EDML (EPICA[1] Dronning Maud Land) ice core was drilled between 2001 and 2006 close to the Kohnen station in East Antarctica at 79°00′ S, 0°04′ E and elevation of 2892 m.a.s.l. (Oerter et al., 2009; Wilhelms et al., 2014). The drill site is characterized by relatively high accumulation rates of approximately 7 cm a^{-1} ice equivalent (Oerter et al., 2004) which enables a high temporal resolution of palaeoclimate signals. Its location on an ice ridge causes a slightly divergent flow with a surface velocity of 0.756 m a^{-1} (Wesche et al., 2007). The EDML ice core is 2774 m long and covers the last 150 ka (Ruth et al., 2007; Veres et al., 2013).

[1] European Project for Ice Coring in Antarctica

FIGURE 3.1: (a) Freshly drilled ice cores before being processed at EastGRIP, season 2017. (b) Visual stratigraphy image of a 50 cm long segment of the EDML ice core (1760.0 – 1760.5 m). The contrast of the image has been enhanced.

3.1.2 NEEM

The NEEM (North Greenland Eemian Ice Drilling) ice core was drilled between 2008 and 2012 in northwestern Greenland (77.45° N, 51.06° W, elevation 2450 m.a.s.l.). Accumulation rate at the drill site is 22 cm a^{-1} ice equivalent at a mean annual temperature of −29° C. The NEEM ice core is 2540 m long and covers approximately the last 100 ka of undisturbed ice (Rasmussen et al., 2013). The purpose of the NEEM project was to obtain a high resolution climatic record of the Eemian interglacial (northern hemisphere). The basal layers of the ice core contained Eemian ice (approx. below 2200 m), however, the stratigraphy was disrupted due to folding and large scale discontinuities (NEEM community members, 2013).

3.2 Measuring Ice Microstructure

3.2.1 Optical Microscopy

The classical optical microscope is a very powerful tool for the analysis of prepared surfaces as well as the bulk of ice specimens. The microtomed surface of ice reveals traces of grain and sub-grain boundaries as sublimation features due to thermal etching (Kipfstuhl et al., 2006; Mullins, 1957; Nishida and Narita, 1996). Focusing into the bulk reveals primary gas inclusions in form of air bubbles or clathrate hydrates (Fig. 3.2a, Weikusat et al., 2015). Impurities are visible in the form of micrometer-sized inclusions (Fig. 3.2c). Also secondary features produced by the pressure relaxation of the ice (Gow, 1971) become visible with time, such as plate-like inclusions (Fig.

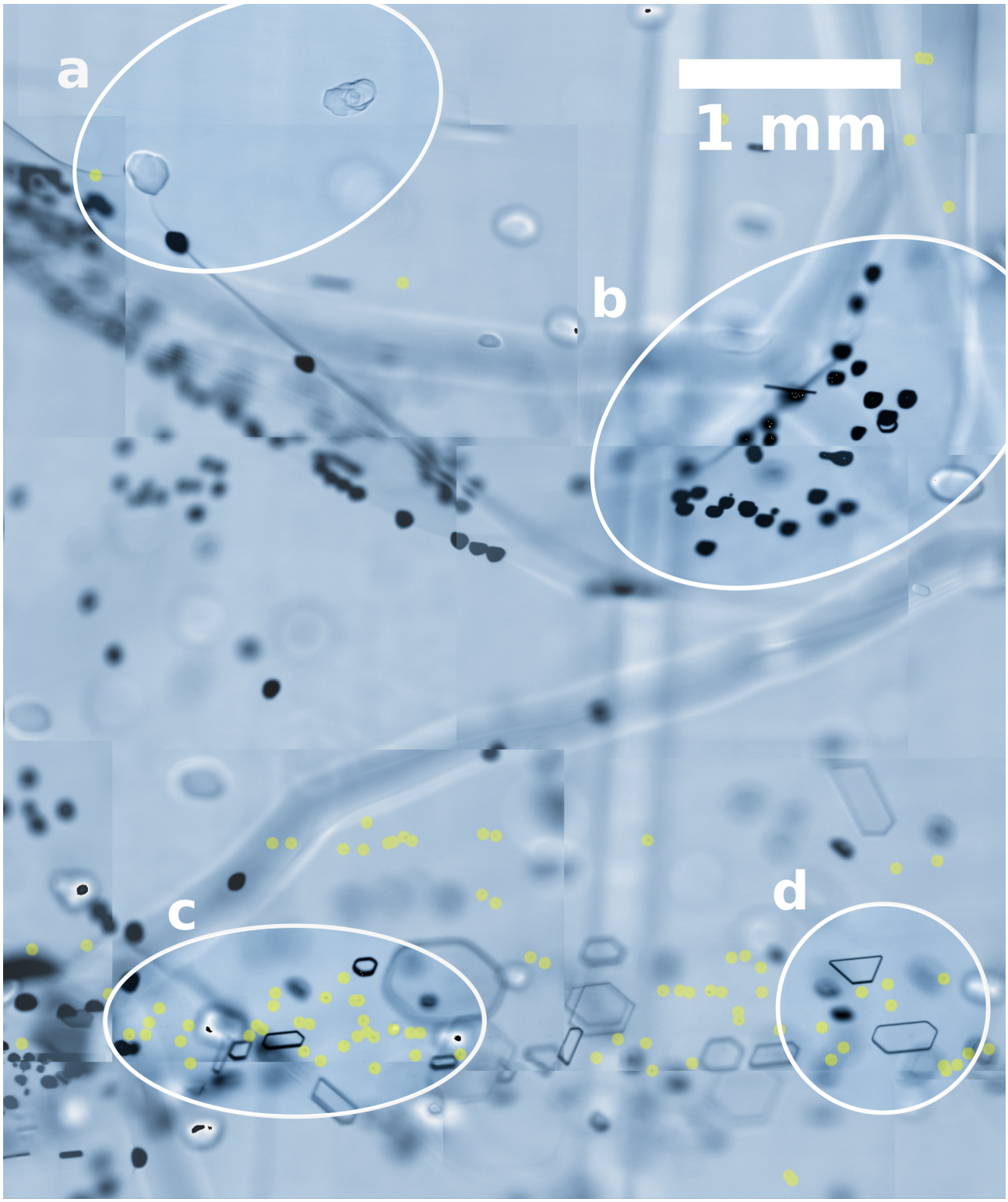

FIGURE 3.2: Detail of a microscope image of the bulk of an ice section (EDML, 2370.9 m, drilled in January 2004, Wilhelms et al., 2014) prepared and mapped in April 2015. The image was colorized in order to increase contrast. (a) Two clathrate hydrates, the left one is "pinning" a grain boundary. (b) Secondary gas inclusions form preferencially along the grain boundaries due to the presssure relaxation. (c) Impurities in the form of micrometer-sized inclusions (marked with yellow). (d) Hexagonal plate-like inclusions (Nedelcu et al., 2009) indicate the crystallographic orientation of the bulk.

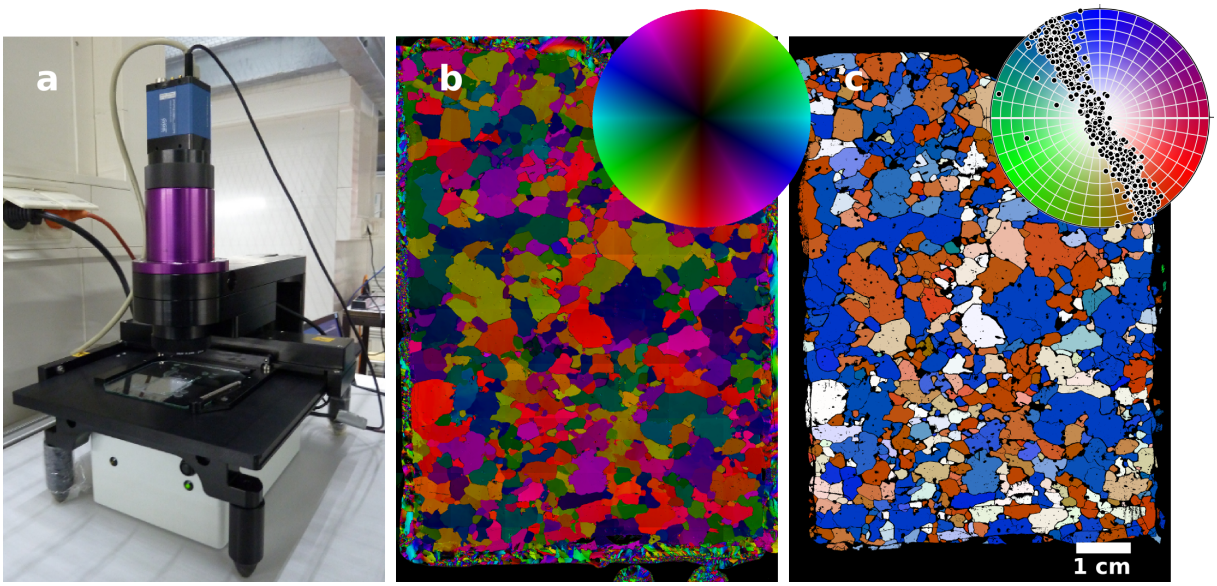

FIGURE 3.3: (a) The G50 Fabric Analyser set up in the ice laboratory (picture by Anneke Tammen). (b) A color-coded c-axis map (Trend image) of a vertical thin section (EGRIP, 685.3 m). (c) Processed c-axis data: segmented grains with average c-axis orientations projected onto the horizontal plane in a stereographic pole figure (Schmidt plot). The c-axes are oriented within one plane forming a girdle-type distribution.

3.2d, Nedelcu et al., 2009) and secondary gas inclusions (Fig. 3.2b) which form due to the decomposition of clathrate hydrates (Weikusat et al., 2012).

The microscope used at the AWI ice laboratory is a Leica DMLM with a CCD camera (Hamamatsu C5405), a frame grabber and a software-controlled x-y stage. Ice samples of up to 10 cm side length can be automatically scanned at the resolution of 3 µm pix^{-1}. The individual images are stitched together using a python script (see Appendix A.1).

3.2.2 Fabric Analyser

The Fabric Analyser by Russel-Head Instruments is an automatic device for the measurement of the c-axis orientations of thin sections of ice (and other birefringent materials). It works on the principle of a crossed-polarized-light microscope with multiple LED light sources with different inclinations, rotating polarizing filters, motorized x-y stage, CCD camera, and a dedicated hardware for the on-line calculation of the c-axis orientations. The maximal resolution is 5 µm per pixel, the maximal scan area is 10×10 cm^2. A more detailed description of the instrument is given by Peternell et al. (2010) and Wilson et al. (2003) and Eichler (2013).

The two-dimensional maps of c-axis orientations are further processed using dedicated software introduced in Eichler (2013). The program applies a set of filters and segmentation algorithms in order to extract grains and grain boundaries and to further analyze the morphology and CPO of the sample.

3.2.3 LASM

The Large Area Scanning Macroscope (LASM) is an instrument especially developed for the scanning of prepared ice surfaces in order to map the grain boundary and subgrain boundary structures (Krischke et al., 2015). The device features a line scan camera and a precise motorized stage to create high-resolution 2D scans of the

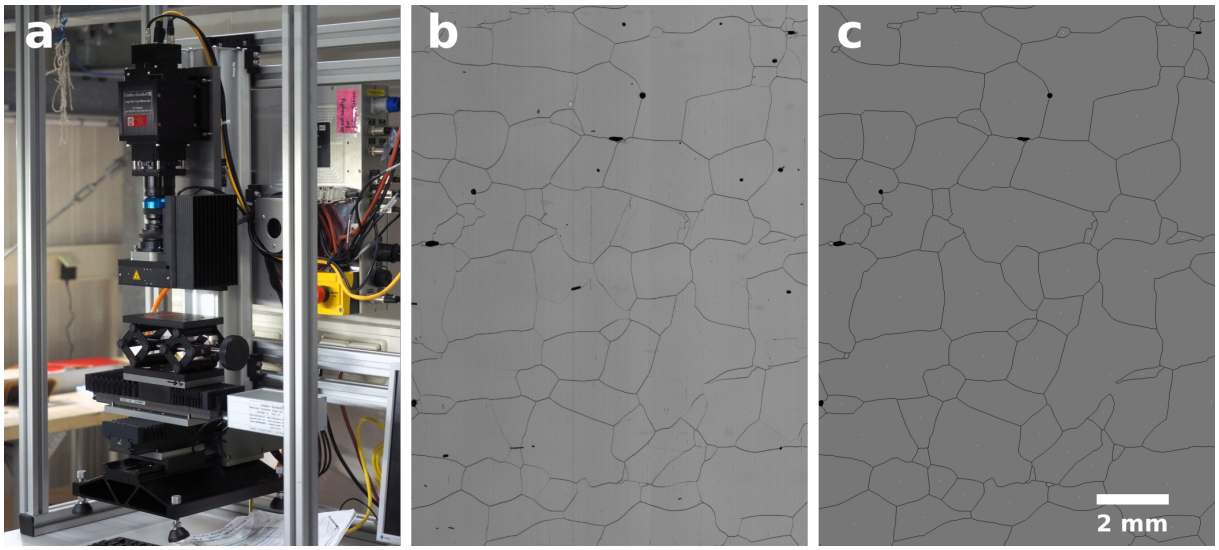

FIGURE 3.4: (a) The LASM instrument. (b) Detail of a line-scan image of a prepared ice surface (NEEM, 1757 m). Black curves are grain boundaries intersecting with the surface, visible due to enhanced sublimation. (c) Same detail of the processed LASM image with segmented grains and grain boundaries.

surface. This setting reduces the time needed for image acquisition to a few seconds. The grey-scale images are processed using an open-source software package (*Ice Microstructure Analyzer*) developed by Binder et al. (2013).

3.3 Raman Spectroscopy

Raman scattering was discovered by C. V. Raman (Raman and Krishnan, 1928). For this discovery he was awarded the Nobel Prize in 1930. The Raman effect is the inelastic scattering of light on molecules and solids. During this process, a tiny portion of incident photons (one in $10^6 - 10^7$) transmit part of their kinetic energy to the matter inducing molecular vibrations. The re-emitted photons experience a loss of energy E which becomes visible as a shift towards a lower light frequency ν:

$$\Delta E = h\Delta\nu \tag{3.1}$$

with the Planck constant h. This *Raman shift* is usually expressed in cm^{-1} as a difference in the wave number Δk:

$$\Delta k = \frac{\Delta\nu}{c} = \frac{\Delta E}{hc} \tag{3.2}$$

with the speed of light c. Due to the laws of quantum mechanics, molecular vibrations can adopt only discrete energetic levels (they are quantized) and, consequently, only transitions between these levels are possible. The occupation probabilities for these energetic states at a given temperature are described by the Boltzmann distribution. Calculating the Boltzmann factor at room temperature (or below) shows that most of the molecules (of any substance) will be at their lowest energetical level – the *ground state*. Hence, the Raman shift at such low temperatures will almost always correspond to the transition from the ground state to the first excitation state.

The number of vibrational modes of a molecule depends on the number of atoms and the symmetry of their arrangement. In the simplest case of a diatomic molecule (for instance N_2) the only vibration is due to stretching of the bond. The Raman shift of light passing through N_2 gas thus has a single value of $\Delta k \approx 2335\,\mathrm{cm}^{-1}$.

The more atoms participate forming a molecule, the more vibrational modes exist, including symmetrical and asymmetrical stretching, bending, twisting, etc. In general, the number of degrees of freedom associated with vibrations of a molecule with N atoms equals to $3N-5$ for a linear molecule and $3N-6$ for a non-linear one. The vibrational modes and the associated Raman shifts are specific for each type of molecule. High-precission measurements of the Raman spectra can reveal not only the chemical composition of a substance but also its phase and thermodynamic conditions. This made Raman spectroscopy a powerful tool for analytical chemistry, physics, and biology.

The basic Raman set-up consists of a monochromatic source of light and a monochromator with a detector for the scattered light. A standard Raman spectrum shows the intensity of detected light as a function of the relative wave number (Raman shift). The practical use of Raman spectroscopy experienced a revival in the 1960s with the discovery of laser, which provided monochromatic sources with sufficiently high intensity and precise wavelength.

Being an optical technique, Raman spectroscopy is best suited for the analysis of the interiors of light-transparent samples – such as ice. In combination with confocal optics, the excitation laser can be focused into a specimen's volume segment as small as a few μm^3, typically up to 1 mm below the sample surface. This is a significant advantage over surface-analytical methods, since many disturbing factors can be neglected, such as surface pollution and possible reactions and rearrangements of trace elements due to processes at the surface or during melting or sublimation. The backscattered light is collected with the same confocal optics and conducted into the spectrometer in order to resolve its spectral distribution. Since the laser power is limited in order to avoid melting, precise focusing and high quality of the prepared sample surface are the determining factors to obtain a discernible spectrum.

The sizes of micro-inclusions in ice are typically close to the optical resolution limit and they appear as single dots with different shading on the image background. This makes estimations of their shapes and volumes on the basis of the micro-photographs hardly possible. Thus, Raman spectra deliver rather qualitative information about the impurity content without any access to their absolute concentrations. Ice itself is also Raman-active so that an ice spectrum is always superimposed on the actual impurity spectra. In general, the characteristic impurity peaks are well distinguishable from the ice signal. However, not all molecules exhibit Raman-active vibrational modes. The most relevant case here is NaCl which is present in relatively high concentrations in polar ice because it is the main part of sea salt. Due to the selection rules, all vibrational transitions are forbidden and thus photons scatter only elastically. NaCl is therefore Raman-inactive and cannot be identified using Raman spectroscopy.

The Raman system used in this study is a WITec alpha 300 M+ combined with a NdYAG laser ($\lambda = 532$ nm) and a UHTS 300 spectrometer with a 600 grooves mm^{-1} grating. The excitation laser, the spectrometer, and the control unit are located in a warm laboratory at room temperature. Fiber optics connect them to the microscope unit which is placed at $-15\,^{\circ}C$. Thus, the system can be operated from the warm room, while sample preparation, mounting, and measurement take place in the cold laboratory. This set-up is more gentle to ice samples than the use of a cryo-stage, since exposure of samples to temperature gradients and moisture can be effectively avoided. A more detailed description of the system can be found in Weikusat et al. (2015).

For the purpose of this thesis, a LabVIEW program was developed for the remote control of the Raman system which enables to acquire Raman data on multiple

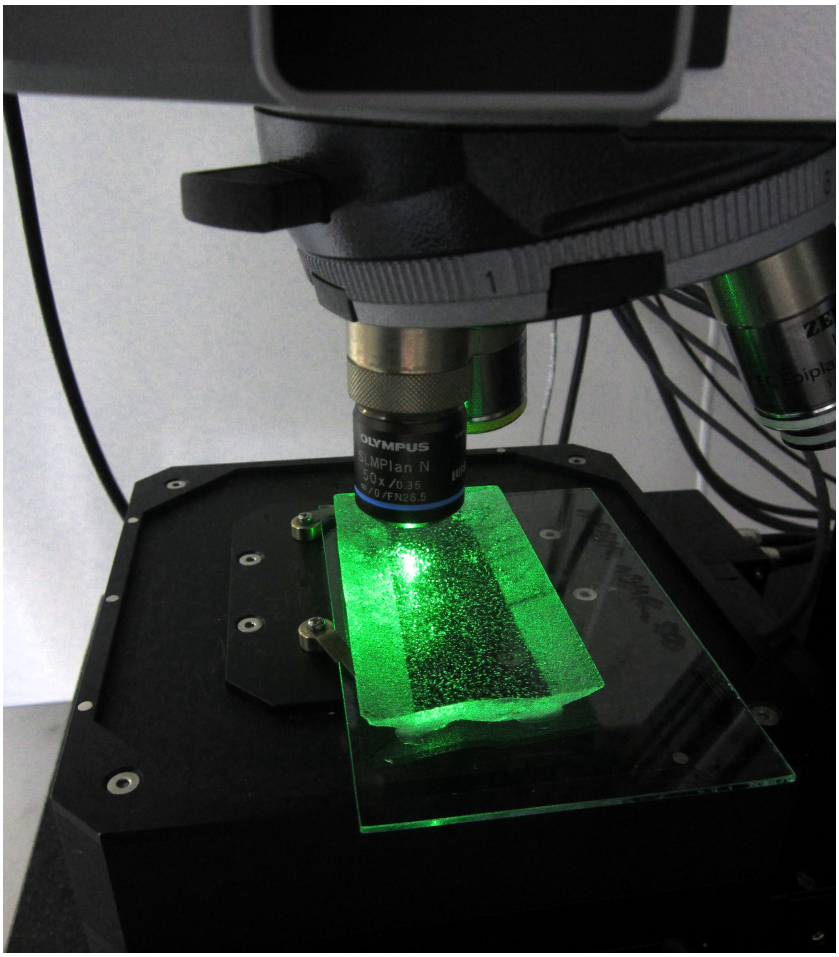

FIGURE 3.5: The WITec alpha 300 M+ Raman microscope in laser modus with a mounted ice specimen (picture by Christian Weikusat).

previously selected spots automatically. This approach significantly increases the efficiency of the Raman analysis of micro-inclusions and yields a significantly higher amount of measured data. A more detailed description of the routine is included in the Appendix (A.2).

Chapter 4

Synthesis

4.1 Main Outcome

This section briefly summarizes the main outcome of the thesis. The points listed below address individual results in an inverse order compared to the objectives in chapter 2, i. e., from more specific findings to rather general implications.

1. Micro-cryo-Raman spectroscopy proved to be an excellent technique for the identification of the chemical composition and phase of microscopic inclusions of condensed matter (micro-inclusions) in ice. The method is non-destructive, fully repeatable, firm against contamination, and non-invasive. The measuring routines developed during this thesis enabled the acquisition of statistically relevant numbers of spectra – higher numbers than ever before.

2. Micro-inclusions seem to be the preferred form of many (or most) impurity components in ice. The particle concentrations measured in melted samples (CFA) systematically underestimate the content of micro-particles in ice which are to a great extent formed by water-soluble salts. However, some of the chemical compounds in the analyzed samples did not form micro-inclusions at all, although they were clearly present in the ice (e. g., nitrate).

3. Micro-inclusions in ice show inhomogeneous spatial distributions. They often form horizontal layers on the mm–cm scale and distinct groups or chains on the sub-mm scale.

4. No correlation between micro-inclusions and the grain boundary network could be observed, which would be indicative of a strong interaction between micro-inclusions and migrating grain boundaries.

5. No other impurity signal could be detected in the grain boundaries or triple junctions which would indicate the presence of dissociated impurities or liquid channels. However, the concentrations may be too low for conventional Raman spectroscopy.

6. The comparison of Raman spectra of micro-inclusions and the overall ionic balance of the corresponding samples (ion chromatography) suggest that the physical and chemical form of impurities depend on the overall budget of the chemical compounds which, over the long resident time in ice, are subject to mixing and chemical reactions. From this point of view and on a limited spatial range, the deforming ice matrix may be better understood as a chemical reactor rather than a frozen archive.

7. The previous point may have relevant (and not necessarily negative) implications for the preservation of the chrono-stratigraphy of climatic signals in ice.

The diffusion rate of impurity-based climate proxies would basically depend on the diffusivity of the final products of the proceeded chemical reactions. Since many (or most) impurities form micro-inclusions with rather low mobilities, the concentration signal can be better preserved in lower depths.

8. With regard to the effect of impurities on mechanical properties of ice many questions remain. The results suggest that the interaction between migrating grain boundaries and micro-inclusions is rather weak and of short duration. Therefore, it is questionable whether the low particle concentrations in ice sheets could have such a remarkable effect on grain size. The role of the dissolved part of impurities remains unclear as well, since their extremely low concentrations did not allow for a detection with the Raman system.

4.2 Results Sorted by Papers

Paper I (Chapter 5)

Jan Eichler, Ina Kleitz, Maddalena Bayer-Giraldi, Daniela Jansen, Sepp Kipfstuhl, Wataru Shigeyama, Christian Weikusat, and Ilka Weikusat (2017). "Location and distribution of micro-inclusions in the EDML and NEEM ice cores using optical microscopy and in situ Raman spectroscopy." In: *The Cryosphere* 11.3, pp. 1075–1090. DOI: 10.5194/tc-11-1075-2017. URL: https://www.the-cryosphere.net/11/1075/2017/tc-11-1075-2017.pdf

We developed a technique for the mapping of visible micrometer-sized second phase inclusions (micro-inclusions) in the bulk of prepared ice specimens. These impurity maps were used to analyze spatial distributions of micro-inclusions and compare them with the positions of grain boundaries. Furthermore, these maps served as the basis for the cryo-Raman analysis. We mapped over 5000 micro-inclusions in four discrete samples from the NEEM and EDML ice cores (Chapter 5: Paper I). The analysis revealed no significant accumulations of micro-inclusions along grain boundaries. This result suggests that the attraction between micro-inclusions and migrating grain boundaries (Zener pinning) is rather a short-time interaction. No evidence for micro-inclusions being dragged by a migrating grain boundary could be found.

The impurity maps revealed that the ice samples contained significantly higher concentrations of micro-inclusions compared to the concentrations of solid particles in the melted ice (Chapter 5: Paper I). This result indicates that, additionally to solid mineral dust particles, many other (eventually water-soluble) chemical compounds also form microscopic inclusions of condensed phase in the ice matrix.

Paper II (Chapter 6)

Jan Eichler, Christian Weikusat, Anna Wegner, Birthe Twarloh, Melanie Behrens, Hubertus Fischer, Maria Hoerhold, Daniela Jansen, Sepp Kipfstuhl, Urs Ruth, Frank Wilhelms and Ilka Weikusat (2018). "Impurity analysis and microstructure along the climatic transition from MIS 6 into 5e in the EDML ice core using cryo-Raman microscopy". Accepted for publication in *Frontiers in Earth Science*. DOI: 10.3389/feart.2019.00020.

The analysis of Raman spectra acquired in-situ from selected micro-inclusions along the climatic transition between the last interglacial (MIS 5e) and the penultimate glacial (MIS 6, Chapter 6: Paper II) further verified the observation put forward in (Chapter 5: Paper I) that a significant part of water-soluble impurities form micro-inclusion in ice. 96% of the Raman spectra in the ice formed during MIS 5e were identified as sulfate particles, mainly gypsum, sodium sulfate, iron-potassium sulfate (likely jarosite), and other unspecified sulfates. In contrast, micro-inclusions in ice formed during MIS 6 were identified mainly as crust-forming minerals: quartz, feldspar, and mica. A number of minerals have been identified in ice for the first time using a cryo-Raman: mica, graphite, anatase, hematite, possibly jarosite, and bloedite. On the contrary, some of the expected species were not present in the statistics at all, such as Ca-carbonate, Ca-plagioclase and nitrate salts. The combination of the Raman analysis with the ion chromatography (IC) suggests that the way impurities incorporate into ice varies not only from species to species, but rather depends on the overall ion budget and chemical reactions between the different compounds.

Paper III (Chapter 7)

Florian Steinbach, Ernst-Jan N. Kuiper, Jan Eichler, Paul D. Bons, Martyn R. Drury, Albert Griera, Gill M. Pennock, and Ilka Weikusat (2017). "The Relevance of Grain Dissection for Grain Size Reduction in Polar Ice: Insights from Numerical Models and Ice Core Microstructure Analysis." In: *Frontiers in Earth Science* 5, p. 66. ISSN: 2296-6463. DOI: 10.3389/feart.2017.00066. URL: https://www.frontiersin.org/article/10.3389/feart.2017.00066

The numerical modeling platform ELLE was used to investigate the effect of grain dissection – splitting of former grains due to strain-induced grain boundary migration (SIBM). The simulations were compared to grain and sub-grain structures along the NEEM ice core extracted from (i) the full crystallographic orientation maps recorded with electron backscatter diffraction (EBSD) and (ii) the c-axis orientation maps from the automatic Fabric Analyser. The results show that grain dissection is an effective grain-size reducing mechanism occurring during dynamic recrystallization additionally to polygonization. It is particularly efficient in ice deforming under stable conditions where the microstructure parameters (grain size, CPO) approach a steady state.

Paper IV (Chapter 8)

Ilka Weikusat, Daniela Jansen, Tobias Binder, Jan Eichler, Sérgio H. Faria, Frank Wilhelms, Sepp Kipfstuhl, Simon Sheldon, Heinrich Miller, Dorthe Dahl-Jensen, and Thomas Kleiner (2017b). "Physical analysis of an Antarctic ice core–towards an integration of micro- and macrodynamics of polar ice." In: *Philosophical Transactions of the Royal Society A: Mathematical, Physical and Engineering Sciences* 375.2086, p. 20150347. DOI: 10.1098/rsta.2015.0347. URL: http://doi.org/10.1098/rsta.2015.0347

The microstructure parameters (CPO, grain size and shape distribution, visual stratigraphy) were evaluated together with measurements of the borehole displacement and modeled strain rate estimates along the whole length of the EDML ice core. The profile was divided into five specific depth zones with characteristic deformation modes and their imprint in the micro- and meso-structure of the ice.

While the CPO can be interpreted mainly as result of strain, the grain topology is strongly affected by recrystallization. Thus, grain-shape preferred orientations can be only detected in depths with relatively high strain rates, such as the lowest part (region 5) where strong shearing parallel to the bedrock occurs. The transition between region 4 and 5, which is characterized through anomalous behavior of many of the parameters, overlaps with the transition between the last interglacial and the penultimate glacial period.

Paper V (Chapter 9)

Johanna Kerch, Olaf Eisen, Jan Eichler, Tobias Binder, Pascal Bohleber, Johannes Freitag, Paul Bons and Ilka Weikusat (2019). "Short-scale variations in high-resolution crystal-preferred orientation data in an alpine ice core – do we need a new statistical approach?". In preparation.

The development and variability of the microstructure (grain size, CPO) was investigated along an alpine ice core (KCC) and compared to the corresponding density and air-content profiles. Similar to polar ice sheets, the CPO in a cold alpine glacier shows a development from nearly isotropic c-axis distribution towards highly anisotropic ice. The strong variability of the CPO is likely a product of deformation localization and the development of shear zones. In order to assess the uncertainty of CPO variability over multiple scales and resolutions, a new statistical approach needs to be adopted.

4.3 Concluding Remarks

In this section we want to come back to our original motivating question: What makes impurity-rich ice soft in simple shear? In Section 2.2 we made the assumption that the multi-correlation between impurities, small grains, strong CPO, and enhanced shear rate arises from a chain of causal mechanisms between the features in question. We also stated that a positive feedback loop could even strengthen the correlations. In fact, one possibility worth consideration is that there is no simple proportionality function between impurities and strain rate. Rather, there is an intrinsic trait of ice to localize deformation. Simulations of ice microstructure deforming in simple shear (Llorens et al., 2016b) demonstrated that localized high-strain bands form even without any impurity effect. Strain localization seems to be a characteristic feature of mechanically anisotropic materials in general (Ran et al., 2018). Thus, variations of the impurity content in different ice layers could simply function as a release mechanism for localized deformation.

4.4 Future Perspectives

The advantages of the micro-cryo-Raman spectroscopy and the routines developed during this thesis could be used for a wide range of applications in the future. A higher counting statistics would provide a more quantitative insight into the composition of micro-inclusions and allow for better estimations of how much impurity content is present in which form. This should be feasible when focusing on regions with higher impurity content such as cloudy bands or other high-concentration layers.

The possibility to analyze ice samples directly (or shortly) after they have been drilled would provide an advantage, because the relaxation effect could be kept at a minimum. This could resolve the uncertainty regarding the composition of the "black dots" which serve as seeds for the formation of secondary gas inclusions during the relaxation of deep ice and which often correlate with the position of grain boundaries (see Fig. 5.7 and the corresponding text in Sect. 5.4.2).

The usage of a second excitation laser with a different wavelength would enable the identification of micro-inclusions which showed strong luminescence at $\lambda = 532$ nm and could not be identified so far.

Additional temperature control (e. g., by using a thermoelectric cooling cell) would allow to study phase transitions of different impurity compounds.

Within the framework of a future project, extensive numerical simulations using the modeling platform ELLE could provide valuable hints regarding the effect of impurities on the evolution of ice microstructure. Preliminary test run by F. Steinbach and P. D. Bons (personal comm.) showed that layers of reduced grain size developed after locally decreasing the mobility of grain boundaries. In a similar way, other scenarios should be systematically tested using ELLE, i. e., the impurity effect on other parameters, such as grain boundary energy.

Chapter 5

Paper I

Location and distribution of micro-inclusions in the EDML and NEEM ice cores using optical microscopy and in situ Raman spectroscopy

Jan Eichler [1,2], Ina Kleitz [1], Maddalena Bayer-Giraldi [1], Daniela Jansen [1], Sepp Kipfstuhl [1], Wataru Shigeyama [3,4], Christian Weikusat [1], and Ilka Weikusat [1,2]

[1] Alfred Wegener Institute Helmholtz Centre for Polar and Marine Research, 27568 Bremerhaven, Germany
[2] Department of Geosciences, Eberhard Karls University Tübingen, 72074 Tübingen, Germany
[3] Department of Polar Science, SOKENDAI (The Graduate University for Advanced Studies), 10-3 Midori-cho, Tachikawa, Tokyo, 190-8518, Japan
[4] National Institute of Polar Research, 10-3 Midori-cho, Tachikawa, Tokyo, 190-8518, Japan

Published in *The Cryosphere*, 5 May 2017.

Abstract

Impurities control a variety of physical properties of polar ice. Their impact can be observed at all scales - from the microstructure (e.g., grain size and orientation) to the ice sheet flow behavior (e.g., borehole tilting and closure). Most impurities in ice form micrometer-sized inclusions. It has been suggested that these µ-inclusions control the grain size of polycrystalline ice by pinning of grain boundaries (Zener pinning), which should be reflected in their distribution with respect to the grain boundary network. We used an optical microscope to generate high-resolution large-scale maps (3 µm pix^{-1}, 8×2 cm^2) of the distribution of micro-inclusions in four polar ice samples - two from Antarctica (EDML, MIS 5.5) and two from Greenland (NEEM, Holocene). The in situ positions of more than 5000 µ-inclusions have been determined. A Raman microscope was used to confirm the extrinsic nature of a sample proportion of the mapped inclusions. A superposition of the 2D grain boundary network and µ-inclusion distributions show no significant correlations between grain boundaries and µ-inclusions. In particular, no signs of grain boundaries harvesting µ-inclusions could be found and no evidence of µ-inclusions inhibiting grain boundary migration by slow mode pinning could be detected. Consequences for our understanding of the impurity effect on ice microstructure and rheology are discussed.

5.1 Introduction

Polar meteoric ice is one of the purest materials on Earth. Impurity mass concentrations in the Antarctic ice sheet vary between ppbm during warm periods and ppmm in the most dusty layers in cold periods (Faria et al., 2010; Legrand and Mayewski, 1997a). Values for the Greenland ice sheet are approximately ten times higher. Impurities enter the ice sheet during deposition in the form of terrestrial dust, salt particles and other aerosols e.g. from bio-activity, ocean, volcanoes or combustion, or in the form of gas inclusions from air bubbles. Trace substances are a subject of intense ice core studies for many reasons. Their chemical and isotopic compositions can be linked to atmospheric and climatic processes (climate proxies), their analysis provides an important insight into processes and constraints of the past of Earth's climate (Dansgaard et al., 1982; EPICA community members, 2004, 2006; GRIP Project Members, 1993; Kuramoto et al., 2011; Wegner et al., 2015). When linked to geologic events (Sigl et al., 2015), they can serve as absolute chronological markers for ice core dating (sulfate and tephra layers from volcanic eruptions, Gow and Meese, 2007). And finally, many material properties of ice are controlled or modulated by its impurity content. This is the case for the dielectric constant and electrical conductivity, measured systematically using dielectric profiling (DEP) and electrical conductivity method (ECM) (Stillman et al., 2013; Taylor et al., 1993; Wilhelms et al., 1998; Wolff et al., 1997), but applies also to mechanical properties of ice - such as creep behavior and viscosity - which are of great interest with respect to ice rheology and ice sheet dynamics. The influence of various impurities on deformation rate has been observed in laboratory tests (e.g., Dahl-Jensen et al., 1997) as well as in the field from borehole tilting and closure (e.g., Fisher and Koerner, 1986). The link between impurity content and strain rate becomes most evident when comparing ice-age ice with ice from warm periods. Observations show that the impurity-rich ice-age ice deforms on average 2.5 times faster in simple shear (Paterson, 1991). Several explanations for this effect have been proposed, however the responsible mechanisms still remain under discussion. Since ice-age ice usually develops a different microstructure - e.g., stronger crystal preferred orientation (CPO), smaller grains (Cuffey et al., 2000a; Paterson, 1991) - the higher strain rates may result from an interplay between impurities, microstructure and recrystallization.

With increasing interest in the impurity content, analysis methods have been refined over the past years. Continuous flow analysis (CFA) became a standard part of ice core processing (Kaufmann et al., 2008) owing to its effectivity and high depth resolution. However, the aim to understand impurity-related processes in polycrystalline ice requires the application of approaches dedicated to the solid state. Thus, advanced analytical techniques, such as scanning electron microscopy (SEM), Raman spectroscopy or laser ablation inductively coupled plasma mass spectrometry (LA-ICPMS) became popular with glaciologists. However, each of these methods brings its specifications and constraints and the results often lead to contradictory conclusions. Comparative studies may be necessary to clear these discrepancies in future.

The composition, form, location and distribution of impurities are different in ice compared to liquid water. Due to the electric dipole moment of the H_2O molecule, water is a good solvent. On the contrary, the ice crystal is not, and will reject most extrinsic substances out of the matrix, forming a second phase (Petrenko and Whitworth, 1999). Only few elements are theoretically able to be incorporated into the ice lattice. According to Jones, 1967 and Jones and Glen, 1969 F^-, Cl^-, K^+ and NH_4^+ in low concentrations are able to substitute oxygen atoms or enter the ice lattice

interstitials. In both cases they would introduce ionic and Bjerrum-defects and significantly affect the charge carrier density of the ice crystal. Since protonic defects can alter dislocation mobilities, ice doped with these species manifests higher strain rates than pure ice (Glen, 1968). However, the doping experiments by Jones and Glen probably represent upper bounds with respect to natural ice which is formed from snow flakes inheriting impurities from atmospheric processes. Another widely discussed form of ice impurities was proposed by Wolff and Paren, 1984 who interpreted DC-conductivity as caused by conduction through acidic environments along grain boundaries and triple junctions. The authors suggested that acids like HCl, HNO_3 and H_2SO_4 would concentrate at grain boundaries lowering the eutectic point of the solute and thus forming liquid veins. The existence of an acidic vein network was supported by Mulvaney et al., 1988 who found sulfur at three triple junctions using energy-dispersive X-ray spectroscopy (EDX), and Fukazawa et al., 1998b who measured a sulfate peak in a triple junction using a Raman microscope. However, other Raman-spectroscopic studies by Ohno et al., 2005, 2006 and Sakurai et al., 2011 found most (or all) sulfates forming salt particles. In contrast, EDX experiments by Cullen and Baker, 2001, Barnes et al., 2002, Barnes, 2003, Baker et al., 2003 and Iliescu and Baker, 2008 found traces of sodium, chlorine and sulfur in filaments, which would grow out of grain boundaries after controlled surface sublimation of natural ice samples. Della Lunga et al., 2014 analyzed the distribution of a variety of elements in discrete samples from the glacial part of the NGRIP ice core using UV-LA-ICPMS. No correlation was found between impurities and grain boundaries in cloudy bands, however, the authors observed concentration peaks at grain boundaries in the cleaner parts of the ice. There is no consensus yet about the abundance and relevance of impurity segregation to grain boundaries.

In terms of mass fraction, most impurities form second phase inclusions, i.e., inclusions of extrinsic material or another lattice-incoherent phase (Alley et al., 1986a; Ashby, 1969; Humphreys and Hatherly, 2004). Due to their typical size of a few micrometers we call them in the following µ-inclusions. Water-insoluble dust particles as well as water-soluble particulate salts are the most abundant µ-inclusions. Their concentrations are highly variable along the ice cores. For instance, dust concentrations in the EDML ice core measured by continuous flow analysis (CFA, Wegner et al., 2015) vary between 10^3 and 10^5 particles per milliliter. Strata with high concentrations of µ-inclusions are visible in ice cores and are often called "cloudy bands" (Svensson et al., 2005). µ-inclusions appear under an optical microscope as dark spots near the optical detection limit - commonly referred to as "black dots" (see Fig.5.1). When using optical microscopy it is impossible to examine their state of aggregate, shape, color or composition, and thus the term "black dot" not only reflects their visual appearance but also our uncertainty about their nature and composition.

High concentrations of µ-inclusions are usually associated with certain changes in ice microstructure. On the large scale, ice-age ice was reported to be characterized by stronger CPO (e.g., Faria et al., 2014a; Gow and Williamson, 1976; Paterson, 1991), cloudy ice exhibits in general smaller grain sizes than clean ice. Since grain growth involves grain boundary migration, impeding grain boundary movement by µ-inclusions would consequently have a grain-size reducing effect. The attractive force between µ-inclusions and grain boundaries is known from material sciences and has been first modeled by Zener (in Smith, 1948) - Zener pinning. When a migrating grain boundary passes a particle, its energy is reduced by the portion of the cross sectional area. Depending on the grain boundary driving force, the pinning pressure and the mobility of the particles, grain boundary can be completely

stopped (pinned), free itself after a while from the particles and continue its motion, or drag the particles with it. Alley et al., 1986a,b reviewed the Zener theory and available data with respect to the pinning effect on normal grain growth in cold ice. They differentiate between a low velocity regime, where the grain boundary is pinned by the impurities, and a high velocity regime, where the grain boundary continues its motion leaving the impurities behind. Alley et al., 1986b conclude that pinning on µ-inclusions occurs in high velocity regime and the concentration of microparticles is too low in general to significantly affect grain growth (the only exceptions are tephra layers from volcanic eruptions). Durand et al., 2006b simulated grain size evolution along the Dome Concordia ice core by modeling normal grain growth controlled by pinning on dust particles. They suggest that dust particles will indeed impede grain growth if they concentrate at grain boundaries. However, a direct proof for such a particle distribution was not provided, since grain boundaries could not be imaged. On the contrary, Raman-measurements of µ-inclusions in the Dome Fuji ice core, presented by Ohno et al., 2005, 2006, showed that major part of the particles (mostly sulfate salts) were located in grain interiors. Faria et al., 2010 evaluated relevant microstructure and impurity data concerning the integrity of the EDML ice core. According to their report, black dots in the microstructure mapping images do not accumulate along grain boundaries for depths down to 2300 m. Only below this depth, and particularly in the deepest 200 m of the core, accumulations at grain boundaries and on the surface of clathrate hydrates were observed.

So far, studies on spatial distributions of µ-inclusions in ice were based on discrete observations of a few dust or salt particles. In order to discuss general concepts, such as the formation of the CFA signal, predominant form of impurities in situ and their effect on recrystallization (e.g. grain boundary pinning), more systematic and statistically relevant approaches are necessary. The aim of this study is to provide a more detailed insight into the in situ concentrations and distributions of µ-inclusions. We mapped over 5000 µ-inclusions within four different ice samples from polar ice cores. Overall and local concentrations are estimated and compared with the available CFA data. Special attention is payed to the correlation between µ-inclusions and the grain boundary network.

5.2 Methods and sample material

The state in which impurities are included in ice is different from their form in melt water (CFA). In order to reveal their distribution and in situ form, more data based on direct measurements of ice samples are needed. Optical microscopy and Raman spectroscopy provide the opportunity to explore the interior of ice samples in a non-destructive way. This is a significant advantage over surface-based methods (e.g., SEM), where contamination and sublimation-related redistribution of impurities have to be considered (e.g., Barnes, 2003). We use microstructure mapping to create large area maps (8×2 cm^2) of the specimens surfaces and interiors. This microscopical technique was introduced by Kipfstuhl et al., 2006 and it enables us to pinpoint visible µ-inclusions as well as grain and subgrain boundaries. We use a Raman microscope to prove that we are dealing with extrinsic material and to investigate the composition of selected µ-inclusions.

As the lower impurity content in warm-period ice provide a better chance to observe and characterize the majority of µ-inclusions over a large sample area and analyze their correlation with the microstructure, we focused our study on samples

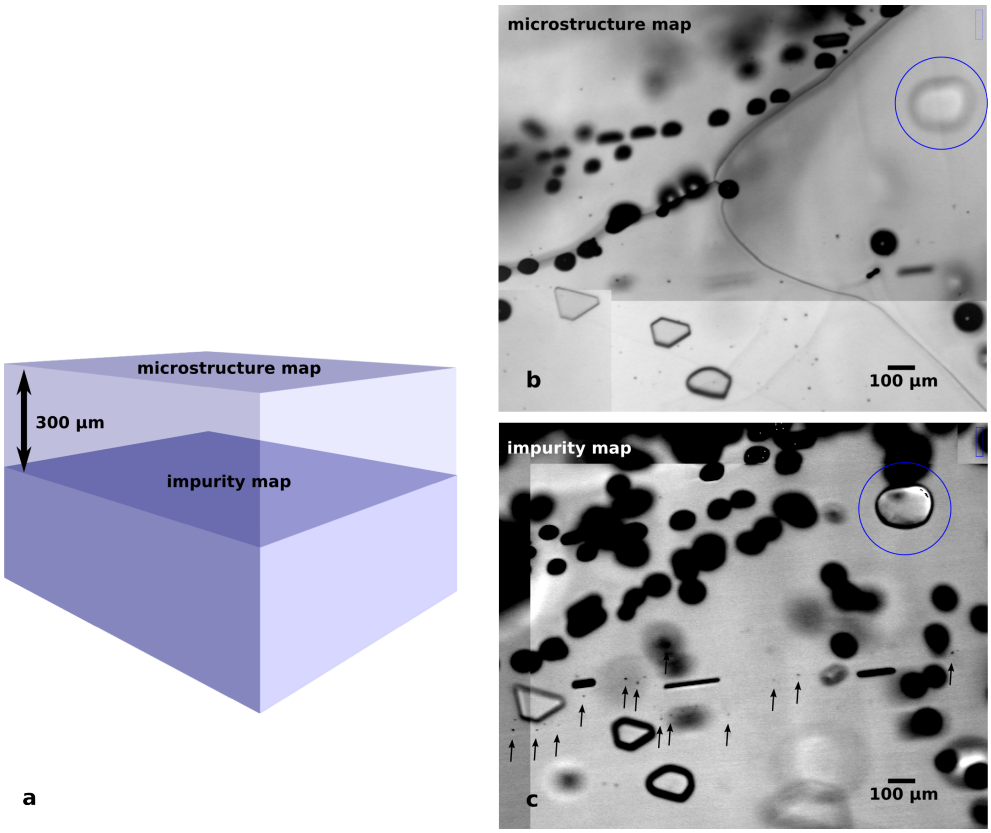

FIGURE 5.1: (a) Schematic of positioning stacked microstructure maps from surface and inside the sample. The focus distance between the two mapping planes in general depends on the application of this method (e.g. investigation of air inclusions or µ-inclusions). In order to correlate µ-inclusions and grain boundary grooves, for this study a distance of 300µm has been chosen. (b) Surface-focused photomicrograph from EDML-2371.9 (2371 m, drilled in 2006). The image shows three grain boundaries as black thin curves and a triple junction. "Black dots" in this map type are due to surface pollution by frost particles and should not be confused with µ-inclusions in the impurity maps. Below the surface - and slightly out of focus - a clathrate hydrate (marked with blue circle) and three Plate-like inclusions (hexagonal objects) are visible. Roundish black objects of the size of up to 100 µm are secondary gas inclusions formed by relaxation of the material. At the surface they are clearly attached to the left grain boundary. (c) Photomicrograph focused ca. 300µm below the surface. The grain boundary grooves disappeared but objects in the sample volume came into focus - the clathrate hydrate and plate-like inclusions are sharp now. "Black dots" in this image (pinpointed with arrows) are chemical impurities in the form of µ-inclusions.

from warmer periods. Furthermore, one of the very few studies which found evidence for a connection of spatial distribution of impurities along grain boundaries reported this evidence as a characteristic of "clean" interstadial ice (Della Lunga et al., 2014). Four samples were analyzed - two from the EDML ice core (Antarctica) and two from the NEEM ice core (Greenland). The EDML samples (EDML-2371.4, EDML-2371.9) originate from 2370 m depth which corresponds to the early Eemian (MIS5.5). The NEEM samples (NEEM-1346.2, NEEM-1346.5) originate from the Holocene, 740 m below surface and around 4000 years b2k (Rasmussen et al., 2013).

5.2.1 Impurity maps

The sample preparation has been described by Kipfstuhl et al., 2006. Specimens of the thickness of around 1 cm are cut with a band saw (see cutting plan in Fig.5.3d). Both surfaces are polished with a microtome knife and exposed to air for a few hours. Sublimation smoothens the surface and creates grooves at sites of high energy, where grain and subgrain boundaries intersect the surface. In this way 2D-maps of grain boundary networks and subgrain structures can be created (Binder et al., 2013). When focusing into the ice volume and choosing transmission light mode, surface features such as etching grooves fade out but other objects inside the sample come into focus. Typical features are gas inclusions (air bubbles and clathrate hydrates), relaxation features (secondary bubbles, plate-like inclusions) and µ-inclusions (see examples in Fig.5.1b,c and Fig.5.2c,d). µ-inclusions appear as dark spots near the resolution limit of the microscope.

We use an optical microscope (Leica DMLM) with a CCD camera (Hamamatsu C5405), frame grabber and a software-controlled x-y stage. Ice samples of up to 10 cm side length can be scanned at the resolution of 3 µm pix^{-1}. The final microstructure map is stitched from up to 1500 individually captured photomicrographs. We combine two of these scans for each sample - a microstructure map focused onto the surface to reveal grain boundaries, and an impurity map focused ca. 300 µm into the sample volume to visualize µ-inclusions (see Fig.5.1a). Such a stack of maps allows us to study inclusions in direct relation to the grain boundary network. Since µ-inclusions are mapped within the sample volume, contamination is not an issue. Due to the obliquity and 3D shape of grain boundaries, their positions inside the sample are not exactly the same as the etching grooves on the surface. To keep this uncertainty low the second scan must be focused close below the surface. Black dots in impurity maps were detected manually. The low contrast and size of black dots in the images did not support the application of automatic detection filters. Visual detection and manual counting of µ-inclusions is a time-consuming process which requires a certain amount of patience and discipline. Since it is based on observer's subjective judgment, the results may contain an observer-dependent variance. The impurity maps presented in this study were generated by three observers independently, however, using the same criteria. Partial comparison of the results at overlapping regions showed a good consistency within the data and thus confirmed the observer-dependent factor being minimal.

5.2.2 Raman spectroscopy

A confocal Raman microscope was used to analyze the composition and mineralogy of selected µ-inclusions. The AWI cryo-Raman system consists of a WITec alpha 300 M+ with an UHTS 300 spectrometer and a Nd:YAG laser (532 nm) set up in the cryolab at −15 °C (Weikusat et al., 2015). Within the scope of this paper, the measured Raman spectra shall serve as a proof that the mapped black dots are in fact chemical impurities in the form of µ-inclusions. A detailed analysis of the detected minerals is being prepared for publication.

5.3 Results

Microstructure and impurity maps were generated for the four samples: EDML-2371.4, EDML-2371.9, NEEM-1346.2, NEEM-1346.5. We localized 5784 µ-inclusions in total (in Fig.5.2,5.3,5.5,5.6 marked with yellow circles). Their size of 2–3 pixels in

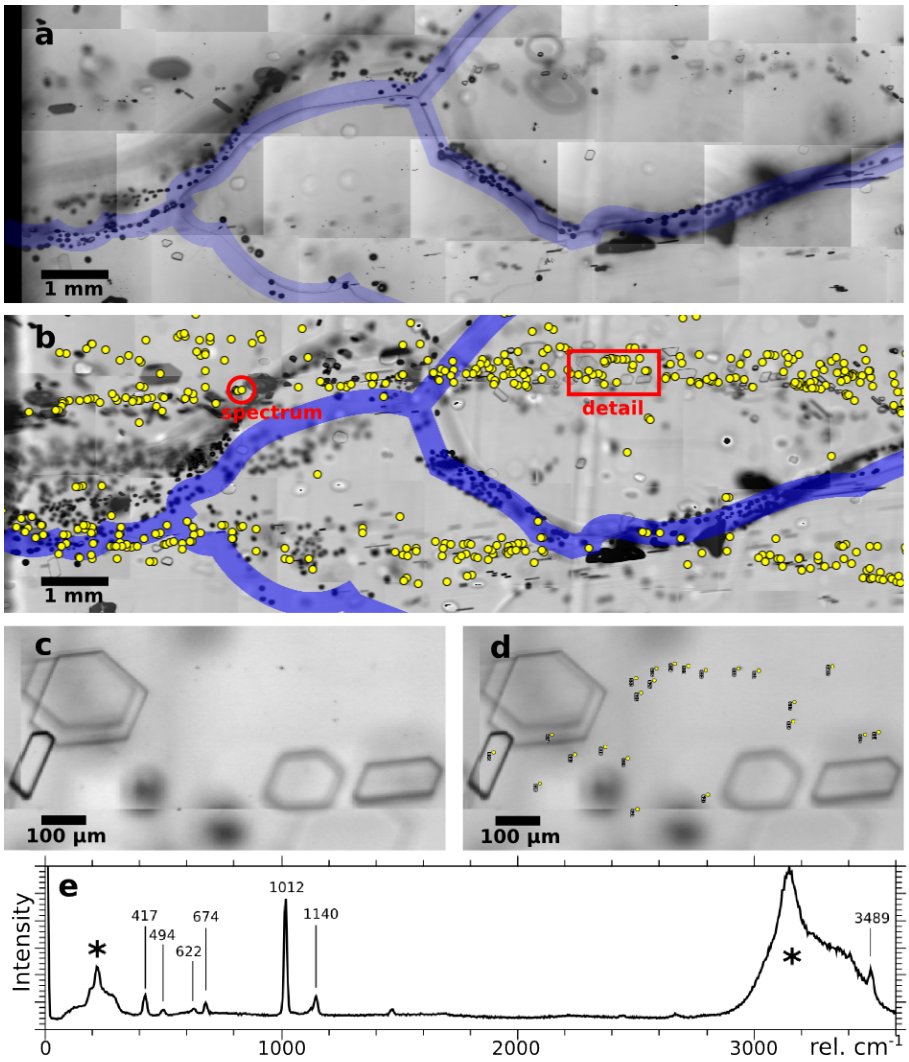

FIGURE 5.2: Double impurity layer in EDML-2371.9 (horizon 1 in Fig.5.3). (a) Surface map with grain boundaries visible as thin dark lines highlighted with blue bands. Blurred lines are grain boundaries at the bottom side of the specimen which are out of camera focus. (b) Impurity map with marked µ-inclusions (yellow circles) and grain boundary network from the surface map. Roundish black objects with the size of several tens of µm are secondary gas inclusions (micro-bubbles) formed due to relaxation (Weikusat et al., 2012). While µ-inclusions follow horizontal layering, micro-bubbles trace the 3D shape of the grain boundaries. (c) A high resolution uninterpreted detail of the upper impurity layer - red rectangle in (b). (d) Same detail with interpreted µ-inclusions. (e) Example Raman spectrum of one µ-inclusion from the upper layer (red circle). Parts of the signal marked with asterisk correspond to the ice spectrum. The positions of the proper peaks are quoted. The inclusion is a gypsum particle ($CaSO_4 \cdot 2H_2O$).

diameter would correspond to 6–9 µm, however their appearance as "black dots" is probably produced by optical effect of much smaller particles of the typical dust size ca. 1–2 µm (Wegner et al., 2015). Raman measurements and correlation with CFA dust and Ca^{2+} peaks however confirm our assumption that these features are real µ-inclusions.

5.3.1 Raman spectroscopy

A limited number of µ-inclusions (20–40 per sample) were selected for the Raman analysis. Using a 50x lens and confocal mode, a great majority (around 90%) of the µ-inclusions could be found again in the Raman microscope. Additionally, their distance from the sample surface (z-coordinate) could be measured due to the confocal setting. The z-coordinates of µ-inclusions are Gaussian-distributed around the focal plane with a half maximum width of 200 µm. We accept this value as the depth of field of the mapping microscope and use it for the calculation of the volume fraction of the impurity maps.

Around 70% of analyzed µ-inclusions showed a Raman spectrum of sufficiently high intensity to separate it from the overall present ice spectrum. The quality of obtained Raman signal depends on several factors. The most limiting ones are the size of the µ-inclusion, the path length of the laser beam through the crystal, the quality of polished surface and the acquisition time. Due to time constraint given the large amount of measured points, integration time was in the range 5–10 seconds with 10 repetitions. Most of the measured inclusions in EDML-2371.4 and EDML-2371.9 - around 40 spectra - could be identified as sulfate salts (see example spectrum in Fig.5.2e). The NEEM samples showed a higher content of water-insoluble inclusions, such as quartz and black carbon. A detailed description of the composition statistics is still in progress and will be shown elsewhere. However, the Raman measurements show that the counted black dots are chemical impurities and thus verify microstructure mapping as a valid method to map the visible in situ impurity content.

5.3.2 Concentration

The numbers of counted µ-inclusion per sample are shown in Tab.5.1. Knowing the depth of field being 200 µm we calculated the volume fraction of the mapped area. In this way, the average concentration of µ-inclusions per ml of water equivalent could be estimated. Comparison with the CFA dust concentration shows a clear difference between the deep EDML ice and the shallow NEEM ice. In EDML, the number of visible µ-inclusions in situ is 2–3 times higher than the content of insoluble particles (dust) in the melt water. In contrast the amount of µ-inclusion in the NEEM samples is comparable or even less than the CFA dust concentration.

5.3.3 Distribution

General spatial distribution

The distributions of µ-inclusions within the four samples are highly inhomogeneous. Similarly to ice-age ice (cloudy ice) also the cleaner Holocene and Eemian ice (MIS5.5) contains horizontal layers of increased impurity concentrations (analogous to cloudy bands) instead of µ-inclusions being distributed homogeneously.

In the EDML-2371.9 sample more than 50% of the counted black dots can be allocated to one of these horizons. We can distinguish a sharp double horizon at 2370.95 m (Fig.5.3a, central part of the sample). This sharp double layer correlates with a cloudy band in the visual stratigraphy scanning image (Fig.5.3b) and with dust and calcium peaks in the CFA profile. Around 9 mm below, there is another (disrupted) impurity layer at 2370.96 m and one more at the bottom part of the section around 2370.99 m. In the sample EDML-2371.4 (Fig.5.5) the layers are not as sharp as in 2371.9 but horizons of higher and lower concentrations are clearly visible. The

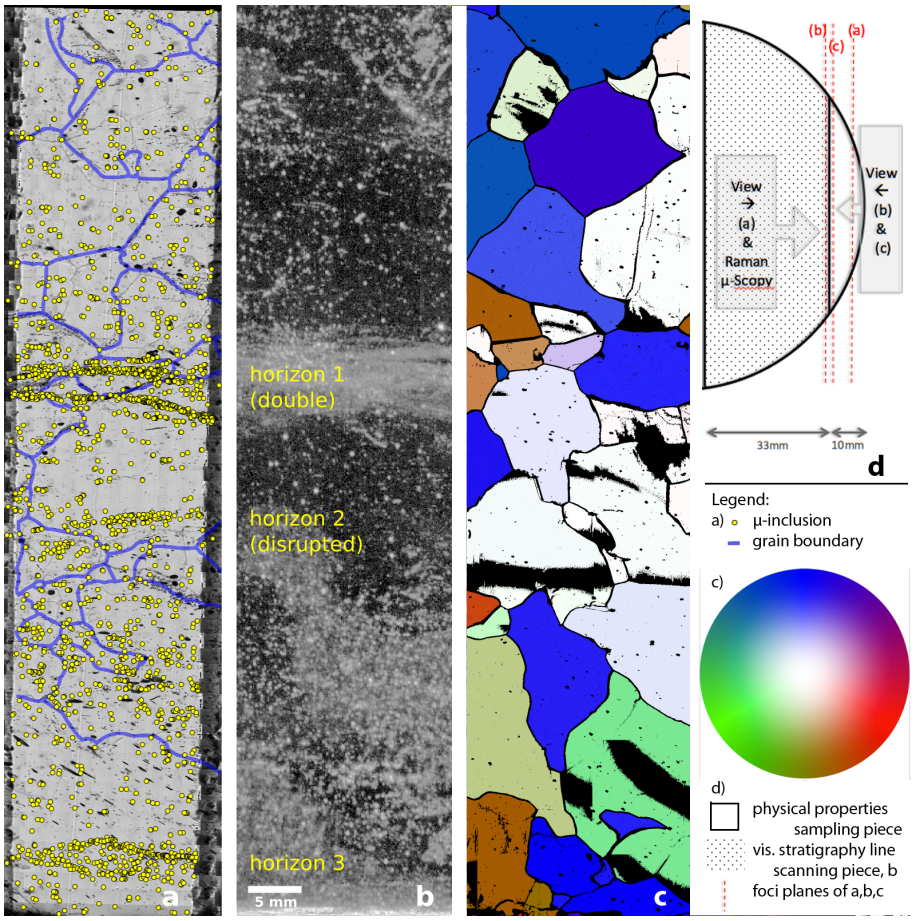

FIGURE 5.3: EDML-2371.9: (a) Impurity map of the whole sample (17 mm × 76 mm) with 2527 µ-inclusion (yellow circles) and grain boundaries from the surface map (blue bands). Blurred lines are grain boundaries at the bottom side of the specimen. Horizontal layers (1–3) of µ-inclusion are clearly visible. (b) A detail from the linescanner image of the same part of the ice core. Horizon 1 is visible as a cloudy band. (c) C-axis orientations of individual grains projected into a horizontal plane. Vertical c-axes appear white, horizontal c-axes appear in full colors depending on their azimuth (see color code in the legend). (a) and (c) refer to different surfaces as shown in the cutting plan (d) and thus the grain boundary networks are not corresponding (3D effect). (d) Cutting plan of the sample preparation.

NEEM samples (Fig.5.6) also show horizontal layering, however not so well defined and more continuous.

While the distribution of µ-inclusions on the cm scale occurs in horizontal or sub-horizontal layers, on the µm scale they are often aggregated in clusters. These groups of two or more adjacent black dots are typical for both - regions with low concentration as well as high-impurity layers.

Distribution with respect to microstructure

Grain boundary grooves from microstructure mapping of the sample surfaces are highlighted in Fig.5.3,5.5,5.6 with blue lines of a thickness of 300 µm. This width was chosen to represent the possible GB-position-error rising from the unknown inclination of the grain boundary below the sample surface. In Tab.5.2, µ-inclusions located within this blue range are considered as potentially interacting with the grain boundary. This is an upper limit assumption considering the fact that a real grain boundary is not thicker than only a few nm. Tab.5.2 shows the fraction of

ice core	EDML		NEEM	
sample	2371.9	2371.4	1346.2	1346.5
depth (m)	2370.9	2370.4	739.9	740.2
sample size (mm)	76 × 17	80 × 21	71 × 21	74 × 23
total number of µ-inclusions	2527	1195	1145	917
ice density (g/ml)	0.9167	0.9167	0.9079	0.9079
number of µ-inclusions / ml water	10668	4972	4197	3019
dust particles / ml water (CFA)	3575	2645	5450	3823

TABLE 5.1: Black dots from optical microscopy versus dust concentration from CFA (Wegner et al., 2015). With the sample size, the focus range of 200 µm and the density of the ice we estimate the concentration of µ-inclusions. The density of the samples has been estimated using images of air bubble density.

µ-inclusions found within a range of 300 µm around a grain boundary. The percentages clearly show that the vast majority of µ-inclusions is located away from grain boundaries. In EDML-2371.4, 89% of µ-inclusions are situated further than 150 µm away from any grain boundary. In EDML-2371.9, the percentage of 93% of µ-inclusions located not in the vicinity of grain boundaries is even higher. Slightly higher percentages of µ-inclusions related to grain boundaries are observed in the NEEM samples: 24% and 15%. The "grain-boundary region" in both sample types has been kept constant for observational reasons such as same imaging resolution, similar focus depth of impurity maps and unknown grain boundary inclination. However the NEEM samples show a significantly smaller grain size (mean radius 1.5 mm) compared to the EDML samples (mean radius 2.5 mm, Weikusat et al., 2009b).

In general no correlation between µ-inclusions and grain boundaries could be detected in any of the analyzed samples. Instead, the distinctive horizons 2 and 3 in EDML-2371.9 are located inside big grains, several millimeters away from the nearest grain boundaries.

In both EDML samples we observe high accumulations of secondary gas inclusions along grain boundaries, which are formed due to relaxation of the material (Weikusat et al., 2012). Their high densities allow us to partly reconstruct the 3-dimensional shape of the grain boundary just by means of the micro-bubbles (Fig.5.2,5.5).

The concentration of µ-inclusions and clusters seems not to depend on shape, size or crystal orientation of individual grains (Fig.5.3c). Black dots follow subhorizontal layering as mentioned above, rather than any microstructural feature.

5.4 Discussion

5.4.1 Impurities in the form of µ-inclusions

We used a microscopic method to map visible impurities within the ice sample volume. Since µ-inclusions are mapped in situ, surface contamination of the sample does not affect the results. The method is limited mainly by the optics of our system, in particular contrast and resolution. Objects smaller than a certain size limit would be virtually not resolved and thus a fraction of small-sized µ-inclusions would be excluded from the analysis. Wegner et al., 2015 analyzed size distributions of dust particles in the EDML ice core using a laser particle detector. The average particle diameter varied between 2–3 µm and only a small fraction of dust particles were smaller than 1 µm in diameter. Thus, the majority of micro-particles were indeed

ice core	EDML		NEEM	
sample	2371.9	2371.4	1346.2	1346.5
depth (m)	2370.9	2370.4	739.9	740.2
total number of µ-inclusions	2527	1195	1145	917
µ-inclusions within 300 µm around a GB	183	127	278	164
percentage	7%	11%	24%	18%

TABLE 5.2: Counted µ-inclusions in the vicinity of grain boundaries (region of 300 µm thickness along grain boundaries) obtained from stacked microstructure maps with grain boundary grooves on the surface and impurity maps focused inside the sample (ca. 300µm below the sample surface).

within the resolution range of an optical microscope and our results should be comparable to the CFA dust data. Individual µ-inclusions were selected for Raman measurements. The obtained spectra confirmed that the optically detected "black dots" are chemical impurities, mainly salt and dust particles. This supports previous studies by Ohno et al., 2005, 2006 and Sakurai et al., 2011 who used Raman microscopy to analyze µ-particles in ice from Dome Fuji. Detailed quantitative studies on composition and size of µ-inclusions are ongoing to estimate the actual proportion of substances present as inclusions or dissolved within the ice lattice respectively.

No signal other than ice spectrum could be detected when focusing into grain interiors, grain boundaries or triple junctions. In all four samples presented in our study, impurity spectra could be detected only when focusing onto visible µ-inclusions. Thus we cannot confirm observations by Fukazawa et al., 1998b and Barletta et al., 2012, who measured acidic environments in triple junctions and grain boundaries via Raman spectroscopy, nor EDX analyses by e.g., Cullen and Baker, 2001 and Iliescu and Baker, 2008 who also found trace elements in grain boundaries. The AWI cryo-Raman should be considered one of the most powerful Raman systems applied to ice. Still, its spatial resolution and sensitivity are limited by the applied optics and by the physics of Raman scattering. Thus, we cannot rule out segregation of trace elements to grain boundaries if their concentrations were very low.

High resolution CFA dust-concentrations measured by Wegner et al., 2015 were taken as reference for comparison with our concentrations of µ-inclusions (Tab.5.1). The ratios dust vs. µ-inclusions differ significantly between the two ice cores. The deep EDML ice in solid state contains 2–3 times more µ-inclusions per volume unit than dust in the melt water (CFA, Wegner et al., 2015). In contrast, the NEEM samples contain comparable amounts of µ-inclusions and dust. However, the NEEM CFA data still need to be flux-calibrated (Wegner, personal communication). Additionally, the presence of air bubbles in the shallower NEEM samples may cause an underestimation of µ-inclusion concentration. As air inclusions appear dark in the impurity maps (Fig.5.6), they may cover a substantial part of µ-inclusions in the image. Another possible explanation is to assume that the NEEM samples contain predominantly insoluble dust particles which are detected in the CFA, whereas the EDML µ-inclusions consist mainly of water-soluble substances. The preliminary analysis of the collected Raman spectra points in this direction. While the two Antarctic samples feature primarily sulfate salts (in agreement with Ohno et al., 2006), we mainly found terrestrial minerals and black carbon in the Greenland samples.

µ-inclusions are distributed in horizontal bands or layers of higher concentration. The annual layer thickness at 740 m in the NEEM ice core was estimated as

12–16 cm (Rasmussen et al., 2013). Thus at most one annual layer would fit in one section and the layering of µ-inclusions in NEEM-1346.2 and NEEM-1346.5 is probably attributed to seasonal variability. The annual layer thickness of the EDML samples (2371 m) is only 5–10 mm (Ruth et al., 2007) so that more than 10 annual layers should be present in each sample. However, the stratigraphy at this depth of the EDML ice core is strongly disrupted, strata are tilted by up to 30 degrees and cm-sized z-folds are present (Faria et al., 2010). The visual stratigraphy, CFA profile and c-axis orientations along the whole EDML bag 2371 are plotted in Fig.5.4. Impurity layers are visible in the linescanner image and correlate with peaks in the dust and Ca^{2+} record. A sharp impurity peak is visible in the EDML-2371.9 section which corresponds to the double horizon of µ-inclusions shown in Fig.5.2b and Fig.5.3. The DEP and CFA conductivities show significant differences, as DEP is recorded on the ice core in solid state while CFA measures the electrolytic conductivity of the melt-water. The DEP variability is independent on dust and Ca^{2+} concentration, while the CFA conductivity shows a sharp peak in EDML-2371.9 correlated to the the dust and Ca^{2+} horizon. This supports our conclusion from the last paragraph stating that a large portion of the µ-inclusions in the EDML samples are water-soluble salts which will increase the CFA conductivity. Another dust peak arises in sample EDML-2371.4, however no correlated signal is found in Ca^{2+} nor CFA conductivity. Furthermore, it is unclear whether the NH_4^+ peak in EDML-2371.4 is correlated to the mentioned dust peak and the shift is due to inaccuracy in depth assignment, or the signals are independent. Further evaluation of the Raman spectra which will be presented elsewhere should help to better understand the origin of the signals.

5.4.2 Zener pinning

The attractive force between a grain boundary and µ-inclusions results from the reduction of grain boundary energy. Assuming a random distribution of spherical inclusions of radius r (Humphreys and Hatherly, 2004), the maximal pinning pressure on a grain boundary can be derived:

$$P_Z = 2\pi r^2 \gamma N_V \tag{5.1}$$

where γ is the grain boundary energy and N_V number of µ-inclusions per volume unit. If the driving force for grain boundary migration $P_{GBM} < P_Z$, then the grain boundary stays in contact with the pinning particles and its migration rate adapts to the mobility of the particles (slow mode pinning). On the contrary, if $P_{GBM} > P_Z$, the interaction time is short and grain boundary proceeds its motion leaving the particles behind (fast mode pinning).

One of the objectives of our study was to catch µ-inclusions “in flagrante” - i.e. in the very act of pinning a grain boundary. However, this aim resulted to be cumbersome since grain boundaries are usually invisible inside the sample volume. In general, we can only estimate positions of grain boundaries from the surface images (microstructure maps). Sometimes, if the curvature and convexity are favorable with respect to the image plane, 3D-shapes of grain boundaries are indeed visible within the sample volume. In such cases, we could observe clathrate hydrates sticking to grain boundary interfaces, deforming their shapes due to the pinning force. However, no µ-inclusions were observed to produce such kind of effects. We studied the distribution of µ-inclusions in a plane of focus over the whole sample area. The density of µ-inclusions is inhomogeneous, however exhibits no correlation with grain boundaries. The typically clustered distribution could in principle be interpreted as

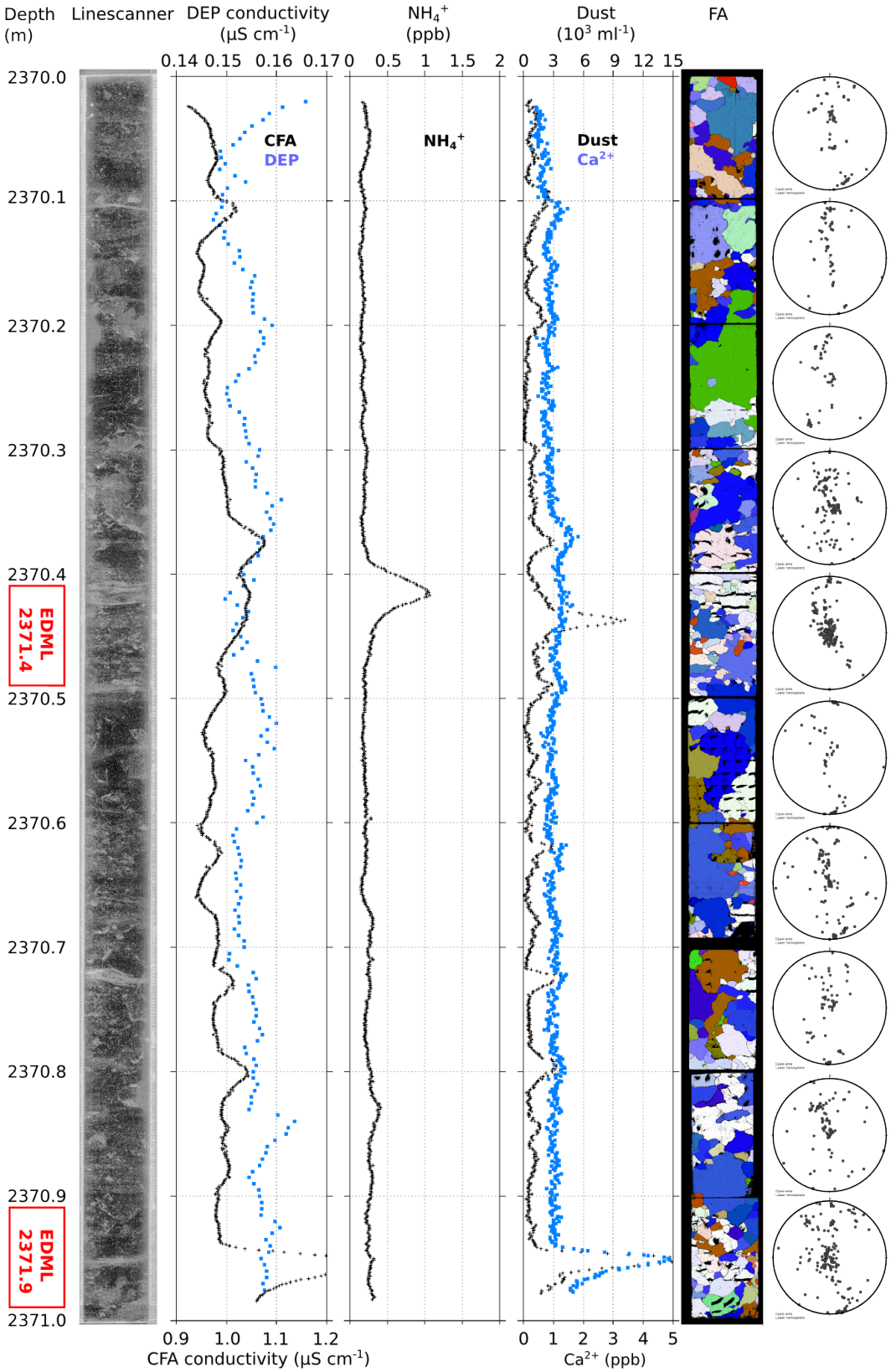

FIGURE 5.4: EDML the whole bag 2371 (2370–2371 m). From left to right: visual stratigraphy (Lambrecht et al., 2004), DEP and CFA conductivity, NH_4^+, Ca^{2+} and dust profile (CFA, Kaufmann et al., 2010; Wegner et al., 2015), c-axis orientations projected into the horizontal plane with the corresponding Schmidt diagrams.

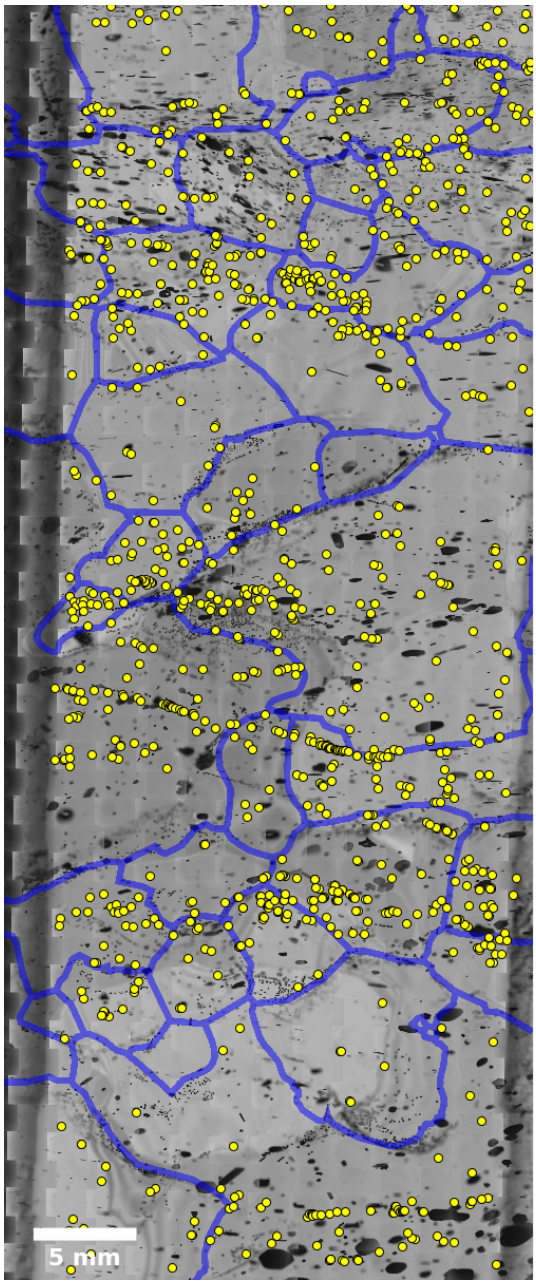

FIGURE 5.5: Microstructure and impurity map of the sample EDML-2371.4. Layering of µ-inclusions (yellow) is less pronounced than in EDML-2371.9. Secondary gas inclusions (small, black and roundish) tend to follow the shapes of grain boundaries. In contrary, the µ-inclusions seem not to accumulate at grain boundaries.

caused by sudden release of µ-inclusions from accelerating grain boundary. However, the clusters which are within themselves unordered also are of no significant shape e.g. rows, planes or ellipsoids. We would expect some kind of alignment in rows or planes or at least some sort of graduation (size, type) of the clusters if they would result from release by a moving grain boundary.

The observations listed above lead us to the conclusion, that only fast-mode pinning can take place in all four analyzed samples:

$$P_{GBM} > P_Z \tag{5.2}$$

This is in agreement with Alley et al., 1986b; Paterson, 1991 and others who suggest that particle concentrations in ice are in general too low to induce slow mode pinning. On the contrary, we cannot confirm the assumption by Durand et al., 2006b, that µ-inclusions would accumulate in high concentrations at grain boundaries. Our results also confirm general observations by Faria et al., 2010 and Svensson et al., 2011 who concluded that impurity layering and thus climatic record would stay preserved even in the deep parts of the EDML ice core and the NGRIP ice core respectively. Svensson et al., 2011 identified annual layering of impurities down to the Eemian part of the NGRIP ice core. Faria et al., 2010 observed no redistribution of µ-inclusions due to pinning or dragging down to 2300 m of the EDML ice core. However, below this depth, and particularly in the deepest 200 meters, the authors found accumulations of "black dots" along grain boundaries and concluded that pinning and dragging is relevant only in the deepest part of the EDML ice core. This finding mismatched our observations in EDML-2371.4 and EDML-2371.9 where we only found secondary bubbles accumulated along grain boundaries. Since microstructure maps described by Faria et al., 2010 were made only few days or hours after drilling the ice core, we decided to record new microstructure maps of the same spots now after ca. 10 years of storage. The comparison indicates that significant changes occur during the relaxation of the material (see example in Fig.5.7). The image of the freshly drilled ice shows a group of "black dots" accumulated at a grain boundary. Image of a re-measurement of the same sample shows that with time these "black dots" have grown and filled with gas and now they are forming typical relaxation air bubbles. There are two possible explanations: 1. Grain boundaries in deep EDML do collect µ-inclusions by dragging but after retrieving the core they serve as seeds for the growing relaxation bubbles and get surrounded with gas. It remains unclear why µ-inclusions in the interior of grains do not evolve into bubbles. 2. Another option is that the "black dots" at grain boundaries observed by Faria et al., 2010 in fact are small micro-bubbles forming due the abrupt drop of pressure after logging the ice core. Weikusat et al., 2012 analyzed compositions of secondary microbubbles using Raman spectroscopy. The authors also remark that secondary bubbles tend to form at locations of "black dots". However, to date there are no data available concerning the composition of these original "black dots" as Raman spectroscopy is currently not available on-site, viz. right after drilling.

Della Lunga et al., 2014 observed impurity concentration peaks at grain boundaries in the clean parts of the Greenland Stadial 22, NGRIP ice core, using LA-ICPMS. However, fundamental differences between the experimental techniques as well as the ice samples impede a direct comparison to our study. Dust concentrations in GS-22 determined by Vallelonga et al., 2012 vary between $2 \cdot 10^5$ ml^{-1} in cloudy bands and $2 \cdot 10^4$ ml^{-1} in the clean bands which is one order of magnitude more than the average concentrations in our samples. Furthermore it remains unclear, what portion of the LA-ICPMS signal is due to visible µ-inclusions. A comparative study applying both techniques to the same specimen could help resolve the contradiction.

The highest local µ-inclusion density in our sample material was found in the double horizon of sample EDML-2371.9 (Fig.5.2,5.3) and could be estimated as $N_V = 37206$ cm^{-3}. When inserting this value in Eq. (1), assuming the mean particle radius $r = 1.5$ µm (in agreement with Wegner et al., 2015) and using $\gamma = 65$ mJ m^{-2} for high angle boundaries (Hobbs, 1974), we obtain the maximal pinning pressure $P_Z = 0.034$

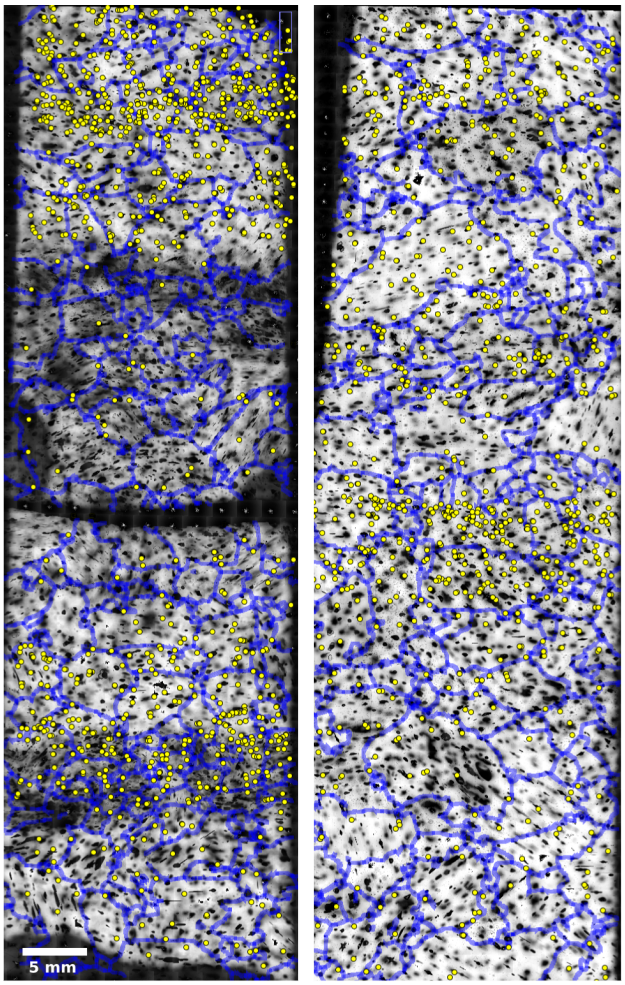

FIGURE 5.6: Microstructure and impurity maps of the two NEEM samples (740 m). Horizontal layering of µ-inclusions is present in both maps. The samples contain a higher density of grain boundaries, the average grain radius is 1.5 mm. NEEM-1346.2 is cracked in the central part. In contrast to the EDML samples, the gas inclusions (black) are homogeneously distributed, since they are primary air bubbles, albeit deformed due to relaxation.

$\mathrm{N\,m^{-2}}$. The driving force for grain boundary migration can be written as:

$$P_{GBM} = \Delta H - \frac{2\gamma}{R} \tag{5.3}$$

where ΔH is the gradient in stored strain energy density across the grain boundary (i.e. strain induced driving pressure) and the second term represents the curvature-driven pressure with the radius R of grain boundary local curvature. Assuming no difference in stored strain energy ($\Delta H = 0$), the boundary migration will be driven only by its curvature. Inserting P_Z and Eq. (3) into Eq. (2) we obtain $R <$ 3.8 m the radius of local curvature necessary to unpin the grain boundary from its surrounding µ-inclusions. Most grain boundaries along the NEEM and EDML ice cores indeed fulfill this condition (e.g., Binder et al., 2013).

In a second marginal case, let us consider a planar grain boundary ($R \to \infty$) whose migration is only driven by the difference in stored strain energy as function of the local dislocation density $\Delta\rho_{dis}$. Following Humphreys and Hatherly, 2004 and

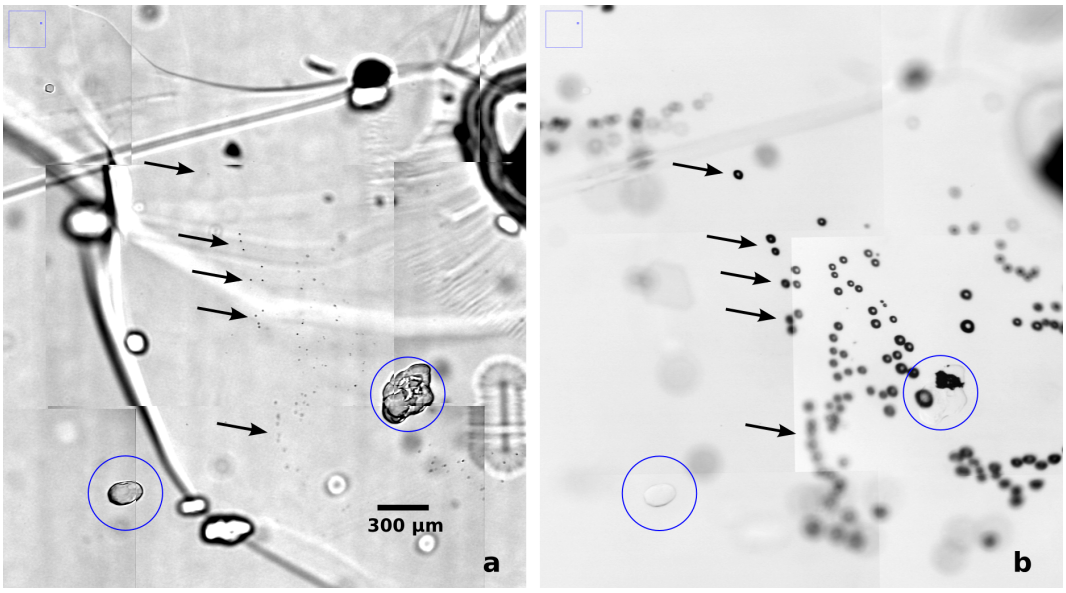

FIGURE 5.7: Two images of the same spot in EDML 2376.0. Two clathrate hydrates are highlighted (blue circles) in both images for comparison. a) Photomicrograph taken at the site immediately after drilling the ice core, 2006. An accumulation of "black dots" within the grain boundary plane can be recognized. These "black dots" are slightly larger than the µ-inclusions counted in our impurity maps. b) The same spot after ca. 10 years of relaxation. Almost all "black dots" at the grain boundary evolved into secondary gas inclusions.

Llorens et al., 2016a, ΔH can be approximated as:

$$\Delta H = \Delta\rho_{dis} \frac{1}{2} G\, b^2 \tag{5.4}$$

where $G\, b^2/2$ is the energy per unit length of a single dislocation line consisting of the shear modulus G and the magnitude of the Burgers vector b. Considering only the basal slip system the mean dislocation energy can be estimated as $G\, b^2/2 = 3.6 \cdot 10^{-10}$ J m^{-1}. Inserting this in Eq. (4) and combining Eq. (4), (3) and (2) we obtain an estimation for the minimal difference in dislocation density required for unpinning: $\Delta\rho_{dis} > 10^8$ m^{-2}. This value is 2–3 orders of magnitude smaller than absolute dislocation densities modeled by Montagnat and Duval, 2000 and Montagnat et al., 2003, and also smaller than a minimum dislocation density access calculated from grain boundary curvatures by Hamann et al. (2007, Fig. 11b).

In the above considerations we made a variety of assumptions and the derived values are only for approximation. Furthermore, in the case of a real grain boundary ΔH acts against the curvature-driven force as described in (3) and thus the final motion and shape are determined by the ratio of these forces. However, the exercise demonstrated that applying Zener's theory to our particular µ-inclusion concentration the pinning effect is comparatively small and will hardly affect grain boundary migration. This is indeed in agreement with what we observe.

5.4.3 Grain size controlling mechanisms

It is difficult to make general conclusions based on the analysis of four discrete samples. Our study indicates that pinning on µ-inclusion occurs in fast mode in large

part of the ice sheets, as already stated by Alley et al., 1986b, and will not significantly affect grain boundary migration. At the same time, with our Raman microscope we find no other form of e.g., dissolved impurities segregated to grain boundaries. However, negative correlations between average grain size and impurity content were found in virtually all ice cores (e.g., Azuma et al., 1999, 2000; Durand et al., 2009; Gow and Williamson, 1976; Gow et al., 1997; Lipenkov et al., 1989; Thorsteinsson et al., 1995). High-impurity ice exhibits generally smaller grains than low-impurity ice at the same depth. This negative correlation can be found at all scales: in seasonal variabilities (cloudy bands, cm), during rapid climatic fluctuations such as Dansgaard-Oeschger events (tens of meters), or comparing glacial and interglacial periods (hundreds of meters).

Grain size has an impact on a variety of ice physical properties (Cuffey, 2006; Goldsby, 2006), and vice versa it is controlled by thermodynamic conditions and processes within the ice sheet. Without deformation and under purely static conditions, mean grain area increases linearly with time. This normal grain growth (NGG) is driven by the reduction of grain boundary surface energy (Alley et al., 1986a) due to the optimization of volume versus interfaces. This model is especially relevant for very small grain sizes well below the equilibrium or steady state grain size (see e.g., Faria et al., 2014c; Jacka and Jun, 1994), such as smallest grain sizes in the uppermost part of the ice sheet (Gow, 1969), but may also apply to some areas where topographic depressions in the bedrock below ice sheets inhibit deformation and NGG can produce extraordinary large grain sizes (stagnant ice, Budd and Jacka, 1989). If deformation introduces additional energy into the system, dynamic recrystallization processes are activated, driven by the energy reduction. Rotation recrystallization (RRX) splits grains into subgrains and thus has a grain-size-reducing effect (Alley et al., 1995; Durand et al., 2008; Wang et al., 2003). During RRX recovery orders dislocations of a deformed grain into subgrain boundaries, which are lower energy states of dislocation assemblages (Hirth and Lothe, 1982; Hondoh, 2010). Subgrain boundaries can develop into grain boundaries by further rotation. On the contrary, strain-induced boundary migration (SIBM) occurs when grain boundaries propagate into regions of high dislocation densities. The effectiveness of SIBM increases with the heterogenous distribution of dislocations (Weikusat et al., 2009b) in polycrystalline ice, which is a direct consequence of the high mechanical anisotropy of the ice crystal. SIBM leads to huge grain sizes in the deep ice (De La Chapelle et al., 1998), however can also lead to grain size reduction, e.g., by nucleation of new grains (SIBM-N Faria et al., 2014c) or by dissection of highly irregular grains. Recent microstructural studies (e.g., Durand et al., 2008; Faria et al., 2014a) show that all recrystallization mechanisms (NGG, RRX and SIBM) concur all over the depth range of an ice sheet, rather than being dominantly active in separate depth zones. The grain size is then a product of the interplay between these processes (dynamic grain growth, Faria et al., 2014c).

It is widely accepted that the grain size is modulated by some impurity effect. The two most manifest candidates for such an effect are: 1. Reduction of grain boundary mobility via dissolved impurities being dragged along by migrating grain boundaries (Alley and Woods, 1996; Alley et al., 1986b; Drury and Urai, 1990; Paterson, 1991; Urai et al., 1986); 2. Zener pinning (Durand et al., 2006b; Fisher and Koerner, 1986), that is, interaction between µ-inclusions and grain boundaries as discussed in section 5.4.2. However, experimental evidences for both models are controversial in ice, as demonstrated by our study. Furthermore, both interpretations are based on the assumption that it is solely NGG which suffers under the effect of impurities leading to smaller grain sizes. However, grain size is a product of all

recrystallization processes together, as discussed in previous paragraph. Therefore we hypothesize that an indirect impurity effect, for instance enhanced deformation and/or effect on dynamic recrystallization triggered by high impurity content could be an alternative candidate responsible for the changes in grain size. Impurities could have a significant influence on strain distribution within grains as well as dislocation mobilities and densities, e.g., via dislocation multiplication. The microstructure effects of increasing dynamic recrystallization versus viscoplastic deformation have recently been tested by a microstructural evolution model (Llorens 2016 a,b). In these model runs the impact is significant on e.g. the grain shape evolution, because deformation tends to flatten grains while recrystallization tends to make them equidimensional. First evidences of changes in the deformation-recrystallization interplay have been observed by means of grain shape analyses (Binder et al., 2013; Weikusat et al., 2017b). However, to test these hypotheses is far beyond the scope of this study.

5.5 Summary

We present high-resolution large-scale maps (3 µm pix^{-1}, 8 × 2 cm^2) of µ-inclusions within four samples from polar ice cores - two from the EDML (2371 m) and two from the NEEM ice core (740 m). For the first time, in situ distributions of a representative number (more than 5000) of µ-inclusions have been studied. A confocal Raman microscope has been used to prove the impurity origin of the inclusions. Discrete µ-inclusions are the only impurity form detected in this study, i.e., we measured no signal attributed to dissolved impurities neither in grain interiors nor in grain boundaries. The comparison with grain boundary network shows no correlation between µ-inclusions and grain boundaries. Therefore we observed no evidence for redistribution of impurities by dragging, nor for slow mode grain boundary pinning as defined by Alley et al., 1986b. The link between grain size and impurities may not be (only) due to hindered normal grain growth in impurity-rich ice. Deformation and dynamic recrystallization enhanced by impurities possibly also have a grain-size-reducing effect.

Data availability

The four impurity maps in original resolution and positions of individual microinclusions are available upon re- quest and will be published in PANGAEA in the future. Thick- section images along the whole EDML ice core are available at doi:10.1594/PANGAEA.663141.

Author contribution

J.E., I.K. and W.S. performed the measurements, processing and interpretation. M.B., D.J., S.K., C.W., I.W. supported the processing and interpretation of data by providing specialists knowledge as well as the general glaciological framework. I.W. provided the initial concept. Under the lead of J.E. all authors contributed to writing of the manuscript.

Competing interests

The authors declare that they have no conflict of interest.

Acknowledgements

This research was funded by HGF grant VH-NG-802 to J.E. and I.W., SPP 1158 DFG grant WE4711/2 to C.W., as well as DFG grant SPP 1158 BA 3694/2-1 and JSPS fellowship ID PE16746 to M.B. The Microdynamics of Ice (MicroDICE) research network, funded by the European Science Foundation, is acknowledged for funding research visits of J.E. and I.K. (short visit grant). We thank Anna Wegner, Melanie Behrens and Maria Hörhold for discussions on solubility of impurities and CFA related issues. The visual stratigraphy line scan image has been made available at www.pangaea.de. We thank the logistics and drilling team of the Kohnen and NEEM stations. NEEM is directed and organised by the Center of Ice and Climate at the Niels Bohr Institute and US NSF, Office of Polar Programs. It is supported by funding agencies and institutions in Belgium (FNRS-CFB and FWO), Canada (NRCan/GSC), China (CAS), Denmark (FIST), France (IPEV, CNRS/INSU, CEA and ANR), Germany (AWI), Iceland (RannIs), Japan (NIPR), Korea (KOPRI), the Netherlands (NWO/ALW), Sweden (VR), Switzerland (SNF), UK (NERC) and the USA (US NSF, Office of Polar Programs). This work is a contribution to the European Project for Ice Coring in Antarctica (EPICA), a joint European Science Foundation/ European Commission (EC) scientific programme, funded by the EC and by national contributions from Belgium, Denmark, France, Germany, Italy, The Netherlands, Norway, Sweden, Switzerland and the UK.

Chapter 6

Paper II

Impurity analysis and microstructure along the climatic transition from MIS 6 into 5e in the EDML ice core using cryo-Raman microscopy

Jan Eichler [1,2], Christian Weikusat [1], Anna Wegner [1], Birthe Twarloh [1], Melanie Behrens [1], Hubertus Fischer [3], Maria Hoerhold [1], Daniela Jansen [1], Sepp Kipfstuhl [1], Urs Ruth [1], Frank Wilhelms [1,4] and Ilka Weikusat [1,2]

[1] Alfred Wegener Institute Helmholtz Centre for Polar and Marine Research, Bremerhaven, Germany
[2] Department of Geosciences, Eberhard Karls University Tübingen, Tübingen, Germany
[3] Climate and Environmental Physics, Physics Institute & Oeschger Centre for Climate Change Research, University of Bern, Bern, Switzerland
[4] Georg-August-Universität Göttingen, Göttingen, Germany

Published in *Frontiers in Earth Science*, 26 February 2019.

Abstract

Impurities in polar ice cores have been studied so far mainly for the purpose of reconstructions of past atmospheric aerosol concentrations. However, impurities also critically influence physical properties of the ice matrix itself. To improve the data basis regarding the in-situ form of incorporation and spatial distribution of impurities in ice we used micro-cryo-Raman spectroscopy to identify the location, phase and composition of micrometer-sized inclusions in natural ice samples around the transition from marine isotope stage (MIS) 6 into 5e in the EDML ice core. The combination of Raman results with ice-microsctructure measurements and complementary impurity data provided by the standard analytical methods (IC, CFA and DEP) allows for a more interdisciplinary approach interconnecting ice core chemistry and ice core physics. While the interglacial samples were dominated by sulfate salts - mainly gypsum, sodium sulfate (possibly thenardite) and iron–potassium sulfate (likely jarosite) - the glacial ice contained high numbers of mineral dust particles - in particular quartz, mica, feldspar, anatase, hematite and carbonaceous particles (black carbon). We cannot confirm cumulation of impurities in the grain boundary network as reported by other studies, neither micro-particles being dragged by migrating grain boundaries nor in form of liquid veins in triple junctions. We argue that mixing of impurities on millimeter scale and chemical reactions are facilitated by the deforming ice matrix. We review possible effects of impurities on physical

properties of ice, however the ultimate identification of the deformation agent and the mechanism behind remains challenging.

6.1 Introduction

Polar ice sheets represent the most direct archives of the past atmosphere. The ice as well as its gas and impurity content originates from snow which once precipitated at the surface, was compacted due to accumulation of new layers, transformed into ice, and further traveled through the ice column. Ice sheets are subject to continuous deformation and flow, which - in case of equilibrium - balances the mass accumulation on the surface with mass loss on the borders. They represent highly dynamic systems which react sensitively to changes in boundary conditions, e. g., temperature, accumulation rate etc. Thus, understanding ice sheet dynamics is of high interest to predict the future ice sheet response in times of changing climate, and is also crucial for correct interpretation of climate signals of the past.

Dissolved and particulate impurities in the ice play an important role for two reasons. On one hand, their concentrations measured in ice cores provide the main basis for reconstructions of the atmospheric aerosol composition in the past but may suffer from redistribution and chemical alteration in the ice. On the other hand, impurities seem to actively affect mechanical properties of ice and cause localized enhanced deformation (Dahl-Jensen, pers. comm.; Jansen et al., 2017; Paterson, 1991). From the very top surface, along the densification process in the firn column down to the deep ice, the interaction of impurities with the physical properties of the snow, firn (Freitag et al., 2013; Fujita et al., 2014) and ice (Paterson, 1991) has been observed, indicating (a) post-depositional changes of the original record, which hampers interpretation with respect to climate reconstruction and (b) changes in deformation rate and the need for a dedicated flow law (Greve, 1997; Placidi et al., 2010). Nevertheless, up to now, neither are the relevant processes understood nor the acting species identified.

The content of impurities in polar meteoric ice is relatively small compared to other polycrystalline materials appearing in nature. Impurities trapped in ice originate from atmospheric aerosols which are a mix of different species with a variety of sources and transport history (Legrand and Mayewski, 1997a). The major components are sea salt aerosols from the interaction between the atmosphere, ocean and sea-ice, aeolian dust particles from continental sources, acidic components – mainly sulfate and nitrate, ammonium and other aerosols related to specific events, e. g. carbonaceous aerosols from biomass combustion (often referred to as black carbon) or tephra and volcanic sulfate from volcanic activity. Relative and absolute concentrations in this mixture underlie strong temporal and spatial variations and their analysis can provide information about past climate conditions, circulation patterns and source distributions. Continuous Flow Analysis (CFA) and Ion Chromatography (IC) deliver high-resolution concentration profiles for many impurity components based on meltwater samples. These methods became essential analytical tools in ice core science (Kaufmann et al., 2008; Röthlisberger et al., 2000b).

Impurities present in the polar ice have been long discussed with respect to their impact on the physical properties of the ice. Deformation experiments on doped monocrystalline ice, laboratory-made polycrystals as well as natural samples from ice cores revealed that various species had an enhancing effect on ice creep. However, the impurity concentrations, stresses and time scales in these experiments in general differ significantly from conditions present in nature, as these can hardly be

achieved in a laboratory. Paterson, 1991 compiled an overview of borehole deformation data and mechanical tests on ice cores and summarized that glacial ice in simple shear deforms on average 2.5 times faster than Holocene ice under the same stress and temperature conditions. He concluded that the higher deformation rates result from the development of strong crystal preferred orientation (CPO) and small grain sizes in glacial ice, which however were produced by high concentrations of impurities – possibly chloride and sulfate ions. The link between impurity content and ice microstructure as main driver for differences in deformation rate was proposed already in earlier studies. This was inspired by the frequently observed finer grain sizes in impurity-rich layers (Fisher and Koerner, 1986, e. g.). Alley et al., 1986a,b derived a theoretical basis of normal grain growth in ice and the effect of extrinsic substances on it. According to their analysis, concentrations of second phase inclusions (i. e. solid particles, micro-droplets etc.) in natural ice are too low to have a significant effect on grain growth via Zener pinning (Smith, 1948). However, Durand et al., 2006b argued that Zener pinning of micro-inclusions was strong enough, if particles would accumulate at grain boundaries due to ongoing migration recrystallization. Nevertheless, such a preferential distribution of micro-inclusions could not be verified as a general case so far (Eichler et al., 2017; Faria et al., 2010). Alley et al., 1986b concluded that impurities dissolved in grain boundaries would significantly reduce grain boundary mobility (migration rate) even at very low concentrations and thus could have a decisive effect on the grain size. Segregation and solution of ions in grain boundaries was promoted by Wolff and Paren, 1984 who suggested that electrical conductivity in ice was due to electrolytic conduction through grain boundaries. High impurity concentrations in grain boundaries and triple junctions would decrease the pressure melting point and lead to melting in veins and thin films along grain boundaries. Rempel et al., 2001 argued for the presence of liquid water in grain boundaries, suggesting that climate signals in ice cores may suffer from gravitational displacement due to anomalous diffusion through the vein network. While this may apply to temperate glaciers with temperatures close to the melting point, the relevance of such anomalous diffusion for ice sheets has not been ascertained for polar ice cores and deserves further investigation.

The above considerations motivate fundamental questions: Which species are abundant in which state (condensed second phase or solution) and what is their location with respect to the lattice and grain boundary network. Do some species (which?) segregate at grain boundaries? Which impurities control deformation rate of ice and in which way? To what extent are impurities in turn affected by the deforming ice? In order to approach these questions analytical techniques dedicated to solid materials became important. Remarkable steps in this direction are the applications of Raman spectroscopy, Energy-dispersive X-ray spectroscopy (EDX) and laser ablation inductively coupled plasma mass spectrometry (LA-ICP-MS) to glacier ice. Each of these methods brings its own specifications and limitations regarding sample preparation, spatial resolution and output data. Thus, the results and interpretations regarding the above questions vary significantly. Several studies reported the presence of dissolved impurities in grain boundaries and triple junctions. Mulvaney et al., 1988 found X-ray spectra of sulfur in triple junctions using EDX. This was supported by Fukazawa et al., 1998a, who reported Raman spectra of nitrate and sulfate in triple junctions in ice samples with high acid concentrations. Raman analyses carried out by Ohno et al., 2005, 2006; Sakurai et al., 2011 on the Dome Fuji ice core revealed that most of the sulfate formed micrometer-sized salt particles, in particular sodium, magnesium and calcium sulfate. However, most of the micro-inclusions were located in the grain interiors. Several EDX studies (Baker, 2003; Barnes, 2003;

Barnes et al., 2002; Cullen and Baker, 2001; Iliescu and Baker, 2008) reported traces of sodium, chlorine and sulfur forming filaments at the sublimed ice surface. Some of the filaments grew at sites where grain boundaries and triple junctions intersected the surface. Della Lunga et al., 2014 investigated the location of impurities using LA-ICP-MS. While in impurity-rich layers (cloudy bands) there was no preferential impurity distributions with respect to the grain boundary network, in samples with lower impurity content, some evidence was found for higher impurity concentrations in the neighborhood of grain boundaries. However, LA-ICP-MS does not allow to distinguish between dissolved impurities and second phase inclusions.

Raman spectroscopy, being an optical technique, can acquire Raman spectra from the inner part of the ice sample, typically up to 1 mm below the specimen surface. Thus, surface contamination, sublimation and redistribution of impurities on the surface are irrelevant as long as the quality of the surface allows appropriate focusing of the excitation laser into the sample. The spatial resolution of a Raman microscope is on the order of µm which makes it suitable for measuring micro-inclusions, i. e. second phase inclusions typically of the size of a few µm. In this study we used the cryo-Raman system at the Alfred Wegener Institute Helmholtz Centre for Polar and Marine Research (AWI) to measure statistically relevant numbers of micro-inclusions in three sections from the EDML ice core along the transition from Marine Isotope Stage (MIS) 6 (penultimate glacial) into MIS 5e (last interglacial). The Raman analysis reveals chemical and mineralogical composition of micro-inclusion in a non-destructive way and without a need for melting the ice samples. The combination with microstructure mapping (Kipfstuhl et al., 2006) and impurity mapping (Eichler et al., 2017) increased the efficiency of the Raman measurements and, more importantly, allowed us to study spatial distributions of micro-inclusions at larger scales and in the microstructural context. Qualitative comparison of the Raman results with the IC, CFA and DEP measurements allows us to approach questions regarding the way of incorporation of different impurity species in natural polycrystalline ice. We discuss possible interaction scenarios between impurities and the deforming matrix.

6.2 Material and methods

6.2.1 Sample material

We analyzed three 10 cm long ice sections from the EDML ice core (79°00′ S, 0°04′ E, elevation 2892 m.a.s.l., Oerter et al., 2009; Wilhelms et al., 2014) around the transition from the penultimate glacial (MIS 6) into the last interglacial (MIS 5e). Sections 2371-4 and 2371-9 originate from bag 2371 (2370.4 and 2370.9 m below surface) with approximate age of the ice of 129.8 ka (Veres et al., 2013) which corresponds to early MIS 5e. Spatial distributions of visible micro-inclusions in sections 2371-4 and 2371-9 were presented and discussed in Eichler et al., 2017. Section 2392-2 (2391.2 m) is dated to 135.5 ka and thus originates from the end of MIS 6. The in-situ borehole temperature at this depth is around −13 °C (Wilhelms et al., 2007) and this lower part of the ice sheet is subject to significant horizontal shear stress (Weikusat et al., 2017b). In addition, several jumps in measured characteristics of the ice (grain size, CPO, grain aspect ratio, bore hole geometry) indicate profoundly different rheological behavior of the material in this depth regime. Fig. 6.1 shows grain structures of the three analyzed samples measured on thin sections using an automatic fabric analyzer and digital image processing (Eichler, 2013). The two interglacial samples reveal large grains (mean grain area of 34.3 mm^2 and 38.7 mm^2 respectively, with

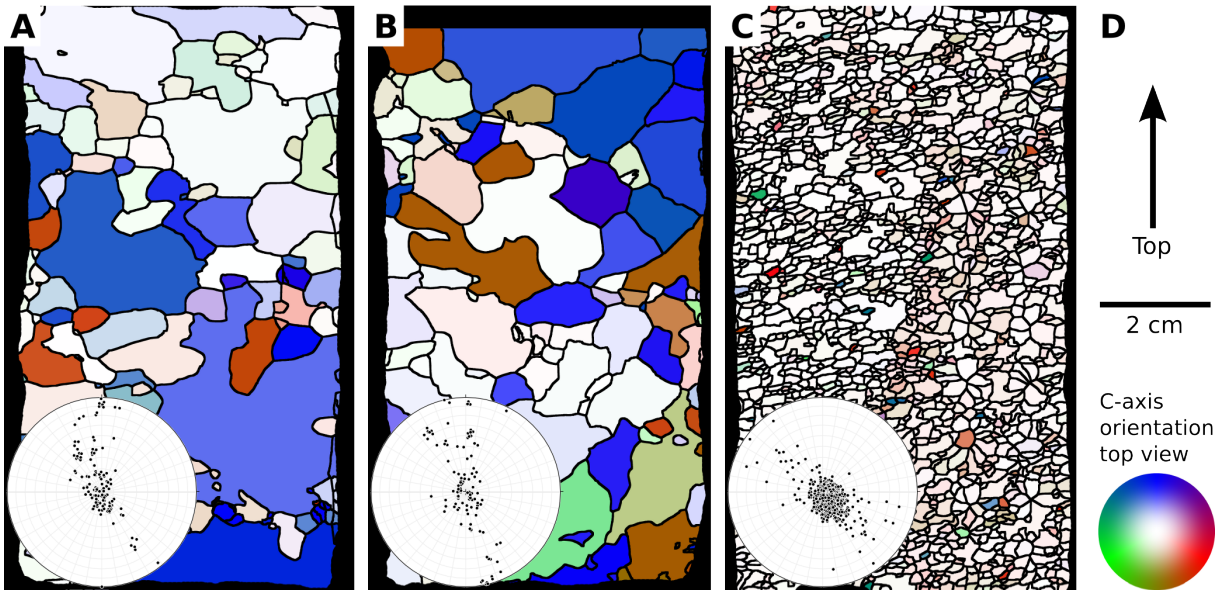

FIGURE 6.1: Different grain sizes and c-axis orientations in the three sections selected for Raman analysis. **(A)** Section 2371-4. **(B)** Section 2371-9. **(C)** Section 2392-2. The pole figures represent stereographic projections of the average c-axis orientations (one point per grain) onto the horizontal plane. **(D)** Legend indicating the orientation of the main ice core axis, scale bar and color code for the orientation of c-axes projected onto the horizontal plane. White color indicates c-axis aligned along the ice-core axis (vertical direction).

largest grains reaching several cm^2) and c-axes distributed in a girdle. In contrast, only 20 meters deeper the MIS 6 sample is characterized by fine grains (mean grain area of 1.6 mm^2) and a highly developed vertical single maximum in the c-axes distribution. The selected region is thus of key importance to understand the deformation mechanisms and their possible relation to impurities.

6.2.2 Sample preparation

We used a standard procedure for preparation of thick sections (typical thickness of 5–10 mm) as described by Kipfstuhl et al., 2006. Both, the upper and the lower side of the section are polished in a first step using a microtome. The lower side is frozen to a glass plate using a thin water film. In order to obtain maximal surface quality, the sample sublimates for several hours under controlled temperature and humidity conditions. This way microtome scratches and other disturbances erase from the surface while grain-boundary grooves become more distinctive and easier to detect. The very clear surface obtained by this sublimation polishing is inevitable as it enables us to (1) locate the micro-inclusions inside the sample volume in order to produce impurity maps for Raman measurements and (2) as a prerequisite to obtain high-quality Raman signals.

6.2.3 Micro-inclusions

Micro-inclusions are micrometer-sized dust particles, salts and droplets trapped in the ice matrix. They seem to be the most common form of impurity incorporation in cold ice, since ice, other than liquid water, is a bad solvent and rejects most substances from its lattice. The condensed phase and size of micro-inclusions are favorable for the application of light microscopy and Raman spectroscopy to localize

them and to record their characteristic Raman spectra. We use a light microscope with an automatic x-y-stage (Kipfstuhl et al., 2006) to generate large area maps of micro-inclusions. The impurity maps of sections 2371-4 and 2371-9 were previously presented and discussed in Eichler et al., 2017. In this study we used these maps to locate the previously found micro-inclusions with the confocal Raman microscope and acquire their Raman spectra. This approach is particularly efficient in samples with relatively low impurity concentrations (2371-4 and 2371-9). Here the search for micro-inclusions using the Raman system alone would be very tedious. The combination of these two methods also enables us to put the recorded Raman spectra in a larger spatial context, i.e., to study the distribution of different spectra along the distance of several millimeters to centimeters.

6.2.4 Cryo-Raman

The Raman effect refers to inelastic scattering of light due to excitation of vibrational modes of molecules or crystals. This leads to a loss of the scattered light energy – the Raman shift – which is specific for each vibrational mode. Raman spectroscopy offers a unique analytical tool to analyze chemical impurities in a non-destructive way. Being an optical technique it is best suited to be applied to light-transparent materials – such as ice. In combination with confocal optics the excitation laser can be focused into a specimen's volume segment as small as a few μm^3, typically up to 1 mm below the sample surface. This is a clear advantage over surface-analytical methods, since many disturbing factors can be neglected, such as surface pollution and possible reactions and rearrangements of trace elements due to processes at the surface or during melting or sublimation. The backscattered light is collected with the same confocal optics and conducted into the spectrometer in order to resolve its spectral distribution. The probability for a photon to be Raman-scattered is very low compared to elastic scattering (about 10^{-7}). Thus, high incident light intensities, long integration times and sufficient concentrations of the analyzed matter are needed. Since the laser power is limited in order to avoid melting, precise focusing and high quality of the prepared sample surface are the determining factors to obtain a discernible spectrum.

The sizes of micro-inclusions in ice are typically close to the optical resolution limit and they appear as single dots with different shading on the image background. This makes estimations of their shapes and volumes on the basis of the micro-photographs hardly possible. Thus the Raman spectra deliver a rather qualitative information about the impurity content without any access to their absolute concentrations. Ice itself is also Raman-active so that ice spectrum is always superimposed on the actual impurity spectra. In general, the characteristic impurity peaks are well distinguishable from the ice signal, however spectral regions with very strong ice-vibrational bands are somewhat "hidden". This applies especially for the O–H vibrations of the ice molecules which can cover the O–H signal of various hydrates. Luckily, the O–H vibrations in minerals are often very strong and shifted to higher frequencies (e. g., gypsum), so that they can be distinguished from the ice signal. In addition, not all molecules exhibit Raman-active vibrational modes at all. The most relevant case here is NaCl being the main part of sea salt and thus present in relatively high concentrations in polar ice. Due to the selection rules all the vibrational transitions are forbidden and thus photons scatter only elastically. NaCl is therefore Raman-inactive and cannot be identified using Raman spectroscopy.

The Raman system used in this study is a WITec alpha 300 M+ combined with a NdYAG laser ($\lambda = 532$ nm) and a UHTS 300 spectrometer with a 600 grooves mm^{-1}

grating. A more detailed description of the system can be found in Weikusat et al., 2015. The excitation laser, spectrometer and control unit are at room temperature, while the microscope unit is placed in the cold laboratory at −15 °C and connected through fiber optics. The laboratory temperature is close to the in-situ borehole temperature so that phase transitions due to different eutectic temperatures are avoided. Furthermore, this setup enables to perform sample preparation in the same cold room where the microscope is placed. This is a clear advantage over the use of a cryo-cell since exposure of samples to temperature gradients and moisture can be completely avoided. Only in this way the carefully prepared sample surface can be preserved during mounting on the microscope stage and protected from moisture deposition.

6.2.5 DEP, CFA and IC

For the comparison with the Raman results, we here present impurity concentration, conductivity and particle concentration measurements from the EDML deep ice core from 2370 – 2394 m depth. Dielectric profiling (DEP) conductivity was measured continuously along whole core sections (data published here for the first time). Electrolytic conductivity, Ca^{2+} concentration and number of particles were measured continuously in millimeter resolution during the EPICA Dronning Maud Land (EDML) campaign using continuous flow analysis (CFA). Parts of the particle-concentration dataset have been published in Wegner et al., 2015, the conductivity and Ca^{2+} profiles are presented here for the first time. Due to dispersion in the CFA system the nominal resolution of the data is about 1 cm. Using sample fractions from the CFA, the ion concentrations of Na^+, Cl^-, Mg^{2+}, Ca^{2+}, SO_4^{2-} and NO_3^- were measured discretely with ion chromatography (IC) at AWI Bremerhaven (data presented here for the first time).

DEP measures the electrical conductivity on ice cores continuously and non-destructively. The instrument consists of two aluminum shells as capacitors, acting as electrodes. An electric field is generated across the ice core diameter from which the real and imaginary part of the relative permittivity is obtained and the latter converted into conductivity (Wilhelms et al., 1998). The genesis of the DEP signal has been discussed previously (e. g. Moore et al., 1992).

CFA is a contamination-free, high resolution method to gain information about impurity concentrations in ice cores. A cross section of the ice core is melted on a heated metal block where only the inner part of the ice is analyzed in sensors downstream of the melt flow. The CFA system used in this study was developed at the University of Bern and is described in detail elsewhere (Kaufmann et al., 2008; Röthlisberger et al., 2000b). Precision of the CFA measurements is typically better than 10 % for the entire studied concentration range, due to the completely contamination-free sampling of the CFA analysis. Here we present the continuous high-resolution data of dissolved Ca^{2+}, electrical conductivity and the amount of undissolved particles (Wegner et al., 2015). Sample fractions were collected in 5 cm resolution for further discrete analysis with IC.

Ion chromatography is commercially available and well established for the measurement of ions in ice cores (Fischer et al., 2007; Ruth et al., 2008; Wolff et al., 2006). For this study a Dionex IC2100 system was used. Anion measurements were conducted with a potassium hydroxide (KOH) eluent using a Dionex AS 18 (2 mm) separation column. A methane sulfonate (MSA^-) eluent was used to conduct the cation measurements using a Dionex CS12a (2 mm) separation column. The uncertainty of the IC analysis is estimated to be better then 5 %, the reproducibility was estimated

to be better than 10 % for glacial concentrations, however, can deteriorate at low concentrations, e. g. interglacial Ca^{2+} (Fischer et al., 2007; Ruth et al., 2008).

6.3 Results

6.3.1 IC, CFA and DEP

Figure 6.2 compares various impurity signals within a 24 m long profile (2370–2394 m) along the transition between MIS 5a and MIS 6, which includes bags 2371 and 2392. The first panel compares electrical conductivities measured by DEP (blue) and CFA (black). Both signals represent a total contribution of all impurities, however each of them is formed due to different physical processes. While electrolytic conductivity in the meltwater (CFA) is a function of the amount of dissolved ions, the electric charge transfer in ice (DEP) is governed by protonic defects and their mobility through the crystal (Jaccard theory). This must be taken into account in order to explain the different behavior along the transition. While CFA conductivity shows an increase of a factor 2-3 in the MIS 6 part in line with the higher ion concentrations, the DEP conductivity keeps average values similar to MIS 5e. Both electrical conductivities correlate relatively well on the centimeter scale. However the CFA signal shows strong peaks on the millimeter to centimeter scale which are not reflected in the DEP signal. In some cases the DEP conductivity even shows an anti-correlating behavior. These narrow peaks, which only occur in the electrolytic conductivity, are clearly an effect of impurities dissolved in the meltwater (possibly Ca^{2+}), which however in the frozen state do not contribute to the dielectric properties.

The climatic transition is characterized by a gradual change in the concentration of virtually all relevant impurity components. Insoluble dust (CFA, number of particles per ml of meltwater) is the most prominent example showing the highest contrast between the glacial and interglacial part. While in the upper part (MIS 5e) the number of particles oscillates roughly around $1.5 \cdot 10^3\,ml^{-1}$ with highest peaks reaching $1.5 \cdot 10^4\,ml^{-1}$, average concentrations of $1.3 \cdot 10^5\,ml^{-1}$ and peaks with $2.5 \cdot 10^5\,ml^{-1}$ are reached below the transition. This represents an increase of two orders of magnitude and is consistent with previous reports (Wegner et al., 2015). The CFA Ca^{2+} shows a similar signal as the CFA dust with well correlated peaks. This suggests that major parts of calcium are of non-sea salt origin (nssCa) as discussed further below, and shares similar sources and transport paths with aeolian dust. The CFA and IC results are in a good agreement and the difference in Ca^{2+} concentration above and below the transition is approximately one order of magnitude.

The six main ions measured by IC are Cl^-, Na^+, Mg^{2+}, Ca^{2+}, SO_4^{2-} and NO_3^- (lower three panels of Fig. 6.2). All IC signals show a concentration increase towards MIS 6, however with varying slopes. The major sea salt components Cl^-, Na^+ and Mg^{2+} correlate with each other and the contrast between MIS 5e and MIS 6 concentration is around a factor of 20 (see Tab. 6.2). The SO_4^{2-} shows a variable signal. The most prominent peaks correlate with peaks in the DEP conductivity, as expected from earlier studies (Moore et al., 1991). The concentration of SO_4^{2-} rises by a factor 4 across the climatic transition. In contrast the NO_3^- concentration reveals a relatively stable signal (around 40 ppbw in MIS 5e) without any significant peaks and a concentration increase by only a factor 2 across the transition.

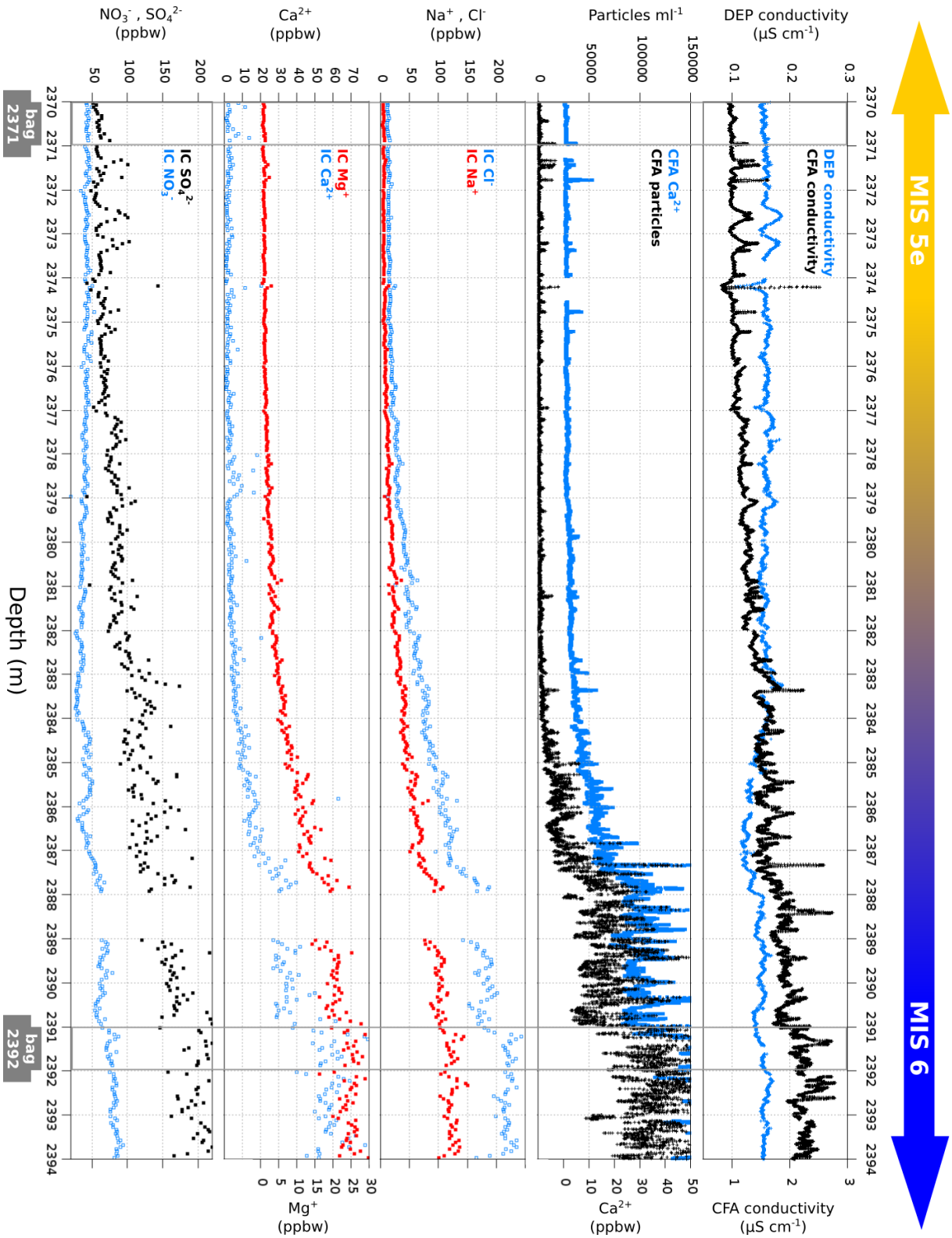

FIGURE 6.2: DEP, CFA and IC data along the transition between MIS 5a and MIS 6 (2370–2394 m). The positions of bags 2371 and 2392 are marked. The concentrations of solid particles have been previously presented by Wegner et al., 2015, all other datasets are presented here for the first time.

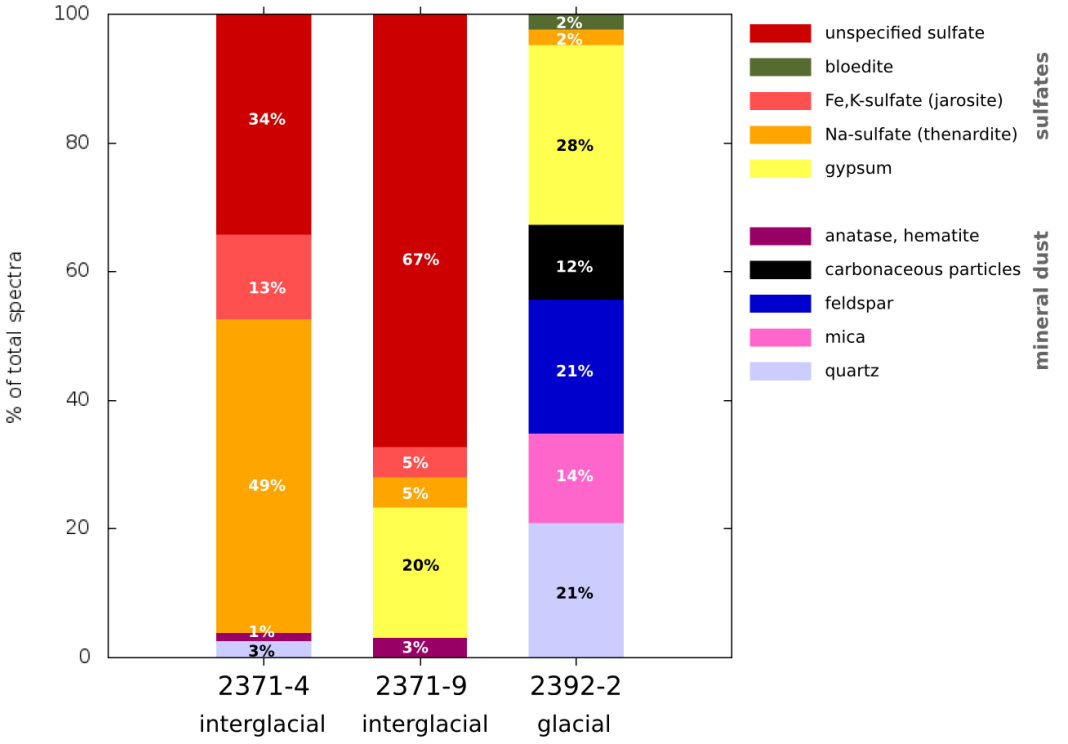

FIGURE 6.3: Relative concentrations of identified species in percent within each sample. Different color families are used to distinguish between sulfate inclusions and mineral dust – cold colors for insoluble dust and rather warm colors for sulfates. While in the interglacial samples sulfate salts form 96 % of the micro-inclusions, in the glacial ice mineral dust is most prevalent.

6.3.2 Raman results

We analyzed in total 290 micro-inclusions within the three measured samples. The Raman spectra of 183 (63 %) micro-inclusions could be identified using reference spectra. 12 (4 %) micro-inclusions showed Raman spectra which could not be identified. In 19 (7 %) cases the signal was disturbed by strong luminescence and 76 (26 %) micro-inclusions showed no signal at all. In order to maximize the signal-to-noise ratio we varied the integration time typically between 2.5 and 5 seconds per accumulation and the number of accumulations between 10× and 20×. However, the total acquisition time per micro-inclusion was limited by the cumulative heating of the particles, which would in extreme cases cause local melting or even destruction of the particles.

Table 6.1 presents the identified impurity species and their absolute numbers in the three analyzed sections. We can differentiate between a group of numerous sulfates versus other minerals often called mineral dust. Most spectra in this group are the three silicates: quartz, mica and feldspar. We also identified a few iron oxides and titanium oxides (hematite, anatase), which also contribute to this group. Carbonaceous particles have been found in form of pure graphite as well as carbon-sulfate mix.

Sulfate particles are relatively easy to detect due to the intense ν_1 vibrational mode of the SO_4 molecule. However, further determination of exact specie depends on the quality of the spectra. Thus a significant number of sulfate inclusions could not be further specified and are referred to as unspecified sulfates.

TABLE 6.1: Raman spectra of micro-inclusions detected in the analyzed ice sections. Characteristic peak wavenumbers are listed in column 3. Columns 4, 5 and 6 show absolute numbers of the different micro-inclusions measured in sections 2371-4, 2371-9 and 2392-2 respectively.

Mineral	Formula	characteristic wavenumbers (cm^{-1})	2371-4	2371-9	2392-2
No spectra	–		23	44	9
Spectra not identified	–		4	2	6
Luminescence	–		3	0	16
Sulfates:					
Unspecified sulfate salt	XSO_4		26	43	0
Bloedite	$Na_2Mg\,(SO_4)_2 \cdot 4H_2O$	991	0	0	1
iron–potassium sulfate	$(Fe, K)\,SO_4$	439, 1010, 1110	10	3	0
sodium sulfate	Na_2SO_4	990	37	3	1
Gypsum	$CaSO_4 \cdot 2H_2O$	1012, OH: 3410, 3498	0	13	12
Mineral dust:					
Anatase	TiO_2	142, 394, 514, 638	0	1	0
Hematite	Fe_2O_3	230, 297, 1325	1	1	0
Carbonaceous particles	C	1360, 1605	0	0	5
Feldspar (group)	$(Ba, Ca, Na, K, NH_4)\,(Al, Si)_4\,O_8$	477, 506	0	0	8
Mica (group)	$(K, Na, Ca, NH_4, ...)\,Al_2\,(Si_3Al)\,O_{10}\,(OH)_2$	406, 700, OH: 3625	0	0	6
Quartz	SiO_2	464	2	0	9
Total number per section			106	110	74

Within the fully identified sulfate spectra, sodium sulfate (possibly thenardite, Na_2SO_4) and gypsum ($CaSO_4 \cdot 2H_2O$) represent the most abundant species. Another frequently observed spectrum showed a very good match with the reference spectra of jarosite ($(Fe, K)\,SO_4$).

Figure 6.3 shows the relative occurrence of the identified species within all three samples. There is a clear difference between ice from the warm period (2371-4 and 2371-9) and the glacial ice (2392-2). First, impurity concentrations from the cold period are much higher than in warm-period ice. In the case of dust concentration this implies to a factor 100 more particles in glacial ice. Second, two thirds of micro-inclusions in the glacial sample are insoluble dust particles and one third are sulfates - mainly gypsum particles. In contrast, the warm period ice contains around 96 % sulfate inclusions and only a minimal fraction, around 4 %, of insoluble dust. The most frequent species in 2371-4 is Na_2SO_4 followed by the group of unspecified sulfates. In 2371-9, unspecified sulfates are most prevalent, followed by gypsum particles ($CaSO_4 \cdot 2H_2O$).

6.3.3 Impurity distribution

Micro-inclusions are distributed rather heterogeneously through the polycrystal. This is evident from their positions in the impurity maps (Fig. 6.4, 6.5 and 6.6) as already stated in Eichler et al., 2017. Micro-inclusions form areas of higher and lower concentrations and tend to align in horizontal bands which extend over grain boundaries. The double horizon in section 2371-9 (Fig. 6.5b) is a clear example of such layering. At the sub-millimeter scale, small groups and chains of micro-inclusions are frequently observed. The Raman spectra reveal no separation patterns or preferred grouping of individual chemical compounds. The different species seem to be well mixed within the analyzed areas.

We found no significant relationship between the positions of micro-inclusions and the grain boundary network neither in the glacial nor interglacial samples. The implications for the interaction between grain boundaries and micro-inclusions (Zener pinning and drag) have been discussed in Eichler et al., 2017. The Raman analysis shows that also compositions of the particles are independent of the distance from grain boundaries. When acquiring Raman signal directly from grain boundaries and triple junctions, only the ice signal could be detected, without any spectra indicating dissolved impurities. However, such attempts were limited only to measurements on the sample surface, since grain boundaries are invisible in the bulk by default.

6.4 Discussion

6.4.1 Raman analysis

We identified the composition of 63 % of the measured micro-inclusions. The remaining 37 % measurements showed either no signal at all, were disturbed by luminescence, or exhibited an unidentified Raman spectrum. A reliable phase identification is dependent on the quality of the acquired spectra. For instance in the case of sulfates, many phases exhibit a very intense main band (ν_1 mode of the SO_4 molecule) around the same Raman shift and can only be identified, if the minor lattice vibrations are also resolved. The quality of the Raman signal strongly depends on the size of each individual micro-inclusion, on the quality of the sample surface, particle–surface distance and other factors. Micro-inclusions without any signal can

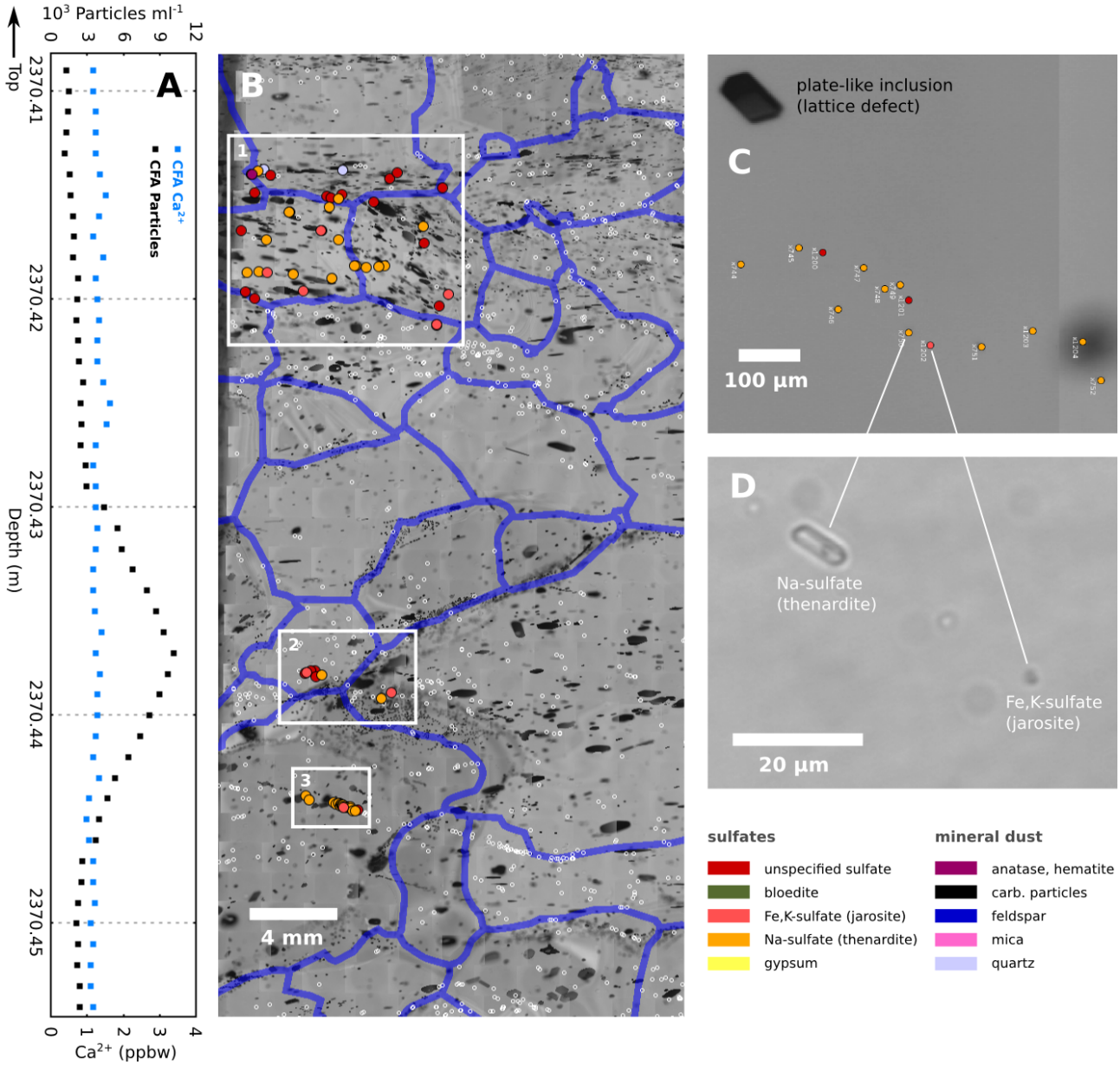

FIGURE 6.4: Detail of section 2371-4 (2370.408–2370.455 m): **(A)** High resolution CFA profile showing Ca^{2+} concentration and number of insoluble particles. **(B)** Impurity map with three rectangular areas of interest. White circles represent positions of individual micro-inclusions presented in Eichler et al., 2017. Colored circles indicate micro-inclusions analyzed with the Raman system. Blue bands indicate positions of grain boundaries at the focus depth of the micro-inclusions. Black objects in the image are effects of ice relaxation: small elliptical micro-bubbles which tend to form close to grain boundaries and larger hexagonal planar lattice defects often called the plate-like inclusions. **(C)** Detail of area 3 with a chain of micro-inclusions. A plate-like inclusion (black, upper left corner) can serve as a marker of the crystallographic lattice orientation. **(D)** Detail of two micro-inclusions from area 3. The sodium sulfate particle (left) exhibits an exceptionally large size. Its elongation direction seems to coincide with the basal plane of the ice crystal.

be attributed either to Raman-inactive species such as NaCl or to cases where the excitation laser focus missed the target. In both cases only ice spectrum could be recorded.

Among the 183 identified micro-inclusions sulfates dominate the statistics. In the MIS 5e samples (2371-4 and 2371-9) they represent 96 % of micro-inclusions. This is in agreement with previous studies by Ohno et al., 2005, 2006 who found sulfate

salts being the major micro-inclusions in Dome Fuji. Sodium sulfate was previously reported by Ohno et al., 2006 in form of mirabilite. The peak positions in our spectra as well as the absence of the O–H peak indicate rather the anhydrous phase thenardite in our samples. However, the O–H vibration may be hidden by the ice O–H bands so that this argument is not very strong. In contrast, the O–H band of gypsum ($CaSO_4 \cdot 2H_2O$) is visible in a number of its spectra so that the phase identification is certain. We identified for the first time iron–potassium sulfate ($(Fe, K)\,SO_4$) in ice using Raman spectroscopy. The spectra showed a very good match with the reference spectra of jarosite. Jarosite was curiously identified by Baccolo et al., 2018 within dust particles in deep ice from Talos Dome. The formation of jarosite in icy environments on Mars was discussed by Michalski and Niles, 2011. We also detected a few particles with relatively good match to the spectra of bloedite ($Na_2Mg\,(SO_4)_2 \cdot 4H_2O$). The unspecified sulfate particles are attributed to at least two different Raman spectra (see Appendix), both with the SO_4 symmetric stretching mode ν_1 at 989 cm^{-1}. Possible candidates are sodium-aluminum sulfate $(Na, Al)\,SO_4$, magnesium sulfate $MgSO_4$, ammonium sulfate $(NH_4)_2\,SO_4$ and similar, or mixtures of these.

The number of dust particles detected in the interglacial samples are relatively low – 2 quartz particles, 2 hematite and 1 anatase. This is in accordance with the low concentrations of dust in the CFA profile. In contrast, the MIS 6 sample (2392-2) contains almost two orders of magnitude higher concentrations of mineral dust (10^5 particles per ml, CFA). This reflects conditions characteristic for glacial periods, namely low accumulation rates in combination with high atmospheric dust content. This is also reflected in the spectra statistics, which is dominated by crust-forming silicates – quartz, mica and feldspar. Interestingly, Ca-containing crustal minerals, such as Ca-plagioclase and Ca-carbonates are completely missing. This could result from the insufficient number of measured spectra in the "dusty" MIS 6 sample. However, another explanation could be that postdepositional changes in the composition of mineral dust occurred as suggested by Baccolo et al., 2018, e. g. due to exposure to strong acids like H_2SO_4. The abundant gypsum particles could be a byproduct of such changes. The discussion below reveals some indications for similar changes affecting also the sea-salt aerosols.

6.4.2 Ion balance

The ionic composition of the water-soluble impurities can be assessed using ion chromatography (IC). Table 6.2 presents concentrations measured by IC in bags 2371 and 2392 (column 2 and 3). Values are averaged along one meter. Molar masses (column 4) are used to calculate molar concentrations for each ion (column 5 and 6). Taking sodium as sea-salt reference and using standard sea-salt ionic ratios (column 7) we can estimate the expected sea-salt (SS) and non-sea-salt (NSS) contribution for each ion (column 8 and 9). All ions reveal an increase of concentration from bag 2371 (MIS 5e) to bag 2392 (MIS 6). Furthermore, the concentration ratios between individual compounds differ significantly between the glacial and interglacial ice.

In bag 2371 nitrate and sulfate are the major ions with $7.01 \cdot 10^{-7}\,mol\,kg^{-1}$ and $6.22 \cdot 10^{-7}\,mol\,kg^{-1}$ respectively, followed by chloride ($3.63 \cdot 10^{-7}\,mol\,kg^{-1}$). The cations Na^+, Ca^{2+} and Mg^{2+} are present in significantly lower concentrations resulting in an overall acidity of the ice. On the contrary, Cl^- and Na^+ dominate the ion budget in bag 2392 with molar concentrations of $6.13 \cdot 10^{-6}\,mol\,kg^{-1}$ and $5.27 \cdot 10^{-6}\,mol\,kg^{-1}$ respectively.

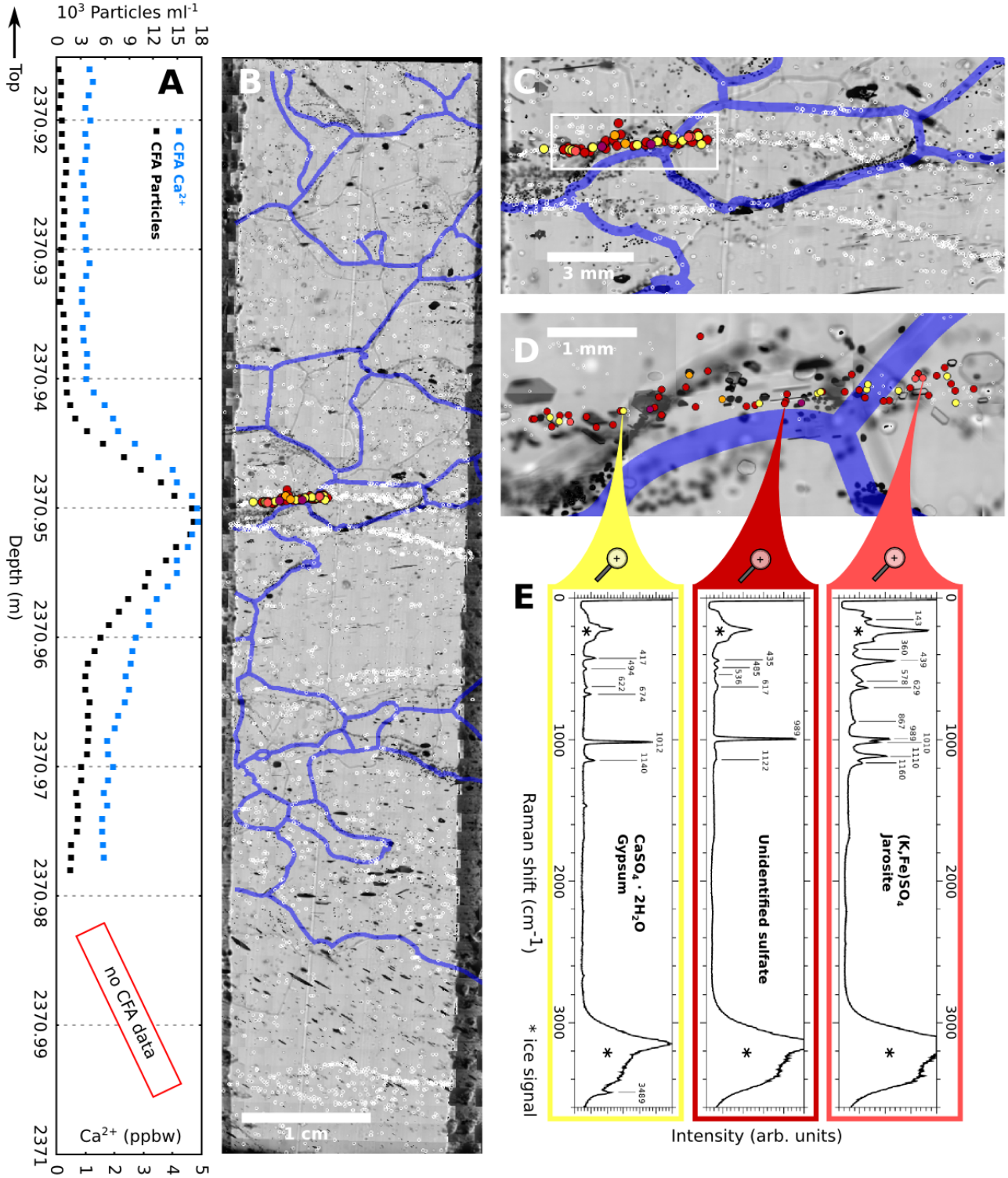

FIGURE 6.5: Detail of section 2371-9 (2370.915–2371.0 m): **(A)** High resolution CFA profile showing Ca^{2+} concentration and number of insoluble particles. **(B)** Impurity map, white circles represent positions of individual micro-inclusions presented in Eichler et al., 2017. Colored circles indicate micro-inclusions analyzed with the Raman system. Blue bands indicate positions of grain boundaries at the focus depth of the micro-inclusions. A horizontal double layer of micro-inclusions at 2370.95 m correlates with a strong peak in the CFA profiles. **(C)** Detail of the double layer with area of interest selected for the Raman measurements in the upper horizon. **(D)** Zoom into the upper horizon. **(E)** Raman spectra of three selected micro-inclusions in the upper horizon.

TABLE 6.2: Mean IC concentrations within two one-meter-long ice core segments (bags) which envelope the studied samples. Bag 2371 (2370-2371 m) originates from MIS 5e, Bag 2392 (2391-2392 m) from MIS 6. Sodium concentrations are used as reference for the calculation of sea-salt fraction for each ion.

	Mass fraction (ppbw)		Molar mass ($g\,mol^{-1}$)	Molar concentration ($mol\,kg^{-1}$)		X/Na sea-salt	SS fraction	
Bag	2371	2392		2371	2392		2371	2392
NO_3^-	43.47	75.65	62.005	$7.01 \cdot 10^{-7}$	$1.22 \cdot 10^{-6}$			
SO_4^{2-}	59.78	212.30	96.061	$6.22 \cdot 10^{-7}$	$2.21 \cdot 10^{-6}$	0.252	4514 %	695 %
Cl^-	12.88	217.44	35.453	$3.63 \cdot 10^{-7}$	$6.13 \cdot 10^{-6}$	1.8	136 %	100 %
Na^+	5.25	121.14	22.989	$2.29 \cdot 10^{-7}$	$5.27 \cdot 10^{-6}$	1	100 %	100 %
Ca^{2+}	4.21	57.57	40.078	$1.05 \cdot 10^{-7}$	$1.44 \cdot 10^{-6}$	0.038	2111 %	1251 %
Mg^{2+}	0.90	25.36	24.305	$3.72 \cdot 10^{-8}$	$1.04 \cdot 10^{-6}$	0.12	143 %	174 %
H^+				$1.80 \cdot 10^{-6}$	$1.54 \cdot 10^{-6}$			

In both segments, Cl^-, Na^+ and Mg^{2+} match very well the sea-salt ion balance and can be considered to originate almost entirely from sea-salt, being transported to the Antarctic plateau in form of NaCl, $MgCl_2$ and their mixtures. This is also reflected in the correlated signals of these three components in Fig. 6.2. On the contrary, the concentrations of SO_4^{2-} and Ca^{2+} exceed the seawater balance about an order of magnitude. This is consistent with their non-sea-salt origin at the EDML site. The main SO_4^{2-} sources are marine biogenic sulfur (Kaufmann et al., 2010) and stratospheric sulfate deposits, whereas most Ca^{2+} is transported together with continental dust and is often used as a dust proxy (Ruth et al., 2008).

The imbalance between major anions and cations can be expressed in the concentration of excess protons H^+ following Eq. 6.1. The concentrations of other ions such as NH_4^+ and MSA^- in our samples are very low so that their contributions to the overall acidity can be neglected.

$$\left[H^+\right] = \left[NO_3^-\right] + 2\left[SO_4^{2-}\right] + \left[Cl^-\right] - \left[Na^+\right] - 2\left[Ca^{2+}\right] - 2\left[Mg^{2+}\right] \tag{6.1}$$

Despite the different ionic concentrations and ratios between bag 2371 and 2392, the H^+ concentrations reveal very similar values in both bags (Tab. 6.2, last row). Thus the ice acidity is nearly constant across the transition between MIS 5e and MIS 6 and is indeed consistent with the DEP conductivity signal (Fig. 6.2).

6.4.3 Sulfate

The Raman analysis revealed that sulfate particles form a dominant part of micro-inclusions in our samples. In the interglacial samples they represent 96 % of all identified spectra. This result is consistent with similar observations by Ohno et al., 2005, 2006 in the Dome Fuji ice core. We cannot confirm observations by Fukazawa et al., 1998a who suggested presence of sulfuric acid in aqueous solution along grain boundaries and triple junctions leading to a network of liquid-filled veins (Rempel et al., 2001). Ionic concentrations in our samples (Tab. 6.2) reveal a sufficient amount of cations as reaction partners to form sulfate salts. Accordingly, most SO_4^{2-} precipitates in form of micro-inclusions rather than liquid H_2SO_4 solution. This, however, can be different in ice with extremely high sulfate concentrations.

6.4.4 Nitrate

The main sources of NO_3^- remain uncertain, however it is a major impurity component in Antarctic ice (Röthlisberger et al., 2000a). As shown in Tab. 6.2, it represents the most abundant ion in terms of molar concentration in the two interglacial samples (bag 2371) and similar concentrations are found also in the glacial part (bag 2392). This is apparently in contradiction to the Raman analysis. In fact, not even one micro-inclusion showed a spectrum that could be clearly attributed to a nitrate salt. This discrepancy may be explained by the relatively high excess of trace anions. In an acidic environment the three main acids – HNO_3, H_2SO_4 and HCl – compete to react with the relatively low amount of cations. Sulfuric acid is the most reactive one being able to replace the other acids in their salts (Iizuka et al., 2008). Thus the final product are various sulfate salts forming micro-particles as shown in the Raman data. However, this does not explain what happens with the nitrate which remains present in the ice, as obvious from the IC measurements. If micro-droplets of concentrated HNO_3 would form, they should be easily detectable with the Raman-microscope. It seems to be conclusive that nitrate ions are present rather in a dissolved form than a condensed phase. This is in agreement with experimental results by Thibert and Dominé, 1998 who suggested HNO_3 (with relatively high diffusion coefficient: $D = 2 \cdot 10^{-11}\,\mathrm{cm^2\,s^{-1}}$ at $-32\,^\circ\mathrm{C}$) forming solid solution in ice. The mean migration distance of NO_3^- after 129 ka would be around 9 cm which would fade away any seasonality in the nitrate signal in our samples. Indeed, the IC profile (Fig.6.2) shows a very stable NO_3^- signal without any distinctive peaks or other kind of variability.

6.4.5 Chloride

The case of HCl may be similar to HNO_3, albeit complicated by the fact that hydrochloric acid and its most prominent salt – NaCl – do not possess a Raman-active mode. Thus the Raman data do not provide any direct information about the form or location of chloride in ice. The IC data in Tab.6.2 indicate that the Cl^- concentration in our samples resembles the sea-salt Cl^-/Na^+ ratio, meaning that no significant loss of Cl^- occurred since deposition. However, the high amount of Na_2SO_4 spectra indicates that a considerable part of Cl^- was replaced from the sea-salt by sulfate. This could occur in a direct reaction with sulfuric acid (6.2) or over several steps, e.g., via (6.3) and (6.4).

$$2\mathrm{NaCl} + \mathrm{H_2SO_4} \rightarrow \mathrm{Na_2SO_4} + 2\mathrm{HCl} \tag{6.2}$$

$$\mathrm{NaCl} + \mathrm{HNO_3} \rightarrow \mathrm{NaNO_3} + \mathrm{HCl} \tag{6.3}$$

$$2\mathrm{NaNO_3} + \mathrm{H_2SO_4} \rightarrow \mathrm{Na_2SO_4} + 2\mathrm{HNO_3} \tag{6.4}$$

The final product of these reactions is the formation of Na_2SO_4 and release of HCl. According to the phase diagram by Thibert and Dominé, 1997 the amount of chloride present in our samples could easily form solid solution even if all the NaCl was converted into Na_2SO_4. The diffusion coefficient of HCl in ice estimated by Thibert and Dominé, 1997 is of the order of $10^{-12}\,\mathrm{cm^2\,s^{-1}}$. This would lead to an average distance of 2 cm after 129 ka. Taking ice thinning into account the Cl^- signal should be well preserved even at 2400 m depth. This is in agreement with the IC profile which shows a good correlation between the Cl^- and Na^+ signals. Our Raman

results in combination with the ion balance from IC are overall in a good agreement with chemical compositions of salt inclusions predicted by Iizuka et al., 2008.

6.4.6 Solid solution

The presence of excess anions in the studied samples raises questions on their incorporation and distribution in the ice. This will mainly depend on the amount of energy needed for their incorporation. It has been postulated that ions with rather small ionic radii such as F^- and Cl^- should be able to substitute water molecules in the ice lattice. The incorporation of one HCl molecule for instance would introduce a Bjerrum L defect and an H_3O^+ ionic defect into the lattice (Petrenko and Whitworth, 1999), both being electric charge carriers. If a significant amount of HCl were available – e. g., due to reaction (6.2) – the electrical properties would change radically. Thus the DEP conductivity in Fig. 6.2 may not be directly linked to the SO_4^{2-} concentration as apparent from its curve shape, but rather to the amount of dissociated Cl^- which, however, depends on SO_4^{2-} via (6.2), (6.3) and (6.4).

Larger molecules are not compatible with the dimensions of the ice lattice and thus cannot substitute water molecules at the lattice sites. They represent high-energy lattice defects and therefore are likely to accumulate at regions of high energy, such as grain boundaries, subgrain boundaries, triple junctions and other impurities. Thibert and Dominé, 1997, 1998 suggested that diffusion through low angle grain boundaries was important for both – Cl^- and NO_3^-. Dissolved ions in grain boundaries and triple junctions are likely to affect several of their characteristics, in particular the mobility (Alley et al., 1986b) and molecular structure via enhanced premelting (Rempel et al., 2001). The absence of Raman signal in grain boundaries and triple junctions suggests that concentrations of Raman-active molecules in the grain boundary network are significantly lower than reported by e. g. Fukazawa et al., 1998a. This does not apply to mono-atomic ions and Raman-inactive molecules, which could still reside in the grain boundaries. However, liquid water phase caused by enhanced premelting should be well distinguishable from the ice Raman spectra, which was not the case.

6.4.7 Transport, mixing and reactions

The comparison of Raman results with concentrations of major ions (IC) indicates that mixing and chemical reactions occurred since deposition of the different impurities. It is difficult to guess when or in which depth these processes occur. It is likely that many chemical processes take place already in the aerosol phase, during precipitation or shortly after it, during snow metamorphism. Porous snow with its large surface area, temperature gradient and light penetrating the upper layers offers a highly reaction-friendly environment for many species (Bartels-Rausch et al., 2014; Dominé and Shepson, 2002). Postdepositional losses of MSA^-, NO_3^- and Cl^- have been investigated by Weller et al., 2004 at the EDML site. In contrast to sites with low accumulation rate there was no significant Cl^- loss with depth in the EDML snow. The Cl/Na ratio persisted close to the sea-salt value. The authors suggested that the main part of Cl^- was located inside the ice crystals in form of NaCl isolated from the other reacting agents. This again would suggest that reactions with other acids (see section 6.4.5) would occur later on, possibly when the pores have already been closed off and the ice was formed.

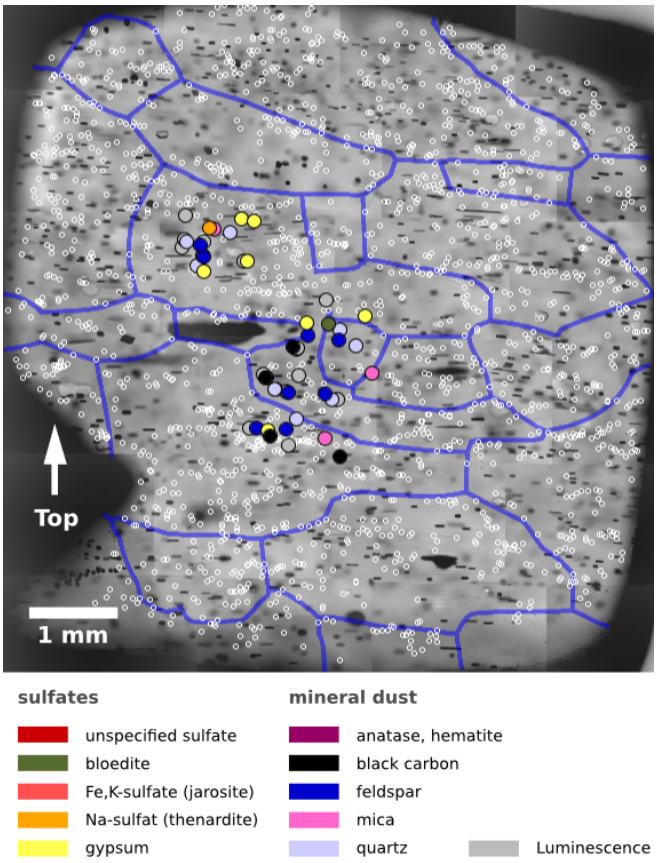

FIGURE 6.6: Impurity map in section 2392-2 (2392.26 m). The impurity analysis of the MIS 6 sample was restricted to an area of approx. 8×8 mm^2. White circles represent positions of individual micro-inclusions. Colored circles indicate micro-inclusions analyzed with the Raman system. Gray circles represent micro-inclusions with strong luminescence. Blue bands indicate positions of grain boundaries at the upper surface, approximately 300 microns above the focus depth of the micro-inclusions.

Below the firn–ice transition impurities are trapped at their locations and the transport and reaction dynamics is reduced significantly. In a completely static matrix the transport of impurities is controlled exclusively by diffusion due to thermic fluctuations. However, as ice deforms it provides more opportunities for mixing and reactions between impurities. Two important flow-related processes are: (1) Accumulation and drag of dissolved impurities by migrating grain boundaries (GB) due to dynamic recrystallization and grain growth. The longer the distance covered by the GB migration, the more dissolved ions can accumulate in it, react with each other and, eventually, precipitate in form of newly formed salt particles. Such microparticles would be left behind because of their low mobility. (2) Strain in a deforming ice polycrystal distributes highly heterogeneously (Jansen et al., 2016; Llorens et al., 2016b; Steinbach et al., 2016) forming localized bands of high strain and strain rate. Under simple shear conditions these shear bands align at low angles to the horizontal shear plane (Llorens et al., 2016b), which typically also corresponds to the orientation of the isochrones. Impurities located in such shear bands are exposed to higher mechanical mixing rates, however without a necessarily disturbing effect on their chronology. Both mechanisms could be relevant for mixing of dissolved

impurities and the formation of new micro-inclusions with increasing depth as suggested by Faria et al., 2010. This could also partly explain their characteristic spatial distributions on the micro-scale, i. e. the frequently observed chains and groups of micro-inclusions (e. g. Fig. 6.4b).

6.4.8 Deformation of ice

As shown in previous studies (Cuffey et al., 2000b; Dahl-Jensen and Gundestrup, 1987; Fisher and Koerner, 1986; Paterson, 1991), impurity-loaded ice in simple shear deforms in general more readily than clean ice. Ambiguous results have however been observed possibly due to oversimplified assumptions on large-scale deformation geometry (plain strain versus shear) and the interaction with anisotropic ice (Paterson, 1983). It is thus worthwhile discussing the actual processes under the likely deformation kinematics. The samples discussed here originate from depths 2370 m and 2392 m, i. e., deep enough in the lowest third of the ice sheet where simple shear due to interaction with bedrock is already expected to dominate the deformation (Dansgaard-Johnsen model). Numerical ice sheet modeling of the EDML site predicts the onset of simple shear below 1700 m and further increase of horizontal shear around 2400 m (Weikusat et al., 2017b). The MIS 6–5e transition is characterized by the highest spatial gradient of impurity concentration along the entire ice core. Thus we can expect a different rheology for the two neighboring parts – the interglacial, clean ice being the "harder" and the glacial, impurity-loaded ice the "softer" layer for shearing. Recent measurements of the EDML borehole deformation, which will be published elsewhere, indeed suggest such a behavior (Jansen et al., 2017).

Investigations of the effect of impurities on the deformation rate of ice often differentiate between dissolved impurities (ions) versus second phase inclusions (micro-inclusions) (Alley and Woods, 1996; Alley et al., 1986a,b; Cuffey et al., 2000b; Durand et al., 2006b; Gow et al., 1997). Furthermore, it is distinguished between a direct effect on the single ice-crystal plasticity (Glen, 1968; Jones and Glen, 1969; Jones, 1967; Petrenko and Whitworth, 1999) versus the interaction between impurities and grain boundaries (Alley et al., 1986a; Durand et al., 2006b; Eichler et al., 2017; Humphreys and Hatherly, 2004). The latter has been suggested as responsible for the frequently observed high impurity content correlating with small grains sizes (Fisher and Koerner, 1986; Paterson, 1991). Impurities either in particulate or dissolved form would slow down grain boundary migration and grain growth. According to Paterson (1991), fine-grained ice in simple shear tend to develop strong CPO faster than coarse-grained ice. Other authors (e. g., Cuffey et al., 2000b; Goldsby and Kohlstedt, 2001) propose other grain-size sensitive deformation mechanisms acting on the micro-scale.

Based on the results presented above following conclusions can be drawn: The amount of dissolved impurities is rather small, since most cations and anions react together forming salt inclusions. Nitrate represents an exception, as demonstrated through its absence in the Raman records and thus is likely to enter in solid solution. However, the concentrations in MIS 5e and MIS 6 are very similar, so that NO_3^- is rather unlikely to be responsible for such dramatic differences in microstructure (Fig.6.1) and rheology. Solid solution of chloride, which introduces protonic defects into the ice lattice and thus increases mobility of dislocations (Petrenko and Whitworth, 1999), depends on the concentration of other major acids to replace Cl^- in the sea salt. As shown in Tab. 6.2, the acidities in both parts of the ice core are very similar, so that the role of dissolved Cl^- may be rather minor as well. However, the concentration of NaCl itself increases by a factor 20 from MIS 5e to MIS 6. Thus,

depending on its phase and spatial distribution, which are inaccessible to the Raman analysis, NaCl could have a significant effect on ice physical properties. Micro-inclusions, which represent the most common form of impurities in ice, are another major candidate responsible for the different properties of glacial and interglacial ice. The number of insoluble particles per volume unit increases by two orders of magnitude along the climatic transition (Fig.6.2). However, the actual mechanism must be further investigated, since contradictory assumptions and observations are associated with our current understanding of Zener pinning as the controlling mechanism (Alley et al., 1986a; Durand et al., 2006b; Eichler et al., 2017).

6.5 Summary

In this study a combination of micro-cryo-Raman spectroscopy and CFA, IC and DEP data was presented in order to investigate the way in which chemical impurities integrate and distribute in solid ice. This is another step towards a more holistic view on ice cores, building a bridge between ice core chemistry and physical properties of ice. For more quantitative comparisons and in order to improve the statistical significance, a higher number of micro-inclusions covering larger areas should be investigated in future studies. This is technically possible, however requires further improvements of the focusing routine in order to reduce the time between individual measurements.

The three studied EDML samples originate from the depth range between 2370 m and 2400 m around the transition from the penultimate glacial period MIS 6 to the early MIS 5e and are characterized by immense differences in impurity concentrations and compositions as well as crystal sizes and orientations. While the glacial impurity concentrations are up to several orders of magnitude higher than the interglacial ones (e. g. dust), the average crystal area decreases by a factor 20. The MIS 6 micro-inclusions are dominated by mineral dust particles. On the contrary, 96 % of the MIS 5e inclusions were sulfate particles, mainly gypsum, sodium sulfate, iron–potassium sulfate (likely jarosite) and other unspecified sulfates. We report for the first time Raman spectra of mica, graphite, anatase, hematite, possibly jarosite and bloedite in an ice core. The spatial distributions of micro-inclusions are highly heterogeneous, forming horizontal layers on the millimeter-scale and small groups or chains of micro-inclusions on the micrometer-scale. No preferential distribution of micro-inclusions with respect to the grain boundary network could be determined, neither in the interglacial nor in the glacial samples. Furthermore, no Raman signal was detected, which would indicate the presence of dissolved impurities in grain boundaries or triple junctions. This puts the relevance of liquid-filled or acid-filled veins into question, at least for concentrations and temperatures present in our samples. Nevertheless, small amount of ions, e. g. as referred by Alley et al., 1986a, could still segregate to grain boundaries without being detected by the Raman microscope. Also, NaCl – the main part of sea salt – has to be excluded from our considerations, since it is inaccessible for Raman spectroscopy, no matter in which phase.

The combination of Raman analysis of micro-inclusions with the concentrations of major ions from IC demonstrates that the way impurities incorporate into ice varies not only from species to species, but rather depends on the overall ion budget, as already suggested by Iizuka et al., 2008. This is evident from the case of missing nitrate salts in the Raman spectra, which we interpret as a result of reactions with stronger acids – mainly H_2SO_4 – leading to the solution of NO_3^- in ice. The presence of Na_2SO_4 suggests that also a part of Cl^- was expelled from the sea-salt

and possibly dissolved in the matrix, while the Na^+/Cl^- sea salt ratio stayed preserved. Similarly, the solid mineral-dust aerosols seem to be affected by the acids, as suggested by the absence of Ca-carbonate and Ca-plagioclase and the abundance of gypsum instead. We conclude that some of these reactions may take place after the deposition of the original aerosols. The deforming ice matrix offers a number of mechanisms which facilitate mixing and reactions between impurities on the micrometer to millimeter scale, without necessarily disturbing their chronology. Thus, our understanding of polar ice as a frozen archive should be reconsidered. Whether a particular impurity signal will be preserved at a certain depth depends on the reactions it was involved in, their products and the mobilities (or diffusion rates) of these products.

The link between impurities and enhanced deformation of ice remains ambiguous, as well as the identification of the responsible impurity species. Our results suggest that the two major actors are likely to be micro-inclusions and sodium sulfate, which is however invisible to the Raman spectroscopy. The effect of dissolved ions might be rather minor, as most of them react and precipitate in form of salt inclusions. The excess ion concentrations are similar in both parts of the ice core. Micro-inclusions represent the most common form of impurities and experience the highest concentration gradient along the climatic transition. However, the identification of the responsible mechanism remains pending. In particular, future investigation still need to resolve, whether characteristic microstructures such as small grains and strong CPOs are the main drivers for enhanced deformation, or its consequence.

Conflict of Interest Statement

The authors declare that the research was conducted in the absence of any commercial or financial relationships that could be construed as a potential conflict of interest.

Author Contributions

Initial concept by JE and IW. JE performed Raman measurements and analysis of the Raman spectra with support from CW. BT performed ion chromatography measurements, CFA data were provided by HF, AW and UR. MB and MH contributed to the analysis of the data. DEP data were provided by FW. DJ, SK and IW contributed to the interpretation of data by providing expertise on the field of ice deformation as well as the general glaciological framework. The manuscript was written by JE with contributions of all coauthors.

Funding

This research was funded by HGF grant VH-NG-802 to JE and IW, SPP 1158 DFG grant WE4711/2 to CW.

Acknowledgments

We thank Rolf Weller for helpful discussions and his expertise in the chemistry of snow and ice. This work is a contribution to the European Project for Ice Coring in Antarctica (EPICA), a joint European Science Foundation/ European Commission scientific program, funded by the EU (EPICA-MIS) and by national contributions from Belgium, Denmark, France, Germany, Italy, the Netherlands, Norway, Sweden,

Switzerland and the United Kingdom. The main logistic support was provided by IPEV and PNRA (at Dome C) and AWI (at Dronning Maud Land).

Supplemental Data

Supplementary material consists of two supplementary figures containing a pure ice Raman signal and characteristic Raman spectra of the different types of micro-inclusions.

Data Availability Statement

The raw Raman data supporting the conclusions of this manuscript will be made availible by the authors, without undue reservation, to any qualified researcher.

6.6 Supplementary material

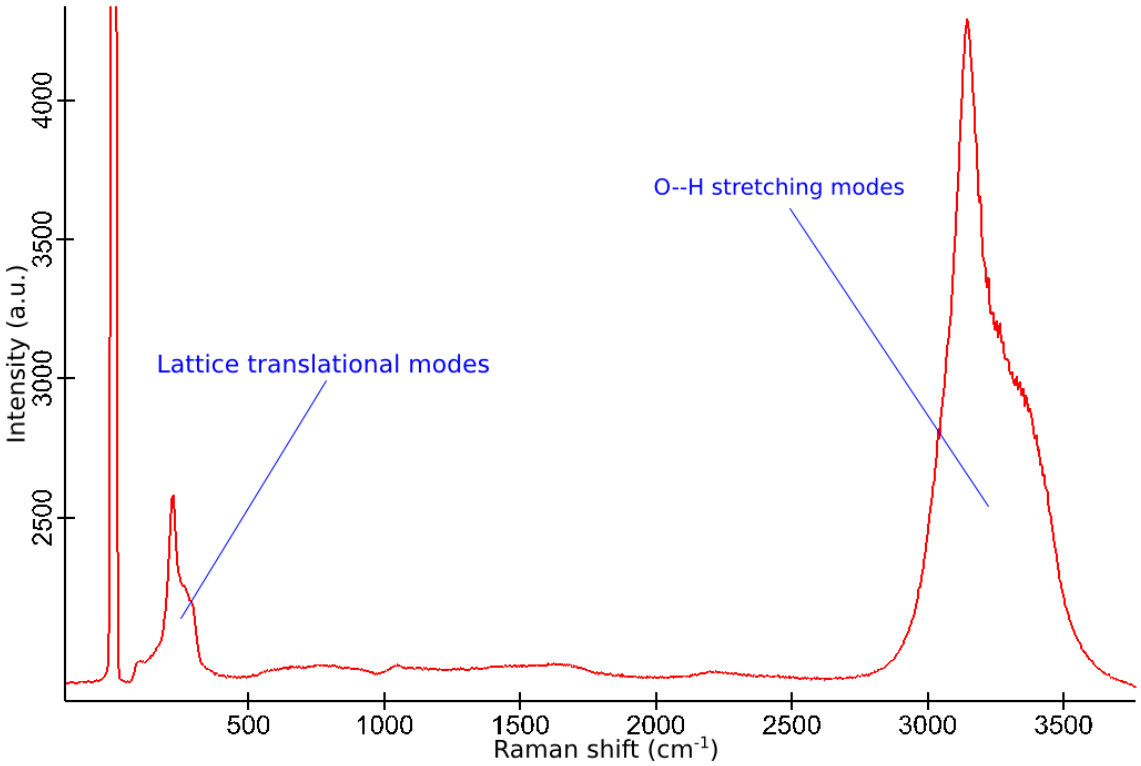

FIGURE 6.7: Example of a "pure" ice Raman spectrum with the characteristic vibrational bands indicated.

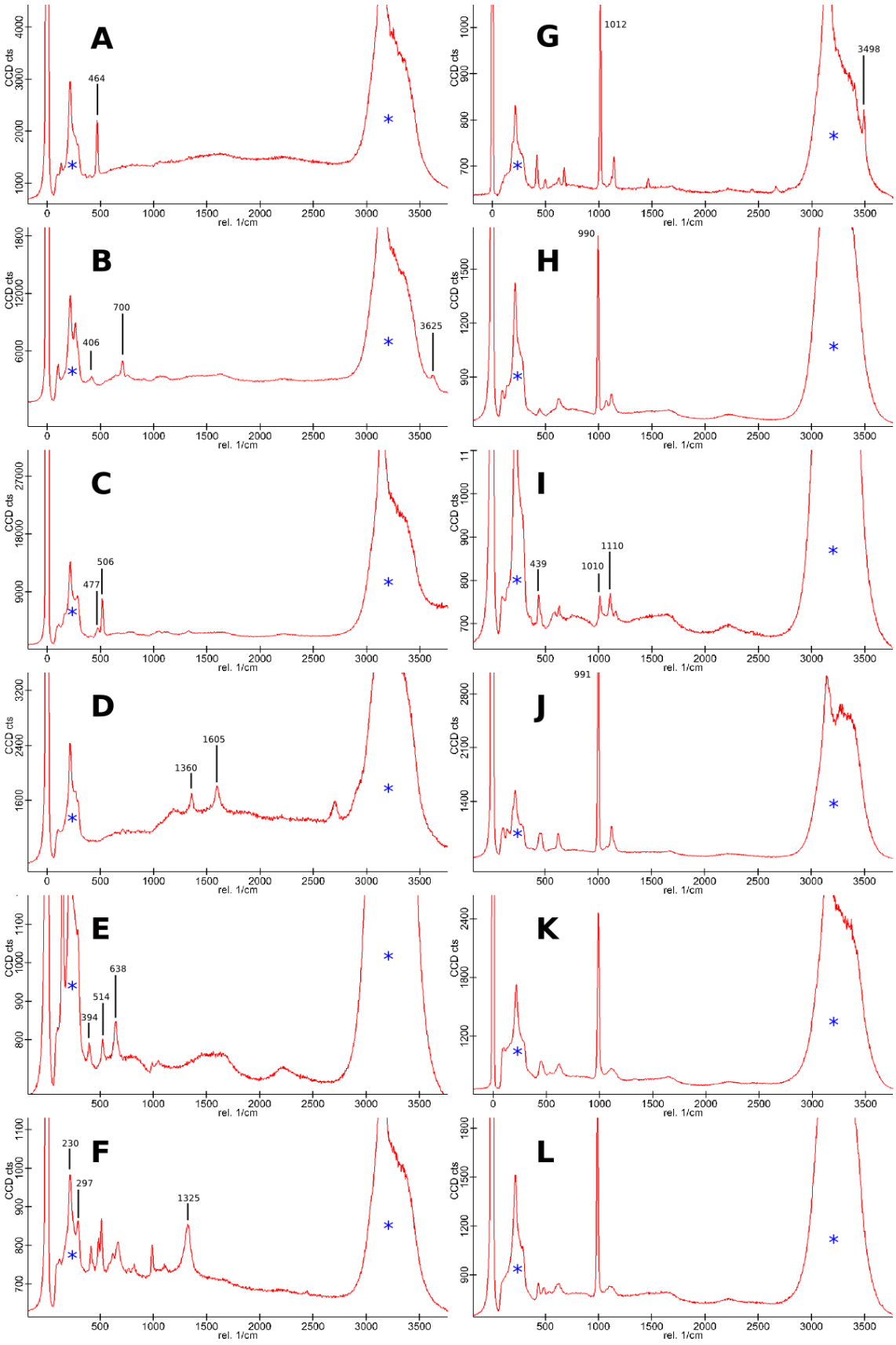

FIGURE 6.8: Example Raman spectra of micro-inclusions: **(A)** quartz, **(B)** mica, **(C)** feldspar, **(D)** black carbon, **(E)** anatase, **(F)** hematite, **(G)** gypsum, **(H)** thenardite, **(I)** jarosite, **(J)** bloedite, **(K)** unspecified sulfate 1, **(L)** unspecified sulfate 2. The ice vibrational bands are indicated with an asterisk.

Chapter 7

Paper III

The Relevance of Grain Dissection for Grain Size Reduction in Polar Ice: Insights from Numerical Models and Ice Core Microstructure Analysis

Florian Steinbach [1], Ernst-Jan N. Kuiper [2,3], Jan Eichler [1,2], Paul D. Bons [1], Martyn R. Drury [3], Albert Griera [4], Gill M. Pennock [3], and Ilka Weikusat [1,2]

[1] Department of Geosciences, Eberhard Karls University Tübingen, Tübingen, Germany
[2] AWI-Glaciology, Alfred-Wegener-Institute Helmholtz-Centre for Polar and Marine Research, Bremerhaven, Germany
[3] Department of Geosciences, Utrecht University, Utrecht, Netherlands
[4] Departament de Geologia, Universitat Autònoma de Barcelona, Barcelona, Spain

Published in *Frontiers in Earth Science*, 26 September 2017.

Abstract

The flow of ice depends on the properties of the aggregate of individual ice crystals, such as grain size or lattice orientation distributions. Therefore, an understanding of the processes controlling ice micro-dynamics is needed to ultimately develop a physically based macroscopic ice flow law. We investigated the relevance of the process of grain dissection as a grain-size-modifying process in natural ice. For that purpose, we performed numerical multi-process microstructure modeling and analyzed microstructure and crystallographic orientation maps from natural deep ice-core samples from the North Greenland Eemian Ice Drilling (NEEM) project. Full crystallographic orientations measured by electron backscatter diffraction (EBSD) have been used together with c-axis orientations using an optical technique (Fabric Analyser). Grain dissection is a feature of strain-induced grain boundary migration. During grain dissection, grain boundaries bulge into a neighboring grain in an area of high dislocation energy and merge with the opposite grain boundary. This splits the high dislocation-energy grain into two parts, effectively decreasing the local grain size. Currently, grain size reduction in ice is thought to be achieved by either the progressive transformation from dislocation walls into new high-angle grain boundaries, called subgrain rotation or polygonisation, or bulging nucleation that is assisted by subgrain rotation. Both our time-resolved numerical modeling and NEEM ice core samples show that grain dissection is a common mechanism during ice deformation and can provide an efficient process to reduce grain sizes and counter-act dynamic grain-growth in addition to polygonisation or bulging nucleation. Thus, our results

show that solely strain-induced boundary migration, in absence of subgrain rotation, can reduce grain sizes in polar ice, in particular if strain energy gradients are high. We describe the microstructural characteristics that can be used to identify grain dissection in natural microstructures.

7.1 Introduction

Knowledge of the properties and processes controlling the flow of ice is essential to understand ice sheet dynamics. Ice sheets creep under gravitational forces (Petrenko and Whitworth, 1999) and their macroscopic flow is affected by properties of individual ice crystals, such as crystallographic preferred orientation (CPO) and grain size (Bader, 1951; Budd and Jacka, 1989; Mangeney et al., 1997; Ng and Jacka, 2014; Steinemann, 1954; Veen and Whillans, 1990). Ice crystals in ice sheets are thought to mainly accommodate deformation by viscoplastic glide and climb of intracrystalline lattice defects, which is known as dislocation creep (Pimienta and Duval, 1987; Shoji and Higashi, 1978). On Earth, the only stable ice polymorph is hexagonal ice Ih, which has a significant viscoplastic anisotropy. The glide resistance on the basal plane, which is perpendicular to the c-axis, is at least 60 times lower than that on the prismatic and pyramidal glide planes (Duval et al., 1983). With deformation, c-axes align in the direction of maximum finite shortening (Azuma and Higashi, 1985) causing a macroscopic mechanical anisotropy of the polycrystalline aggregate (Budd and Jacka, 1989; Gao and Jacka, 1987).

Dislocation creep depends on the CPO and is grain size insensitive. However, other deformation mechanisms such as *grain boundary sliding* or *diffusion creep* are known to depend on grain sizes (Raj and Ashby, 1972; Shoji and Higashi, 1978) and may be strain rate controlling at low stresses (Goldsby and Kohlstedt, 1997a, 2001; Pettit and Waddington, 2003). An understanding of grain size evolution in ice sheets including all relevant processes and proposed models (Durand et al., 2006a; Ng and Jacka, 2014) is essential to include the full suite of deformation mechanisms into ice flow modeling.

In various deep ice cores, grain size is observed to increase with depth until a stable value is reached (Fitzpatrick et al., 2014; Jun et al., 1998; Montagnat et al., 2012). Where drill cores penetrate the glacial to Holocene transition, a distinct decrease in grain size and increase in CPO strength is found (Faria et al., 2014a; Montagnat et al., 2014; Weikusat et al., 2017b, and references therein). The North Greenland Eemian Ice Drilling (NEEM) ice core reflects this typical microstructural evolution. In NEEM, a relatively stable grain size of about 10 to 12 mm^2 is observed below a depth of ca. 400 m, but the CPO progressively strengthens further down (Binder, 2014; Kipfstuhl, 2010; Montagnat et al., 2014; Weikusat and Kipfstuhl, 2010). A distinct change toward strongly aligned c-axes that form an elongated, vertical single maximum is observed at the transition from Holocene to glacial ice at 1,400 m depth (Binder, 2014; Montagnat et al., 2014). In the glacial ice, the grain sizes are smaller and more variable than in Holocene ice. This is observed to correlate with higher impurity load in glacial ice. However, the relation of grain size and CPO with impurities is still under discussion (Eichler et al., 2017).

The grain size in ice results from a combination of grain growth and grain-size-reducing mechanisms. The downward increase in grain size in shallow ice toward stable grain sizes implies a stronger relative contribution of grain-size-reducing mechanisms when stable grain sizes are achieved. As ice in ice sheets mostly

deforms at temperatures close to its pressure melting point, recrystallization is expected to accompany viscoplastic deformation (Duval, 1979; Jacka, 1994; Kipfstuhl et al., 2009). Recrystallization includes rotation of crystal lattices, as well as grain boundary migration and/or formation of new grain boundaries (Faria et al., 2014c).

The migration of grain boundaries during *normal grain-growth* (NGG) is driven by surface energy minimisation (Alley et al., 1986a,b; De La Chapelle et al., 1998; Duval, 1985; Smith, 1964; Weaire and Rivier, 1984). NGG leads to an increase of mean grain area with time and equidimensional grains with slightly curved grain boundaries forming 120° angles at grain boundary triple junctions. *Strain-induced boundary migration* (SIBM), however, is driven by strain energies that result from the elastic lattice distortion caused by dislocations (Humphreys and Hatherly, 2004, pp. 251–253). During SIBM, grain boundaries migrate toward highly strained areas in adjacent grains and leave behind dislocation-free regions. This usually causes irregular grain boundaries and bulges toward high-energy regions (Means, 1981). SIBM in ice is assumed to cause increasing grain sizes (Duval and Castelnau, 1995) and has been termed *dynamic grain-growth* when combined with NGG (Faria et al., 2014a,c; Urai and Jessell, 2001).

During *recovery*, dislocations arrange in lower energy configurations (Urai et al., 1986; White, 1977). This leads to the gradual transformation of low-angle dislocation walls into subgrain boundaries (Weikusat et al., 2017a) and eventually into new high-angle grain boundaries. This process of rotational recrystallization or *polygonisation* leads to a grain size reduction (Alley et al., 1995; Rössiger et al., 2011). The formation of new grains by spontaneous nucleation is a further mechanism of grain-size reduction, but is thought to be very unlikely in the absence of strong chemical driving forces, as is the case for ice (Drury and Urai, 1990; Faria et al., 2014c; Humphreys and Hatherly, 2004). During *bulging nucleation*, small grains separate from the serrated grain boundary formed by SIBM assisted by subgrain rotation. Bulging nucleation is suggested to reduce grain sizes in ice (De La Chapelle et al., 1998; Duval and Castelnau, 1995; Montagnat et al., 2015) and is observed in creep tests on columnar ice at high temperatures and stresses (Chauve et al., 2017). The deformation-induced recrystallization mechanisms (SIBM, polygonisation and nucleation) are together termed *dynamic recrystallization*. Of these mechanisms, SIBM and polygonisation are thought to be dominant in glaciers and ice sheets.

While bulging recrystallization driven by SIBM assisted by other processes can reduce grain sizes in ice, SIBM in isolation is generally assumed to result in a grain-size increase in glaciology. However, SIBM has been observed to decrease grain size in deformation experiments on rock analogs by Means (1983, cf. Figure 4 therein) and Urai (1983, cf. Figure 14 therein). Both studies observed SIBM with rapidly migrating bulges, eventually migrating through a grain and splitting it into two parts when reaching an opposite grain boundary. This causes an effective mean grain-size reduction by forming two "new" grains with similar CPO. Resulting groups of grains with similar orientation were called "orientation families" by Urai (1983). This process was termed *grain dissection* by Urai et al. (1986) and Urai (1987) is known as *geometric dynamic recrystallization* in metallurgy (Humphreys and Hatherly, 2004, pp. 461–465; Meer et al., 2002; Figure 7.1). Grain dissection is readily observed, if time-resolved microstructure evolution is available, corresponding movies of grain dissection in rock analogs are presented by Urai and Humphreys (2000). Grain dissection is only effective when the grain size is similar to the size of grain-boundary bulges. At larger grain sizes, bulges cannot reach the other side of a grain and polygonisation or bulging nucleation would dominate. At smaller grain sizes, bulges

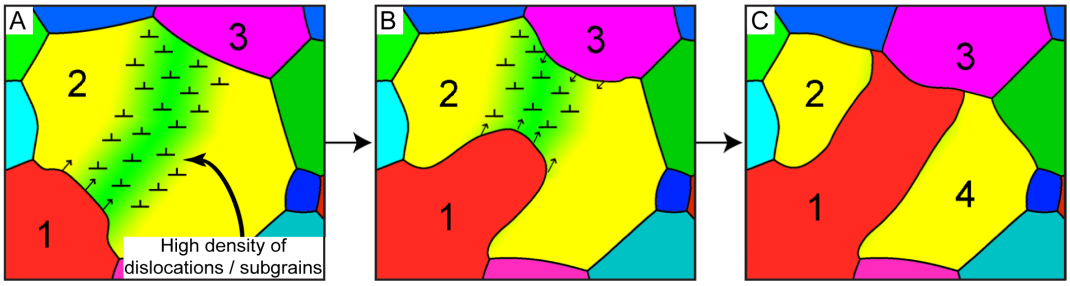

FIGURE 7.1: Schematic illustration of the grain dissection process according to Means (1983) and Urai (1983). (A) A bulge of grain 1 is migrating into a high dislocation-density area to reduce locally high strain energies in grain 2. (B) The bulge of grain 1 is migrating further through the high strain-energy area of grain 2. (C) The bulge ultimately reaches grain 3, dividing grain 2 into two grains. Bulging stops due to low energy gradients and driving forces between grain 1 and 3. The new grain 4 and grain 2 are characterized by a similar lattice orientation; an orientation family.

sweep over a whole grain and thus remove it, which leads to a mean grain-size increase. It follows that grain dissection is most effective at a stable grain size, when polygonisation and grain dissection operate in conjunction.

Grain dissection has not yet been explicitly observed in natural ice microstructures. Breton et al. (2016) report grain dissection in deformation experiments on laboratory-prepared ice and suspect a grain-size-reducing character. So far, it is assumed that stable grain sizes in ice are achieved by an interplay of dynamic grain-growth, polygonisation and potentially nucleation processes (Alley et al., 1995; Chauve et al., 2017; De La Chapelle et al., 1998; Hidas et al., 2017; Mathiesen et al., 2004; Montagnat and Duval, 2000; Rössiger et al., 2011). However, in rock analogs and bischofite, grain dissection is observed as an effective grain-size-reducing process, in particular at steady-state grain sizes (Jessell, 1986; Urai, 1987).

In this study, we investigate whether grain dissection is a relevant process during ice microdynamics. We consider the role of grain dissection in the grain size evolution in glacier/ice sheet ice and assess under which conditions it can potentially be an efficient grain-size-reducing mechanism. We use two approaches: (1) micro-dynamical modeling using the Elle microstructure-modeling platform coupled to a full-field crystal viscoplasticity code (VPFFT) and (2) microstructure and crystallographic orientation maps of natural ice. We use natural ice samples from NEEM ice core as it represents microstructural behavior typical for various other ice cores and a sufficiently large microstructural dataset from NEEM ice core is readily available. We denote ice deposited in the last glacial period, i. e. after Eemian, but before Holocene, "glacial ice" and ice deposited in the Holocene "Holocene ice."

7.2 Methods

7.2.1 Microstructural Modeling

The Elle Modeling Platform

The open-source numerical modeling platform Elle (Bons et al., 2008; Jessell et al., 2001; Piazolo et al., 2010) is optimized to model coupled or interacting microstructural processes. Elle was applied in various studies on ice microstructures, such as single and polyphase grain-growth (Roessiger et al., 2014; Rössiger et al., 2011). The

full-field crystal viscoplasticity code (VPFFT) by Lebensohn (2001) coupled to Elle was used to simulate strain localisation, dynamic recrystallization and folding in ice with and without air bubbles (Bons et al., 2016; Jansen et al., 2016; Llorens et al., 2016a,b; Steinbach et al., 2016).

Here, only the essentials of the modeling approaches for deformation and recrystallization are summarized. For more detail on the principles of Elle, the reader is referred to Jessell et al. (2001) and Bons et al. (2008), for the VPFFT code to Lebensohn (2001), and for the coupling of both codes to Griera et al. (2013). Details on the grain boundary migration and recovery codes are presented in Becker et al. (2008) and Borthwick et al. (2013), respectively. The Elle/VPFFT algorithms to model dynamic recrystallization can be found in Llorens et al. (2016a) and Steinbach et al. (2016). If not indicated differently, we used previously published input parameters for our numerical models (see Llorens et al., 2016a,b; Steinbach et al., 2016). The basic simulation setup is summarized in Table 7.1, whereas Table 7.2 contains more detailed information on the input parameters.

Microstructure Discretisation

In Elle, the two-dimensional microstructure of polycrystalline ice is discretised in a set of contiguous polygons, called flynns, in a cell with fully wrapping and periodic boundaries. The flynns are defined by straight boundaries than link boundary nodes (*bnodes*) in either double- or triple junctions. The *bnodes* are successively moved to achieve grain boundary migration. During grain boundary migration, the development of quadruple or higher-order *bnode* junctions is not allowed, as well as island flynns with only one surrounding neighbour *flynn*. To store intracrystalline properties, such as crystal orientation, local stresses, strain rates or dislocation densities, a set of unconnected nodes (*unodes*) is superimposed on the *flynn* network. For our simulations, the *unodes* are arranged in a regular grid of 256×256 *unodes*, which is a requirement of VPFFT. Crystal orientations are mapped onto *unodes* using Euler triplet angles following the Bunge convention (Bunge, 2013).

Topology checks are carried out at all times during the simulations to ensure compliance with topological restrictions (see Figure 7.2). The topology checks maintain the resolution defined by the set minimum (0.5 mm) and maximum (1.1 mm) *bnode* separation. A new topological check allows for grain dissection: Two unconnected (non-neighbouring) double-junction *bnodes* are merged if they approach closer than the set minimum separation (Figure 7.2, (c)). This effectively splits the *flynn* adjacent to both *bnodes*, into two daughter *flynns*, which constitutes a grain dissection event. A dissection is not performed if less than three *bnodes* are between the two non-neighbouring *bnodes*, as this would lead to an unviable daughter *flynn* (Figure 7.2, (d)). The number of dissection events is tracked throughout the simulation.

Modelling crystal viscoplasticity and dynamic recrystallisation

The full-field crystal viscoplasticity code (VPFFT) is based on calculating the stress field from kinematically admissible velocity fields that minimises the average local work-rate under compatibility and equilibrium constraints (Griera et al., 2013; Lebensohn, 2001; Lebensohn et al., 2009). VPFFT assumes intracrystalline deformation in ice Ih accommodated by dislocation glide on basal, pyramidal and prismatic slip systems. The non-linear viscous, rate-dependent flow law predicts the strain rate and stress at each point in the computational grid defined by *unodes*. The non-basal slip resistance is set 20 times higher than for basal slip (Table 7.2) as a

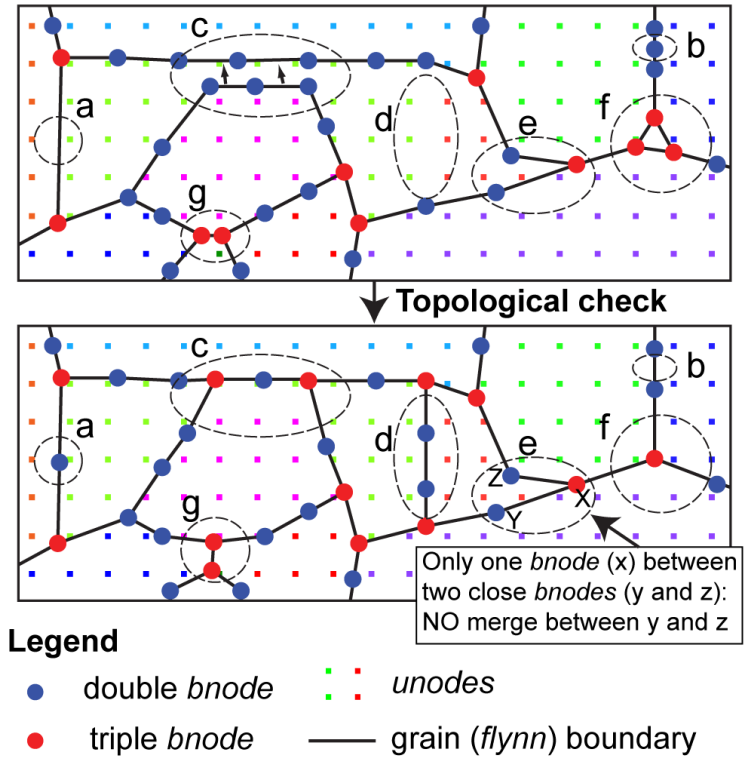

FIGURE 7.2: Microstructure discretisation and topological events necessary if bnodes move due to deformation or grain boundary migration. Insertion (a) and deletion (b) of a bnode to keep a constant resolution (c) Merging two non-neighboring bnodes, this numerically defines grain dissection (d) Insertion of new grain boundary by polygonisation between unode clusters above a critical misorientation (e) No merging of two non-neighboring bnodes as number of other bnodes between the two close bnodes is < 3 (f) Deletion of small flynn containing no unodes (g) Neighbor switch in triple bnodes.

compromise between accuracy and computational efficiency. Systematic trial simulations for the studies by Llorens et al. (2016a,b, 2017) and Steinbach et al. (2016) showed that with the use a ratio of 20 instead of 60 does not significantly alter the microstructural evolution. A significant effect on the number of grain dissection events is therefore considered unlikely.

Since the strain rate and stress fields are initially unknown, VPFFT uses an iterative spectral solver based on the Fast Fourier Transformation. VPFFT computes the viscoplastic response for a short time-step during which velocities are assumed constant. The updated lattice orientations are remapped onto the rectangular unode grid and the displacement field is applied to all *bnodes*. Furthermore, geometrically necessary dislocation-densities are calculated by means of the plastic-strain gradient following Brinckmann et al. (2006). Following Gao (1999), the plastic strain gradient is calculated from the partial derivatives of the plastic strain tensors, which are calculated by VPFFT.

The strain energy at a given position is a function of the dislocation density and the dislocation line energy E_D, which is proportional to square of the Burgers' vector length of the respective dislocation type (Humphreys and Hatherly, 2004, pp. 17-18). In ice I_h, the Burgers' vector of non-basal dislocations is approximately two times longer compared to basal ones (Hondoh, 2000). Hence, non-basal dislocations can provide about four times higher strain energies. Previous numerical models by

TABLE 7.1: Overview of the settings of the numerical simulations. Each simulation is labelled with the initial mean grain-area in mm^2 (G) and with the strain rate with R10 and R11 standing for $2 \cdot 10^{-10}$ and $2 \cdot 10^{-11}$ s^{-1}, respectively. All simulations were repeated three times to average the number of grain dissection and polygonisation events.

Simulation name	Initial number of grains	Initial mean grain area (mm^2)	Numerical strain rate (s^{-1})
G05R10	2003	4.99	$2 \cdot 10^{-10}$
G10R10	1000	10.00	$2 \cdot 10^{-10}$
G15R10	667	14.99	$2 \cdot 10^{-10}$
G20R10	500	20.00	$2 \cdot 10^{-10}$
G30R10	333	30.03	$2 \cdot 10^{-10}$
G40R10	250	40.00	$2 \cdot 10^{-10}$
G60R10	167	59.88	$2 \cdot 10^{-10}$
G80R10	125	80.00	$2 \cdot 10^{-10}$
G05R11	2003	4.99	$2 \cdot 10^{-11}$
G10R11	1000	10.00	$2 \cdot 10^{-11}$
G15R11	667	14.99	$2 \cdot 10^{-11}$
G20R11	500	20.00	$2 \cdot 10^{-11}$
G30R11	333	30.03	$2 \cdot 10^{-11}$
G40R11	250	40.00	$2 \cdot 10^{-11}$
G60R11	167	59.88	$2 \cdot 10^{-11}$
G80R11	125	80.00	$2 \cdot 10^{-11}$

Llorens et al. (2016a,b) and Steinbach et al. (2016) assume all dislocations are on basal planes and at constant Burgers' vector length, which underestimates strain energies. Here, we use an updated approach that scales the strain energies to the non-basal activity in each *unode* which is predicted by VPFFT to allow up to about four times higher strain energies due to the presence of non-basal dislocations.

Following each VPFFT step, recrystallisation is modelled using Elle. Each recrystallisation step comprises successive steps of discrete implementations of grain boundary migration, recovery and polygonisation. Each mechanism is modelled using a fixed numerical time step and temperature (see section Simulation Setup; Tables 7.1-7.2 for input parameters). For numerical stability reasons, the order in which the discrete implementations are performed on the numerical microstructure is first polygonisation, followed by grain boundary migration and recovery. This loop is repeated until the numerical time for the recrystallisation processes equals the one envisaged for one deformation increment by VPFFT, which determines the numerical strain rate (see Steinbach et al., 2016 and Figure 2 therein). As the numerical time steps and the resulting microstructural changes per step are low, we assume that the effective microstructural response is not significantly different from conditions during which the mechanisms operate concurrently.

Grain boundary migration is modelled using a front-tracking approach moving individual *bnodes* towards lower energy positions (cf. Becker et al., 2008; Llorens et al., 2016a). In this energy minimisation approach, the *bnode* displacement is calculated from multiplying its velocity with a fixed time step (section Simulation Setup; Table 7.2). The *bnode* velocity is proportional to the grain boundary mobility and driving force. The temperature dependant mobility is calculated following Nasello et al. (2005) by using an Arrhenius term with an experimentally derived intrinsic mobility and activation energy. The driving force is calculated from the change in local

TABLE 7.2: Overview of crucial input parameters used for the numerical simulations. Parameters where chosen to be consistent with published literature using similar numerical simulations or experimental data.

Symbol	Explanation	Input value
D_{min}	Minimum bnode separation	5×10^{-4} m
D_{max}	Maximum bnode separation	1.1×10^{-3} m
Δt_{DRX}	Time step for one recrystallisation loop	1.25×10^{7} s
N	Number of recrystallisation loops per one step of VPFFT within one simulation step for high and (low) strain rate setups	2 (20)
ε_{incr}	Incremental strain per simulation step	0.01
$\frac{\tau_{basal}}{\tau_{non-basal}}$	Ratio non-basal / basal glide resistance (Llorens et al., 2016a,b; Steinbach et al., 2016)	20
M_0	Intrinsic mobility grain boundary migration (Nasello et al., 2005)	$0.023\,\mathrm{m^4\,J^{-1}\,s^{-1}}$
M_r	Rotational mobility used for recovery code (Llorens et al., 2016a)	$5.5 \times 10^{-7}\,\mathrm{Pa^{-1}\,s^{-1}\,m^{-2}}$
γ_{surf}	Ice grain interface surface energy (Ketcham and Hobbs, 1969)	0.065 J m-2
E_{line}	Energy per meter of dislocation for basal plane dislocations (non-basal energy can be up to about four times higher) (Schulson and Duval, 2009)	$3.6 \times 10^{-10}\,\mathrm{J\,m^{-1}}$
α_{HAGB}	Critical misorientation for high-angle grain boundary (HAGB) (Steinbach et al., 2016; Weikusat et al., 2010, 2011)	5°

surface- and strain-energy that result from a change in position of that *bnode*. These energy fields are determined with four trial positions close to the actual *bnode* position. The change in surface energy is due to a change in length of the grain-boundary segments to neighbouring *bnodes*. The change in strain energy results from reducing the strain energy to zero in the area swept by the *bnode* and its adjoining boundary segments.

For the recovery mechanism, an energy minimisation approach is used that, analogous to the grain-boundary migration approach, calculates the lattice reorientation with a rotational mobility term (Borthwick et al., 2013; Llorens et al., 2016a; Moldovan et al., 2001). The approach is based on decreasing the lattice misorientation between two *unodes* towards a lower energy configuration (see Borthwick et al., 2013 and Llorens et al., 2016a for details). Recovery reduces the local dislocation density proportional to the decrease in lattice misorientation and allows the development of subgrains. The subgrains are defined as *unode* clusters with a certain minimum misorientation with neighbouring clusters. The polygonisation routine detects these clusters and adds new high-angle grain boundaries defined by *bnodes*, if the cluster misorientation is above a critical angle. This is done by Voronoi decomposition of the *unode* clusters using the Voronoi points surrounding the cluster as new *bnodes* (Steinbach et al., 2016). We use a critical angle of 5° to be consistent with both published numerical studies (Llorens et al., 2017; Steinbach et al., 2016) and subgrain boundary quantifications by Weikusat et al. (2010, 2011),

who report critical angles from 3° to 5° for ice I_h. A lower critical angle would slightly increase the amount of polygonisation. However, lower critical angles reduce numerical stability as the amount of topological errors is increased.

Simulation setup

The simulation setup comprises two numerical strain rates applied to eight model setups with different initial mean grain-areas (Table 7.1). Each initial microstructure was discretised in a 14.14 × 7.07 cm box (ratio height/width = 2) and deformed under pure shear conditions to approximately 50% vertical shortening at incremental strains of 0.5% over 140 time-steps. Different strain rates were achieved by varying the number of recrystallisation loops per strain increment. Two or 20 recrystallisation loops, per $1.25 \cdot 10^7$ s time, per VPFFT strain increment of 0.5%, achieved strain rates of $2 \cdot 10^{-10}\,s^{-1}$ or $2 \cdot 10^{-11}\,s^{-1}$, respectively. The time step was chosen as a compromise between numerical stability and computational efficiency. The achieved strain rates are higher than reported for the NEEM ice core, where the estimated mean vertical strain rate is $3.2 \cdot 10^{-12}\,s^{-1}$ (Montagnat et al., 2014). Therefore, the numerical strain rates are only qualitatively comparable with natural strain rates (Steinbach et al., 2016). The temperature in the simulations was set to −30° C, which is comparable to Holocene ice conditions in NEEM ice core (Sheldon, et al., 2014). The initial grain sizes were set by varying the initial number of grains in a foam texture (Table 7.1). The initial c-axis orientations were adjusted to be similar to measured second-order orientation tensor eigenvalues from NEEM ice core at approximately 700m depth, defining a weak single maximum CPO which is realistic for many ice cores (see review by Faria et al., 2014a). As summarised in Table 7.1, the simulations are labelled using a terminology that indicates their mean initial grain area in mm^2 (G) and the order of magnitude in strain rate (R). Hence, for instance the simulation starting with a grain area of $20\,mm^2$ at a strain rate of $2 \cdot 10^{-11}\,s^{-1}$ is named G20R11.

During the simulations, the numbers of split events by grain dissection and polygonisation is automatically counted for each time-step. As outlined in section Microstructure Discretisation, a grain dissection event during the simulation is defined as a topological event during which two non-neighbouring bnodes are merged into one. This way, the number of grain dissection and polygonisation events is slightly overestimated. Technically, it is not a grain dissection event when two bnodes or grain boundaries close without splitting a grain. The same holds for polygonisation, where all events are counted, including those where a resulting grain is too small and is immediately deleted. Nevertheless, counting split events remains the most reproducible way to estimate the efficiency of grain dissection compared to polygonisation.

To improve statistics, each of the 16 simulations indicated in Table 7.1 was repeated three times. For each repetition the initial CPO was slightly varied to allow for some variation between the simulations. The numbers of both polygonisation and grain dissection events for each step were normalised to the actual number of grains at this simulation step. The resulting value can be regarded as the number of events per grain in the respective time-step of the simulation.

7.2.2 Microstructure characterisation of NEEM ice core samples

Microstructure and crystallographic-orientation mapping for this study is performed using both EBSD (electron backscatter diffraction) and the automated Fabric

Analyser. Using cryo-EBSD, we study three ice core sections from Holocene ice at 442.7 m, 718.8 m and 889.3 m depth and four ice core sections from the glacial ice at 1737.7 m, 1937.7 m, 1993.8 m and 2103.8 m depth.

Each ice core section of approximately 90 × 55 mm was cut into 10 to 15 EBSD samples using the method of Weikusat et al. (2011a). The samples were imaged by optical microscopy at the Alfred Wegener Institute (AWI) in Bremerhaven before being transported to Utrecht University. All ice core sections, except the ice core section at 442.7 m depth, were mapped using the Nova Nanolab equipped with an EBSD detector (Oxford Instruments HKL Technology, Abingdon, UK) and a cryo-stage (Quorum Technologies Ltd. Ringmer, UK). These EBSD patterns were acquired, processed and indexed using the Channel 5 software of OI-HKL Technology. The ice core section at 442.7 m depth was mapped using a FEI Helios NanoLab G3 UC equipped with the same EBSD detector and cryo-stage. The EBSD patterns of this ice core section were indexed using the Aztec software (Oxford Instruments, High Wycombe, UK). The reader is referred to Weikusat et al. (2010) for an extensive description of the EBSD sample preparation, sample transfer and the EBSD mapping conditions we used.

A total number of 216 EBSD maps is used for this study, 91 in the Holocene ice and 125 maps in the glacial ice. Depending on the grain size and the area of interest, the EBSD maps vary in area from 0.5 mm^2 to 6 mm^2. Each of these EBSD maps was visually checked for signs of grain dissection according to the schematic descriptions of grain dissection by Means (1983), Urai (1983) and Figure 7.1. A grain dissection event was counted only between second-neighbors with only one grain separating the two dissected grains and if the full orientation difference between the dissected parts was smaller than 3°. The number of grain dissection structures was counted with the area of the EBSD map and its mean grain area. This counting is intended as a qualitative estimate of the frequency of grain dissection in the NEEM ice core. The area of the EBSD map was divided by the observed number of grain dissection events in this map. This provides a measure for the average area necessary to observe one grain dissection event. Afterwards, the average grain size of the EBSD map was divided by this measure resulting in a corrected value. Essentially, this procedure is similar to simply dividing the number of dissection events by the number of grains, but allows correcting for the difference in average grain size, EBSD-map area and for the low number of grains in an EBSD map. We counted completed grain dissection in EBSD maps, which implies that the dissection itself may have occurred in the past and adds a "memory effect" that increases the relative occurrence values. Therefore, the resulting unit is "number of grain dissection events per grain" and can be regarded as the relative chance of a grain being dissected or having been dissected based on the EBSD dataset.

The automated Fabric Analyser (G50 by Russell-Head Instruments) provides high-resolution c-axis-orientation maps of ice thin sections (Wilson et al., 2003). The obtained "c-axis maps" are an essential addition, as they provide better statistics by covering a larger area and, thus, more grains than EBSD maps. Furthermore, more samples per depth can be analysed (Weikusat and Kipfstuhl, 2010).

For our study, 13 c-axis maps (total area 1.15 m^2 and 8392 grains) from the Holocene part of the NEEM ice core were reviewed to detect grain dissection. In contrast to the EBSD, the Fabric Analyser only provides orientations of the c-axes. This limitation has an effect on the identification of grain dissection events in c-axis maps. Therefore, c-axis maps from the glacial part are not suitable for the search for grain dissection events as c-axis misorientations are too low to identify high-angle boundaries. Furthermore, when two second-neighbouring grains share the same

crystallographic orientation, there is a high probability for them being a product of grain dissection. However, if the full orientation information is missing, such a conclusion may be erroneous.

To avoid erroneously counting grain dissection because of only using c-axis information, we added a grain-connectedness criterion and searched c-axis maps only for grains where grain dissection appeared imminent, but has not yet been completed. For each c-axis map, the number of imminent grain dissection events was counted and divided by the number of grains. Effectively, the result is the same statistical parameter that is derived from EBSD maps, but only for imminent grain dissection events, which results in lower values obtained from c-axis maps than from EBSD maps. One can envisage that more sophisticated ways of determining recent dissection events is possible even in c-axis maps only. However, we did not further explore these and, therefore, the EBSD and c-axis results can so far only be compared qualitatively.

Grain dissection observed in EBSD maps or c-axis maps can potentially be a sectioning effect of a 3D sample. Both methods only show a snapshot of a continuously evolving microstructure, hence an uncertainty remains whether a bulge would have completed the dissection in the third dimension. However, this stereological issue is unproblematic with respect to grain size evolution as grain sizes in ice are also determined from two-dimensional sections (see methods of Binder, 2014). Any interpretation of a natural microstructure is associated with some uncertainty, as it only provides a snapshot of the evolution. Although each counted (imminent) dissection event is not certain, we can assume that the number of interpreted events does correlate with the true number of events.

7.3 Results

7.3.1 Numerical simulation results

An overview of selected microstructures after 50% of vertical shortening is shown in Figure 7.3. The final microstructure is marked by curved grain boundaries and only a few equidimensional grains. The c-axes are mainly aligned towards a single maximum CPO as shown by stereographic projections and by common red colours in c-axis azimuth maps. Microstructural similarities are only observed between simulations with common strain rates, independent of initial grain area. As expected, the high strain-rate simulations show smaller final grain areas, whereas the low strain-rate simulations show larger final grain areas. Dislocation densities are higher and more homogeneously distributed at a high strain rate than at a low strain rate.

The circles in Figure 7.3 represent regions where a splitting of a grain by polygonisation appears imminent. In particular, the grain indicated by circle A in the final microstructure of simulation G10R11 contains two distinct regions with different c-axis azimuth. This grain is expected to split into two grains by polygonisation in the following numerical time-step. Red squares in Figure 7.3 indicate regions where grain dissection appears either completed (square E) or imminent (squares C and D). Especially square D provides information on the driving force for bulging. Here, two bulges migrate into an area of a grain that exhibits the highest dislocation densities in the microstructure. Close examination of the centre of square D reveals high dislocation densities distributed in stripes. The dislocation densities vary strongly locally, also within regions with overall high dislocation densities.

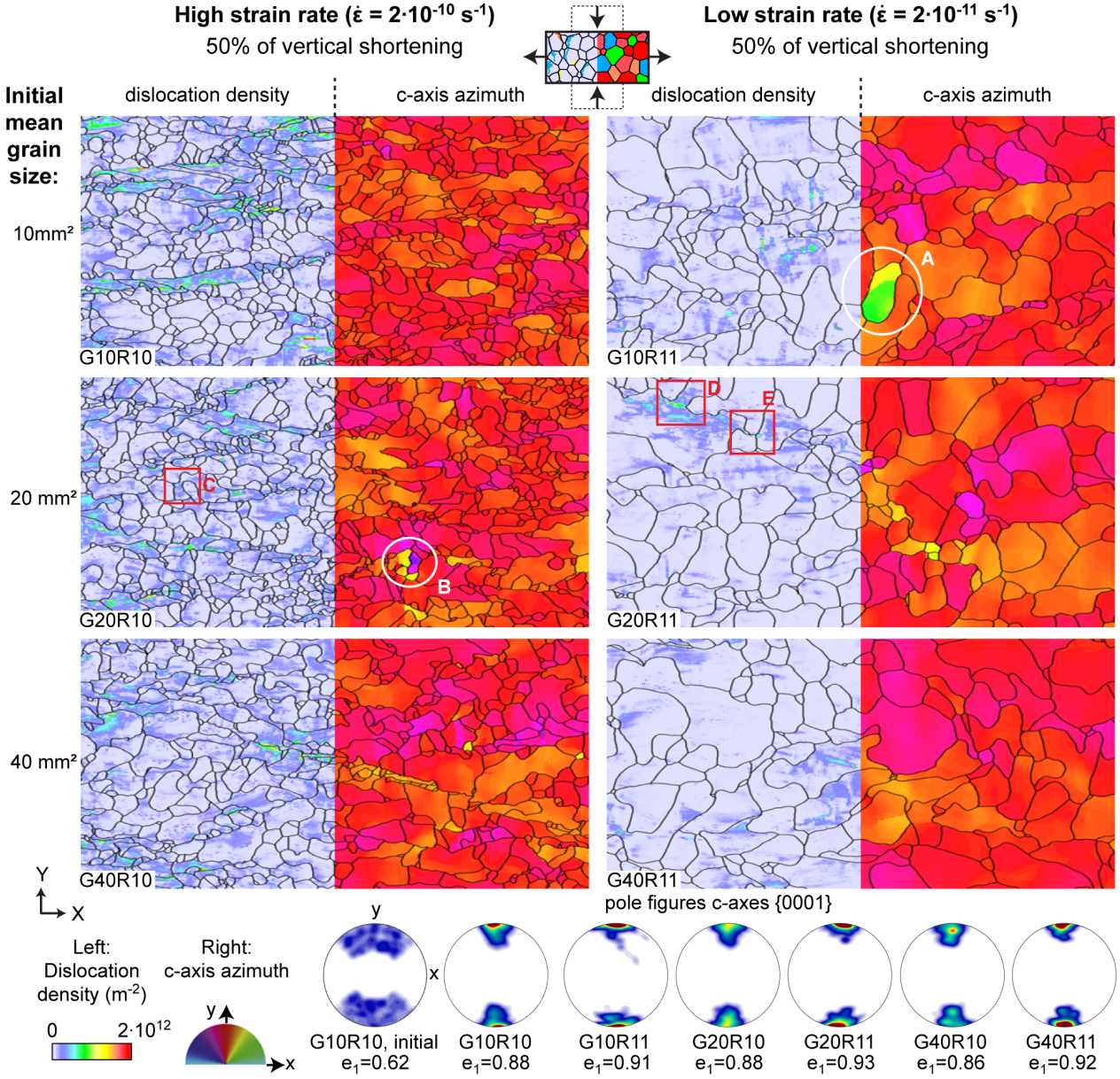

FIGURE 7.3: Overview of numerical microstructures after 50% of vertical shortening (i.e., final simulation step) with grain boundary networks (black lines) for the whole deformation box. The box is subdivided in the color code for dislocation density (left) and for the c-axes azimuths (right), where red colors indicate vertically oriented c-axes. The corresponding pole figures and first eigenvalues of the second order orientation tensor (e_1) are shown below. The initial pole figure and first eigenvalue of G10R10 are provided as an example of the starting configuration. The squares indicate regions where grain dissection has either occurred or is most likely imminent, while the circles show subgrain boundaries likely to develop into new high-angle grain boundaries by polygonisation.

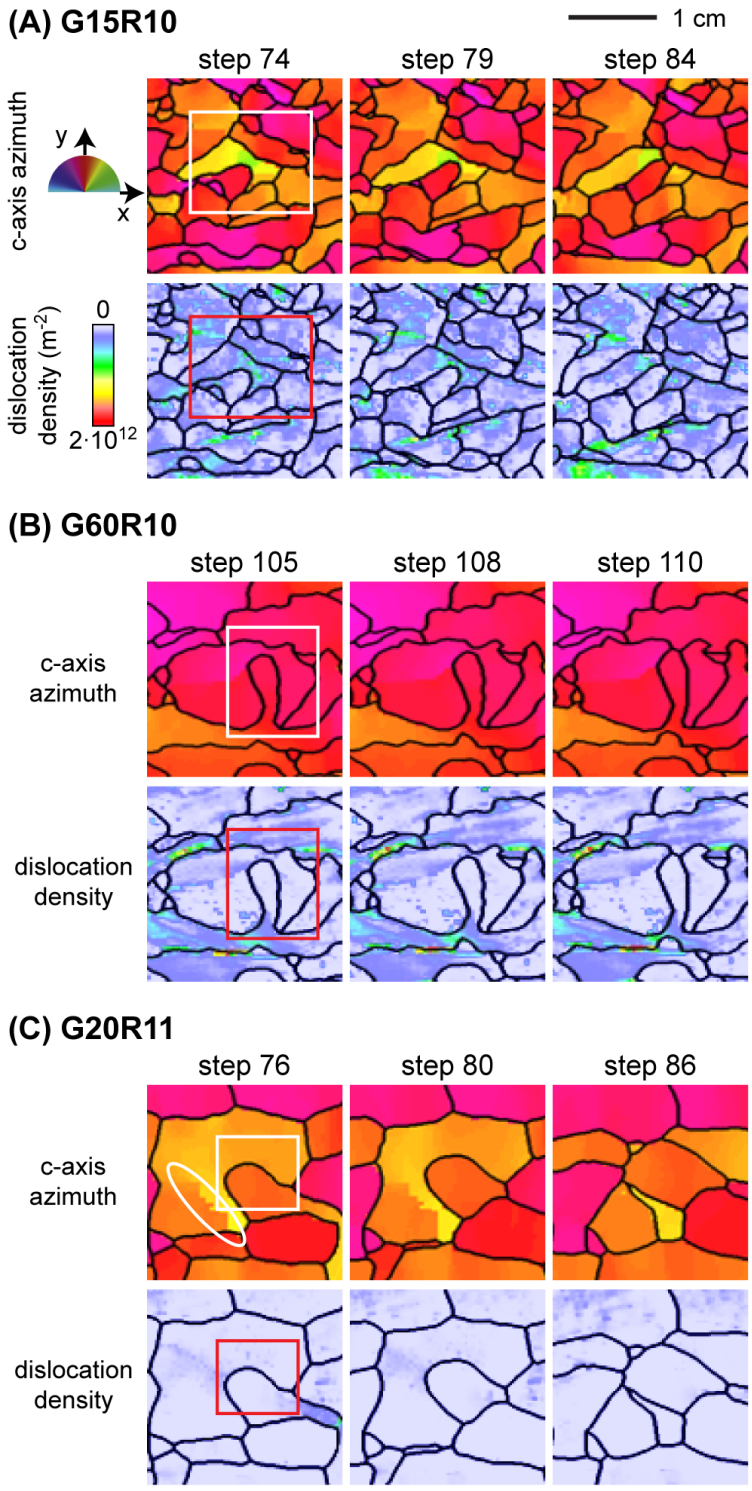

FIGURE 7.4: Detail of several examples of grain dissection events observed in the numerical simulations. The images are 1 by 1 cm snapshots and are color coded for c-axis azimuth and dislocation density. The squares indicate rapidly-migrating bulges merging with an opposite grain boundary (grain dissection). The white ellipse shows where a subgrain boundary develops into a high-angle grain boundary by polygonisation. (A) Simulation G15R10. (B) Simulation G60R10. (C) Simulation G20R11.

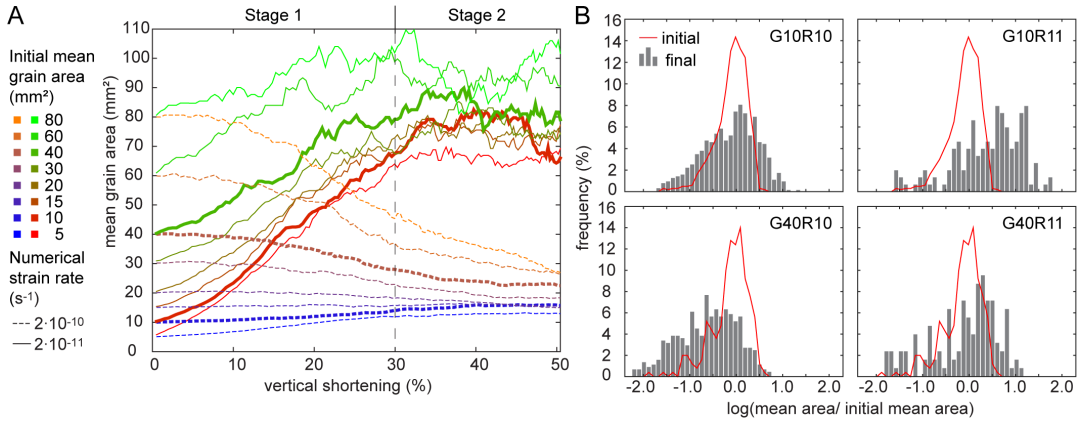

FIGURE 7.5: Overview of grain-area evolution in the numerical simulations. (A) Mean grain-area as a function of vertical shortening. In a first stage until approximately 30% shortening, mean grain areas either increase or decrease, which is followed by a second stage of more stable grain areas. Simulation results shown in detail in (B) (10 mm^2 and 40 mm^2) are highlighted as bold lines. (B) Grain area histograms of selected simulations at initial and final simulation step. Areas were normalized to initial mean values.

All 16 numerical simulations show situations, during which strongly-bulging grain boundaries migrate through a grain and either merge with the opposite grain boundary or with another bulge (cf. supplementary material). Both situations cause splitting of a grain into two parts in the sense of grain dissection. Figure 7.4 illustrates several examples of grain dissection during the simulations. For example, simulation G15R10 shows a grain boundary bulging into an area of high variation in lattice orientation from step 74 to 84. Ultimately, this bulge migrates through the grain and merges with the opposite boundary. A similar situation is observed in results from simulation G60R10, where a rapidly migrating bulge merges with the opposite boundary, which dissects a grain into two parts. The example from G20R11 illustrates both an event of grain dissection and polygonisation. The bulge indicated by the square migrates towards- and finally merges with the opposite grain boundaries. This dissects the former grain into three parts. The small new grain in the upper left of the bulge shrinks and disappears within the following simulation steps. Furthermore, the bulging grain itself is dissected between simulation step 76 and 80, as visible on the right hand edge of the images. The white ellipse marks a subgrain boundary that develops into a high-angle grain boundary by polygonisation (Figure 7.4C). All bulges move towards high dislocation-density areas, leaving behind an area free of dislocations. The local dislocation-density field is highly heterogeneous.

Both the low and the high strain-rate simulations with initial grain areas up to 15 mm^2 are marked by mean grain-area increase (Figure 7.5A). Mean grain-area decrease is observed in high strain rate simulations with initial grain areas higher than 20 mm^2. The mean grain-area evolutions can be classified in two stages. The first stage up to 30% of vertical shortening is characterised by a regular change in grain area, which either increases or decreases. In the following second stage, an approximate stable mean grain area of 17 ± 0.5 mm^2 and 80 ± 2.1 mm^2 is reached in the high and low strain-rate simulations, respectively. Some simulations appear not to have reached a steady state, even at 50% shortening (G80R10 and G60R10; dotted lines in Figure 7.5). Grain-area histograms (Figure 7.5B) show that the grain size distribution broadens with strain from the initial near log-normal distribution.

The number of polygonisation and grain dissection events (Figure 7.6) for each of

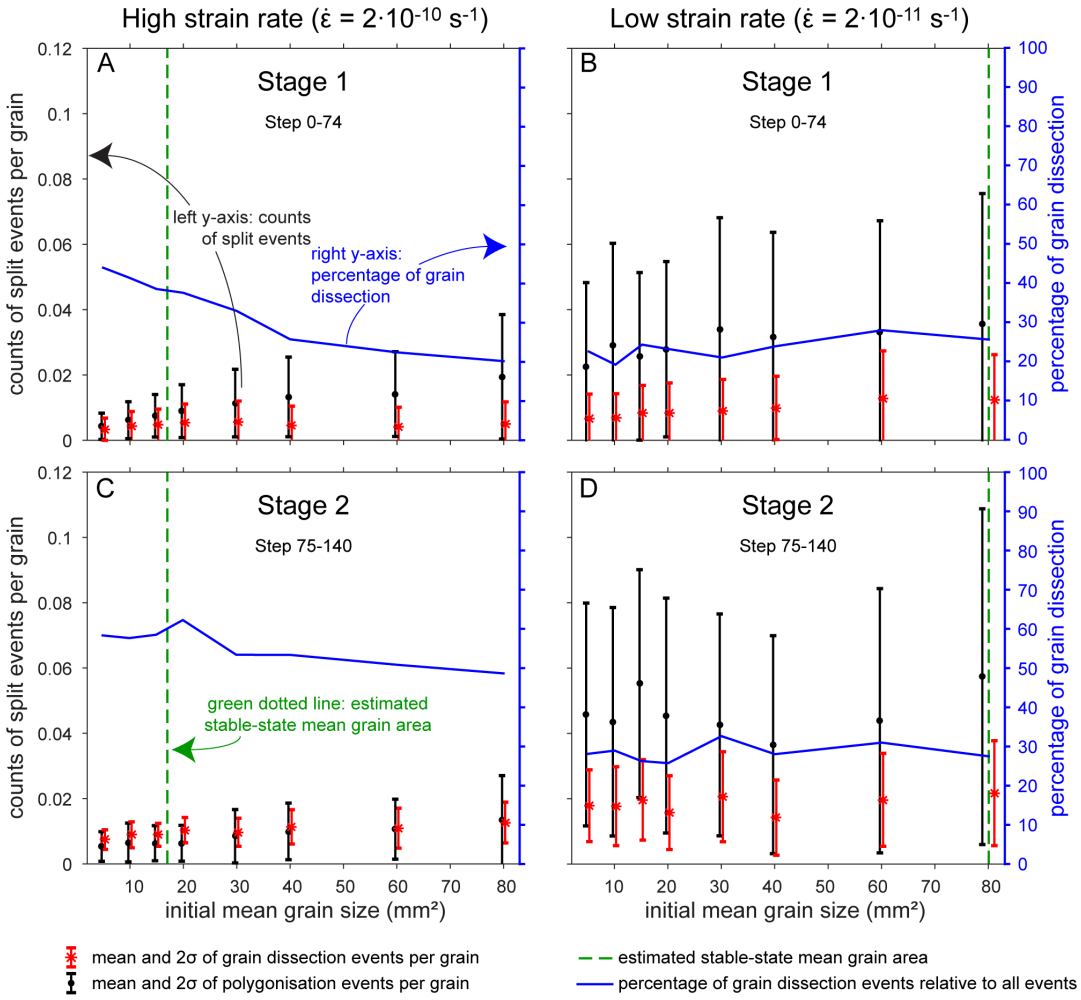

FIGURE 7.6: Statistics of grain-dissection and polygonisation events per grain. Data is sorted for the (A,B) first and (B,D) second stage of grain size evolution and (A,C) high and (B,D) low strain rate. The first stage was taken from step 0 to 74 (0–31% shortening) and the second one step from 75 to 140 (from 31% shortening). Error bars indicate two standard deviations (2) of the counting statistics. The dotted green line indicates approximate stable mean grain areas for the high and low strain-rate simulations. The blue line and right y-axis show the mean percentage of grain-dissection events per grain from the total number of splitting events by grain dissection and polygonisation.

the eight initial grain-sizes and two strain rates was averaged over the two stages observed in mean grain-area evolution (Figure 7.5). The first stage was taken from step one to 74 (0 to 31% of vertical shortening) and the second one from step 74 to 140 (31 to 50% of vertical shortening). The highest frequencies of both grain dissection and polygonisation events per grain are observed at the low strain rate (left y-axis, black and red symbols in Figure 7.6). Hence, a comparison of their relative frequency is necessary, which is illustrated in the blue curve of Figure 7.6 (right y-axis) that shows the percentage of mean grain dissection events from the total mean number of both grain dissection and polygonisation events per grain. Large errors (standard deviation) for the low strain-rate simulations are a result of the large grain sizes and, therefore small number of grains. In general, the highest fractions of grain dissection events are observed at the high strain rate, although polygonisation generally dominates over grain dissection. However, dissection events dominate when the grain size is close to equilibrium (green dotted lines in Figure 7.6) in the high strain rate

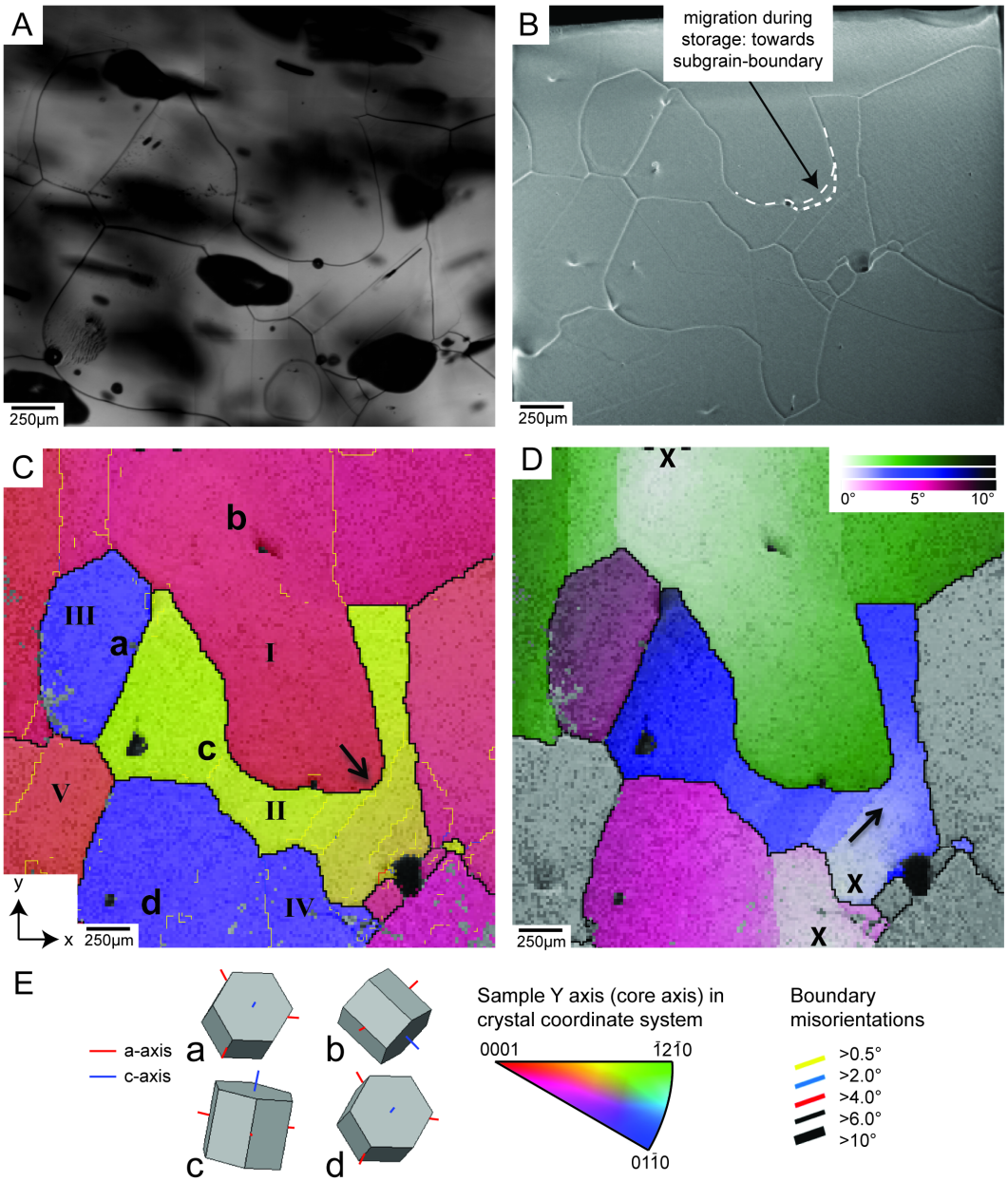

FIGURE 7.7: Optical-microscopy, SEM and EBSD maps of an ice core sample at 718.8 m depth in the NEEM ice core. (A) Part of the optical-microscopy image taken just after sample preparation. (B) SEM image of the mapped part of the EBSD sample with the edge of the EBSD sample in the upper part of the image. (C) EBSD map, with the y-axis parallel to the (vertical) core axis. (D) Map showing the orientation difference of up to 10° relative to the three spots marked with "X". (E) Schematic illustration of measured full CPO (c- and a-axes) at positions (a–d), and color codes for CPO and boundary misorientation.

experiments. This is observed for small initial mean grain-size simulations already from stage 1 and also for large initial mean grain-size simulations during stage 2. Here, we observe 50% or more split events by grain dissection.

7.3.2 EBSD and Fabric Analyser results from NEEM ice core

Figure 7.7 shows an example of grain dissection in the NEEM core at 718.8 m depth. The black spots in the optical microscopy image of Figure 7.7A are air bubbles at or

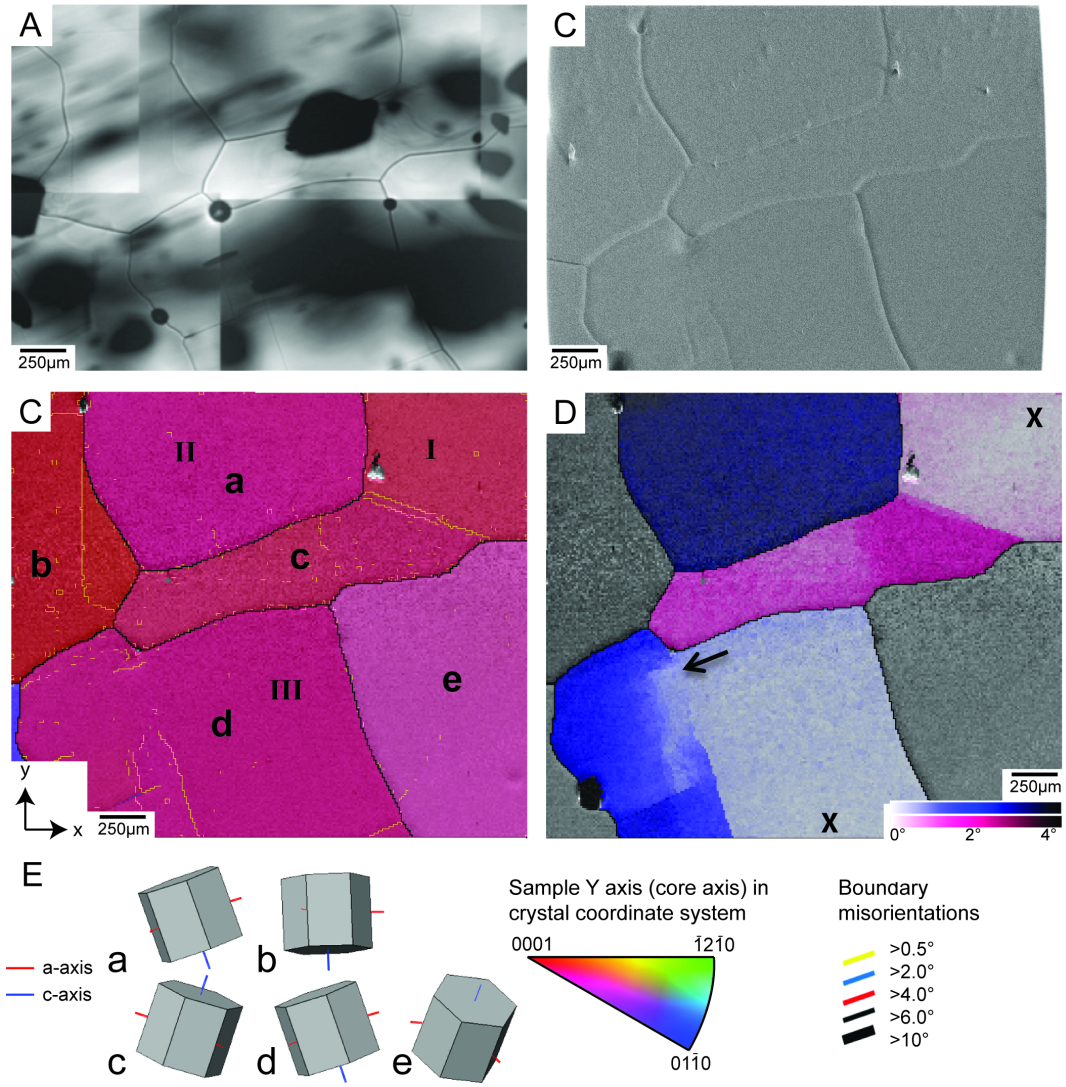

FIGURE 7.8: Optical-microscopy, SEM and EBSD maps of an ice core sample at 442.7 m depth in the NEEM ice core. (A) Part of the optical-microscopy image taken just after sample preparation. (B) SEM image of the mapped part of the EBSD sample. The curved edges are a result of the beam being blocked by the electron column. (C) EBSD map, with the y-axis parallel to the (vertical) core axis. (D) Map showing the orientation difference of up to 4° relative to the two spots marked with "X". (E) Schematic illustration of measured full CPO (c- and a-axes) at positions (a–e), and color codes for CPO and boundary misorientation.

just below the surface (Kipfstuhl et al., 2006). The comparison of this image with the SEM image (Figure 7.7B) shows that the bulge of grain I migrated slightly into grain II during the nine days of sample transport and storage. The map in Figure 7.7D shows a strong orientation gradient of approximately 10° in grain II. Most of this orientation gradient is accommodated by four parallel low-angle ($< 2°$) subgrain boundaries in grain II. The orientation gradient map indicates a comparatively low misorientation of about 2 to 3° between grain III and IV, which is also visible in the schematic illustrations of CPO at positions (a) and (d) in Figure 7.7E.

Figure 7.8 shows another example of grain dissection in Holocene ice at 442.7 m depth in the NEEM ice core. The comparison of the optical microscopy image with the SEM image (Figure 7.8B), which was taken eleven days after sample preparation, shows that the surface changed very little during transport and storage at Utrecht

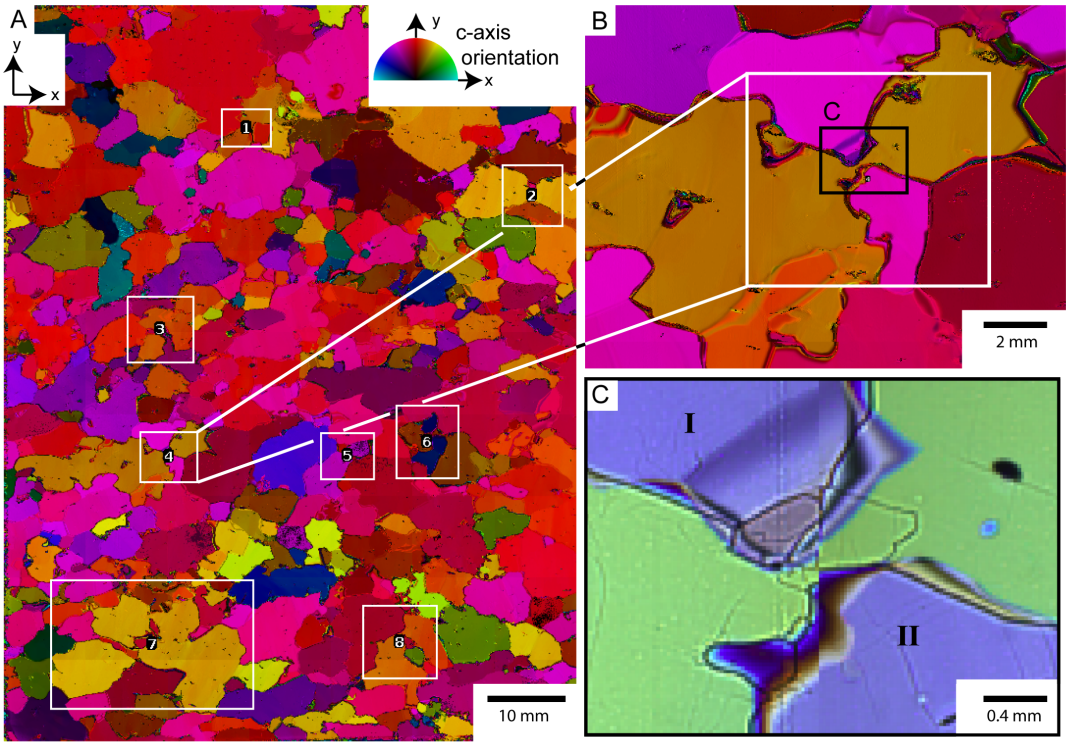

FIGURE 7.9: Grain dissection events in c-axis map, y-axis parallel to (vertical) core axis. (A) C-axis orientation map of a 7 × 9 cm thin section from the NEEM ice core at 1211.7 m. Colors indicate the azimuth of c-axes relative to the vertical y-axis. Imminent dissection events are marked with white rectangles. (B) Detail of a dissection event. Grain boundaries are highly irregular due to dynamic recrystallization. The orange grain is almost split in two grains that are still connected through a very narrow bridge. (C) Photomicrograph, with cross-polarized light, of the same spot showing the connecting bridge in detail. Dark lines are grain-boundary grooves at the surface. Subgrain-boundaries develop at the thin bridge between the dissected subgrains.

University. The EBSD map in Figure 7.8C shows a strong bulge in grain I between grains II and III. Grain II and III differ by about 3° in 3D crystallographic orientation (Figure 7.8D) showing that grain II and III have a very similar CPO (Figure 7.8E). Grain III shows a very low orientation gradient, except for the part close to the bulge of grain II as indicated by the arrow. This low orientation gradient is also reflected in the low misorientations along subgrain boundaries of about 0.5° in this area (Figure 7.8C).

The c-axis maps obtained using the Fabric Analyser were processed manually to detect potential grain dissection events. As described in section 7.2.2, we selected only events where grain dissection appears imminent and the future fragments are still connected through a thin bridge. Figure 7.9 shows a 7 × 9 cm thin section from the NEEM ice core at 1211.7 m depth, grain dissection events are marked by white rectangles. As shown in Figure 7.9C, dissected grains often develop subgrain boundaries across the connecting bridge. This is in agreement with the EBSD data showing high orientation gradients and formation of subgrain boundaries within the dissected grains.

The frequencies of grain dissection events as a function of depth across the Holocene-glacial ice transition are shown in Figure 7.10. There appears a downward trend towards more dissection events, counted in EBSD images, in the Holocene ice, but with only three samples, this trend may not be significant (Figure 7.10A).

There is, however, a significant decrease in dissection frequencies in the samples from glacial ice, from about one per grain to one per every four grains. Counts of imminent split events observed in c-axis maps are only available for Holocene ice down to 1279 m depth. The average number of imminent split events is much about one per one hundred grains (0.010 ± 0.003). This number is much lower than split events counted in EBSD images as only imminent events are counted in the c-axis maps. The frequencies of grain dissection in c-axis maps do not show a significant trend towards higher or lower grain-dissection frequencies with depth.

7.4 Discussion

7.4.1 Time-resolved numerical microstructure evolution under the influence of grain dissection

All simulations show situations that can be identified as grain dissection in the sense of the descriptions by Urai (1987) and Means (1983) and Means (1989) (see movies, supplementary material). The simulations provide a time series to study the interaction of this process with polygonisation, recovery, grain boundary migration and viscoplastic deformation and their relative contribution to microstructure evolution. The numbers of grain dissection and polygonisation events are similar (Figure 7.6), which indicates that both mechanisms significantly contribute to microstructure evolution. Thus, grain dissection cannot be considered as a transient or negligible effect during the simulations, which underlines the necessity to assess its importance for ice micro- to macrodynamics. It needs to be assessed under which boundary conditions such as bulk grain size, strain rate, temperature or stress configuration, grain dissection is most efficient.

Significant numbers of dissection events, compared to the number of polygonisation events, can be seen in the high strain rate simulations (Figure 7.6A and 7.6C). Here, in five of eight simulations, the grain size evolution is marked by grain size decrease, which indicates the grain-size-decreasing character of grain dissection. Additionally, if the grain size does not change significantly from the start or has equilibrated to steady-state values during the second stage of grain size evolution (Figure 7.5A), grain dissection dominates over polygonisation (Figure 7.6). In particular, grain dissection is most effective during the second stage of the high strain-rate simulations (Figure 7.6C). The observation of efficient grain dissection at steady-state conditions is consistent with experimental results by Jessell (1986) and Urai (1987). When the mean grain size is larger than the equilibrium one and thus grain size decreases, polygonisation dominates over dissection, as is observed in the high strain-rate simulations and in rock analogue experiments by Herwegh et al. (1997).

It remains questionable how suitable mean grain areas are to assess if a steady-state microstructure is reached. Although trending towards more steady values, the final mean grain-areas still vary significantly (Figure 7.5A). The grain area distributions are broadened and more heterogeneous towards the end of the simulations (Figure 7.5B), which is expected from observations of natural ice microstructures under dynamic recrystallisation (Kipfstuhl et al., 2009). Obtaining mean grain areas from a broadened grain area distribution can be responsible for the observed variability in final grain areas. Furthermore, at low strain rates, the final number of grains is lowered, which additionally affects the mean grain-area calculation.

The numerical approach is currently limited to 2D simulations. The numerical modelling of processes such as SIBM leading to grain dissection or polygonisation

in 3D remains a goal for future developments. In 3D, SIBM can either lead to amoeboidal grains or truly dissected grains (Urai et al., 1986, Fig. 25 therein). True dissection in 3D requires bulging along a surface of high dislocation densities. With respect to this, the occurrence of grain dissection can still be expected in 3D. Also the process of 3D polygonisation requires gradients in lattice misorientations and dislocation densities along a surface to develop new high-angle grain boundaries. While the occurrence of polygonisation in natural ice is verified (Alley et al., 1995; De La Chapelle et al., 1998), similar initial structural conditions may as well lead to 3D grain dissection. However, 3D and 2D grain dissection remain slightly different processes. In 3D, grain dissection occurs not at point, but over a period in time during which two boundaries merge. This may cause an over- or underestimation of the frequency of grain dissection when being limited to 2D simulations, however, general and qualitative remain valid. For a more quantitative estimate of the frequency of 3D grain dissection in future research, either stereological corrections or 3D numerical simulations are required.

Experimentally observed bulging nucleation (Chauve et al., 2017) can theoretically be modelled with the current numerical resolution. The required processes such as SIBM and subgrain rotation are implemented. However, we do not observe significant bulging nucleation. This may be related to the model resolution, but more likely to the 2D nature of the simulations: With only two dimensions available, splitting off a bulge by necking is unlikely as the region left behind the bulge is strain-energy free. Furthermore, as surface energies tend to straighten the boundaries and can readily remove small, yet distinct bulges. For efficient bulging nucleation, small bulge widths relative to large grain sizes are required. Under such conditions, we estimate grain dissection less likely as small bulges likely cannot migrate through the whole of a large grain causing dissection, which is consistent with Means (1989). Hence, grain dissection would probably neither be inhibited nor fostered, if bulging nucleation was modelled using higher resolutions.

Compared to natural vertical strain rates at the NEEM ice core that are in the order of $10^{-12}\,s^{-1}$ (Montagnat et al., 2014), our numerical strain rates are about an order of magnitude higher and results in larger grain sizes than observations in the NEEM ice core (Binder, 2014). Using lower numerical strain rates is feasible, yet even larger grain sizes are produced. The grain size depends on the effective grain boundary mobility that is an Arrhenius-type function of an intrinsic mobility, activation energy and temperature (Nasello et al., 2005). As Steinbach et al. (2016) describe, the numerical setup currently uses literature values for intrinsic grain boundary mobility and activation energy from experimental studies by Nasello et al. (2005). We suggest that the mobility and activation energy are not sufficiently constrained to reproduce realistic grain sizes at natural strain rates. In particular, dissolved impurities are suspected to reduce mobilities (Alley et al., 1986b), but are currently not taken into account in the numerical routine. Further investigations of this issue are beyond the scope of this contribution and remains part of future research.

7.4.2 Grain dissection along NEEM ice core

EBSD results on frequencies of grain dissection from Figure 7.10A imply that grain dissection in the NEEM ice core is most efficient in the Holocene ice and in particular around 700 to 900 meter depth (35 to 60% estimated finite shortening based on NEEM annual layer thicknesses by Rasmussen et al., 2013). However, whether this trend is real or a result of the limited number of processed samples is uncertain. In particular, this becomes obvious when comparing with results from c-axis maps

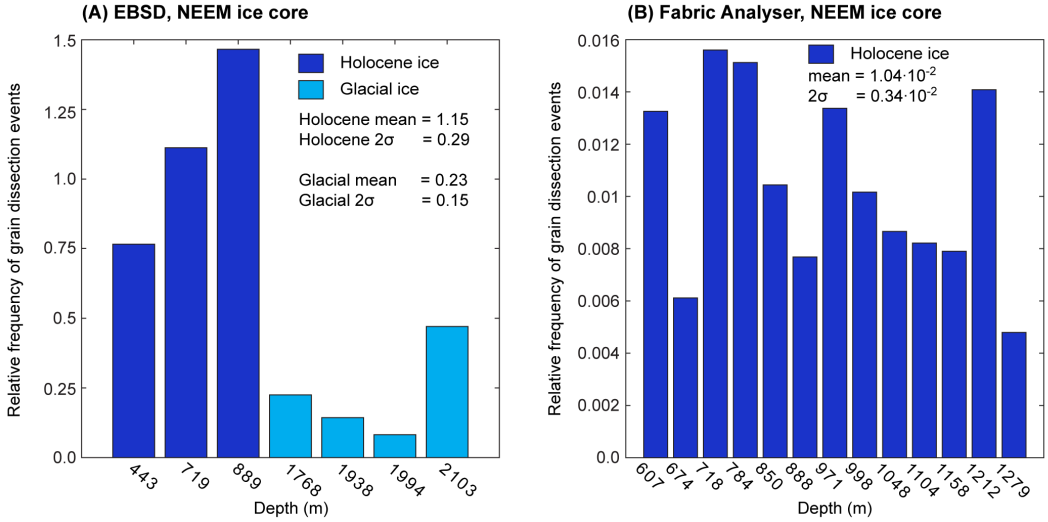

FIGURE 7.10: Frequency of grain dissection events. (A) Results obtained from EBSD maps plotted as a function of depth across the transition from Holocene to glacial ice. (B) Results from c-axis maps (Fabric Analyser). The generally lower frequencies for c-axis maps are a result of only counting imminent grain dissection events in c-axis maps and completed dissection events in EBSD maps.

(Figure 7.10B), where no evident trend in the number of imminent grain dissection events is visible.

The results in Figure 7.10 can be compared with mean grain-boundary curvature data from NEEM ice core presented by Binder (2014, Figures 7.1 to 7.8 therein). The study by Binder (2014) converts mean grain-boundary curvature to dislocation densities and observes highest curvatures from about 600 to 1300 m depth (30 to 75% estimated finite shortening based on Rasmussen et al., 2013). Our EBSD samples marked by highest relative numbers of grain dissection events are taken from this region of high mean grain-boundary curvature. This implies that strong grain boundary curvature may be indicative for the potential activity of grain dissection. Another characteristic of this region are stable grain sizes (Binder, 2014). The higher efficiency of grain dissection in Holocene ice of NEEM ice core (Figure 7.10A) is in accordance with the observations from simulations that grain dissection is most efficient relative to polygonisation, if the microstructure is in steady state (Figure 7.6C).

The deformation mode in NEEM ice core is interpreted to change from vertical shortening to simple shear at about the transition from Holocene to glacial ice, when c-axes in Holocene ice trend towards a vertical single maximum (Montagnat et al., 2014). As ice crystals in the Holocene part are mainly vertically shortened, a higher density of non-basal dislocations may be expected in Holocene ice, in particular towards the Holocene-glacial ice transition. The activation of non-basal planes is explicable with the single maximum CPO in which the basal planes are in an unfavourable orientation to accommodate vertical shortening. Alternatively, a constant non-basal activity would imply a strain rate decrease with depth as the ice becomes harder to deform. Non-basal dislocations provide higher line energies (Schulson and Duval, 2009, pp. 16-18), which in turn implies higher energy gradients driving SIBM and more grain dissection. This may be reflected in Figure 7.10A showing a trend towards more efficient grain dissection with depth in Holocene ice, but a significantly less grain dissection in glacial ice. Future research could further investigate, whether a change in deformation conditions from pure to simple shear during

numerical simulations, will cause similar trends.

7.4.3 Characteristics of grain dissection in simulation and nature

Evidence that microstructures exhibit imminent or completed grain dissection events can be found in (1) a distinct distribution of orientation gradients, (2) heterogeneous strain-energy distribution leading to localised occurrence of SIBM, (3) irregular shape of grain boundaries and (4) equal orientations of next-neighbour grains, which Urai (1983) describes as equal orientation families (Figure 7.7, Figure 7.8, Figure 7.9). Typically, all characteristics (1) to (4) are observed together in natural samples and simulations. Another characteristic important for grain dissection could be (5) the relation of bulge width and mean grain size. The characteristics below can be used as microstructural indicators for the occurrence of grain dissection. However, we remark that direct evidence is only provided by a time-resolved microstructure evolution.

1. Orientation differences indicate high stored strain-energies and can be observed as high densities of subgrain boundaries and orientation gradients. Both EBSD maps, c-axis maps and simulations reveal that grain dissection is accompanied by high orientation gradients (subgrain boundaries) in the dissected grain. The spatial distribution shows these high gradients as high densities of subgrain boundaries on the convex side of bulges (Figure 7.9C and Figure 7.4A, 7.4C). The observation of grain dissection accompanied with subgrain boundaries can be seen as an indication that grain dissection and polygonisation are not completely independent processes but rather act simultaneously, possibly strengthening each other, and cause splitting of grains with high strain-energy gradients.

2. Dislocations induce strain energies that drive SIBM. If the dislocation-density difference between the bulging and dissected grain is high, rapid bulge migration is possible (Figure 7.4, supplementary movies). The direction of grain boundary migration is indicated by locally high orientation gradients that are favourably consumed by the expanding grain (arrow in Figure 7.8C). In some cases, this direction could be verified using the observed migration of grain boundaries during storage of samples (see dotted line, from grain I in II, Figure 7.8B). SIBM causing grain dissection is a localised process as the dislocation energies can be highly heterogeneous within one grain (grain II, Figure 7.8, Figure 7.3, Figure 7.4A, 7.4B). Locally high strain energies lead to localised SIBM, which in turn causes directed bulging of grain boundaries and dissection instead of overgrowing of grains. Therefore, localised SIBM may be an essential feature of grain dissection. This assumption is consistent with simulation results, where grain dissection is observed when grain boundaries bulge in areas with locally high dislocation densities (simulation G15R10 in Figure 7.4). The combination of localised SIBM and grain dissection is further supported by geological studies. For instance, Tullis et al. (1990) observe increased bulging and less polygonisation if the dislocation density distribution is more heterogeneous. The heterogeneous distributions of dislocations in ice are expected, considering that strain localisation is suggested to be a common mechanism in ice micro-dynamics (Jansen et al., 2016; Llorens et al., 2016a; Steinbach et al., 2016). Although these studies describe strain localisation on the scale of polycrystals, their results also show intracrystalline localisation, which is required

for localised SIBM and grain dissection. Additionally, Steinbach et al. (2016) indicate that strain localisation may occur over a range of different scales.

3. The elongated shape of some bulges is caused by strong gradients in stored strain energy and accompanied by relatively high orientation gradients. This is reflected between grain I and grain II-III in Figure 7.7D and detail images of simulation G60R10 results (Figure 7.4B). When examining natural microstructures, an irregular grain boundary network and high orientation gradients reflecting strain energy gradients may be indicative for an increased influence of grain dissection.

4. Equal orientation of next-neighbour grains or orientation families (grains III and IV, Figure 7.8C) can only serve as an indication for completed grain dissection if the full CPO (a-axes as well as c-axes) is known. This is the case for EBSD measurements and numerical simulations. However, as a-axes can also align (Miyamoto et al., 2005), even in EBSD-maps, the recognition of orientation families can become difficult when the CPO is very strong. Although an orientation family is clearly observed, other indicators for grain dissection such as an irregular grain boundary network should accompany the observation. Obbard et al. (2006) observed orientation families in GISP2 (Greenland ice sheet project 2) ice core samples. Orientation families may be produced by grain dissection, rather than by polygonisation. In fact, in the misorientation distribution data shown by Obbard et al. (2006), there was no difference between the correlated and un-correlated distributions. This implies that misorientations are controlled by the strong CPO (Fliervoet et al., 1999). In addition, there is a lack of $5^{c}irc$ to $15^{c}irc$ misorientation boundaries, which would be expected if polygonisation was the main grain-size-reducing mechanism (Trimby et al., 1998; Trimby et al., 2000). The occurrence of a relatively high amount of $5^{c}irc$ to $15^{c}irc$ c-axis misorientations has been suggested as a signature of polygonisation in ice (Alley et al., 1995; Durand et al., 2008). However, the EBSD study of Obbard et al. (2006) shows that c-axis data can overestimate the occurrence of the $5^{c}irc$ to $15^{c}irc$ boundaries.

5. The prevalence of grain dissection could be related to grain size itself. Means (1989) shows that grain dissection is most frequent when mean grain size and bulge width are similar. We can identify three situations (a-c) to describe this dependency: (a) If the grain size is significantly larger, a bulge will remain close to the position of the original boundary and does not migrate through a grain. In this situation, grain dissection is not possible. (b) On the other hand, if the grain size is significantly smaller than the bulge width, the bulge shape itself cannot develop and the migrating boundary consumes a whole grain instead of dissecting it. (c) Dissection and resulting grain-size reduction is only possible when bulges are about half a grain diameter wide. Our results appear to support these dependencies. In NEEM glacial ice, the grain size is smaller and grain dissection is less common than in Holocene ice (Figure 7.10A). In our simulations, the frequency of grain dissection was higher for high strain rate simulations leading to smaller grain sizes (Figure 7.6). This may illustrate the two end-members of grain size being larger (NEEM glacial ice) or smaller than the bulge width (simulations at low strain rate). A further investigation and quantification of such dependencies should form part of future studies on grain dissection.

It was argued above that grain dissection is more important when the grain size is close to steady state than at either smaller or larger grain sizes. Although grain dissection is most significant at this grain size, polygonisation events may still outnumber grain dissection events. Therefore, we interpret that with such equilibrium conditions, suitable bulge width as described above (situation 5c) are achieved through a combination of polygonisation and SIBM. A steady state is only reached when deformation conditions are stable. High frequencies of dissection events can thus be regarded as indicators for relatively constant conditions. This appears to fit the observations in the NEEM ice core, where high frequencies of grain dissection are found at the base of the Holocene ice (Figure 7.10A). While microstructures stabilise downward in Holocene ice, both the CPO (Montagnat et al., 2014) and the grain size (Binder, 2014) change at the transition to glacial ice. According to the recrystallisation diagram by Faria et al. (2014c), this change reflects a change in deformation conditions. In turn, this implies less grain dissection relative to polygonisation, which seems to fit our observation of low frequencies in grain dissection in glacial ice (Figure 7.10A).

The proposed mechanisms controlling grain sizes in ice are classically polygonisation (Alley et al., 1995; De La Chapelle et al., 1998) or bulging nucleation (Chauve et al., 2017; Montagnat et al., 2015) leading to decreasing grain sizes and grain boundary migration leading to a grain size increase (De La Chapelle et al., 1998; Duval and Castelnau, 1995). A mixture of both is suspected to cause steady grain sizes in the middle of ice-sheets columns. However, SIBM may provide an additional grain-size-reducing process, if grain dissection is initiated (Means, 1989). Therefore, equilibrium grain sizes may be achieved with only SIBM, whereas polygonisation or nucleation need additional grain-size-increasing mechanisms to achieve equilibrium.

7.5 Conclusions

In this study, we investigate the importance of grain dissection as a feature of strain-induced boundary migration (SIBM) in ice using numerical simulations and natural microstructures from the NEEM ice core. For the first time, we present evidence that grain dissection is a common mechanism during ice deformation. The efficiency of grain dissection is probably independent of depth and rather a function of the state of the microstructure and deformation conditions. In particular, grain dissection is most efficient in depths in the ice column where deformation conditions remained constant over time and microstructures approach steady state in terms of grain size or CPO. Here, grain dissection is an efficient mechanism in addition to polygonisation, to achieve grain size reduction and maintain a balance between grain-size-increasing and -decreasing mechanisms. In turn, this implies that SIBM not necessarily leads to grain size increase, but eventually to the dissection of grains, especially at high strain energy gradients.

Future models that describe grain-size evolution during ice deformation, should incorporate grain dissection and further investigate its frequency as a function of grain size, deformation mode, CPO or other microstructural properties. This should lead to a parameterisation of grain dissection, which forms the precursor for including the process in a grain-size sensitive ice flow law required to describe large-scale ice flow.

Data availability

The video supplement related to this article is available online on figshare.com: https://doi.org/10.6084/m9.figshare.5160997.v1

Conflict of Interest

The authors declare that the research was conducted in the absence of any commercial or financial relationships that could be construed as a potential conflict of interest.

Author Contributions

Initial concept by FS and EK. FS performed numerical modelling with support from AG and PB. EK did electron backscatter diffraction analyses supported by MD and GP. JE processed the Fabric Analyser data. IW provided the glaciological input, samples and NEEM Fabric Analyser measurements. Major parts of the paper were written by FS, EK and JE with contributions of all co-authors.

Funding

We acknowledge funding by the DFG (SPP 1158) grant BO 1776/12-1 and the Helmholtz Junior Research group "The effect of deformation mechanisms for ice sheet dynamics" (VH-NG-802). We acknowledge support by the DFG and the Open Access Publishing Fund of the University of Tübingen.

Acknowledgments

We are thankful for the support of the Elle community and the discussions with Daniela Jansen, Maria-Gema Llorens and Johanna Kerch that helped improving the manuscript. We thank Sepp Kipfstuhl for the possibility to use microstructure images from NEEM ice core. NEEM is directed and organised by the Center of Ice and Climate at the Niels Bohr Institute and US NSF, Office of Polar Programs. It is supported by funding agencies and institutions in Belgium (FNRS-CFB and FWO), Canada (NRCan/GSC), China (CAS), Denmark (FIST), France (IPEV, CNRS/INSU, CEA and ANR), Germany (AWI), Iceland (RannIs), Japan (NIPR), Korea (KOPRI), The Netherlands (NWO/ALW), Sweden (VR), Switzerland (SNF), United Kingdom (NERC) and the USA (US NSF, Office of Polar Programs). We are grateful for the thoughtful reviews by Janos Urai and two anonymous reviewers.

Chapter 8

Paper IV

Physical analysis of an Antarctic ice core—towards an integration of micro- and macrodynamics of polar ice

Ilka Weikusat [1,2], Daniela Jansen [1], Tobias Binder [1], Jan Eichler [1,2], Sérgio H. Faria [3,4], Frank Wilhelms [1,5], Sepp Kipfstuhl [1], Simon Sheldon [6], Heinrich Miller [1], Dorthe Dahl-Jensen [6] and Thomas Kleiner [1]

[1] AWI-Glaciology, Alfred-Wegener-Institute Helmholtz-Centre for Polar and Marine Research, Bremerhaven, Germany
[2] Department of Geosciences, Eberhard Karls University, Tübingen, Germany
[3] BC3-Basque Centre for Climate Change, Ikerbasque, Bilbao, Spain
[4] NUT-Nagaoka University of Technology Nagaoka, Niigata, Japan
[5] Georg-August-Universität Göttingen, Göttingen, Germany
[6] CIC, Niels Bohr Institute, University of Copenhagen, Copenhagen, Denmark

Published in *Philosophical Transactions of the Royal Society A: Mathematical, Physical and Engineering Sciences*, 26 December 2016.

Abstract

Microstructures from deep ice cores reflect the dynamic conditions of the drill location as well as the thermodynamic history of the drill site and catchment area in great detail. Ice core parameters (crystal lattice-preferred orientation (LPO), grain size, grain shape), mesostructures (visual stratigraphy) as well as borehole deformation were measured in a deep ice core drilled at Kohnen Station, Dronning Maud Land (DML), Antarctica. These observations are used to characterize the local dynamic setting and its rheological as well as microstructural effects at the EDML ice core drilling site (European Project for Ice Coring in Antarctica in DML). The results suggest a division of the core into five distinct sections, interpreted as the effects of changing deformation boundary conditions from triaxial deformation with horizontal extension to bedrock-parallel shear. Region 1 (uppermost approx. 450 m depth) with still small macroscopic strain is dominated by compression of bubbles and strong strain and recrystallization localization. Region 2 (approx. 450–1700 m depth) shows a girdle-type LPO with the girdle plane being perpendicular to grain elongations, which indicates triaxial deformation with dominating horizontal extension. In this region (approx. 1000 m depth), the first subtle traces of shear deformation are observed in the shape-preferred orientation (SPO) by inclination of the grain elongation. Region 3 (approx. 1700–2030 m depth) represents a transitional regime between triaxial deformation and dominance of shear, which becomes apparent in

the progression of the girdle to a single maximum LPO and increasing obliqueness of grain elongations. The fully developed single maximum LPO in region 4 (approx. 2030–2385 m depth) is an indicator of shear dominance. Region 5 (below approx. 2385 m depth) is marked by signs of strong shear, such as strong SPO values of grain elongation and strong kink folding of visual layers. The details of structural observations are compared with results from a numerical ice sheet model (PISM, isotropic) for comparison of strain rate trends predicted from the large-scale geometry of the ice sheet and borehole logging data. This comparison confirms the segmentation into these depth regions and in turn provides a wider view of the ice sheet.

This article is part of the themed issue 'Microdynamics of ice'.

8.1 Introduction

Variations in net mass transport of ice towards the ocean lead to variations in ice flux and eventually sea-level variations. Ice sheets possess the highest potential to cause drastic changes within the global water cycle owing to their large water reservoir. This horizontal movement of ice is expressed in the surface velocities measured locally with ground-based GPS surveys (Wesche et al., 2007) or by remote sensing techniques on larger scales (Rignot et al., 2011). The observed surface velocities, however, result from a superposition of several components: (i) basal sliding owing to a temperate base of the ice, (ii) possible deformation of the bed material (sediments, glacial till), and (iii) the internal deformation of the material ice itself. While the former two components play an important role at the margins of the polar ice sheets, especially in fast-flowing outlet glaciers or ice streams, the internal deformation of ice is the main component in the interior of Antarctica and Greenland. In the upper part of the ice column, vertical thinning is the dominating process. The major ice deformation component in the geographically horizontal direction, that is, the direction towards the ocean, is shearing on horizontal planes owing to friction at the interface between ice and bedrock. This horizontal shearing becomes the dominant deformation component with depth. The balance between the different components of ice deformation contributing to horizontal transport is difficult to determine as the available data originate mainly from surface observations. As a first approximation, the Dansgard–Johnsen (Dansgaard and Johnsen, 1969) assumption is often considered, which assumes a constant vertical strain rate in the upper two-thirds of the ice column, which then decreases linearly to no vertical deformation at the frozen bed. Thus, in general, in the lower third, the shear deformation is more or less the dominant process. This holds for the most typical and common locations in an ice sheet, therefore excluding extraordinary sites such as domes. Especially in areas with low ice flow velocities, this estimation appears to be a good approximation, reconfirmed by the simulated evolution of vertical strain rate profiles in up-to-date models. With respect to improved implementation of the crystalline lattice- preferred orientation (LPO) anisotropy effects in flow models (Azuma and Goto-Azuma, 1996; Bargmann et al., 2012; Durand et al., 2007; Faria, 2006; Faria et al., 2002; Gödert and Hutter, 1998; Martin and Gudmundsson, 2012; Seddik et al., 2008; Thorsteinsson, 2002; Veen and Whillans, 1994), the exact identification and reconstruction of the relation between vertical compression and horizontal shear and its development with depth are required. An anisotropic description can lead to substantial feedback effects in terms of effective viscosity with respect to the principal deformation directions.

The contributions of vertical compression in the upper part and horizontal shear in the lower part of the ice sheet can be estimated, using information obtained from

ice coring. Ice cores and their boreholes provide us with local insights into dynamical processes below the surface. The evolution of c-axis distributions (LPO) with depth is an indicator of the changing dominance of the deformation modes (Montagnat et al., 2014). Thus, c-axis distributions measured from ice core samples directly represent the mechanical contribution to microdynamic processes. This information can be complemented by grain topology (size and shape) data also to represent the recrystallization (thermodynamic) contribution (Faria et al., 2014a). Grain size and grain shape are structural parameters that can be evaluated in order to support conclusions made from the LPO measurements with respect to deformation modes. Such characteristic grain size and shape microstructures are well known and also used as shear-sense indicators, e.g. as 'oblique foliation' in mylonitic rocks (Passchier and Trouw, 2005, p. 128). Mylonites are rocks found in shear zones which experienced large ductile strain rate, but under colder homologous temperatures (T/T_m) than ice. Owing to the high homologous temperature for natural ice in general ($T/T_m \gg 0.7$) and the slow creep flow in most deep ice coring sites, such effects of deformation modes are very moderate and difficult to discern, because recrystallization strongly overprints deformation effects and masks typical deformation microstructures (Faria and Kipfstuhl, 2005; Humphreys and Hatherly, 2004; Llorens et al., 2016a,b). Furthermore, deformation mechanisms, such as small-scale folding initiated by grain kinking, provide new insights into the microdynamic processes with consequences for mesoscale (Jansen et al., 2016) and possibly also macroscale structures (Bons et al., 2016). The meso- to macroscale impact of changing deformation regimes with different deformation modes and mechanisms with depth can be monitored by repeatedly logging the borehole geometry after certain time intervals, which also reveals the onset of shear deformation dominance with depth. Comparison of the described observations with strain rate components predicted by a flow model can illuminate possible misconceptions in our understanding of large-scale ice flow.

The aim of this contribution is to revisit the idea of deformation modes at the EDML site from meso- and microstructural data (Hamann et al., 2008) in combination with new observational data, which became available recently. We combine these with strain rate estimates provided by a large-scale three- dimensional flow model, and thus consider also a broader ambient flow field than the purely one-dimensional Dansgard–Johnsen (Dansgaard and Johnsen, 1969) assumption. This combination provides us with a solid understanding of shear versus compressive deformation for the EDML ice core location.

8.1.1 Introduction—EDML ice core

The European Project for Ice Coring in Antarctica (EPICA) in the Dronning Maud Land (in short: EDML) ice core was drilled between 2001 and 2006 at the Kohnen Station, Antarctica (position 79°00′ S, 0°04′ E, elevation 2892 m.a.s.l.) (Oerter et al., 2009; Wilhelms et al., 2014). The location is shown in figure 8.1 and was chosen because of the relatively high accumulation rate at the drill site, which enabled palaeoclimate proxy records to be obtained with a high temporal resolution. Furthermore, its location in the Atlantic sector of Antarctica allows for a comparison with the Greenland ice cores (EPICA community members, 2006). The core reached a length of 2774 m, penetrating down to just above the bedrock at 2782 m vertical ice thickness. The ice surface topography exhibits a slightly divergent flow along an ice ridge with 0.756 m a^{-1} observed surface velocity (Wesche et al., 2007). The accumulation

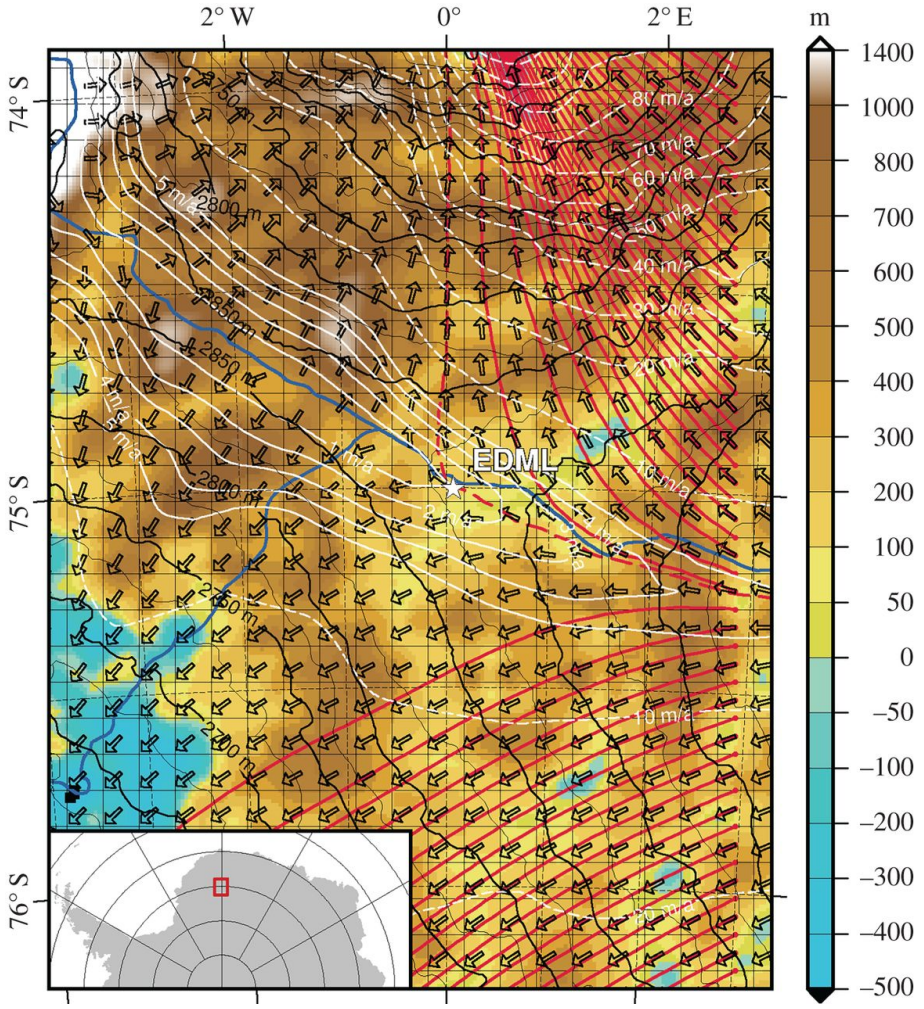

FIGURE 8.1: Map of the EDML ice divide area with input and output information of the ice flow model. The divide line is shown in blue (Zwally et al., 2012). White isolines and arrows are the magnitudes and directions of surface velocities, respectively, calculated by the model. The resulting streamlines seeded at the eastern margin of the domain are shown as solid red lines, whereas the streamline passing the grid location next to the EDML site (the location of the presented strain rates) is shown as the dashed red line. The blue to brown colour code represents the bedrock topography while black isolines show the surface elevation; both from the Bedmap2 dataset (Fretwell et al., 2013). The square grid is the model grid with 10 km spacing.

rate is 64 kgm^{-2} a^{-1} (ice equivalent 7 cm a^{-1}) (Oerter et al., 2004). The annual average surface temperature (10 m-firn temperature) is −45° C and the borehole bottom temperature is −3° C. This leads to bed conditions with subglacial water, which penetrated into the hole during the termination of drilling (Wilhelms et al., 2014).

Numerical flow models with palaeoclimate forcing have been used to determine an appropriate site for the EDML ice core (Calov et al., 1998; Savvin et al., 2000) prior to the actual drilling and have also assisted with the dating and interpretation of the palaeoclimate records of the EDML deep ice core (Huybrechts et al., 2007). The first two studies (Calov et al., 1998; Savvin et al., 2000) present temperature and shear strain rates versus depth for their proposed drill sites at 73°57′ S, 03°35′ W and 73°59′ S, 00°00′ E, respectively. As both locations are several hundreds of kilometres away from the EDML site, the given profiles cannot be used for comparison. Although the study by Huybrechts et al. (Huybrechts et al., 2007) is to our knowledge

the most recent in-depth flow modelling study for the EDML site, as they apply a higher-order flow model nested in a large-scale model under palaeoclimatic forcing, unfortunately we cannot compare the results, because neither strain rate nor temperature versus depth profiles are reported.

8.2 Methods

8.2.1 Fabric analysis

The C-axis distribution data (LPO/fabrics; figure 8.2) are derived from thin sections measured with an automated fabric analyser system of the Australian Russell-Head type (Peternell et al., 2010) that applies polarized light microscopy, where the thin section is placed between systematically varying crossed polarizers (Wilson et al., 2003). We mainly used the G20 system, measuring approximately 150 vertical and horizontal thin sections in depth intervals of about 50 m (dataset: Weikusat et al., 2013a). For cross- and quality checks, we also applied the improved G50 system for 60 additional vertical thin sections, with partly bag-continuous sampling (dataset: Weikusat et al., 2013b). A few examples of the in total approximately 210 crystal LPO measurements are displayed for illustrative reasons in figure 8.2 and figure 8.3b as classical pole figures. These so-called Schmidt diagrams show the natural variability among at least 100 measured grains per section. Additionally, as a more continuous display of all thin section data, we calculated eigenvalues of the second-order orientation tensor of the c-axis distributions (Durand et al., 2006b; Wallbrecher, 1979), which portray the distribution as an enveloping ellipsoid with the eigenvalues being its three principal axes (figure 8.4b, dataset: Weikusat et al., 2013c,d). This method is well suited to quantify a three-dimensional unimodal or girdle distribution of orientation data. The breadth of the distribution is described by the absolute magnitude of the eigenvalues, that is, it describes how many grains are aligned with the preferred direction. Additionally, the Woodcock parameter is given (figure 8.4b; Woodcock, 1977), which lies in the interval $[0, 1]$ for girdle LPOs and $[1, \infty]$ for unimodal LPOs.

8.2.2 Grain size and shape characteristics by light-microscopy microstructure mapping in plain and polarized light

In addition to the LPO investigations, further microstructural data such as grain size evolution and shape-preferred orientations (SPOs) gave insight into, and in turn can influence, the deformation conditions and related processes (e.g. Herwegh and Handy, 1998; Passchier and Trouw, 2005). The grain size and shape evolution along this core were examined, using approximately 300 vertical and horizontal thick and thin sections (10 m interval). Owing to the preferred sublimation along the grain boundaries, they develop etch grooves on sublimation-polished surfaces that are visible in plain light illumination (Kipfstuhl et al., 2006). These grooves can then be mapped on microphotographs, revealing the grain boundary network. The grain boundary networks were extracted, using fully automatic image analysis, and evaluated for structural parameters of the grains wherever possible (Binder et al., 2013, figure 8.3a), with manual corrections when necessary. The data from vertical sections were complemented by grain structural parameters derived from photographs taken between crossed polarizers for horizontal sections (during the fabric analysis procedure). Here, semi-automatic image analysis with edge detection segmented the image into grain boundary networks (figure 8.3b).

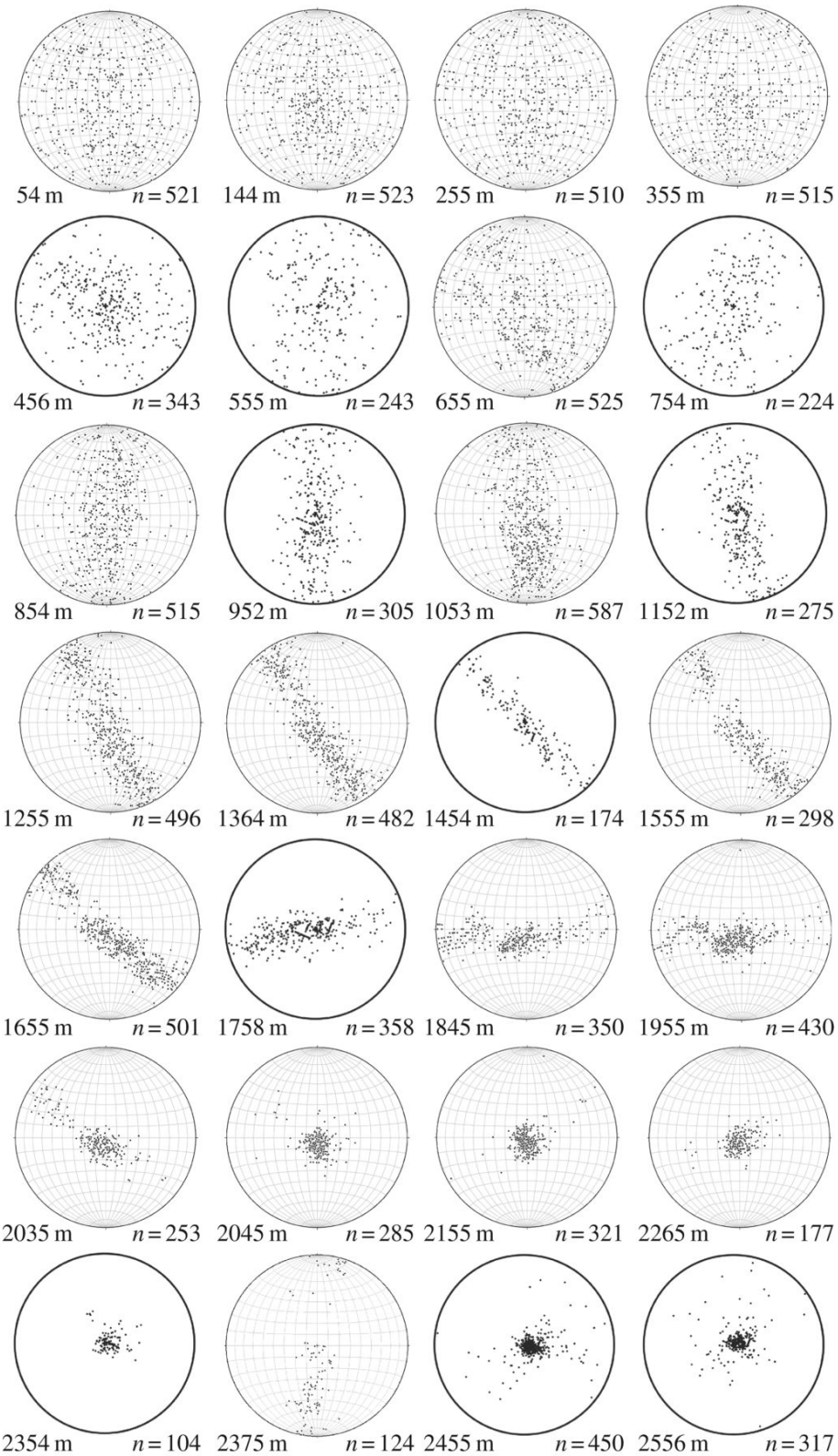

FIGURE 8.2: Examples of stereographic projections of the lattice-preferred orientation (LPO). Classical glaciological projection into the geographical horizontal plane (the drill-core axis is at the centre of the circle in each diagram). Pole figures show the classical Schmidt diagram. Gridlines illustrate measurements on vertical thin sections (rotated for this display), whereas diagrams without gridlines originate from horizontal thin sections. Numbers on the left of each diagram give sample depth; on the right of each diagram are the number of c-axes (one per grain) plotted. Please note that changes in the orientation of the girdles are related to orientation mismatch between core pieces (drill runs), and not to a sudden change in stress/flow direction.

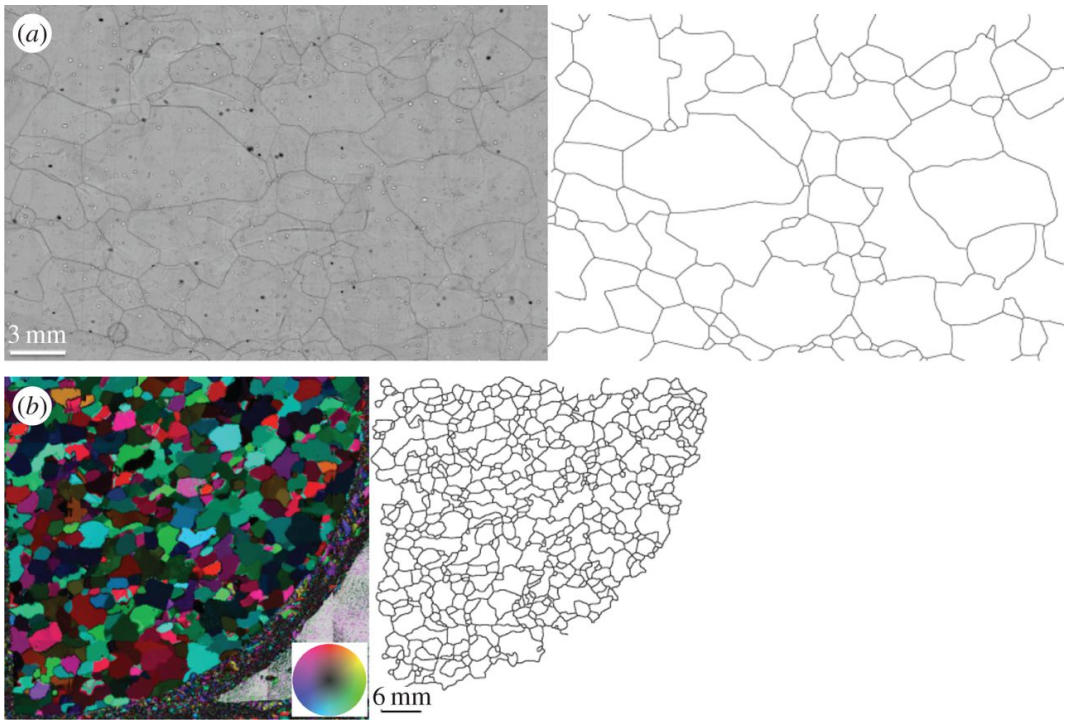

FIGURE 8.3: (a) Example of a microstructure mapping picture (1553.0 m depth) and the resulting grain boundary network obtained by image segmentation. Left-hand picture shows strong black lines which are grain boundaries revealed by sublimation etching. (b) Example of an AVA (Achsensverteilungsanalyse) picture (1056.0 m depth) for LPO measurements (automatic fabric analyser) and the resulting grain boundary network obtained by image segmentation via edge finding. Left-hand picture, false-colour code; see wheel legend.

From the grain boundary networks, we obtained the two-dimensional grain size, e.g. as areas by pixel counting of individual grains (figure 8.4d) and shape parameters (SPOs). The magnitudes of grain elongations given as aspect ratios (figure 8.4e) and grain elongation directions (figure 8.4f) are calculated from the principal axes of an ellipse fitted to each segmented grain. The distributions of the directions are shown as circular histograms ('rose diagrams') in figure 8.5b (display method adopted from Azuma et al., 1999, 2000). Although the drilling process does not allow for an oriented ice core, the relative orientation among individual drill runs has been retained by fitting characteristic core break surfaces during core logging as well as possible and by drawing a continuous 'top line' on one side of the core (Hvidberg et al., 2002). In the girdle LPO depth range, a change in orientation is identified from the changing direction of the girdle in the stereographic projections (figure 8.2). However, in the brittle zone (approx. 800–1200 m), where orientation loss happened more frequently, it is less obvious as the data show only a weak girdle pattern in this depth region. The grain elongation direction data reveal possible inclinations from the horizontal and vertical sections (figure 8.5b, §3c). The raw data of inclination measurements from the elongation directions from vertical sections reflect a jump between 1655 and 1758 m (cf. figure 8.2) owing to a loss in azimuthal orientation of the core during logging, which was caused by a break between 1686 and 1696 m. This jump corresponds to a core rotation of about 40° (cf. figure 8.2) and significantly masks the signal in the raw measurements of elongation directions. A second recognizable azimuthal loss shows less rotation ($10 - 20°$) between 1955

and 2035 m depth, but with higher ambiguity owing to the strongly developed single maximum LPO. The rotational symmetry of the single maximum distribution does not allow a reliable reconstruction of the likely true inclination. However, the effect on grain elongation inclination data is minor. It may however contribute to the increasing variability in this depth range. The 40° jump between 1686 and 1696 m was corrected in the grain elongation inclinations by means of trigonometry, assuming that the steeper inclination at 1696 m is the true dip of the three-dimensional elongation plane. Thus, the data shown here represent a lower bound of the actual inclination. The correction assumes a maximum dip, which is however unknown. Furthermore, only absolute values are given, as the dip direction leading to clockwise or anticlockwise inclination depends on the core and sampling orientation.

8.2.3 Visual stratigraphy line scanning

Visual stratigraphic layering was recorded continuously along the core with a line scanner (LS) developed at the Alfred Wegener Institute in Bremerhaven, Germany, and the Niels Bohr Institute at the University of Copenhagen, Denmark (Faria et al., 2018; Svensson et al., 2005).

Typical LS samples are 1 m ice slabs that have been cut lengthwise from the EDML core, with their upper and lower surfaces polished with a hand-held microtome blade. Oblique dark- field, indirect illumination of each slab is scanned along the core axis by a digital line-scan camera. The line-scan camera can capture only the light that has been scattered by inclusions in the ice matrix, such as microscopic particles or air bubbles, because ice itself is transparent. Thus, the degree of brightness recorded by the camera is proportional to the concentration of inclusions in the sample, in such a manner that a clear piece of ice, free of inclusions, appears dark (figure 8.5a).

Images recorded with the LS system reveal the visual stratigraphy of an ice core in great detail (1 pix = 0.1 mm) because of the high resolution and sensitivity of the digital line-scan camera. Strata as thin as 1 mm can be easily detected with this method. Any small change in the optical properties of the ice matrix, usually caused by a change in the mean size or concentration of inclusions, gives rise to a new horizon.

8.2.4 Borehole logging

During the EDML drilling campaign, the borehole was logged at several stages of drilling progress. The logging system continuously recorded the tilt of the borehole with respect to the vertical (inclination) as well as the heading of the borehole with respect to magnetic north (azimuth) by means of a compass (Gundestrup et al., 1994). Additionally, the diameter of the borehole was measured. Here, we use the change of the borehole course (inclination and azimuth; figure 8.4a) owing to the local ice deformation between two measurements (January 2004 and November 2005) to estimate the strain regime at the EDML site. Changes in diameter of the borehole, which do occur, are not evaluated in this study.

8.2.5 Strain rate estimations from the ice flow model

To derive a velocity–depth profile at the EDML site, we used the parallel ice sheet model (PISM v 0.6.1) (Bueler et al., July 2007; Martin et al., 2011; Winkelmann et al., 2011).

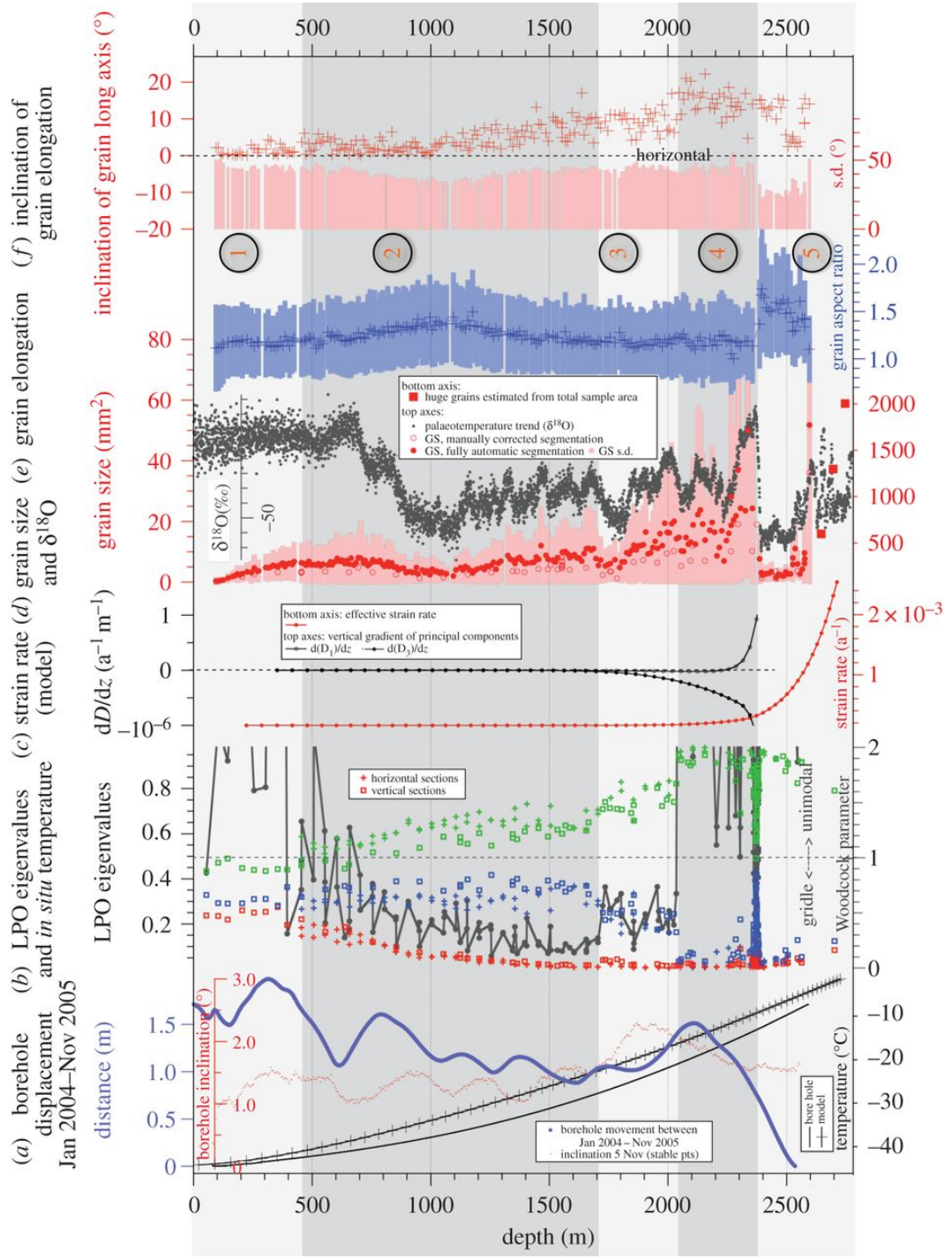

FIGURE 8.4: Compilation of ice core micro- and mesostructure data with borehole and modelling data. Shaded regions denote regions of deformation modes explained in the text. (a) Borehole data and modelled temperatures. (b) LPO data given in eigenvalues of the second-order orientation distribution tensor (red, blue, green) and Woodcock parameter. (c) Derivatives of the selected strain rate tensor components derived from the shallow ice approximation model PISM. (d) Grain size data from the microstructure map and δ^{18}O values (‰ standard mean ocean water) from stable water-isotope measurements for palaeotemperature reconstruction (grey). Dataset: doi:10.1594/PANGAEA.754444 down to 2416 m depth. Below 2416 m depth unpublished data (H Meyer and H Oerter 2016, personal communication). (e) Grain elongation given as the aspect ratio of the short and long axis of a fitted ellipse. Mean and standard deviation (s.d.) per 10 cm section of microstructure maps. (f) Grain elongation directions given as the mean angle of the long axis of the fitted ellipse with the horizontal direction (0°). Corrections, assuming measured dip at 1696 m depth being maximum, lead to lower bound inclinations. Actual three-dimensional inclinations can be higher.

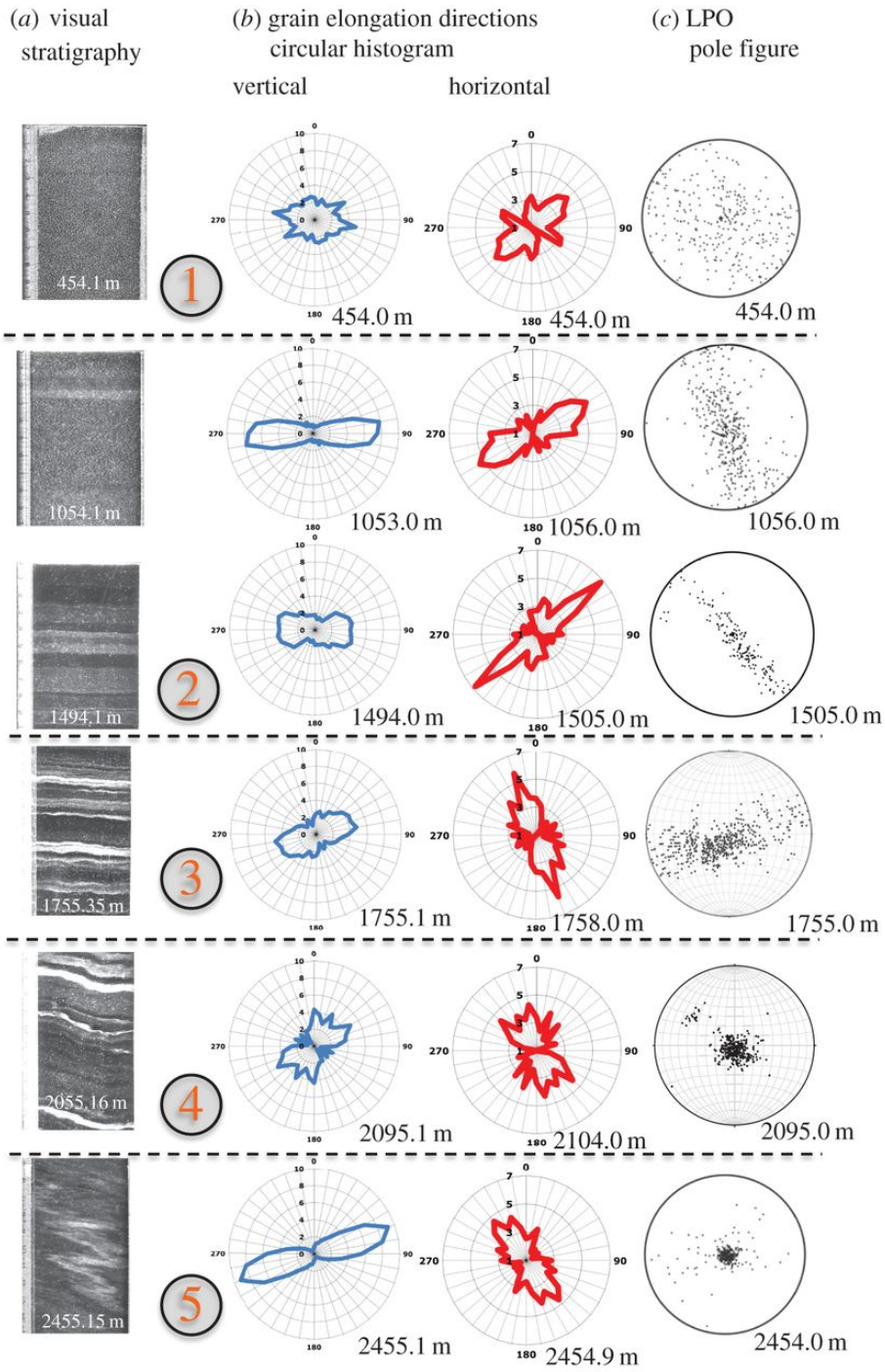

FIGURE 8.5: (a) Visual stratigraphy line scanner images, selected. (b) Distributions of grain elongations given as circular histograms (rose diagrams) measured in sections vertically (right) and horizontally (left) cut from the ice core. Radial axes give the frequency in % with a fixed axis range (7% for horizontal sections, 10% for vertical sections). For vertical sections, directions 0° and 180° are along the core axis. For horizontal sections, azimuthal orientation corresponds to those in LPO pole figures. (c) Selected LPO stereographic projections for direct comparison.

The deformation of polycrystalline ice is modelled, using the Nye generalization (Nye, 1957) of the Glen–Steinemann power-law rheology (Glen, 1955; Steinemann, 1954). The effective viscosity, which connects the strain rate tensor with the deviatoric part of the Cauchy stress tensor, depends on strain rate, pressure, temperature

and water content (Lliboutry and Duval, 1985; Paterson and Budd, 1982), where the last two quantities are diagnostically calculated from the enthalpy field. The enthalpy scheme used in PISM is fully described in Aschwanden et al. (2012), to which the interested reader is referred.

At each time step of a PISM simulation, the geometry, temperature, water content and basal strength of the ice sheet are included into momentum balance equations to determine the velocity of the flowing ice.

Instead of solving the full set of Stokes equations for the momentum balance, PISM solves, in parallel, two different shallow approximations: (i) the non-sliding shallow ice approximation (SIA Hutter, 1983), which describes ice as flowing by shear in planes parallel to the geoid, and (ii) the shallow shelf approximation (SSA Morland, 1987), which describes a membrane-type flow of floating ice, or of grounded ice which is sliding over a weak base. The ice flow velocity of the grounded ice is computed with a hybrid scheme based on a weighted superposition of both shallow solutions (SIA + SSA), where the SSA solution acts as a sliding law (see Bueler and Brown, 2009 for details). The computed three-dimensional velocity field thus contains horizontal longitudinal (membrane) stresses from the SSA solution as well as vertical shear stresses from the SIA solution.

The present-day state of the Antarctic ice sheet was computed based on the present-day geometry Bedmap2 (Fretwell et al., 2013), and varying datasets for present-day boundary conditions such as: surface temperature (Comiso, 2000; Fortuin and Oerlemans, 1990; Wessem et al., 2014), surface mass balance (Arthern et al., 2006; Berg et al., 2006; Wessem et al., 2014) and geothermal heat flux (Maule et al., 2005; Shapiro, 2004) and the update from Purucker (2012) based on the method of Maule et al. (2005). The original dataset of Maule et al. (2005) has been capped at a value of $0.07\,\mathrm{W\,m^2}$ according to the SeaRISE- Antarctica recommendations (Bindschadler et al., 2013). Using all combinations of the boundary conditions above, with the restriction that RACMO2.3/ANT (Wessem et al., 2014) data for surface skin temperature and accumulation rate are used together for consistency, we have set up an ensemble of 15 different simulations. We have chosen the combination RACMO2.3/ANT surface forcing together with the Shapiro & Ritzwoller (Shapiro, 2004) heat flux as our reference simulation. Other combinations have been applied to estimate the sensitivity of the model to varying forcing data. We have chosen the same set of parameters within the PISM model that have been used for the ice sheet modelling project SeaRISE Antarctica (see 'Potsdam' model in Nowicki et al., 2013), where the model was forced with constant present-day climate. Although surface temperatures and accumulation rates have changed over time in the palaeoclimate context, we prescribe the constant present-day climate in order to avoid a complete recalibration of the model that would be far beyond the scope of this study. As the temperature field near the base—where most of the deformation takes place—is mainly controlled by the geothermal heat flux, we expect to have a reasonable uncertainty estimate owing to our ensemble set-up.

Each simulation was conducted in a series of subsequent grid refinements (all based on the initial 1 km present-day geometry) using 40, 20 and 10 km horizontal resolution and 41, 81 and 101 vertical layers, respectively. We used the flux correction method provided by PISM in addition to a prescribed (present-day) calving front position to result in an ice sheet that is close to the observed present-day geometry. After initialization (1 a), a short relaxation period (100 a) and a purely thermal spin-up with the geometry held fixed (200 k years) on the 40 km grid using only the non-sliding SIA, the model ran for 100 k years, 20 k years and 4 k years on the 40, 20 and 10 km grid, respectively, in the hybrid (SIA + SSA) mode. The individual boundary

conditions that have been chosen for one ensemble member were held constant over time, thus forming a present-day climate equilibrium model realization.

All components of the strain rate tensor as well as the effective strain rate D_e (figure 8.4c) and the three principal strain rates, D_1 , D_2 and D_3 (eigenvalues of the strain rate tensor, figure 8.4c), have been derived from the simulated velocity field diagnostically on the PISM grid.

8.3 Results and data

8.3.1 Lattice-preferred orientation

The c-axis distributions show a typical evolution with depth for a drill site located on an ice divide: a broad distribution represented by all three eigenvalues around one-third (figure 8.4b) appears uniform in the pole figure display (figure 8.2) and is almost constant in the upper 450 m. Below this, LPO develops continuously into a vertical great-circle girdle distribution by narrowing of the girdle towards three distinct eigenvalues (in the following referred to as e_1, e_2, e_3) down to 1650 m depth. In a transitional region (approx. 1700–2030 m), the LPO evolves towards an elongated single maximum well defined by the inflection point of the e_2-trend (figure 8.4b): above approximately 1650 m e_2 grows; below 1650 m e_2 decreases. Although increasing strictly monotonically with depth in the upper two-thirds of the core, also the e_1-trend shows a change in slope at approximately 1650 m depth. The gradual evolution of the single maximum is generated by a gradual concentration of c-axes within the girdle, observable in panel 5 of figure 8.2 and a slight re-widening of the central part of the girdle in the pole figure (see also figure 8.2). This is confirmed by the Woodcock parameter (figure 8.4b), which rises at this depth level towards unimodal distributions. This is followed by a collapse of e_3 and e_2 into a single maximum at approximately 2030 m depth (figures 2 and 4c). In a narrow layer (from 2345 to 2395 m depth), the LPOs become highly diversified with tendencies of single maximum to girdle and back to single maximum distributions represented by a wide range of values in e_3 and e_2 (0–0.5) and in e_1 (0.5–0.9) (figure 8.4b). This is the lower half of the Eemian (marine isotope stage 5.5 (MIS5.5)) layer, characterized by lower $\delta^{18}O$ values (figure 8.4d), which indicates higher precipitation temperatures than derived from the overlying ice of the last glacial period. Statistical evaluation is difficult, as the Eemian ice exhibits the largest grain sizes observed in the EDML core, except for the basal layer (figure 8.4d).

Systematic offsets of the eigenvalues e_2 and e_1 between vertical and horizontal sections (figure 8.4b, e.g. in region 2) are due to the ambiguity of measurement of c-axes lying close to the observation plane. Data at the periphery of a pole figure (projection onto a thin section plane) are of low quality and thus partly excluded from the population in display and LPO data processing, leading to the described bias. The automatic fabric analysers used here calculate the extinction angle, where no light gets through the system, by fitting the light amplitude values for each step of the polarizers to a sinusoid curve (Peternell et al., 2009; Wilen et al., 2003). The low-quality effect of c-axes in a plane normal to the observation axes is caused by the G20 instrument often being unable to resolve the quadrant pair of the azimuth of these orientations. The G20 used a rotating prism to realize three viewing axes and images are taken from three directions. This includes a fourfold symmetry of the extinction angles for the viewing directions. The automatic fabric analyser software philosophy excludes any possibly false information, thus any ambiguous data values are not included. The G50 instrument uses a quarter-wave ($\lambda/4$) plate to

determine the azimuth, so that fast/slow directions by adding or subtracting $\lambda/4$ resolve the azimuth symmetry of the quadrants (defined by the crossed polarizers; for further details on crystal orientation and interference effects, see for example Heilbronner and Barrett, 2014). Comparison measurements verified this effect.

8.3.2 Grain size

The grain size generally increases with depth ($0.3 - 2000\,\mathrm{mm}^2$), but is strongly affected by the impurity content of ice from different climatic stages (figure 8.4d). Over the first 700 m, the grain size increases and decreases again with depth until reaching the last glacial maximum (LGM) ice (MIS2, approx. 1000 m), which is identified by the most depleted stable water isotope values (figure 8.4d EPICA community members, 2006; EPICA Community Members, 2010; H Meyer and H Oerter 2016, personal communication: stable oxygen isotopes of deep ice core EDML (deeper than 2416 m)). Correlation coefficients for grain size and δ^{18}O confirm the correlation on this large scale with 0.65 for depths below 700 m and 0.79 for depths below 900 m depth. Below, the mean grain size increases again down to a depth of approximately 1700 m, followed by a steep size decrease down to approximately 1750 m (MIS4). Below this, grains increase again down to approximately 2300 m (Eem, MIS5.5), but show a higher variability within samples than in all stages above. A sharp decrease down to the smallest measured grain size values is observed just below the MIS5.5 ice (approx. 2400 m), followed by a sudden increase (approx. 25 times) to grains of similar or larger size than the section size in the deepest basal ice layers. Further doubling to tripling of grain size occurs in this basal layer estimated from the deepest three samples measured ('square' symbol and separate bottom axis in figure 8.4d).

The above-described trend in grain size can be observed fully automatically as well as by manually correcting segmentation of images (excluding the three basal samples). Both methods give diverging results at various levels with the manually corrected segmentation giving approximately 10% smaller values in most depth levels (figure 8.4d). Thus, the fully automatic segmentation may not capture all (slightly weaker) grain boundaries. These weaker boundaries, in principle, are an indication for newly formed grain boundaries developing from subgrain boundaries during dynamic recrystallization (Weikusat et al., 2009b; §4.1 in Faria et al., 2014c). This seems to occur along the whole EDML ice core (Weikusat et al., 2009a). However, a deeper analysis of these mechanisms, e.g. to decipher the actual processes of grain boundary formation, is only possible in combination with high- resolution full-crystal orientation measurements Montagnat et al., 2015; Weikusat et al., 2010, 2011, and lies beyond the scope of this work.

8.3.3 Grain shapes

A visualization of SPO given as grain elongations in the vertical and horizontal sections is shown in figure 8.5b,c as circular histograms (also called 'rose diagrams'), which show the magnitude and direction of elongation. Statistical evaluation (figure 8.4e,f) is not possible for horizontal sections owing to few samples. In general, only moderate mean aspect ratios up to 1.8 are observed (figure 8.4e). Large standard deviations in all samples indicate that only a few grains are actually elongated, whereas many exhibit an equi-dimensional habitus. However, for vertical sections, we observe clear trends in the mean values: first, increasing elongations from 1 to 1.5 down to 1100 m depth, followed by a decrease down to approximately 1700 m

depth. Between 1700 and 2200 m, aspect ratios remain stable at small average elongations of approximately 1.2, with an increased variability observed among samples below approximately 2050 m depth. Low values approach approximately 1 and indicate equi-dimensional grain shapes on average. Most intensely elongated grains in the EDML ice core are observed at a sudden transition of aspect ratio from 1.1 to 1.7, located between 2356 and 2393 m depth. Below approximately 2575 m depth range statistical analysis is not reliable owing to the very large grain size.

Grain elongation directions, defined as angles of the long axis of a fitted ellipse with the horizontal, show large variations within individual sections (figure 8.8; s.d. in figure 8.4f). Statistical analysis, however, reveals elongation of grains in the horizontal direction (0°) down to approximately 1000 m depth. This is remarkable as between 500 and 1200 m the relative azimuthal core orientation was lost repeatedly in the brittle zone. The geographical azimuthal (N–E, S–W) orientation of the drill core controls the actual observed angle of inclined features. Three- dimensional-sectioning effects of orientations of lines or planes, e.g. during sample preparation as in this study or in geological outcrops, are well known in structural geology (Twiss and Moores, 2007). These sectioning effects lead to minimum bound measurements of angles, and isolated single measurements cannot prove horizontal orientation. Repeated sectioning of samples down to approximately 1000 m depth all showing on average 0° angles thus reveal a truly horizontal-preferred elongation direction. On average, grain elongation directions start to incline slightly from the horizontal to a few degrees down to approximately 1700 m. This has to be considered as a lower bound owing to the three-dimensional cutting effect of inclined objects. The inclination of grains progressively increases to about 10° at a depth of approximately 2030 m. Elongation directions appear to stabilize below this.

Comparison of the vertical girdle LPO presented in the standard glaciological stereographic projections into the horizontal (figure 8.5c) with grain elongations in horizontal sections (figure 8.5b, right column) shows that the mean orientation of the girdle plane, that is, the average plane containing all c-axes, and the orientation of the grain elongations in the horizontal are perpendicular to each other.

8.3.4 Visual stratigraphy

The visual stratigraphy in the uppermost 950 m is generally horizontal, straight and faint (figure 8.5a). The last feature results from the fact that air bubbles in this zone are by far the largest and most efficient light scatterers, so that the visual stratigraphy is dominated by depth variations in the number and size of air bubbles. The ice core in this zone appears so bright under the LS that the recorded images seem partially washed out, with a faint stratigraphy. Within the bubble–hydrate transition zone (BHT zone, 800–1200 m Faria et al., 2010), stratigraphic variations in the number and size of air bubbles gradually increase with depth. Below the BHT zone, all bubbles have transformed into air hydrates, which have a refractive index more similar to that of ice and are consequently inefficient light scatterers. Therefore, the ice stratigraphy below 1200 m is defined by variations in the concentration of micro-inclusions (e.g. salt or dust particles). In sufficiently high concentrations, micro-inclusions can scatter the incident light and make the ice seem opaque, forming strata of light-grey appearance of millimetres to decimetres thickness, called cloudy bands (Faria et al., 2009; Gow and Williamson, 1976). Owing to their intensity and frequency, cloudy bands are the main stratigraphic feature of deep (bubble-free) polar ice.

From the lower part of the BHT zone at approximately 950 m depth down to around 1600 m depth, the EDML stratigraphy remains undisturbed and horizontal (figure 8.5a). Just a few cloudy bands occasionally show minimal undulations with amplitudes not larger than a couple of millimetres. Below 1700 m depth, these undulations gradually increase in intensity and frequency, to such an extent that below 1700 m depth microscale folds develop and some flimsy cloudy bands become slightly inclined or disrupted (figure 8.5a). However, it is only beneath 2050 m depth that well-defined mesoscale folds (with amplitudes up to a few centimetres) and sloped strata (inclined up to 15° from the horizontal) become dominant (figure 8.5a). Further down, the intensity of such disturbances increases notably: cloudy bands appear ragged and fuzzy at diverse inclinations, sometimes up to 30° with respect to the horizontal.

Below 2200 m depth, the strong layer mixing and low concentration of microinclusions make cloudy bands too faint and disrupted to be identified. Notwithstanding, at 2386 m, cloudy bands suddenly reappear neatly parallel, horizontal and well defined again. Faria et al. (Faria et al., 2009; Faria et al., 2014a,c) have pointed out that this striking stratigraphy change accurately coincides with a sharp increase in impurity content that marks the transition from the last interglacial (MIS5.5) to the penultimate glacial period (MIS6), approximately 130 000 years ago (figure 8.4d). It coincides with conspicuous changes in ice microstructure, e.g. an abrupt reduction in grain size (5 mm to less than 1 mm) and an increase in grain elongation (aspect ratios 1.2–1.7), within a depth interval of less than 10 m (figure 8.4d,e).

Drastic variations in intensity, inclination and folding of cloudy bands are recognized below 2400 m depth. Intense cloudy bands inclined up to 45°, kink folding, multiple z-fold and other serious stratigraphy disturbances become frequent. As a general trend, the intensity of the cloudy bands gradually reduces with depth until they completely disappear below 2600 m, where the temperature rises above −7°C and the average grain size increases dramatically (figure 8.4d).

8.3.5 Borehole data

The measured borehole inclination and azimuth were smoothed, using a Butterworth low-pass filter to eliminate the influence of movements of the cable and erratic movements of the logger owing to unevenness of the borehole walls. The logger depth is taken as the paid out cable length. This set of three coordinates (inclination, azimuth, depth) was then transformed into hree-dimensional Cartesian coordinates x, y, z of the borehole track by integrating the data along the path. Owing to the integration, the possible error in the borehole track increases with depth. The data presented in this study were recorded in January 2004 and November 2005. Both logs reached a depth of approximately 2550 m, which is still about 200 m above the bedrock. Later, re-logging data could not be included here owing to a failure of the azimuthal measurement, preventing the calculation of the shape of the borehole. However, these latter data would not have included the lower approximately 200 m, because the intrusion of subglacial water made the lowermost part of the borehole inaccessible. As the water rose faster than it could be removed, this also caused the end of the drilling (Oerter et al., 2009; Wilhelms et al., 2014).

The calculated borehole displacement and the inclination of the hole are displayed in figure 8.4a. The gradient of the borehole displacement is largest below approximately 2050 m depth (figure 8.4a), indicating the depth where shear becomes dominant. Above, the displacement is fluctuating around approximately 0.5 m, which is partly owing to the rather high noise of these measurements compared

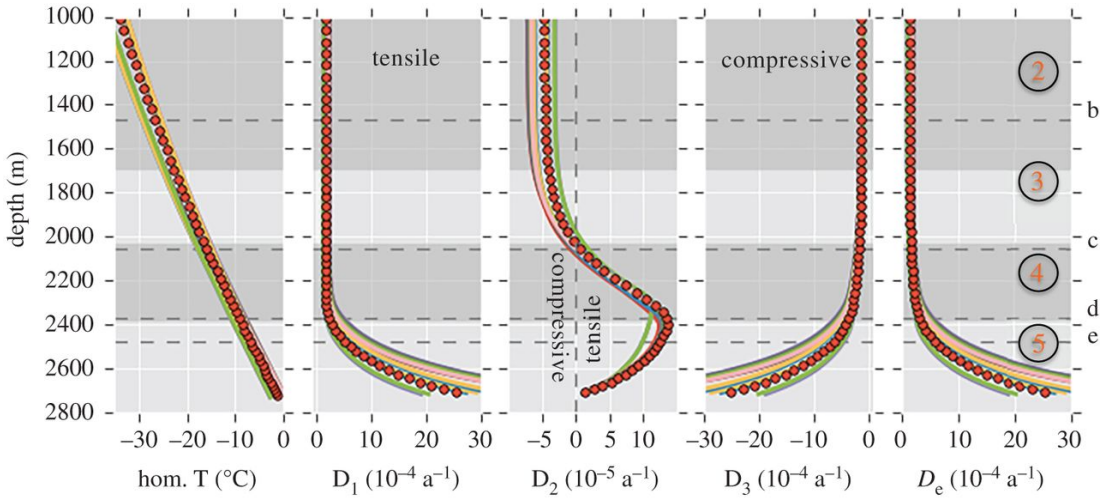

FIGURE 8.6: Modelled temperature (pressure corrected), the principal components D_1, D_2, D_3 of the strain rate tensor and the effective strain rate from 15 model runs with varying surface and basal boundary conditions. Our reference simulation is shown as filled red circles, whereas all other simulations are presented as highly overlapping lines with randomly chosen colours. The annotated horizontal dashed lines indicate the selected depth levels for the eigenvectors shown in figure 8.7. The vertical dashed line in the D_2 panel is placed at zero strain rate and indicates the transition between compressive and tensile conditions.

with the small displacement signal owing to the slow deformation. The absolute total displacement is in accordance with the measured surface velocity (0.756 m a^1 Wesche et al., 2007) at the site over 2 years, lacking any evidence of significant basal slip below the EDML drilling site despite the occurrence of subglacial water.

8.3.6 Strain rate estimates from the model

The simulated temperature–depth profile extracted from the PISM grid at the grid location next to the EDML site (approx. 1.5 km away) is shown in figure 8.4a. Comparison with the measured borehole temperature (same figure 8.4a) reveals a distinct difference, as modelled temperatures are always higher (approx. 5°C, maximum) than the observations. In the lowest part of the borehole, temperature observations are missing, but observed water at the ice–bed interface indicates temperate ice conditions. Thus, the simulated basal temperature of approximately −1.4°C (pressure corrected) underestimates the temperature at the base. The overall curvature of the simulated temperature–depth profile is smaller (more linear) than the observation, most likely indicating that the model underestimates the downward advection of cold ice from the surface. Assuming that the zeroth-ordered stress terms from the momentum balance equations are still the largest contributions to the effective stress at the EDML site, we expect the model to overestimate the deformation of ice, mostly in the ice column except for the basal zone.

The magnitude of the horizontal surface velocity obtained by the model is approximately 1.4 m a^1, and is thus twice the observed value (0.756 m a^1 Wesche et al., 2007), but still within the same order of magnitude. As the base is cold in the model, this surface velocity originates from internal deformation only. The simulated velocity has a stronger northern component than reported in Wesche et al., 2007. This corresponds well with the local surface slope from the gridded Bedmap2 dataset (Fretwell et al., 2013, see surface contours in figure 8.1).

Figure 4c shows the derived effective strain rate with depth that is approximately constant down to approximately 1700 m depth. The effective strain rate increases between approximately 1700 and approximately 2400 m owing to the increasing influence of shear strain with another significant gain below 2000 m depth, and increases further with a higher gradient below approximately 2400 m. The derived first principal strain rate D_1 (with $D_1 > D_2 > D_3$) is always positive (tensile) along the depth profile and increases towards the base up to approximately $420 \times 10^{-5}\,a^{-1}$ (figure 8.6). The third principal strain rate D_3 is always negative (compressive) along the depth profile with the minimum of approximately $-412 \times 10^{-5}\,a^{-1}$ at the base. This component mostly compensates D_1 ($D_1 + D_2 + D_3 = 0$, incompressibility condition for ice). The second principal strain rate D_2 is one magnitude smaller than D_1 or D_3 and reaches the maximum ($14 \times 10^{-5}\,a^{-1}$) at approximately 2400 m depth. Although relatively small, the differences between D_1 and D_3 towards the bed result in the slightly positive (tensile) component D_2. D_2 increases at approximately 1700 m depth evolving from compressional towards tensile and crosses the compressional/tensile border at approximately 2020 m depth, further intensifying its tensile nature. With depth, D_2, decreases towards zero again. Additionally, the vertical gradients of the strongest principal strain rates D_1 and D_3 are shown in figure 8.4c to highlight the onset of the evolution of changing deformation at approximately 1700 m depth.

The three-dimensional orientations of strain rate eigenvectors are presented in figure 8.7. In shallow depths, the orientation of D_3 (compressive, blue) is vertical, D_1 (tensile, red) is orientated perpendicular to the ridge, and D_2 lies parallel to the ridge (figure 8.7a). Down to approximately 1000 m depth, the overall deformation can thus be described as a classical extensional regime as expected on ice divides: extension normal to the ridge, almost no deformation, that is, very small D_2 (figure 8.6) along the ridge and vertical compression (triaxial deformation). At approximately 1000 m depth, the direction of D_3 (compressive, blue) and D_2 begin to tilt by rotation around the D_1 direction perpendicular to the ridge (figure 8.7b). At approximately 1700 m depth, D_2 starts to increase (figure 8.6, central panel), whereas its orientation continues to rotate within the ridge plane around direction of D_1. This D_2 increase describes a development from compressive towards tensile nature of this eigenvector. With this, the overall deformation mode changes from a classical divide (extensional) regime towards the basal regime (simple shear). This is also visible in the increasing obliqueness of D_3 away from the vertical (figure 8.7b versus c) and a further decreasing value of D_2 (figure 8.6). At approximately 2030 m depth, the D_2 value reaches zero per year (figure 8.6, central panel), which can be described as a confinement in this direction and thus indicates almost ideal simple shear in the non-coaxial plane strain. However, this situation only holds for a very thin depth layer, as it is caused by a transition back to triaxial deformation (general shear) with increasing D_2 towards positive, thus tensile, values (figure 8.6). D_3 (compressive) is now approximately 45° inclined (figure 8.7c). At approximately 2360 m depth, D_1 (tensile) finally rotates away from the direction perpendicular to the ridge. D_1 (tensile) rotates quickly between approximately 2370 and 2380 m depth (figure 8.7d) to a NW–SE orientation. Below this D_1 (tensile) and D_3 (compressive) the axes are both approximately 45° with the basal bedrock plane (figure 8.7e) and D_2 is now tensile, though still very small. This describes the situation as expected for bed parallel shear.

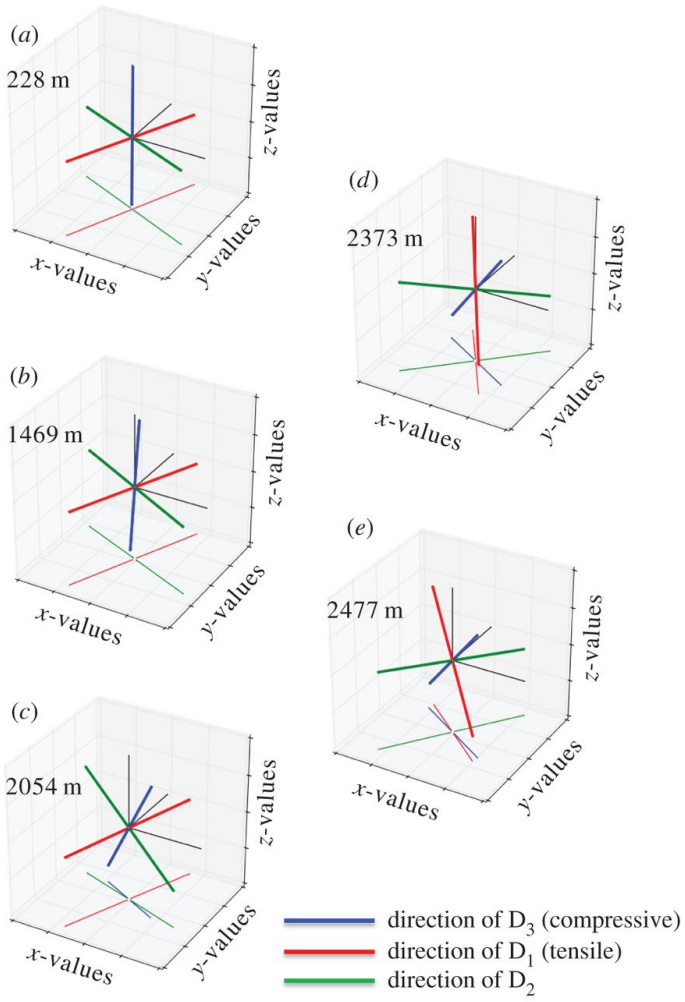

FIGURE 8.7: (a–e) Normalized strain rate eigenvectors at selected depth levels. Directions with respect to the polar stereographic projection (EPSG: 3031). The vectors are projected also to the basal plane of the coordinate system to avoid visual misinterpretation. x, east; y, north; z, up.

8.4 Discussion

The described microstructural parameters from LPO measurements, grain size and elongation distributions as well as the mesostructural characteristics from layering in the visual stratigraphy record can be interrelated in five depth regions along the EDML core. We combine these results with borehole logging observations and strain rate evolution with depth provided by numerical ice sheet modelling (PISM) from the surrounding macroscopic geometries and balances. The combined evaluation of these data shows that the structural observations can be interpreted as the effects of the transition from vertical compression with transverse extension to horizontal shear. The depth horizons are indicated as grey regions in figure 8.4. It is worth noting that the boundaries of these regions should not be understood as sharp borders in all cases. Thus, depth indications do slightly deviate, because with this multi-parameter approach slightly different reaction times of the deformation and recrystallization processes forming the observed responses may lead to slightly deviating characteristic depths.

By the chosen model spin-up, we ensure that the ice sheet geometry corresponds to the current state. This is essential for realistic strain rates at the borehole location,

as the main drivers for ice flow are local ice thickness and surface slope. However, our model set-up results in a temperature versus depth profile that deviates from the observation. Nevertheless, to the best of our knowledge, no Antarctic-wide modelling study and free evolving geometry with palaeoclimate forcing has shown to result in realistic present-day geometry as well as realistic temperature–depth profiles as observed at ice core locations. This is the subject of ongoing research (e. g. ice sheet model intercomparison project (ISMIP6) Nowicki et al., 2016).

The first panel of our central figure (figure 8.4a) shows the temperature derived from the modelling results in comparison with the temperatures measured in the borehole. The reasons for the difference between modelled and measured temperatures are threefold. First, the present-day climate forcing does not include variations in accumulation rates or surface temperatures over time. Second, the relatively smooth bedrock topography on the 10 km model grid may hinder the model to generate realistic horizontal flux divergence that influences the amount of downward advection at the EDML location. Last, without the flux correction method applied to the surface mass balance the resulting ice thickness tends to be too large at the EDML site (approx. 200 m, figure 8.2d in Nowicki et al., 2013). The correction for this (a reduced surface mass balance) causes a reduction in vertical advection which affects the shape of the temperature profile.

Although the simulated temperatures deviate from the observations, they better represent the reality than the parametrized temperature depth profile used in Seddik et al. (2008), where the temperature is assumed to be constant (approx. -43°C) down to two-thirds of the ice column and to increase linearly below that down to bed (pressure melting point). Furthermore, Seddik et al. (2008) prescribe the depth of the onset of significant shear deformation by (i) prescribing a Dansgard–Johnsen-type profile for longitudinal strain rates and (ii) the prescribed temperature profile that allows relevant shear deformation only below two-thirds of the column. Bargmann et al. (2012) followed a similar approach, but implemented the measured borehole temperatures into their one-dimensional model. However, the main aim of Bargmann et al. (2012) and Seddik et al. (2008) was to model the evolution of the ice LPO, whereas we use an isotropic model to confirm our interpretation of the observational data by considering the full three-dimensional flow field influenced by the surrounding bedrock and surface topography.

8.4.1 Region 1 (approx. uppermost 450 m)

In the upper part of the ice core, the still small strain rates do not suffice to align the c-axes, which are observed to have an almost random distribution, and to produce SPO of grains. This missing SPO with the long axis of grain elongation directions pointing to various directions in shallow depths has been similarly reported for the Dome Fuji and Dome C ice cores (Azuma et al., 1999, 2000; Wang and Azuma, 1999). Deformation of the air–ice composite material in this depth range is facilitated by the compression of bubbles. This agrees well with the expected depth for the dissociation pressure of air–clathrate hydrate at EDML and the observation of the first clathrates (Uchida et al., 2014). The compression of bubbles leads to a linear relation of bubble size with depth (Bendel et al., 2013). At first inspection, most points of the ice matrix seem to show only subtle traces of deformation (figure 8.4b,d,e,f), but higher-resolution analyses reveal that highly localized recovery and recrystallization occur already in these shallow depths (Kipfstuhl et al., 2009; Weikusat et al., 2009b, 2011). This indicates that deformation is inhomogeneous on the microscale, especially close to air bubbles (§3c and appendix B in Faria et al. (2014c)),

as predicted also by microstructural modelling (Steinbach et al., 2016). Flow model calculations yield low macroscopic strain rates (figure 8.4c), which is in accordance with the average small change with depth of borehole displacement down to 2000 m depth. The rather large wiggling of the borehole data in this upper depth range could in principle be attributed to changing rheology or temperature; however, the borehole displacement data are rather noisy as expected owing to the small surface velocity. With repeated borehole logging after 10 years, we expect more robust data with a better noise–signal relation.

Under these conditions, grain boundary migration dominates the microstructure evolution and masks the deformation habitus of grains (Llorens et al., 2016a,b). This has been observed with respect to the appearance of triple junctions (Faria and Kipfstuhl, 2005) as well as grain boundary irregularities (Weikusat et al., 2009b). Identification of deformation kinematics by the available data is therefore not possible in this depth region. A statistical analysis of bubble shape or distribution would be possible but challenging owing to the high variability. First experiences, e.g. with micro-computer tomography measurements, show that the statistical problem is significantly larger with bubble observations (Redenbach et al., 2009) than with the microstructural observation shown in this study. It can be speculated that compression owing to overburden pressure of newly accumulating snow prevails, but the observed bubbles are of round shape in the vertical and horizontal sections. The reason for the bubble behaviour is that evaporation–precipitation equilibrium processes inside air bubbles act much faster (Alley and Fitzpatrick, 1999) than the slow strain rate deformation and thus cannot notably change the bubble shape.

In this depth range, the overall deformation yields a classical extension regime as expected on ice divides: extension normal to the ridge, almost no deformation along the ridge and vertical compression (triaxial deformation; figures 6 and 7a).

8.4.2 Region 2 (approx. 450–1700 m depth)

The progressive evolution of a vertical girdle LPO (figure 8.4b) and simultaneous strengthening of grain elongation perpendicular to the LPO girdle (figure 8.5b,c) and along the horizontal plane suggest the dominance of a horizontal extension as described before by Lipenkov et al. (1989). Grain elongation directions are parallel to the horizontal, although the azimuthal orientation of the core was repeatedly lost in the brittle zone, leading to a random sample cutting direction. This indicates true horizontal elongation down to approximately 1000 m depth and thus triaxial deformation with one dominating extensional component.

Flow model calculations predict that at approximately 1000 m depth the compressive direction (D_3) starts to incline away from the vertical (figure 8.7b), which is indeed reflected in the SPO as the dip of grain elongation becomes inclined from the horizontal to several degrees (figure 8.4f), whereas the borehole was inclined by only approximately 1.5° throughout this region and below down to approximately 1700 m depth (see borehole inclination in red in figure 8.4a). The microstructure develops aspects of 'oblique foliation', typical for shear zones in quartzite rocks (Passchier and Trouw, 2005). This is caused by the principal deformation axes leaving the geographical vertical–horizontal orientation towards an inclined one, and can be interpreted as a first effect of a small shear component becoming relevant. The effects of this are still subtle, and only visible in the grain shape, without any influence on the visual stratigraphy, which remains intact (figure 8.5a).

In this region the grain size also decreases with the changing type of ice (Holocene to glacial), which has also been described for most other deep ice cores (Gow and Williamson, 1976; Herron and Langway, 1982; Lipenkov et al., 1989).

8.4.3 Region 3 (approx. 1700–2030 m depth)

The successive evolution from the vertical girdle LPO towards a vertical single maximum LPO (figures 2 and 4c) indicates a transition from dominating triaxial deformation towards horizontal shear. Flow model calculations show that D_2 starts to increase (figure 8.6) at approximately 1700 m while rotating within the ridge plane. D_2 development from compressive towards tensile (figure 8.6) and increasing obliqueness of D_3 (figure 8.7b,c) describe the change from the extensional regime typical at ice divides towards an increasing shear contribution. The transition from dominating triaxial deformation towards horizontal shear causes an increase in the dipping angle of grain elongations in vertical sections up to 10°, forming a microstructure close to the 'oblique foliation' observed in figure 8.8. This angle is well above the observed borehole inclinations, which also at this depth are less than 2° shortly after coring. This microstructure notably appears more pronounced in so-called cloudy bands with a higher impurity load. This can be interpreted as an implication for the higher influence of deformation versus recrystallization on the microstructure, owing to either strain localization or inhibited grain growth (Eichler et al., 2017). The further destabilization of the dominance of triaxial deformation produces millimetre-scale undulations in the visual stratigraphy, because the principal compression direction becomes inclined towards 45° during bed-parallel shear deformation. The successive transition depths from triaxial deformation with horizontal extension and vertical compression to shear deformation suggested by these structural observations are in accordance with predictions by the flow model. Model predictions show a decreasing compressive component (D_3) at approximately 1700 m depth (cf. vertical derivatives in figure 8.4c), whereas the tensile component D_1 remains approximately constant. This deviating evolution of D_1 and D_3 is clearly represented by the increasing D_2 , which develops from slightly compressional towards extensional behaviour in this depth region (figure 8.6). The low strain rate is also reflected by the upper part of the borehole (down to approx. 2030 m), as observed in January 2004 being hardly tilted until November 2005.

At the transition from region 3 to region 4 at approximately 2030 m depth, model predictions suggest plane strain deformation as almost ideal simple shear with D_2 being zero per year (figure 8.6).

8.4.4 Region 4 (approx. 2030–2385 m depth)

The single maximum LPO along the vertical core axis is fully developed after a sudden final collapse of the girdle between 2035 and 2045 m. This sudden change in the LPO was also detected as a clear reflector in radio-echo sounding (RES) data, which is caused by the dependence of the electromagnetic wave velocity from the crystallographic orientation (Diez and Eisen, 2015; Diez et al., 2015; Eisen et al., 2007). Grain elongation direction histograms derived from vertical sections (figure 8.5b left) show a broad, but distinct distribution (cone angle of 45°) with a slight tendency towards double/multiple maxima. This can be interpreted as grains being partly elongated perpendicular to the main compression direction in shear, thus lining up in the instantaneous stretching direction (Passchier and Trouw, 2005), and grains partly being further rotated towards the shear plane (Llorens et al., 2016a,b). These multiple

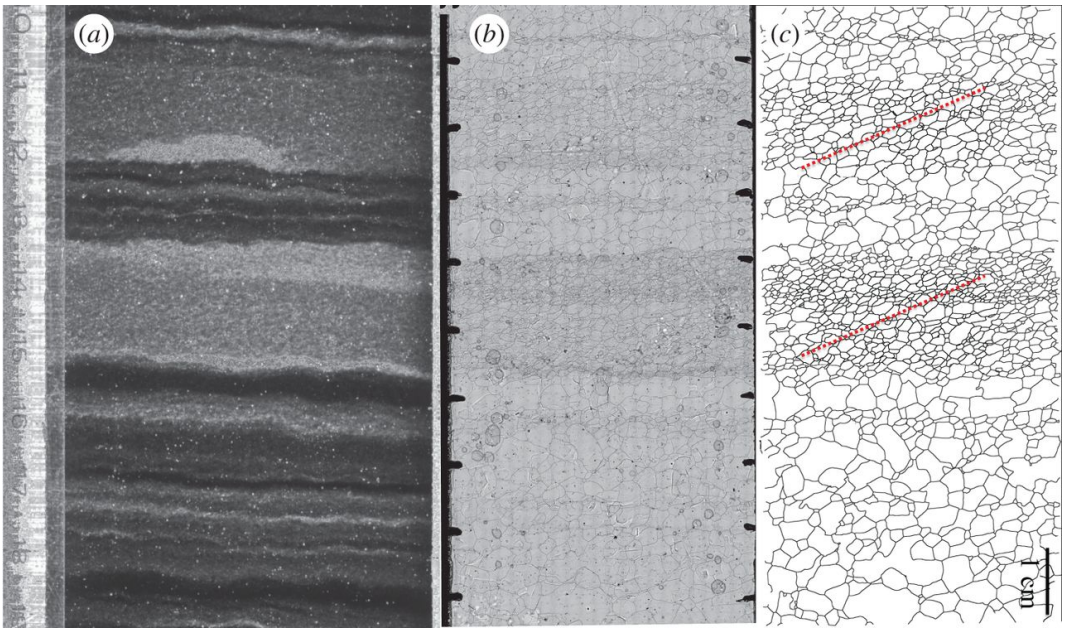

FIGURE 8.8: Example 'oblique foliation' characterized by inclined, elongated grains in ice (1785.0–1785.1 m depth). (a) Visual stratigraphy section. (b) Corresponding sublimation etched surface microstructure map. (c) Resulting segmented grain boundary network with the approximate inclination of maximum obliqueness sketched (dotted red line) in cloudy bands. Note that the measurement data of this obliqueness given in figure 8.4f average over the whole 10 cm section, which results in a smaller value. (Online version in colour.)

maxima in the SPO description should not be confused with multiple maxima in the LPO. Elongation of grains is caused by deformation. Nucleation usually serves as an explanation for the multiple maxima of LPO, but does not induce grain elongation. In this region, the overall deformation changes again to triaxial deformation (general shear) with increasing D_2 (figure 8.6). The principal compressive direction (D_3) is now approximately 45° inclined. The increasing component of bed-parallel shear readily causes millimetre-scale z-folding by amplifying small undulations, which leads to local tilting of stratigraphic layers ($10 - 45°$). RES reflectors fade out in this depth ('echo-free zone') owing to the loss of layer coherency (Drews et al., 2009) caused by the intensely disturbing flow characteristic for bed-parallel shear deformation (Wang et al., 2002).

The bottom layer of region 4 (approx. 2365–2385 m depth) is characterized by the lower border of the Eemian ice (MIS5.5) layer at approximately 2360–2390 m depth (figure 8.4d). However, being approximately 400 m above bedrock, this layer is nearly at the same altitude as the bedrock heights just downstream of EDML, as depicted in figure 8.1: the EDML site lies on a region at approximately 100 m a. s. l. bedrock altitude, whereas the bedrock approximately 50 km downstream elevates to approximately 500 m a. s. l., so that the ice in this depth flows against it. This may have an effect upstream as the ice has to flow around this. The abrupt jump to smaller grain sizes (figure 8.4d) at this transition is classically explained by impurity influence on grain size (Alley and Woods, 1996; Alley et al., 1986a; Durand et al., 2006a; Paterson, 1991; Weikusat et al., 2013c), which is confirmed by the correlation coefficients of grain size with isotope measurements (Lambert et al., 2007). Just above the depth of the sudden changes in grain size and shape, we observe a high variability in the fabric data over short depth intervals. In a layer of less than 20 m thickness around 2375 m depth, multiple maxima LPO and girdle LPO

occur with strong variations in neighbouring samples. As the ice is of interglacial origin with low impurity content at this depth, we observe large grain sizes, which in turn raises questions about the statistical significance of LPO measurements and LPO eigenvalue calculations. However, the variations in different types of ice (δ^{18}O taken as the 'proxy' for ice types) in some layers seem to allow grain size to increase locally. The difference in these ice types is characterized by varying impurity concentrations. We use a 'proxy' for the ice types however, because picking one impurity is not meaningful with our current knowledge. This may be due to the combined effects of several impurities, as suggested by Fitzpatrick et al. (2014). Impurities and their effect on grain size is often explained by the 'slowdown' or ineffectiveness of grain boundary migration by changing the grain boundary mobility (Alley et al., 1986a; Paterson, 1991). This phenomenon acts on the microstructural scale (grain and subgrain scale), whereas good correlations are well known on larger scales only (e.g. our grain size–ice-type 'proxy' correlation with δ^{18}O). Direct microstructural evidence on the microstructural scale, such as impurity accumulation along grain boundaries, is difficult to prove (Barnes, 2003; Della Lunga et al., 2014). This effectively changes the deformation–recrystallization balance under increasing strain rate (Llorens et al., 2016a,b; Weikusat et al., 2009a). The step in grain elongation magnitude (figure 8.4e) suggests an increased influence of deformation on grain topology moving the microstructure from a recrystallization dominated one towards a deformation microstructure (see a comparison of end members in figure 2 in Llorens et al., 2016b). Furthermore, although the ice is mainly clear, we see some isolated cloudy bands that are strongly folded, which is an effect of the very strong shear deformation. The characteristic deformation microstructure and strong folding of cloudy bands suggest an alternative hypothesis: localized strain in certain layers. This is in accordance with the macroscopic deformation setting, which predicts an increased strain rate at that depth by the model (figure 8.4c) as well as a qualitative observation of a closing borehole (Wilhelms et al., 2014). To assess this hypothesis, further detailed studies on the processes of ice interacting with impurities are needed.

The boundary zone between regions 4 and 5 at approximately 2380 m depth is to some extent a remarkable layer with respect to the overall deformation predicted by the model: the principal tensile direction (D_1) has left the direction perpendicular to the ridge and rotates very quickly to an along-ridge orientation (figure 8.7d).

8.4.5 Region 5 (greater than approx. 2385 m depth)

The top of region 5 (approx. 2385–2405 m depth) is characterized by its stratigraphy, which is well defined, ordered and seemingly straight. This is slightly surprising in contrast to the significantly disturbed layers just above. However, we also observe small but sudden changes in the layer inclination and flattened z-fold that may suggest that folding has occurred in the past or on other scales which are difficult to evaluate from ice core information. Possible changes of the predominant deformation mechanism showing microshear deformation have been interpreted from striking microstructure observations (slanted brick wall pattern Faria et al., 2006; Faria et al., 2009). This is in accordance with the extremely high grain shape values in figures 8.4e,f and 8.5b. In spite of the high in situ temperature (figure 8.4a) around -10°C, the grain size in the depth range 2385–2450 m does not increase, possibly owing to the high impurity content and shear rate, but increases to very large sizes below 2500 m depth.

Only below approximately 2405 m depth, we observe strong kink folding of the stratigraphic layers, which is a clear indication for high shear rates in recent times.

The single maximum LPO slightly inclined from the vertical (figure 8.2) observed in this narrow transition zone and extreme grain elongations up to aspect ratios of 1.8 (figure 8.4e) are also indicative for high shear rates. Shear shows stronger effects on microstructure as under higher strain rates the balance between deformation-induced and recrystallization-induced effects is changing significantly in favour of deformation (figure 8.4c).

The bottom of region 4 as well as the top of region 5 represent a very interesting, but complex, boundary zone. We want to emphasize the ambiguous depth of this boundary, in the sense that different parameters differ strongly in the zone between region 4 and region 5: (i) the LPO changes and shows anomalous behaviour between 2365 and 2380 m depth, (ii) grain shapes elongate suddenly between 2385 and 2395 m depth, (iii) grain sizes change at the lower Eemian layer border (2356–2386 m depth) and show (iv) grain growth only from 2520 m depth again, and stratigraphy shows anomalous straight banding between 2385 and 2405 m depth. The processes and predominating deformation regimes in this region are not yet understood as they are strongly punctuated and probably catalysed by strong changes in material properties owing to different impurity contents in glacial–interglacial–glacial ice layering. Further investigations on impurity effects on rheology and microstructure are needed.

In the flow model, in region 5, tensile and compressive axes are both at approximately 45° with respect to the bedrock, with a small tensile component D_2 (figure 8.6), as expected for bed-parallel simple shear.

At this point, it has to be emphasized again that the slight depth deviations of the region borders in different parameters are probably owing to slightly different reaction times and feedback loops of the processes forming the responses by changing the material in the micro- and mesostructure.

8.5 Conclusion

Detailed observational data from the ice core micro- and mesostructure can be interpreted to constrain the main deformation modes (e.g. compression versus shear) along the ice column. We use an isotropic model to confirm this interpretation by considering the overall three-dimensional flow field driven by ice sheet geometry. By combining several parameters from SPO and LPO, we find indications for the deformation and recrystallization processes being active at the EDML site. We show that it is the balance of both which determines microstructure and possibly flow behaviour.

Recent microstructural modelling studies (Llorens et al., 2016a,b, 2017) combined deformation by a viscoplastic full-field approach (taking strong crystal anisotropy into account Lebensohn, 2001) with recrystallization (dynamic and static, continuous and discontinuous Bons et al., 2008). These simulations suggested that the effect of recrystallization on the LPO should be minor. The model set-ups have been chosen for comparison with clean and cold polar ice, where, for example, nucleation is supposedly rare. Notwithstanding, under certain conditions, such as high debris load or high temperatures, effects of discontinuous recrystallization can occur (Samyn et al., 2008). Observations of recrystallization effects on LPOs in ice cores, however, often suffer from poor statistics, because they are limited to the lowest layers, typically characterized by very large grains (Faria et al., 2014a and references therein). As mainly unimodal or girdle LPO occurs at EDML, i.e. only a narrow layer (bottom layer of region 4) with multi-maxima LPOs has been observed, we

suggest that the LPO at EDML is affected mainly by deformation, and thus the transition between the regions described above appears most clearly in the LPO fabric data. In contrast, grain shape data show rather subtle deformation trends, as they are strongly overprinted by recrystallization. These subtle trends are, however, consistent with the interpreted deformation modes from LPO.

Impurities can have an impact on the balance between deformation- and recrystallization- induced changes in grain topology. Impurities are postulated to affect recrystallization, by slowing down grain boundary migration through pinning or dragging, and deformation itself by providing dislocation sources. Polar ice is always at a high homologous temperature ($\gg 0.7\,T_m$), which leads to high recrystallization activity through rotation recrystallization and strain-induced grain boundary migration recrystallization.

Evaluation of the LPO, grain elongation distributions and visual stratigraphy leads to a division into five distinct regions along the core. Here the results are interpreted as the effects of triaxial deformation with horizontal extension changing towards bedrock-parallel shear. This is in good agreement with modelled strain rate trends as well as borehole deformation observations.

Down to approximately 1000 m depth, triaxial deformation with vertical compression and horizontal extension clearly dominates. The influence of shear on the grain structure and fabric starts at approximately 1000 m depth and becomes more prominent between 1700 and 2030 m depth, intriguingly observable in the smooth transition between girdle and single maximum LPO and in the borehole geometry. A final collapse of the eigenvalues in a narrow zone between approximately 2030 and 2050 m depth marks the transition to bed-parallel shear. Shear is the dominating deformation down to the base, but is interrupted by a narrow layer with changing conditions, with abnormal LPO leading into a region of high shear activity, with extreme values in grain shapes.

Owing to relatively small strain rates at the drilling location on the ice divide, only subtle changes in SPO can be observed at EDML, but we suggest including these analyses in future ice core studies especially in mechanically more active regions such as the forthcoming East Greenland ice core project. These analyses can help to assess the share of ice deformation and basal sliding with respect to transport of ice towards the ocean.

Competing interests

The authors declare that there are no competing interests.

Funding

This research was funded by HGF grant no. VH-NG-802 to D.J. and I.W., as well as SPP 1158 DFG grant no. BO 1776/12-1 to I.W. S.H.F. acknowledges financial support from the Ramón y Cajal Research Grant RYC-2012-12167 of the Ministry of Economy and Competitiveness of Spain.

Acknowledgements

We thank the scientific editors and one anonymous referee for suggestions. We thank Denis Samyn for a thorough review. We thank Hanno Meyer and Hans Oerter (personal communication, May 2016) for providing the unpublished dataset of water stable isotope measurements δ^{18}O below 2416 m depth. We thank David Russel-Head

for his patient support concerning the fabric analysers. This work is a contribution to the European Project for Ice Coring in Antarctica (EPICA), a joint European Science Foundation/European Commission scientific programme, funded by the EU (EPICA-MIS) and by national contributions from Belgium, Denmark, France, Germany, Italy, the Netherlands, Norway, Sweden, Switzerland and the UK. The main logistic support was provided by IPEV and PNRA (at Dome C) and AWI (at Dronning Maud Land).

Chapter 9

Paper V

Short-scale variations in high-resolution crystal-preferred orientation data in an alpine ice core – do we need a new statistical approach?

Johanna Kerch [1,2], Olaf Eisen [1,3], Jan Eichler [1,5], Tobias Binder [1], Johannes Freitag [1], Pascal Bohleber [2,4], Paul D. Bons [1], and Ilka Weikusat [1,5]

[1] Alfred Wegener Institute Helmholtz Centre for Polar and Marine Research, 27568 Bremerhaven, Germany
[2] Institute of Environmental Physics, Heidelberg University, 69120 Heidelberg, Germany
[3] Department of Geosciences, University of Bremen, Bremen, Germany
[4] Institute for Interdisciplinary Mountain Research, Austrian Academy of Sciences, Innsbruck, Austria
[5] Department of Geosciences, Eberhard-Karls-University Tübingen, 72074 Tübingen, Germany

Submitted to *Journal of Geophysical Research*, 7 March 2019.

Abstract

We analysed crystal-preferred orientation of c-axis and microstructure data from the Alpine ice core KCC at an unprecedented resolution and coverage of any Alpine ice core. We find that an anisotropic single-maximum fabric develops as early as 25 m depth in firn under vertical compression and strengthens under simple shear conditions towards the bedrock at 72 m depth. The analysis of continuously measured intervals with subsequent thin section samples from several depths of the ice core reveals a high spatial variability in the crystal orientation and crystal size on the 10 cm-scale as well as within a few centimetres. We quantify the variability and investigate the possible causes and links to other microstructural properties. Our findings support the hypothesis that the observed variability is a consequence of strain localisation on small spatial scales with influence on fabric and microstructure. From a methodological perspective, the results of this study lead us to challenge whether single thin sections from ice cores provide representative parameters for their depth to be used to infer the fabric development in a glacier on the large scale. Previously proposed uncertainty estimates for fabric and grain size parameters do not capture the observed variability. This might therefore demand a new statistical approach.

9.1 Introduction

One of the foremost goals of contemporary glaciological research is to advance our understanding of the internal deformation of glaciers and ice sheets to better constrain the dynamic components of modelled projections of their development under changing climate conditions. To this end, the physical properties of polycrystalline glacier ice have been studied on a number of deep ice cores from the polar regions for more than 40 years, as reviewed in Faria et al., 2014b. The analysis of crystal-preferred orientation (CPO, fabric) and microstructure (μS) on ice core samples provides evidence to draw conclusions on dominant deformation and recrystallisation (RX) regimes at different depths in the ice column (Weikusat et al., 2017b), and may also be of importance for the interpretation of climate records (Faria et al., 2010; Kennedy et al., 2013). To clarify the terminology in this study, *microstructure* includes the shape and size of grains, grain boundaries (GBs), bubbles and other spatial features in ice, while *fabric* is only used for crystallographic orientation of crystals.

The inherent plastic anisotropy of individual ice crystals (Duval et al., 1983) leads to their alignment in preferred orientations under the local stress conditions along the flow path (Azuma and Higashi, 1985). Dynamic recrystallisation occurs as a consequence of the accumulated strain energy (Llorens et al., 2017; Schulson and Duval, 2009), and the presence of pore space and impurities contribute to the complex development of fabric and microstructure (Azuma et al., 2012; Durand et al., 2006b; Eichler et al., 2017; Steinbach et al., 2016). As a result of these inter-dependent micro-scale processes, the viscous behaviour of the ice bulk is changing, which, in turn, can lead to an enhancing feedback on the deformation (Azuma and Goto-Azuma, 1996). To establish a thorough understanding of how dynamic processes on the micro-scale, recorded as a temporal snapshot in ice-core data, are connected with the observations on the macro-scale, remains a major challenge in the study of ice-physical properties (Eisen et al., 2007).

While it has repeatedly been demonstrated that it is essential to include the crystal anisotropy into ice flow models (Graham et al., 2018; Martin et al., 2009; Pettit et al., 2007; Seddik et al., 2008), it is difficult to obtain the necessary amount of data from an ice core which is representative for the CPO development in the vertical dimension, while the sampling in the horizontal dimension is, in any case, limited to the cross-section of the core. In fact, it is currently not constrained how much ice-core data can be considered as representative. Due to the time-consuming nature of fabric studies, sampling for this purpose is typically in the order of one sample per tens of metres of ice core. Sampling is thus at a very low resolution with much less than a few per cent of the core analysed. (appendix 9.7, Table 9.4). Despite this, the results are assumed to reflect the general fabric evolution in the ice column. However, some studies report the observation of small-scale features like fine-grained layers in the microstructure and sudden spatial changes between distinct fabric patterns on a resolution of about 15 m (DiPrinzio et al., 2005; Fitzpatrick et al., 2014; Jansen et al., 2016; Montagnat et al., 2014). It stands to question if these structures are common to most ice cores, potentially (1) distorting the perceived representation from low-resolution ice-core fabric studies, and (2) disregarding information on deformation processes on smaller scales.

Only a few studies are focused on the fabric of non-polar (e.g. alpine or sub-polar) glacier ice, with most of them being older than 30 years and/or from temperate glaciers (Table 9.1; see also the review paper from Hudleston, 2015). While the measurement techniques were certainly less sophisticated in the past, and these

thus provided statistically less representative data sets, it was reported that samples from nearby locations (within a few metres) showed distinctly different fabric (Kamb, 1959; Rigsby, 1951) and bands with small crystals and single-maximum fabrics were observed in an ice core (Vallon et al., 1976). Non-polar glaciers offer the opportunity to study glaciological processes that can be assumed to follow the same physical laws as in polar regions, on a smaller spatial scale and a more constrained temporal scale, providing upper limits for the duration of microstructural processes. The ice temperature is generally higher compared to the non-basal parts of polar ice sheets and often similar to the temperatures encountered at the base of polar ice sheets, approaching the pressure-melting point, where temperature-driven microstructural processes may be enhanced (Faria et al., 2014a). They can thus serve as in-situ or natural laboratories with deformation conditions that are not feasible in laboratory experiments and several orders closer to those in polar ice sheets. However, the majority of non-polar ice cores from the last 30 years were analysed with a climatological focus (e.g. Bohleber et al., 2013; Preunkert et al., 2000; Schwikowski et al., 1999; Thompson et al., 2006). Only recently, some low-resolution fabric data from an ice core drilled in 1992 on the Tibetan Plateau (Thompson et al., 1995) were reported and compared to polar fabric data (Li et al., 2017).

The cold high-Alpine glacier Colle Gnifetti (CG) has long been the subject of extensive glaciological research, with a focus on its archive of midlatitude climate (Wagenbach et al., 2012). In the present study we provide the first comprehensive fabric analysis on this Alpine glacier, obtained from a recent ice core. For the first time, we systematically analyse the variability of fabric on a scale of centimetres to decimetres within continuously analysed depth intervals.

While the crystallographic evolution is the main focus of the study, other physical properties and microstructural parameters (grain size, density, bubbles) are considered for the benefit of discussing the context of physical processes that could influence the fabric development at Colle Gnifetti. Following the findings of our study, we discuss the significance of defining a representative scale length for fabric studies.

9.2 Study site

The high-Alpine glacier Colle Gnifetti, Monte Rosa Massif, on the border between Switzerland and Italy, is characterised by a high spatio-temporal variability in net snow accumulation which is primarily a result of insolation-driven snow consolidation counteracting the effect of wind erosion (Wagenbach et al., 1988). On average, net snow accumulation is mainly made up by precipitation during the warm seasons, with a minor but highly variable contribution by winter snow. The average net accumulation rate at KCC was determined around 22 cm water equivalent per year (Bohleber et al., 2018).

The ice core KCC was drilled to bedrock in 2013 (N 45°55.736, E 7°52.576, 4484 m a.s.l., Bohleber et al., 2018) in about 100 m distance to the ice core KCI, drilled in 2005 (Bohleber et al., 2013), on a flank towards an ice cliff. KCC is 72 m long and the firn-ice transition was found to be at a depth of about 36 m. A borehole temperature between $-13.6\,°C$ in 13 m depth and $-12.4\,°C$ at the bedrock was measured in 2014 (Hoelzle et al., 2011, no change since 2011, pers. comm. M. Hoelzle, University of Fribourg, 2014), implying that the ice is frozen to bedrock. Radiocarbon dating revealed a basal ice age of $\sim$4000 years BP from the ice core sections at bedrock (Hoffmann et al., 2017). Therefore, we can assume that ice from different depths of

TABLE 9.1: Early and more recent crystallographic studies on non-polar or subpolar glaciers. We would like to mention current projects involving crystal-orientation measurements on temperate and polythermal ice on Rhone Glacier, Switzerland (Hellmann et al., 2018) and Storglaciären, Sweden (Monz and Hudleston, 2018), and Jarvis Glacier, Alaska (Gerbi et al., 2018). *Section* refers to a thin section sample.

Authors	Region	Type & Temperature	Fabric resolution; sample description
Rigsby, 1951	Emmons glacier, Mt. Rainier, Washington, USA	Mountain and valley glacier, temperate	11 surface locations, stagnant and fast flowing ice; $\sim$40 sections with 1725 crystals
Meier et al., 1954	Saskatchewan Glacier, Alberta, Canada	Valley glacier, temperate	8 surface locations
Rigsby, 1960	Emmons, Saskatchewan and Malaspina Glacier, Alaska, USA; Moltke Glacier and Nunatarssuak Ice Ramp, Thule, Greenland	3 temperate, 2 polar sites	surface locations, 8000 crystals
Kamb, 1959, Allen et al., 1960	Lower Blue Glacier, Washington, USA	Valley glacier, ablation zone, temperate	9 surface locations, 144 sections
Taylor, 1963	Burroughs Glacier, Alaska	Ablation zone, temperate	2 surface locations
Higashi, 1967	Mendenhall Glacier, Alaska	Temperate	30 samples
Jonsson, 1970	Isfallsglaciären (and Storglaciären), Sweden	Small valley glacier, ablation zone, polythermal	9 locations at glacier base (tunnel), oriented ice blocks, 81 sections
Hooke, 1973	Barnes ice cap, Baffin Island, Canada	Ice cap margin, cold ($-10\,^{\circ}$C)	4 shallow ice cores and surface locations; 18 sampling sites in intervals of $\sim$5–10 m
Vallon et al., 1976	Vallée Blanche, Mt. Blanc, France	Valley glacier, accumulation zone, 3550 m a.s.l., temperate	Ice core (30 m firn and 150 m ice); ca. 50 sections in intervals of $\sim$10 m
Hudleston, 1980	Barnes ice cap, Baffin Island, Canada		
Tison and Hubbard, 2000	Glacier de Tsanfleuron, Switzerland	Plateau glacier, 2400–2900 m a.s.l., temperate	8 ice cores (along-flow transect), 5 in the ablation zone, 3 in the accumulation zone without reaching bedrock, 170 m in total; 348 sections with 3000 crystals
Li et al., 2017	Guliya ice cap, Tibetan Plateau	Ice cap, 6200 m a.s.l., cold ($-2\,^{\circ}$C)	Ice core, 309 m to bedrock; sampled $\sim$1 % in intervals of $\sim$10 m
This study	**Colle Gnifetti, Switzerland/Italy**	**Mountain glacier, 4484 m a.s.l., cold (below $-10\,^{\circ}$C)**	**92 sections from 72 m ice core, 12% of glacier thickness sampled, $\sim$67000 crystals**

The most prominent studies showing fabric diagrams and giving microstructural quantities that could be found (and were accessible) in peer-reviewed literature in English are summarised here. We do not claim that this table is complete.

the core has experienced quite a different deformation history despite the ice core's short length. Surface velocities at Colle Gnifetti were last measured from 2014 to 2016 and were of the order of 1 m a^{-1} close to the KCC borehole (Licciulli, 2018).

9.3 Laboratory measurements and processing

The ice core was stored at −18 °C during transport and at −30 °C before and after processing. Vertical thin sections (33 × 100 mm^2, ca. 300 μm thick) of the ice core were prepared with a standard microtoming procedure in 13 intervals between 25 m and 72 m depth. Over each interval they provide continuous records of up to 110 cm length in depth. *Continuous* refers to measurements of several adjacent sections in an ice core segment or bag. The azimuthal orientation of the sections may vary due to deliberate rotation of core segments during processing, which was noted and considered in the analysis, or accidental loss of orientation information during core logging. Crystallographic c-axis orientations were measured by means of polarised light microscopy (e.g. Heilbronner and Barrett, 2014; Peternell et al., 2009; Wilson et al., 2003) with an automatic fabric analyser from Russell-Head Instruments (FA, model G50). Additionally, microstructural maps (Kipfstuhl et al., 2006) were acquired with a Large Area Scanning Macroscope (LASM, Schäfter+Kirchhoff, Binder et al., 2013) from the same section surface to obtain supporting information on pore space and grain boundaries. The KCC fabric data consist of 92 vertical thin sections and samples 12 % of the entire ice core.

For each pixel of the thin section the measurement provides the orientation of the crystallographic c-axis by two angles, azimuth ϑ in the interval $[0, 2\pi]$ and colatitude φ in the interval $[0, \pi/2]$, with respect to the (nearly) vertical ice-core axis. The c-axis is expressed as a vector $\vec{c}$ with unit length:

$$\vec{c}(\vartheta, \varphi) = (\sin(\varphi)\cos(\vartheta), \sin(\varphi)\sin(\vartheta), \cos(\varphi)). \tag{9.1}$$

The obtained FA data are processed using the open-source software `cAxes` developed at AWI (Eichler, 2013) for automatic pixel-wise image analysis, excluding pixels with quality below 50 % (Peternell et al., 2009) and setting a lower grain size threshold of $A_{\min} = 0.2\,\text{mm}^2$ (constrained by the section thickness $>$ 200 µm).

Eigenvalues λ_i ($i = 1, 2, 3$; $\lambda_1 \leq \lambda_2 \leq \lambda_3$; $\sum \lambda_i = 1$) of the second-order orientation tensor $a_{ij}^{(2)}$ are calculated from the c-axis distribution of a thin section sample (Adam, 1989; Durand et al., 2006a; Wallbrecher, 1986) and are weighted with the grains' cross-section area A as proposed and discussed by Gagliardini et al., 2004. These are standard parameters to classify the type and strength of the crystallographic-preferred orientation and can be associated with different deformation regimes e.g. Weikusat et al., 2017b. We can calculate a statistical uncertainty for the eigenvalues σ_λ depending on the sample size of the crystal ensemble N_g following Durand et al., 2006a:

$$\sigma_\lambda = (-1.64\lambda^2 + 1.86\lambda - 0.14) N_g^{-1/2}. \tag{9.2}$$

We remark that this equation will not give a positive uncertainty estimate below $\lambda = 0.081$. The uncertainty σ_A, which accounts for sectioning and population effects when calculating the mean grain size $\bar{A}$ as determined from the number of pixels per grain in a 2-D section, is estimated by

$$\sigma_A = 2\bar{A}(0.02 + 0.44\, N_g^{-1/2}). \tag{9.3}$$

However, this uncertainty is based on the assumption of regular grain features during normal grain growth (Anderson et al., 1989; Durand et al., 2006a) which can no longer be assumed to be the dominant process as soon as RX processes set in (Faria et al., 2014a). The measurement uncertainty associated with the FA instrument was

shown to be small enough to be neglected compared to the sampling uncertainty (Montagnat et al., 2012).
For the centimetre-scale analysis along the measured core segments we apply a sliding window frame of 2 cm height and 2 mm step size for the calculation of second-order orientation tensor eigenvalues and mean grain size. The median number of grains per window with area $33 \times 20\,\mathrm{mm}^2$ is 143 with an interquartile range of $90 - 217$.

Additionally, the high-resolution density profile for the upper 50 m of the ice core was determined by evaluating 2D projected X-ray computer tomography images (XCT, Freitag et al., 2004). Visual stratigraphy images (Svensson et al., 2005) were recorded over the full length and qualitatively analysed with focus on the visibility of well-defined layers and layer inclination. The number density and size of closed-off bubbles in the ice was determined from the LASM images using the open-source software `ImageJ`. The records of dust-related impurities and stable water isotopes presented in Bohleber et al., 2018 were available for comparison with the crystal data (more extensively discussed in Kerch, 2016).

9.4 Results

9.4.1 Physical properties profile

We present the comprehensive data set from a classical thin section-scale fabric analysis, but from continuously measured intervals instead of just one thin section sample per interval. Figure 9.1 shows the depth profile of area-weighted second-order orientation tensor eigenvalues for KCC, the mean and maximum grain size per section and the high-resolution density from XCT. The uncertainties are calculated with Eq. 9.2 and 9.3. Additionally, the standard deviation of the grain size distribution is indicated towards higher grain sizes. Schmidt diagrams for individual thin sections are shown in appendix 9.7, Fig. 9.6.

The data reveal how a distinct anisotropy of c-axes evolves with depth. A weakly anisotropic fabric can already be observed in the firn. The crystal anisotropy quickly increases across the firn-ice transition down to 53 m, developing a broad single-maximum fabric. In the lower 20 m of the core a small portion of grains are forming a weak girdle pattern in combination with narrowing of the strong single maximum, with a minimum spherical aperture (cone angle) of 9° at the bedrock, and increasingly inclined to the vertical, with a maximum inclination angle of the c-axis eigenvector at bedrock of 27°.
Remarkable is the high variability of eigenvalues within continuously measured intervals, at all depths of the ice core, with the exception of the deepest 70 cm long interval close to bedrock. This variability exceeds the estimated population-dependent uncertainty and does not show a discernible trend. In the following, the c-axis eigenvalue $\lambda_3 e$ is considered as a single parameter to further investigate the small-scale fabric variability, as single-maximum fabric is recognised as the dominant fabric type. Table 9.2 lists the average c-axis eigenvalue and difference between extreme values for each interval. The difference exceeds 0.1 in most intervals.

The mean grain size $\bar{A}$ lies between $1\,\mathrm{mm}^2$ and $18\,\mathrm{mm}^2$ calculated from $155 - 1707$ grains per section, with 75 % of the entire grain population smaller than $8\,\mathrm{mm}^2$. Note that for most sections 75 % of all grains are smaller than the calculated mean grain size. The grain size tends to increase from the firn towards a depth of approximately 48 m and subsequently shows a sharp decrease in the interval near the bedrock. However, the variability in mean grain size within an interval increases, in

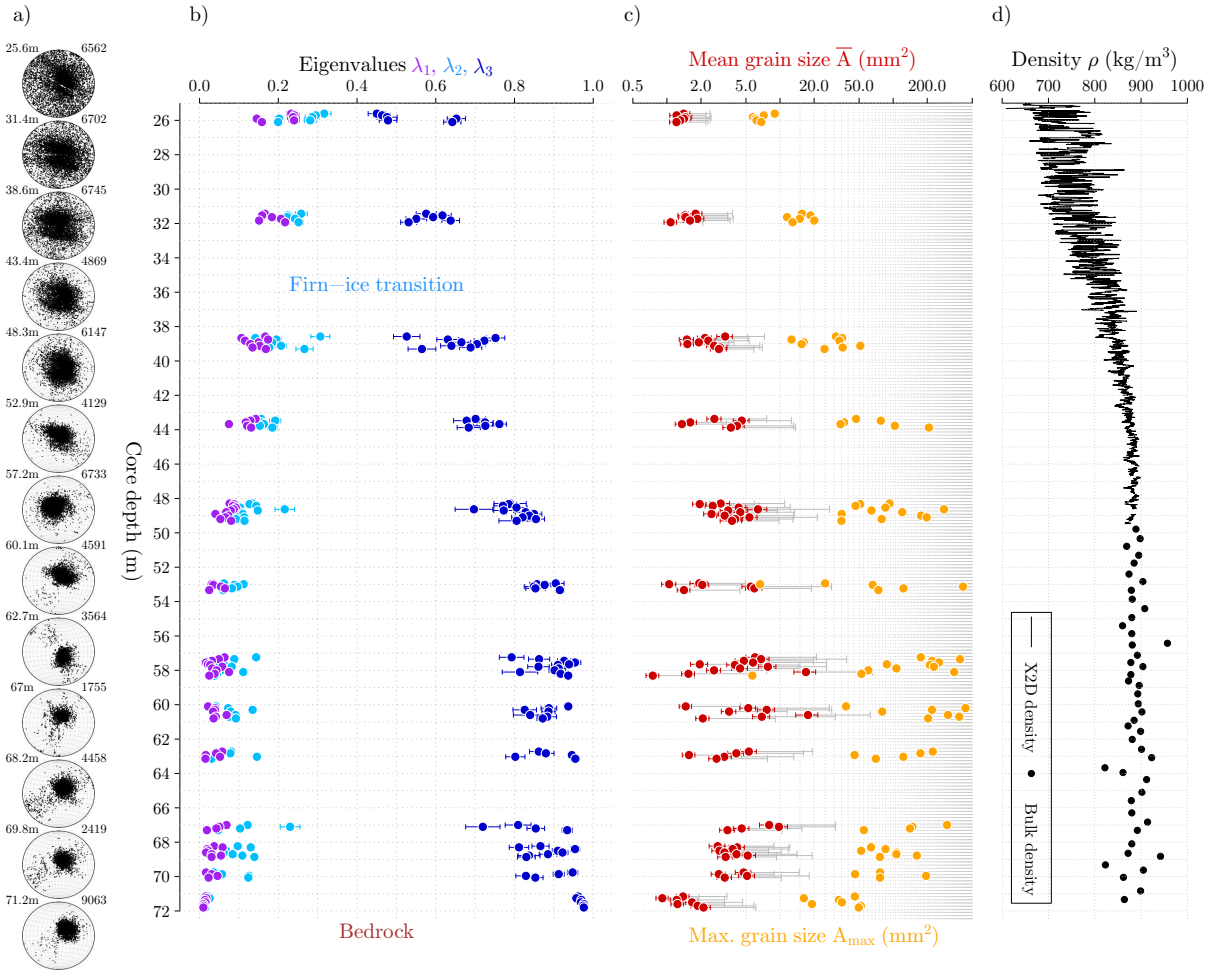

FIGURE 9.1: Evolution of a) c-axis distributions, b) c-axis orientation tensor eigenvalues (area-weighted), c) grain sizes and d) density with depth. Uncertainties $2\sigma_\lambda$ (blue) and $2\sigma_A$ (red) are calculated with Eq. 9.2 and 9.3. The standard deviation of the mean grain size (red) is additionally shown as grey whiskers (on a logarithmic scale). The maximum grain size is shown in orange. C-axis distributions are presented per continuously measured interval (Schmidt diagrams with the centre corresponding to the ice core axis). Each dot represents a single grain as identified from the thin section data. The top depth and number of grains are indicated on the top left/right of each pole figure. The azimuthal orientation of the Schmidt diagrams varies but could not be further constrained.

conjunction with a strong increase in the maximum grain size A_{max} up to 4 cm^2 in 48 – 68 m depth. The calculated uncertainty associated with the sectioning and population effect for calculating the mean grain size is much lower than the standard deviation.

9.4.2 Visual stratigraphy

We identify six depth zones in which the characterisation of the visual stratigraphy changes (Table 9.3, Fig. 9.8), considering the contrast between and the thickness of alternating lighter and darker bands in the visual stratigraphy linescan images. For most of the core a stratigraphic order can be observed, which, however, cannot be discerned in the images in the bottom 5 m. The layer inclination varies strongly in the firn and increases towards bedrock in the ice with maximum values of 30°. As we do not know the orientation of the ice core (and thus that of the image plane) with

TABLE 9.2: Mean c-axis eigenvalues $\bar{\lambda}_3$ with standard deviation and variability for each interval (indicated by top depth and length) of continuous measurements, calculated on the thin section (Fig. 9.1) and cm-scale (Fig. 9.3).

Top depth (m)	Length (m)	Mean c-axis eigenvalue $\bar{\lambda}_3$ (thin section-scale)	Variability $\lambda_{3,\max} - \lambda_{3,\min}$ (thin section-scale)	Mean c-axis eigenvalue $\bar{\lambda}_3$ (cm-scale)	Variability $\lambda_{3,\max} - \lambda_{3,\min}$ (cm-scale)
25.61	0.59	0.53 ± 0.09	0.2	0.54 ± 0.12	0.48
31.43	0.6	0.58 ± 0.04	0.11	0.6 ± 0.06	0.31
38.58	0.79	0.66 ± 0.07	0.23	0.67 ± 0.08	0.4
43.37	0.6	0.71 ± 0.03	0.08	0.72 ± 0.06	0.25
48.3	1.04	0.8 ± 0.04	0.16	0.81 ± 0.07	0.34
52.94	0.49	0.88 ± 0.03	0.07	0.87 ± 0.04	0.19
57.24	1.14	0.89 ± 0.05	0.16	0.9 ± 0.05	0.21
60.1	0.8	0.88 ± 0.04	0.11	0.9 ± 0.05	0.21
62.73	0.51	0.89 ± 0.06	0.15	0.9 ± 0.07	0.3
67	0.4	0.83 ± 0.09	0.21	0.85 ± 0.10	0.45
68.23	0.72	0.88 ± 0.05	0.14	0.89 ± 0.06	0.25
69.76	0.4	0.89 ± 0.05	0.12	0.89 ± 0.05	0.17
71.16	0.71	0.97 ± 0.01	0.02	0.96 ± 0.01	0.05

TABLE 9.3: Observations from visual stratigraphy line scan images (Fig. 9.8). Several zones are identified by changes in the qualitative description; changes in inclination occur in slightly different depth zones. Inclination is counted from the horizontal perpendicular to the ice core axis.

Zone	Depth	Qualitative description	Inclination
I	$0 - 14$ m	bands (thinner than 25 cm) of weak contrast	$0 - 43$ m:
II	$14 - 38$ m	well-defined transitions between lighter/darker bands with decreasing thickness, bands (< 10 cm) disappear at the firn-ice-transition	$5 - 15°$ in 59 % of images, varying strongly
III	$38 - 55$ m	more uniform appearance, thickness of weakly discernible alternating bands exceeds those of zone II	$43 - 51$ m: no or little inclination
IV	$55 - 64$ m	clearer banding without well-defined transitions	$51 - 63$ m: $10 - 15°$
V	$64 - 71$ m	layers $\sim$ cm with good contrast, but increasingly irregular appearance	63 m $-$ bedrock:
VI	$71 - 72$ m	uniform appearance	$15 - 20°$, max. $30°$

respect to the geographical coordinates and flow direction, layer inclination values can only be minimum estimates. Also, a possible borehole inclination during drilling might have an unquantifiable effect on the layer inclination. However, borehole inclination measurements from 2016 revealed inclination angles below 5° between 10 and 60 m depth and $5 - 10°$ down to bedrock (Licciulli, 2018). This is not sufficient to account for the observed layer inclination in the visual stratigraphy record and has probably mostly developed over 3 years since the drilling.

About 20 melt layers (thickness $\mathcal{O}$(cm)) were found in the firn part of the ice core, as is to be expected at this drilling site (Alean et al., 1983), often with coarse grains in the vicinity of the melt features.

On visual inspection of the thin section microstructure images, we assess how

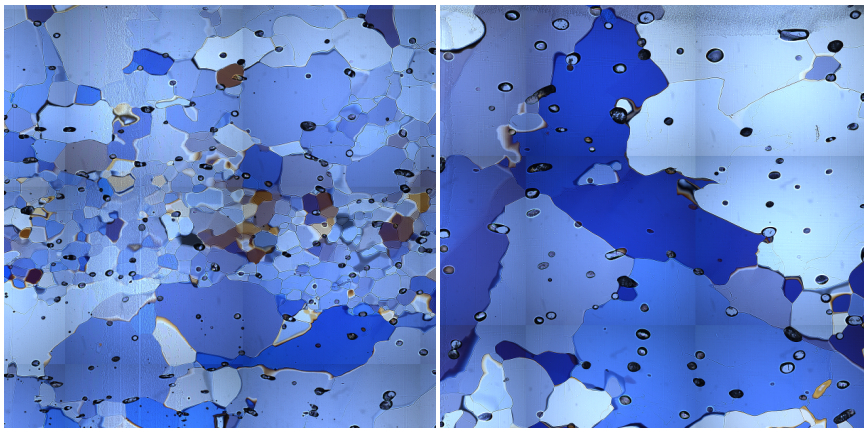

FIGURE 9.2: FA image details ($2.5 \times 2.5\,\mathrm{cm}^2$). Left: Example of a fine-grained layer. Right: Example of a coarse-grained layer.

often we observe a distinct change in grain size in layers, regardless of the mean grain size in these layers. In more than a third of all sections we find such grain size layer transitions. Fine-grained layers (19 observations, Fig. 9.2) occur most frequently at depths between the firn-ice transition and 60 m. An estimated 17 % of all thin section samples contain thick layers of large grains (average maximum grain size: $2.5\,\mathrm{cm}^2$) with some being part of the same large-grain layer extending over more than one section, between a depth of 48 and 69 m. Below 62 m grains of similar size are often clustered within sections of heterogeneous size distribution. Almost a third of all sections exhibit a heterogeneous grain size distribution without a clear layered structure. Only one third of all sections have a nearly homogeneous grain size distribution, mostly in the firn and very close to bedrock.

9.4.3 High-resolution physical properties

Following the stratigraphic observations we acknowledge the need to study fabric and microstructure on a smaller-than-section scale. We show the results from the high-resolution centimetre-scale analysis for all measured ice core intervals in Fig. 9.3. The c-axis eigenvalue λ_3 is given, together with the mean grain size $\bar{A}$, grain and bubble number, and the particle dust record from continuous flow analysis (Bohleber et al., 2018). A depth interval is shown in detail in Fig. 9.4, including the density ρ and bubble area A_b.

The high-resolution analysis reveals an extreme variability in the fabric and microstructure parameters on the sub-decimetre scale with gradients in eigenvalue of up to 0.2 over a few centimetres. The uncertainty is small compared to the variations. The difference between extreme values within an interval is roughly twice as high as when comparing per-section eigenvalues (Table 9.2). Below 53 m depth the eigenvalue appears to spike towards lower values while it is high on average (Figure 9.3), matching the observation of layers with larger and less oriented grains within a more strongly oriented matrix. Fine-grained layers cannot be resolved well as they are often thinner than the sliding computation window. The variability in the c-axis eigenvalue is accompanied by an equally variable mean grain size which is changing often in accordance with the eigenvalue, with a significant (Spearman's) rank correlation coefficient (r_s) of $-0.33 < r_\mathrm{s} < -0.79$ for 8 out of 13 intervals (Appendix 9.7: correlation computation). The anticorrelation between the mean grain size and the number of bubbles N_b is strong in all intervals ($-0.38 < r_\mathrm{s} < -0.91$).

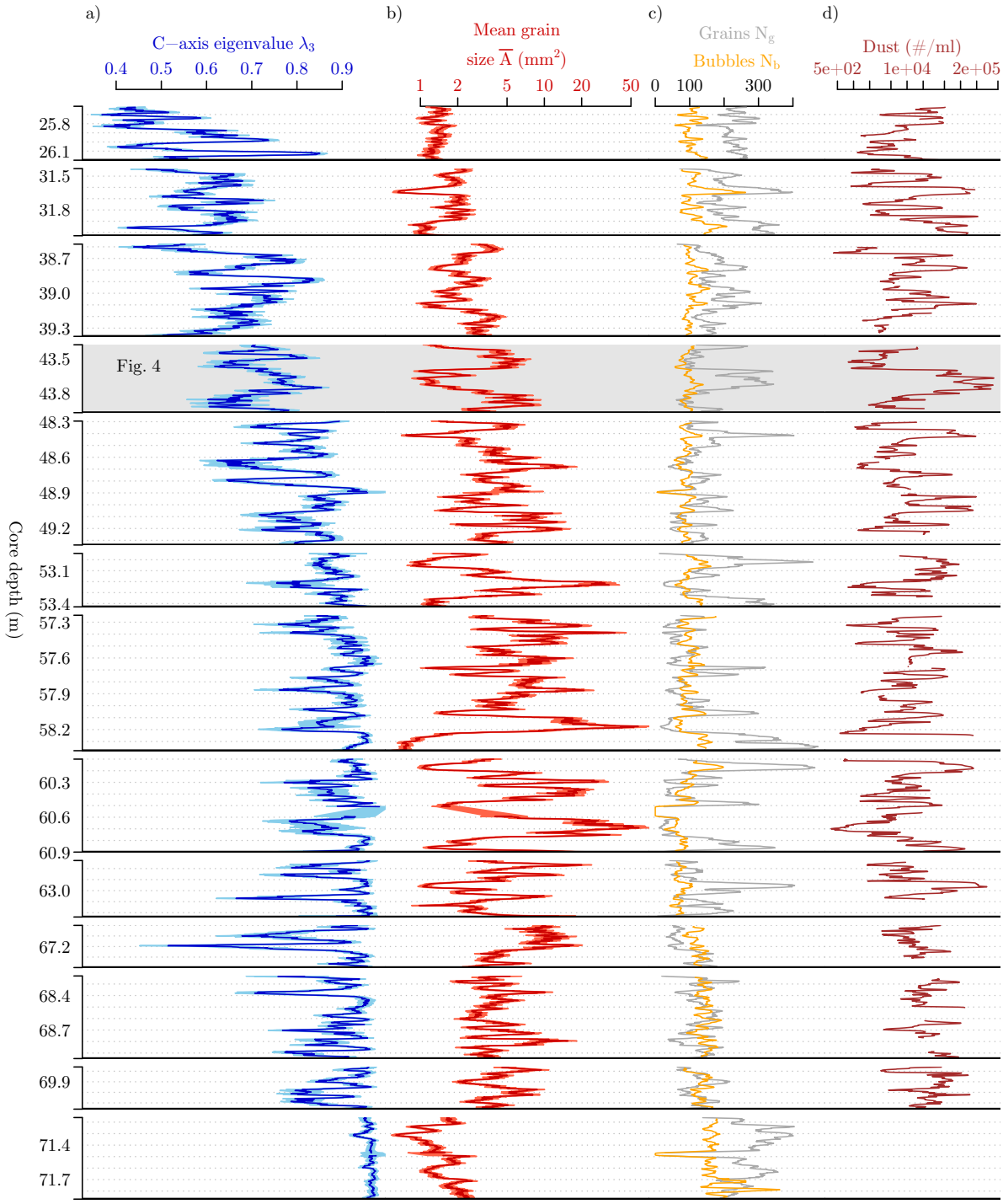

FIGURE 9.3: Physical properties parameters derived from cm-scale fabric analysis with 2 cm sliding window. The depth axis is discontinuous; horizontal black lines indicate axis breaks. a) Eigenvalue and b) mean grain size (logarithmic scale) are shown with uncertainty following Eq. 9.2 and 9.3. c) The grain number N_g is inversely related to the mean grain size and compared to the number of bubbles N_b. d) The insoluble particle concentration (referred to as "dust") from continuous flow analysis is additionally shown (logarithmic scale) for comparison. The shaded section is shown in detail in Fig. 9.4.

In 10 out of 13 intervals we obtain significant correlation coefficients between the mean grain size and the dust content ($-0.51 < r_s < -0.9$). The close-up from 43 m depth (Fig. 9.4) shows that for a higher density ρ there are more but smaller bubbles

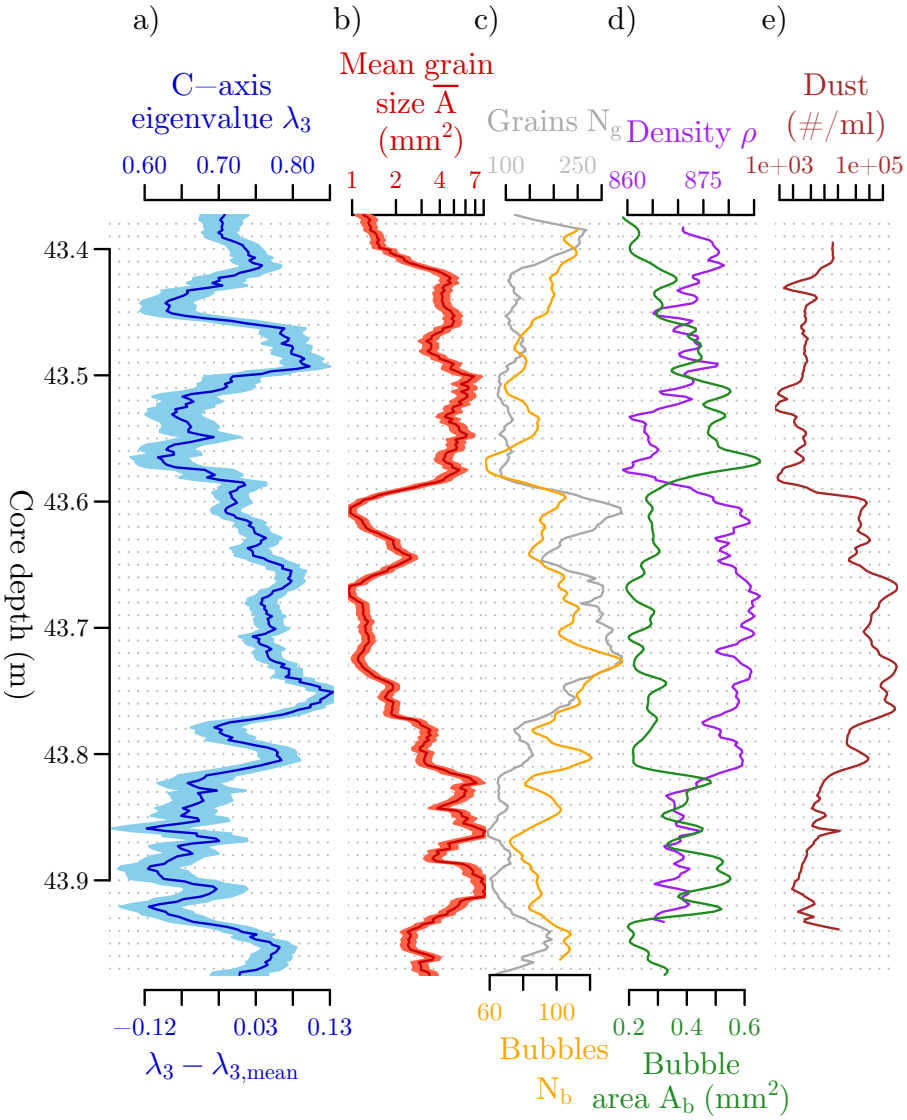

FIGURE 9.4: Excerpt from Fig. 9.3 showing a medium depth interval below the firn-ice transition. a) – c) as in Fig. 9.3. d) Density and the mean bubble area A_b are additionally shown. e) as d) in Fig. 9.3.

($0.56 < r_s < 0.87$ above 44 m depth). Furthermore, the density at this depth changes in accordance with the dust content.

9.5 Discussion

9.5.1 Depth-evolution of crystal anisotropy

The presented data of crystal-preferred orientation from a non-temperate, midlatitude, high-altitude glacier shows clearly that the development of an anisotropic CPO is not confined to the larger scale of polar ice sheets. In contrast, already in the firn, at one third of the glacier depth, we observe an anisotropic CPO pattern, as has been hypothesised by Diez et al., 2014 following a seismic velocity analysis at the site. The dominant fabric type is a single-maximum, which, in the upper part of the glacier, results from vertical compression in the firn and across the firn-ice transition, and

may be enhanced by simple shear due to the surface slope at the flank of CG. In the lower third of the ice core, the inclined single maximum is consistent with simple shear (Azuma, 1994; Llorens et al., 2017; Qi et al., 2019, in press), as we can assume that the glacier is frozen to bedrock. This assessment is further supported by a recent ice-flow model for Colle Gnifetti (Licciulli, 2018), yielding high vertical strain rates $\dot{\varepsilon}_{zz} < 1.9 \cdot 10^{-9} \mathrm{s}^{-1}$ and an elevated horizontal strain rate $\dot{\varepsilon}_{zy}$ in the upper 10 m of the firn, and a steadily increasing horizontal strain rate from 30 m depth to bedrock ($\dot{\varepsilon}_{zy} < 2.9 \cdot 10^{-10}\,\mathrm{s}^{-1}$). The faint girdle pattern we see in the Schmidt diagrams of the last 10 m above bedrock is indicative of a component of diverging flow (Gow and Meese, 2007). This suggests a more complex flow pattern in the bottom part of the glacier than the surface flowline implies at the KCC drilling site (Bohleber et al., 2018). It runs towards the eastern ice cliff, possibly with a component of extensional flow towards the saddle. However, the girdle is not as clearly recognised in single sections of individual intervals, supporting our approach of assessing continuously measured intervals to obtain a better representation of the crystal anisotropy for a given depth. When examined individually, some thin section samples exhibit specific structures, which are, in fact, contributing to the interval girdle. Figure 9.5a shows steeply inclined bands of crystals with higher colatitude (darker red) that deviate from the surrounding grain matrix. We interpret these to be tilted-lattice bands, which, for polar ice cores, have been shown to indicate small-scale folding (Jansen et al., 2016). In Fig. 9.5b a number of grains distributed over the section are constituting a second maximum of c-axes which is oriented approximately 90° from the dominant single maximum towards the horizontal. It is currently not resolved why these grains deviate from the matrix but a second maximum is usually interpreted as a consequence of recrystallisation under simple shear conditions (Alley, 1992; Qi et al., 2019, in press).

By including anisotropic deformation and the most relevant recrystallisation mechanisms in a microstructural model, Llorens et al., 2016a find that the grain size is mainly controlled by the recrystallisation processes, accompanied by secondary effects like grain dissection (Steinbach et al., 2017). Thus, the observed grain size variability with concentrations of very large or small grains is indicative of ongoing recrystallisation in this shallow mountain glacier. Exemplary microstructure images are shown in appendix 9.7, Fig. 9.7, illustrating the occurrence of various grain and subgrain topological features such as bulging GBs and intricate subgrain boundary structures. These are typically observed in polar firn and ice as well as experimentally deformed ice under comparably low stress undergoing dynamic recrystallisation (Hamann et al., 2007; Kipfstuhl et al., 2009; Weikusat et al., 2017a), but the discussion of further microstructural parameters is beyond the intended scope of this paper.

9.5.2 Short-scale variability

Our analyses on the sub-section scale show that layers of distinct grain size and layers of varying fabric strength can be observed at many depths. The variations are much stronger than previously known from low-resolution studies which could imply effects on the integrity of stratigraphic records (Faria et al., 2010) and also be highly relevant for the interpretation of geophysical data to map intraglacial structures (Diez and Eisen, 2015; Eisen et al., 2007; Fujita et al., 2006; Hofstede et al., 2012; Horgan et al., 2008; Kerch et al., 2018b; Matsuoka et al., 2003). The comparison of high-resolution data series reveals a good correlation between the presented

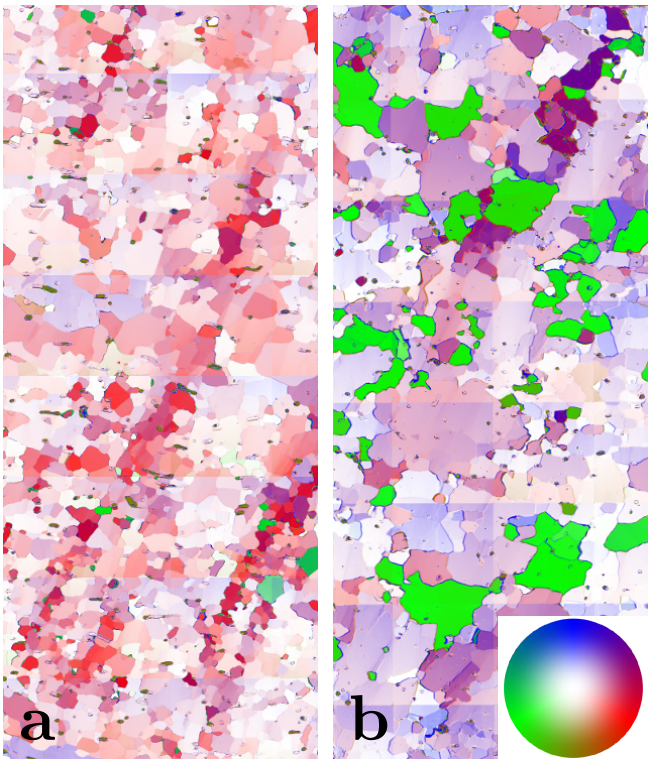

FIGURE 9.5: FA image details ($3.1 \times 7.5\,\mathrm{cm}^2$). Left: Tilted-lattice bands (darker red) in 60.8 m depth. Right: Unconnected crystals (green) forming a second maximum inclined to the main single maximum (purple) in 70.1 m depth. The colour code indicates the c-axis orientation: the white center corresponds to a vertical orientation, parallel to the ice core axis.

microstructural parameters, but it is very difficult to establish the order of causal dependencies; feedbacks between coupled processes are very probable.

There is evidence on a large spatio-temporal scale in ice cores, that the microstructure could be governed by the impurity content (Durand et al., 2006b). However, the process identified to be the main driver for this relation (Zener pinning) is under discussion (Eichler et al., 2017). This raises the question whether the same mechanisms could also play a role on the cm-scale? Our results strongly suggest that this is the case as particle content and mean grain size show a strong anticorrelation. While the ice from Colle Gnifetti is relatively pure for a midlatitude glacier due to the high altitude, its dust content exceeds the dust load in Holocene ice from polar cores by a factor of 10 (Wagenbach and Geis, 1989), increasing the chance of observing a connection between microstructure and particle content. Recently developed techniques such as LA-ICP-MS (Della Lunga et al., 2017; Reinhardt and others, 2001; Spaulding et al., 2017) could provide spatially resolved data on particle distribution with respect to microstructural features to study the interaction processes in detail.

Another parameter which is highly variable from the deposition processes on the glacier surface is the density. Extremes in density are melt layers that are observed not only in alpine glaciers but also in polar ice sheets (Schaller et al., 2016). We cannot directly connect outstanding layers in microstructure or fabric with original melt layers. However, even without melt layers, initial density fluctuations in the snow, which could be linked to the concentration of calcium in polar cores (Hörhold et al., 2012), can be expected to evolve into a sequence of layers in which bubbles have different characteristics, e.g. many small bubbles or fewer large bubbles. Steinbach

et al., 2016 show in their microstructure model how bubbles can initiate strain localisation. In our data we see a clear connection between the bubble number density and the mean grain size, which feeds back into the idea that grain size variations are connected to density variations (Roessiger et al., 2014). As mentioned before, Llorens et al., 2016a show that recrystallisation processes are most evident in grain evolution. An existing grain size variability would be enhanced by this.

But how does all this affect the fabric evolution and what are the consequences for the bulk deformation? The small-scale variability in the CPO mostly correlates weakly with the microstructure variability in general, with local exceptions of strong correlation, especially where there is a strong contrast in microstructure parameters. Thus, the role of the microstructure variations for the fabric variations appears to be that of initial perturbations which subsequently lead to local enhancement of strain rate. This has been hypothesised before (Montagnat et al., 2014) but has not been presented with much evidence due to a lack of continuous data. As a result of locally enhanced deformation small-scale shear zones (Hudleston, 2015; Riese et al., 2019, in review) might develop. This would, in turn, allow for thick layers of ice deforming at a lower rate to be dominated by recrystallisation. However, we do not have information on the lateral scale to draw conclusions on the effect on the bulk deformation. We certainly recommend to collect high-resolution borehole deformation data to be able to connect fabric information and in-situ deformation on this particular length scale, e.g. by means of ultrasonic profiling (Gusmeroli et al., 2012), even if they can only provide a reduced two-dimensional representation of CPO. Our results are in line with Svensson et al., 2003 who conducted a case study on the seasonal variability in ice crystal properties on the cm-scale and observe small-grain layers corresponding to the spring season but cannot find a seasonal variability of the c-axis orientations. Additionally, we find no evidence of a connection between the thickness of fabric layers with the thickness of annual layers as determined from impurity records (Bohleber et al., 2018).

9.5.3 Do we need a new statistical approach?

From a methodological standpoint, our study provides evidence that, a priori, one thin section sample does not provide sufficient statistics to draw reliable conclusions for a depth interval of several tens of metres. An apparent fabric variability may simply be the result of statistical undersampling. The statistical uncertainty as proposed by Durand et al., 2006a does not appear to be an appropriate uncertainty measure for our data if this uncertainty is supposed to account for the variation in adjacent samples. Consequently, the task at hand is to establish which sample length scale is in fact representative for a given interval-of-interest. The same holds for the sampling interval, i.e. the distance between samples where no measurements are conducted. This sampling interval and the sample length make it mandatory to readdress the estimation of an appropriate statistical error based on such representative scales.

Furthermore, our results demonstrate that the choice of a representative length scale for CPO data is also dependent on the research question, considering the activity of several contributing and coupled processes on different length scales. More specific, the evaluation of fabric data needs to be adjusted to the resolution of complementary methods applied to the ice core or glacier, e.g. radar and seismics as well as continuous logging techniques, to advance our understanding of glaciological processes across different methodological approaches and spatial scales.

9.6 Conclusions

This study confirms the observation of a comparable development of crystal anisotropy in cold alpine glaciers and in polar glaciers or ice sheets, despite a factor of 35 (compared with the NEEM ice core) difference in thickness. Additionally, we observe and describe a strong variability in the microstructural parameters and crystal orientation during a high-resolution analysis of continuous measurement intervals. Thus, we can assume that this variability should also develop in polar glaciers, which emphasises the usefulness of non-polar glacier environments for the study of glacial processes in general. We consider different causes for the variability, recognising that different causes may dominate on different length scales. Acknowledging the interconnectivity of the analysed parameters, we conclude that the high variability in CPO may develop as a result of deformation localisation (shear zones) on different length scales, following initial differences in density and microstructural parameters which, in turn, are influenced by the impurity concentration and the seasonal cycle of environmental conditions. The possible consequences of such shear zones on bulk deformation (e.g. folds) and the interpretation of stratigraphic parameters are still under investigation (Bons et al., 2016; Montagnat et al., 2013; Ran et al., 2018; Riese et al., 2019, in review).

Our results lead us to question the current single-section mode of CPO evaluation and call for a new statistical approach based on a higher and scale-specific data coverage, and/or an adjusted uncertainty estimate. Furthermore, our findings reinforce the demand for high-resolution and high-coverage proxy methods (e.g. ultrasonic sounding in the borehole and the laboratory (Mikesell et al., 2017; Vaughan et al., 2016), high-resolution dielectric profiling (Wilhelms, 2005), polarimetric radar (Drews et al., 2012; Li et al., 2018) and seismics (Kerch et al., 2018b)) to be applied in order to obtain a more complete understanding of the vertical and lateral crystal anisotropy structure and its role for large-scale glacier deformation.

Data availability

The data sets for the ice core KCC (fabric, microstructure, eigenvalues, density, linescans) are published in the open-access database PANGAEA®(Kerch et al., 2018a, doi:10.1594/PANGAEA.887838) and also available upon request.

9.7 Supplementary material

Collection of major polar fabric studies from the last 20 years

TABLE 9.4: Resolution of fabric studies on polar ice cores. *Section* refers to a typically 10 cm long thin section sample; *continuous* refers to measurements of several adjacent sections in an ice core segment or bag.

Authors	Ice core	Length [m]	Fabric resolution; intervals between samples	estimated % of total length
Gow et al., 1997	GISP2	3054	ca. 500 sections	1.7 %
Thorsteinsson et al., 1997	GRIP	3029	ca. 100 sections; mostly 25–55 m intervals	0.3 %
Wang et al., 2002	NGRIP	2930	142 sections; 5–66 m intervals	0.5 %
Montagnat et al., 2014, Eichler et al., 2013	NEEM	2540	ca. 700 sections; 10 m intervals, partially continuous (bags of 55 cm)	3 %
Treverrow et al., 2016	Dome Summit South	1196	185 sections; 5–6 m intervals	0.9 %
Azuma et al., 1999	Dome Fuji	2500	ca. 240 sections; 20 m interval, partially continuous	1 %
Gow and Meese, 2007, DiPrinzio et al., 2005	Siple Dome	1004	ca. 100 sections; 20 m intervals	1 %
Wang et al., 2003, Durand et al., 2007, 2009	EPICA Dome C	3260	ca. 200 sections; 11–50 m intervals	0.7 %
Weikusat et al., 2017b	EPICA DML	2774	210 sections; 50 m intervals, partially continuous	0.8 %
Montagnat et al., 2012	Talos Dome	1620	10–20 m intervals	1 %
Fitzpatrick et al., 2014	WAIS	3405	20 m intervals	0.5 %

Correlation computation for cm-scale data series

As the data are in general not normally distributed we compute correlation coefficients between various data sets available in this study by considering the ranks of the bivariate data (Spearman correlation coefficient)

$$r_s = 1 - \frac{6 \sum_{i=1}^{n} d_i^2}{n(n^2 - 1)} \tag{9.4}$$

with the sample size of paired values n, the rank difference d and $-1 < r_s < 1$. The significance of the obtained correlation coefficient is tested. The data of this study can be regarded as a time series for which each data point is not necessarily independent of its neighbours (Mudelsee, 2003, "serial dependence"). The autocorrelation of a data series of length n for a lag τ is used to evaluate the non-randomness of the data and provide the distance or time lag within which subsequent data points cannot be considered as independent. Considering τ and the short length of data sequences computed from continuous fabric data we derive an effective sample size, i.e. smaller than the original sample size, from which a correlation with another data set might be calculated under the assumption of randomness of the data points. Only eigenvalues calculated from successive, but not overlapping, frames are used to derive correlation coefficients, which limits the sample size to 50 data points per metre. By choosing a different frame set that is shifted by $2n$ mm (with n = [1,9]) and repeated calculation we obtain several values for the correlation coefficient for the same continuous interval, providing a robust estimate of correlation on the 2 cm scale. All bivariate data sets are downsampled to the lower resolution of the two variables.

Supplementary figures

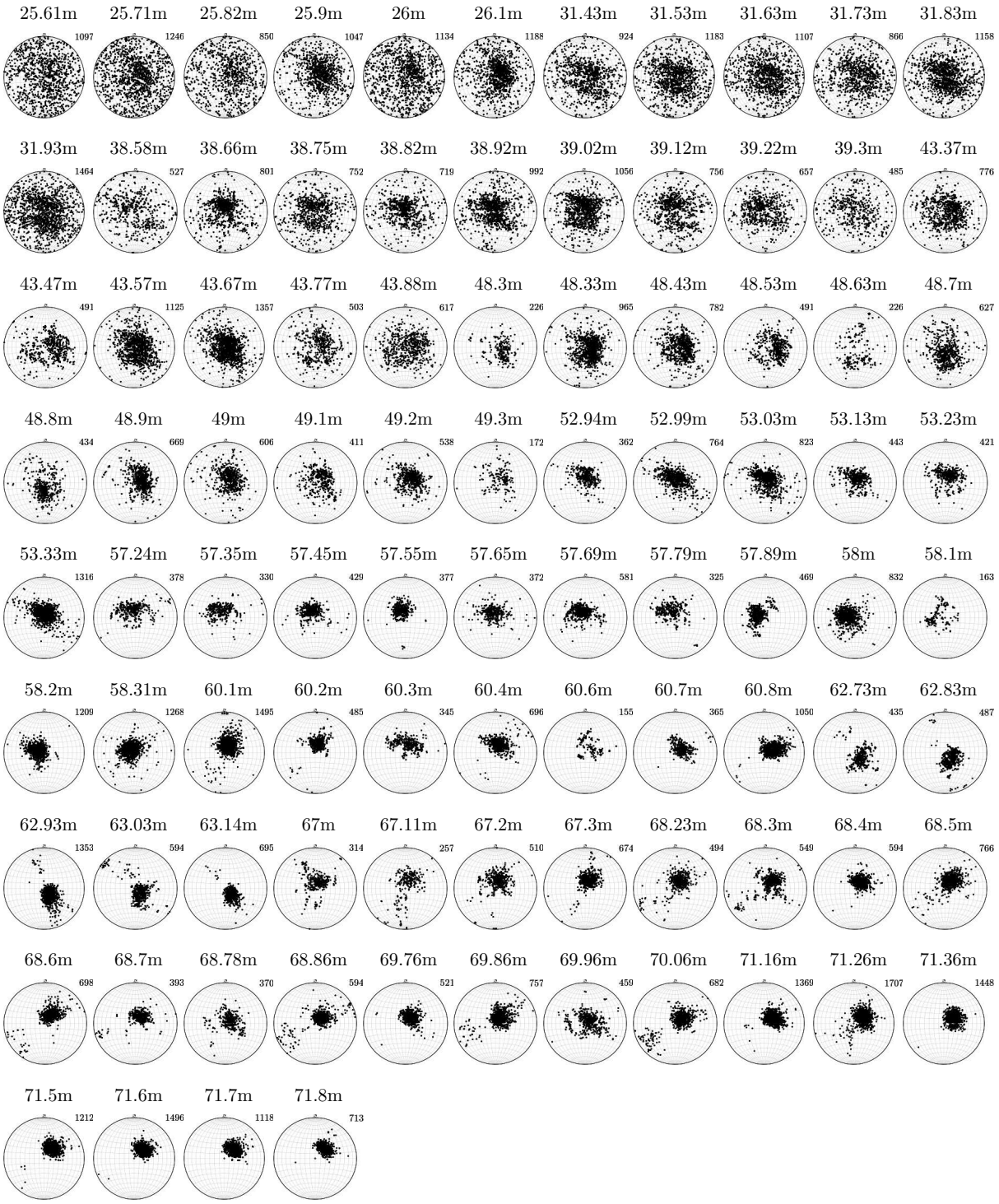

FIGURE 9.6: Schmidt diagrams for all KCC thin sections. The number of grains is indicated on the top right of each polefigure.

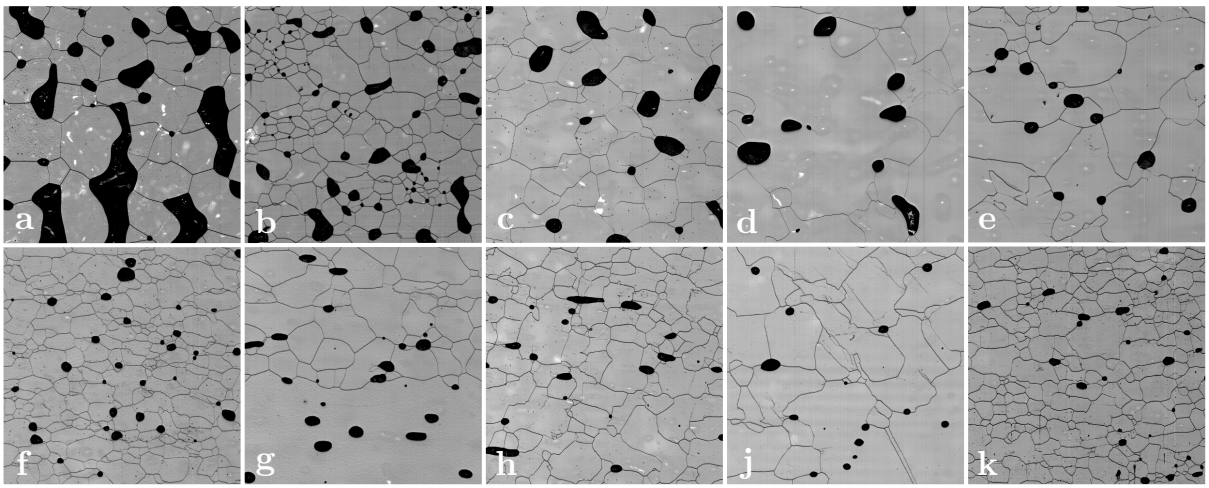

FIGURE 9.7: Exemplary microstructure (LASM) image details (1 cm^2) from different depths of the ice core KCC. a) 25.9 m: firn. b) 31.63 m: deep firn with small-grain clusters in regions with many small bubbles. c) 38.66 m: bubble cluster just below firn-ice transition. d) Zigzagging subgrain boundaries. e) 49 m: Protruding grains and bubble alignment. f) 53.03 m: small-grain section. g) 57.35 m: small-to-large-grain transition; note that only within the large grain bubbles are not located on grain boundaries. h) 62.93 m: angular grains and inclined/elongated bubbles. j) 67.1 m: irregular grains and parallel GBs. k) 71.26 m: small-grain disribution close to bedrock.

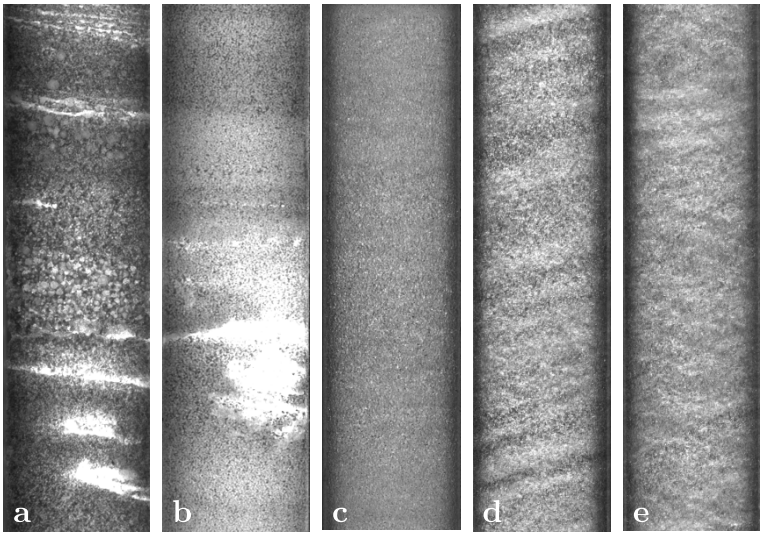

FIGURE 9.8: Exemplary visual stratigraphy linescan images (approx. 8 $\times$ 31 cm^2) from different depths of the ice core KCC. a) 6 m depth: thin melt layers, ice lenses and coarse grains in firn. b) 24 m depth: banding and large ice lense, presumably from percolating melt in deep firn. c) 47 m depth: barely visible transitions and no discernible inclination. d) 65 m depth: inclined layers. e) 70 m depth: Layers appear very irregular.

Appendix A

Programs and Scripts

A.1 Microstructure Mapping

A.1.1 Running a Microscope Scan

The microscope used for microstructure mapping of the sublimation features at the sample surface and for impurity maps (see Sec. 3.2.1 5.2.1 and 6.2.3) is a Leica DMLM with a CCD camera (Hamamatsu C5405), frame grabber and a software-controlled x-y stage. The system can be controlled either manually or using a software interface: `NIH Image 1.62`. The automatic scan is run using a macro called `XY_Tisch.01a_2.5x` (developed by Fernando Valero and Sepp Kipfstuhl) which can be loaded in the control software. A detailed tutorial for the usage of the macro can be found elsewhere. After a successful microscope scan the measurement directory contains the following files:

- a plane text document with the scan protocol called `measurement_name_Prot`. This file contains some useful information such as the dimensions of the scan (number of images in x and y directions) and can be read using a text editor.
- a TIFF image called `measurement_name_Skala`.
- a number of TIFF images (up to several thousand) called `measurement_name_0001`, `measurement_name_0002` etc., which are the actual microscope captures of the sample.

A.1.2 Image Stitching (Manual)

The individual images need to be stitched together in the right order and applying the right overlap parameters in order to obtain the final continuous microstructure map of the specimen. The simplest and fastest way is to apply a constant set of four parameters to shift the adjacent images. This was implemented in a Python script called "microSM.py".

In order to use the script you will need to have installed Python and the Python Imaging Library (PIL) which you may find in the official software repositories of your operating system. You can also download the newest version here: `http://www.pythonware.com/products/pil/`.

Using "microSM.py" is very intuitive and the few control steps are prompted by the program itself. The recommended procedure is to copy the script in the measurement directory and run it from there in a terminal:

```
cp microSM.py pathtodirectory/../../measurement_directory
cd pathtodirectory/../../measurement_directory
python microSM.py
```

The script orders the images into a two-dimensional matrix. The corners of the neighboring images are attached to each other and shifted by a given offset in pixels (two values for the right neighbor and other two for the lower neighbor). The default values (-155, 12, -9, -88) have been successfully tested for the current settings of the microscope set up in the ice laboratory D-0197 at AWI. Thus, the default offset is: right neighbor 155 pixels to the left and 12 pixels down. Lower neighbor 9 pixels left and 88 pixels up. After the initialization, the script will ask whether the default offset settings should be used or a custom offset parameters should be defined. The default settings are chosen by entering 1 (followed by the ENTER key). Any other input will lead to the custom offset definition. After this step, the dimensions (number of columns and rows) of the stitched matrix are asked. These can be found in the protocol text file (`measurement_name_Prot`). And finally the name of the measurement has to be entered, which is the common string for all the image names including the last underscore. This string can be also copied from the `_Prot` file. After entering the sample name the script stitches all the images and exports the result in a new image file `stitched.tif`.

An example run of the script from a terminal looks like this:

```
../neem_1346_201_3$ python microSM.py
-----------------------------------------------------------------
microSM: A Python script for stitching and background correction
of microstructure-mapping-images
Version: 16.1.2019
Offset parameters:       right neighbor horizontal: -155
                         right neighbor vertical: 12
                         lower neighbor horizontal: -9
                         lower neighbor vertical: -88

Use standard offset? (1 = yes; 0 = no, define my own offset): 1
using standard offset parameters...

Enter number of images in x-direction: 14
Enter number of images in y-direction: 64
Enter sample name: neem_1346_201_3_

illumination image found...
stitched.tif was created successfully.
../neem_1346_201_3$
```

Background Correction

As an optional feature, a background correction was implemented in the "microSM.py" script. Depending on the setting of the microscope, the illumination field is barely uniform but rather bright in the center and darker at the edges of the image. After stitching the images together this effect produces a characteristic grating in the result image. This background artifact can be significantly reduced subtracting the illumination background of an empty image from all the captured images. This correction is performed automatically if the directory, in which "microSM.py" was called, contains an additional TIFF image with the name "illumination" (without suffix). This image should contain a blank capture of the illumination background

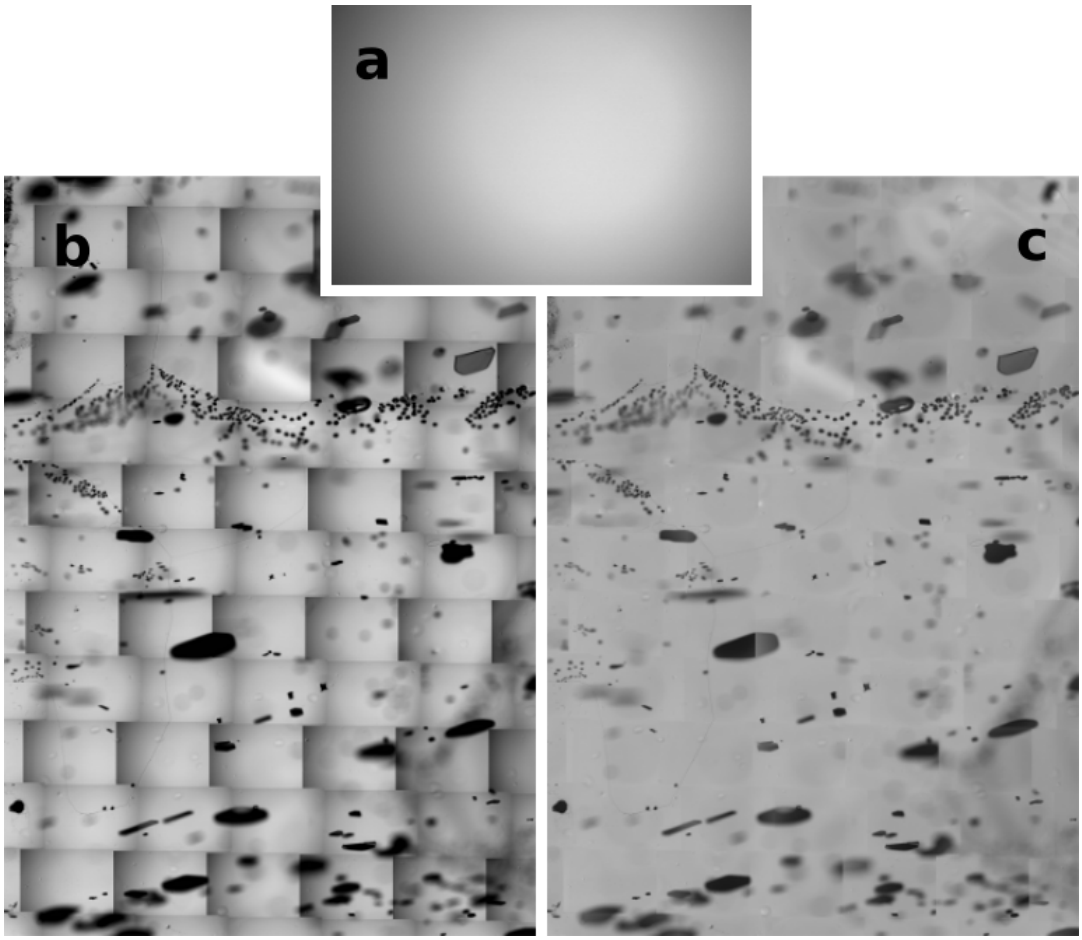

FIGURE A.1: An example of the background correction implemented in the "microSM.py" script. (a) The illumination image. (b) Stitched microstructure map without subtracting the background illumination. (c) corrected mircrostructure map after subtracting the illumination image.

without any objects. The illumination image should be captured for each microstructure scan individually. If there is no such image in the directory, the python script will proceed without background correction automatically.

A.2 Remote Control of the Raman System

Preconditions:

- WITec Control (microscope PC)
- LabVIEW with valid license (remote control PC)
- WITec Control LabVIEW Driver (remote control PC)

Control of the Raman system using the WITec Control FOUR software is described elsewhere (Kleitz, 2015). Additionally, the WITec Control software package allows external access to most of its functionality using LabVIEW. The LabVIEW extension for WITec Control (not included in the default installation) provides a set of pre-built "Virtual Instruments" (VIs) for the communication with the Raman system. These functional blocks can be combined and implemented into more complex LabVIEW programs.

The remote control is enabled by selecting "COM Automation" → "Allow Remote Write Access" from the default tree menu of the WITec Control FOUR program.

Automatic Multi-Point Raman Acquisition

The program "MultipointAcquistion.vi" was written with the aim to automatically perform multiple Raman acquisition at different discrete positions in the sample. Figure A.2 shows the front panel of the program. Figures A.3–A.6 contain the block diagram of the virtual instrument. The program complies with two major tasks:

1. Read on-line the current (x,y,z)-coordinates of the positioning system of the Raman microscope and save them in an array. The array can be exported in an ASCII text file.
2. Remotely control (write on) the sample positioning system and acquire Raman spectra at previously specified coordinates from an array. The array can be imported from an ASCII text file.

In the Read mode the virtual LED "HasReadAccess" is green. The user operates the Raman microscope (which is set in optical mode) via the WITec Control software. MultipointAcquisition.vi reads continuously the coordinates of the positioning system. After focusing onto a point of interest (micro-inclusion, gas inclusion, etc.) press "save" in MultipointAcquisition.vi. This will add the current x, y and z coordinates to the array. The array can be exported in an ASCII text file pressing "export". Note that the x-y reference frame is given by the limits of the positioning system. Thus there is an absolute zero-position, usually set in the center of the reference frame. In contrast, there is no such absolute position for the z-axis. The zero-z position is set by the user so that the z-coordinates are always only relative to this position. A good practice is to set $z = 0$ at the upper surface of the specimen each time the Witec Control program is started. However, the surface position changes significantly with time due to sublimation.

> Warning: Operating the z-control can seriously damage your sample AND the microscope, if the objec lens hits the sample surface. No automatic mechanism is included in order to prevent this. Please make sure the z-coordinates in the array are corresponding to your current reference frame before starting the automatic Raman acquisition.

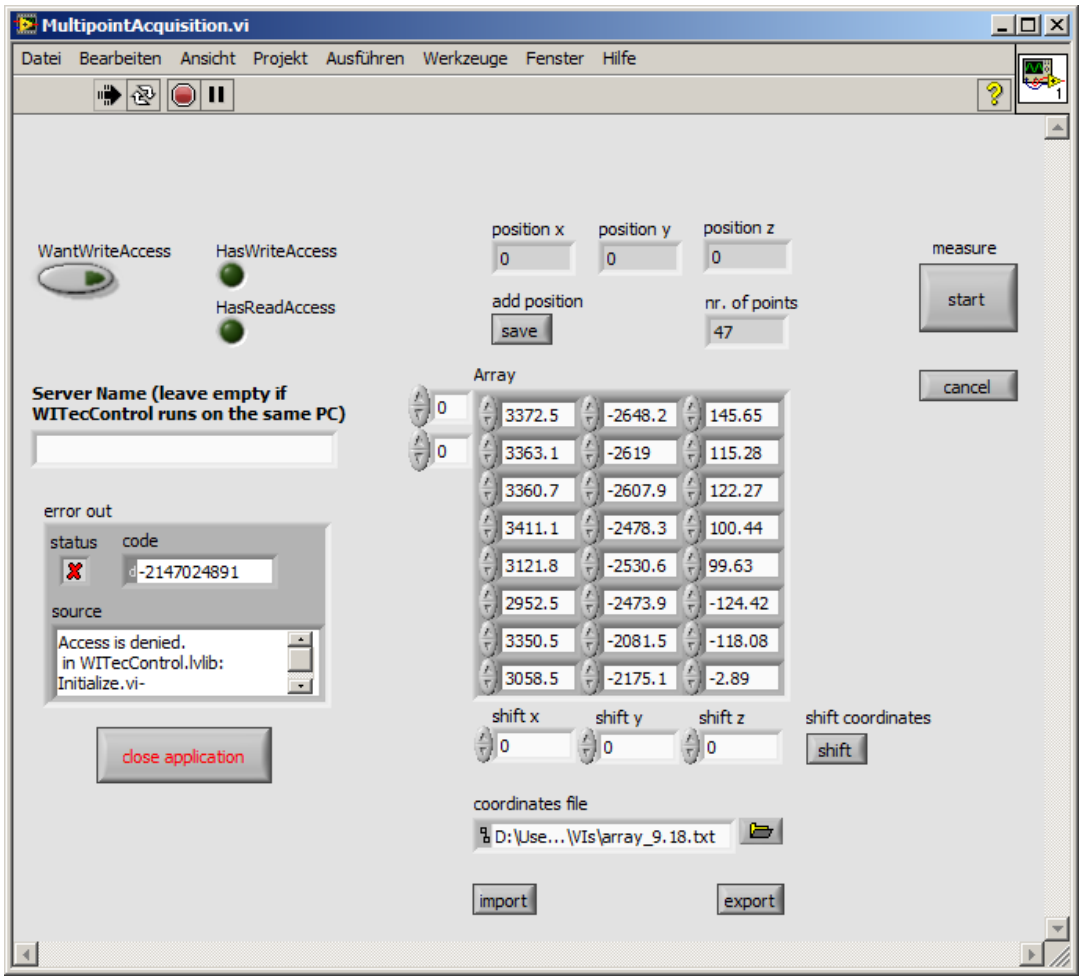

FIGURE A.2: The front panel (GUI) of the MultipointAcquisition.vi.

Before starting the multi-acquisition routine, the single-spectrum acquisition parameters need to be set in the WITec Control software. All spectra will be acquired with the same settings. Double-check the z-reference frame. Change manually the microscope mode to Raman acquisition and turn the Laser on. The Write access can be requested by pressing "WantWriteAccess" and is signalized with the "HasWriteAccess" LED. However, it is set automatically when starting the Raman acquisition routine. After pressing "start" (upper left corner) the multiple Raman acquisition routine starts. All the following steps are run automatically. Write access is requested. The z-control is driven to the zero-position and reset. The stage is driven to the first position indicated in the coordinates array. A single spectrum is acquired. The stage is driven to the next position and the steps are repeated until the last Raman spectrum is acquired. The z-controller is driven back to zero. The Write modus is terminated. The multi-acquisition routine can be aborted pressing "cancel". In such a case the current Raman acquisition finishes before the Write access is given back to the WITec Control software.

> Disclaimer: MultipointAcquistion.vi is an experimental project. The author (Jan Eichler) is not liable for any claim, damage or other liability arising from the use of the software.

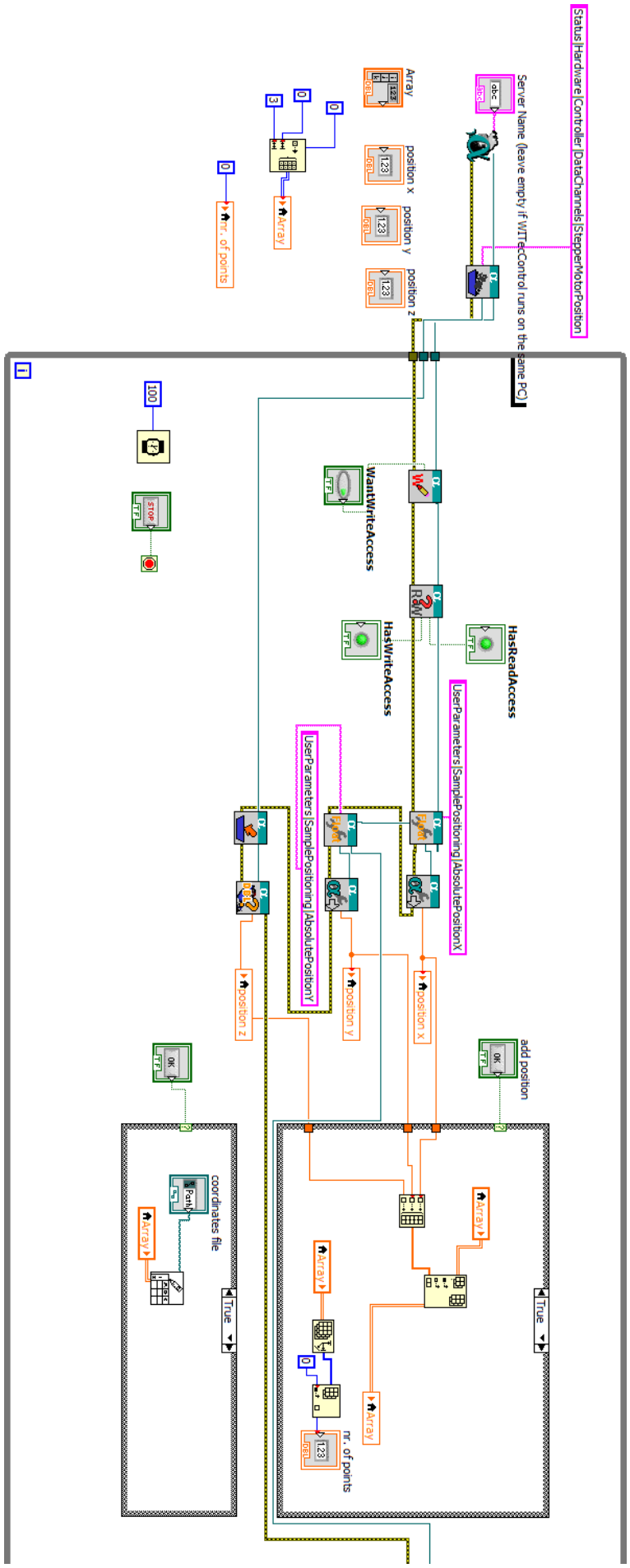

FIGURE A.3: MultipointAcquisition.vi, block diagram part 1.

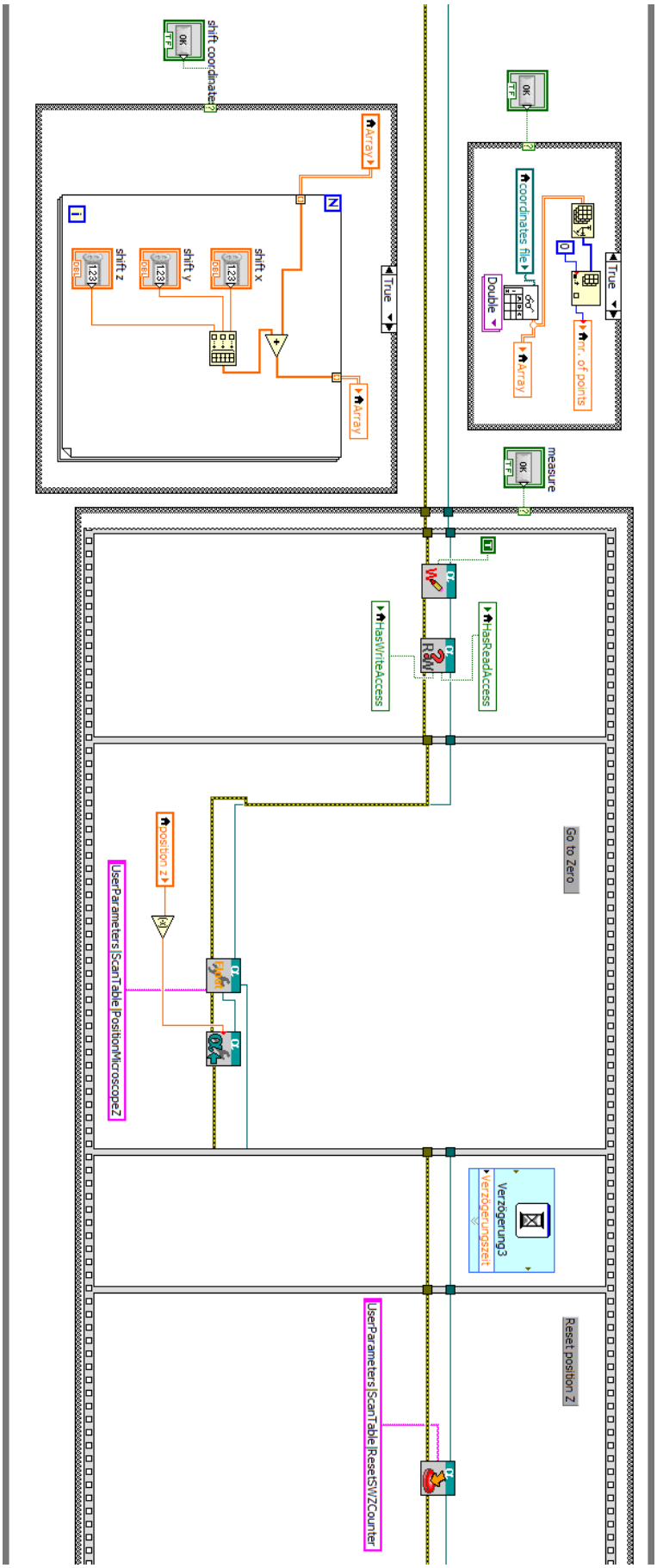

FIGURE A.4: Block diagram part 2.

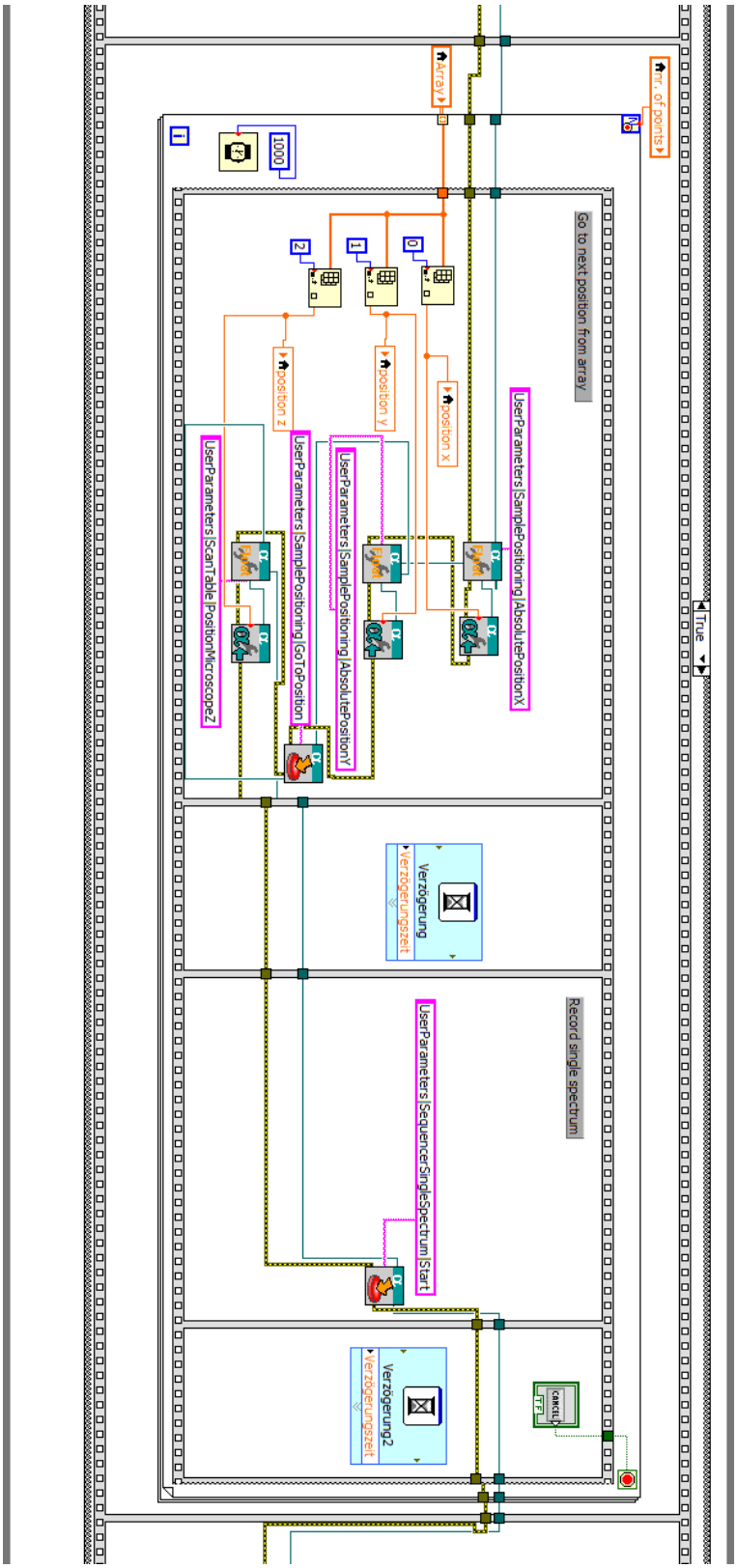

FIGURE A.5: Block diagram part 3.

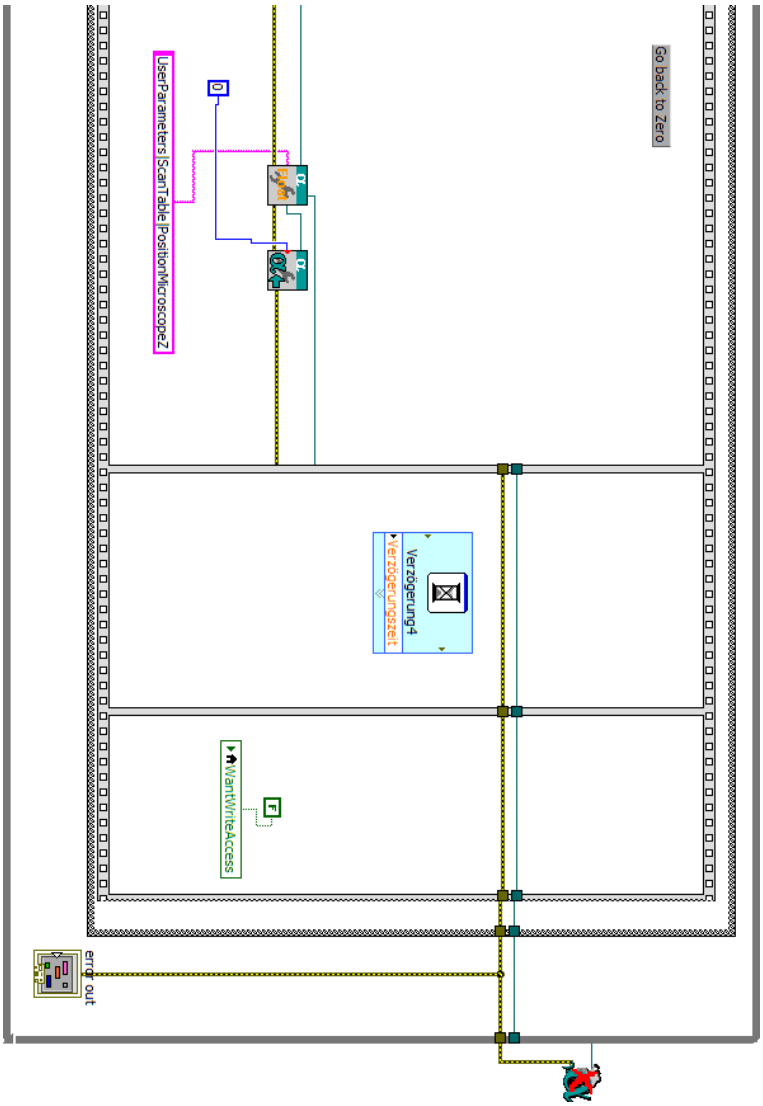

FIGURE A.6: Block diagram part 4.

Bibliography

Adam, J. F. (1989). "Methoden und Algorithmen zur Verwaltung und Analyse axialer 3-D-Richtungsdaten und ihrer Belegungsdichten." In: *Goettinger Arb. Geol. Palaontol.* 40. Z 1317 - 40 1989, p. 100.

Alean, Jürg, Wilfried Haeberli, and Bruno Schädler (1983). "Snow accumulation, firn temperature and solar radiation in the area of the Colle Gnifetti core drilling site (Monte Rosa, Swiss Alps): distribution patterns and interrelationships." In: *Z. Gletscherkd. Glazialgeol.* 19.2, pp. 131–147.

Allen, C. R., W. B. Kamb, M. F. Meier, and R. P. Sharp (1960). "Structure of the lower Blue Glacier, Washington." In: *Journal of Geology* 68.6, pp. 601–25.

Alley, R. B. (1988). "Fabrics in polar ice sheets: Development and Prediction." In: *Science* 240, pp. 493–495.

Alley, R. B. (1992). "Flow-law hypotheses for ice-sheet modelling." In: *J. Glaciol.* 38, pp. 245–256.

Alley, R. B. and J. J. Fitzpatrick (1999). "Conditions for bubble elongation in cold ice-sheet ice." In: *Journal of Glaciology* 45.149, pp. 147–153.

Alley, R. B. and G. A. Woods (1996). "Impurity influence on normal grain growth in the GISP2 ice core, Greenland." In: *J. Glaciol.* 42.141, pp. 255–260.

Alley, R. B., J. H. Perepezko, and C. R. Bentley (1986a). "Grain Growth in Polar Ice: I. Theory." In: *J. Glaciol.* 32, pp. 415–424.

Alley, R. B., J. H. Perepezko, and C. R. Bentley (1986b). "Grain Growth in Polar Ice: II. Application." In: *J. Glaciol.* 32, pp. 425–433.

Alley, R.B., A.J. Gow, and D.A. Meese (1995). "Mapping c-axis fabrics to study physical processes in ice." In: *J. Glaciol.* 41.137, pp. 197–203.

Anderson, MP, GS Grest, and DJ Srolovitz (1989). "Computer simulation of normal grain growth in three dimensions." In: *Philos. Mag. B* 59.3, pp. 293–329.

Arthern, Robert J., Dale P. Winebrenner, and David G. Vaughan (2006). "Antarctic snow accumulation mapped using polarization of 4.3-cm wavelength microwave emission." In: *Journal of Geophysical Research* 111.D6. DOI: 10.1029/2004jd005667.

Aschwanden, Andy, Ed Bueler, Constantine Khroulev, and Heinz Blatter (2012). "An enthalpy formulation for glaciers and ice sheets." In: *Journal of Glaciology* 58.209, pp. 441–457. DOI: 10.3189/2012jog11j088.

Ashby, M. F. and P. Duval (1985). "The creep of polycrystalline ice." In: *Cold Reg. Sci. Technol.* 11, pp. 285–300.

Ashby, M.F. (1969). "Boundary defects and the mechanism of particle movement through crystals." In: *Scripta Metallurgica* 3.11, pp. 843 –848. ISSN: 0036-9748. DOI: http://dx.doi.org/10.1016/0036-9748(69)90192-6. URL: http://www.sciencedirect.com/science/article/pii/0036974869901926.

Azuma, N. (1994). "A flow law for anisotropic ice and its application to ice sheets." In: *Earth Planet. Sci. Lett.* 128, pp. 601–614.

Azuma, N. (1995). "A flow law for anisotropic polycrystalline ice under uniaxial compressive deformation." In: *Cold Reg. Sci. Technol.* 23.2, pp. 23137–147.

Azuma, N. and K. Goto-Azuma (1996). "An anisotropic ice flow law for ice sheet ice and its implications." In: *Ann. Glaciol.* 23, pp. 202–208.

Azuma, N. and A. Higashi (1985). "Formation processes of ice fabric pattern in ice sheets." In: *Ann. Glaciol.* 6, pp. 130–134.

Azuma, N., Y. Wang, K. Mori, H. Narita, T. Hondoh, H. Shoji, and O. Watanabe (1999). "Textures and fabrics in Dome F (Antarctica) ice core." In: *Ann. Glaciol.* 29, pp. 163 –168. DOI: 10.3189/172756499781821148.

Azuma, N., Y. Wang, Y. Yoshida, H. Narita, T. Hondoh, H. Shoji, and O. Watanabe (2000). "Crystallographic analysis of the Dome Fuji ice core." In: *Physics of Ice Core Records*. Ed. by T. Hondoh. Sapporo: Hokkaido University Press, pp. 45–61.

Azuma, Nobuhiko, Tutomu Miyakoshi, Syuhei Yokoyama, and Morimasa Takata (2012). "Impeding effect of air bubbles on normal grain growth of ice." In: *Journal of Structural Geology*, p. 10. DOI: 10.1016/j.jsg.2012.05.005. URL: http://dx.doi.org/10.1016/j.jsg.2012.05.005.

Baccolo, Giovanni, Giannantonio Cibin, Barbara Delmonte, Dariush Hampai, Augusto Marcelli, Elena Di Stefano, Salvatore Macis, and Valter Maggi (2018). "The Contribution of Synchrotron Light for the Characterization of Atmospheric Mineral Dust in Deep Ice Cores: Preliminary Results from the Talos Dome Ice Core (East Antarctica)." In: *Condensed Matter* 3.3. ISSN: 2410-3896. DOI: 10.3390/condmat3030025. URL: http://www.mdpi.com/2410-3896/3/3/25.

Bader, Henri (1951). "Introduction to Ice Petrofabrics." In: *The Journal of Geology - Glaciological Issue* 59.6, pp. 519–536.

Baker, I. (2003). "Imaging Dislocations in Ice." In: *Microsc. Res. Techn.* 62, pp. 70–82.

Baker, I, D Cullen, and D Iliescu (2003). "The microstructural location of impurities in ice." In: *Canadian Journal of Physics* 81.1-2, pp. 1–9. DOI: 10.1139/p03-030. eprint: http://dx.doi.org/10.1139/p03-030. URL: http://dx.doi.org/10.1139/p03-030.

Bargmann, S., H. Seddik, and R. Greve (2012). "Computational modeling of flow-induced anisotropy of polar ice for the EDML deep drilling site, Antarctica: the effect of rotation recrystallization and grain boundary migration." In: *Int. J. Numer. Anal. Meth. Geomech* 36 (7), pp. 892–917. DOI: 10.1002/nag.1034.

Barletta, Robert E., John C. Priscu, Heidy M. Mader, Warren L. Jones, and Christopher H. Roe (2012). "Chemical analysis of ice vein microenvironments: II. Analysis of glacial samples from Greenland and Antarctica." In: *Journal of Glaciology* 58.212, pp. 1109–1118. ISSN: 0022-1430. DOI: doi:10.3189/2012JoG12J112. URL: http://www.ingentaconnect.com/content/igsoc/jog/2012/00000058/00000212/art00007.

Barnes, Piers R. F. (2003). "Comment on "Grain boundary ridge on sintered bonds between ice crystals" [J. Appl. Phys. 90, 5782 (2001)]." In: *J. Appl. Phys.* 93, pp. 783–785. DOI: 10.1063/1.1521800.

Barnes, Piers R. F., Robert Mulvaney, Kenneth Robinson, and Eric W. Wolff (2002). "Observations of polar ice from the Holocene and the glacial period using the scanning electron microscope." In: *Annals of Glaciology* 35.1, pp. 559–566. ISSN: 0260-3055. DOI: 10.3189/172756402781816735. URL: http://www.ingentaconnect.com/content/igsoc/agl/2002/00000035/00000001/art00089.

Bartels-Rausch, T., H.-W. Jacobi, T. F. Kahan, J. L. Thomas, E. S. Thomson, J. P. D. Abbatt, M. Ammann, J. R. Blackford, H. Bluhm, C. Boxe, F. Dominé, M. M. Frey, I. Gladich, M. I. Guzmán, D. Heger, Th. Huthwelker, P. Klán, W. F. Kuhs, M. H. Kuo, S. Maus, S. G. Moussa, V. F. McNeill, J. T. Newberg, J. B. C. Pettersson, M. Roeselová, and J. R. Sodeau (2014). "A review of air–ice chemical and physical interactions (AICI): liquids, quasi-liquids, and solids in snow." In: *Atmospheric*

Chemistry and Physics 14.3, pp. 1587–1633. DOI: 10.5194/acp-14-1587-2014. URL: https://www.atmos-chem-phys.net/14/1587/2014/.

Bartels-Rausch, Thorsten, Vance Bergeron, Julyan H. E. Cartwright, Rafael Escribano, John L. Finney, Hinrich Grothe, Pedro J. Gutierrez, Jari Haapala, Werner F. Kuhs, Jan B. C. Pettersson, Stephen D. Price, C. Ignacio Sainz-Diaz, Debbie Stokes, Giovanni Strazzulla, Erik S. Thomson, Hauke Trinks, and Nevin Uras-Aytemiz (2012). "Ice structures, patterns, and processes: A view across the icefields." In: *Reviews of Modern Physics*.

Becker, J.K., P.D. Bons, and M.W. Jessell (2008). "A new front-tracking method to model anisotropic grain and phase boundary motion in rocks." In: *Computers & Geosciences* 34.3, pp. 201–212. DOI: 10.1016/j.cageo.2007.03.013.

Bendel, Verena, Kai J. Ueltzhöffer, Johannes Freitag, Sepp Kipfstuhl, Werner F. Kuhs, Christoph S. Garbe, and Sérgio H. Faria (2013). "High-resolution variations in size, number and arrangement of air bubbles in the EPICA DML (Antarctica) ice core." In: *Journal of Glaciology* 59.217, pp. 972–980. DOI: doi:10.3189/2013JoG12J245. URL: http://www.ingentaconnect.com/content/igsoc/jog/2013/00000059/00000217/art00015.

Berg, W. J. van de, M. R. van den Broeke, C. H. Reijmer, and E. van Meijgaard (2006). "Reassessment of the Antarctic surface mass balance using calibrated output of a regional atmospheric climate model." In: *Journal of Geophysical Research* 111.D11. DOI: 10.1029/2005jd006495.

Binder, T., C.S. Garbe, D. Wagenbach, J. Freitag, and S. Kipfstuhl (2013). "Extraction and parameterization of grain boundary networks, using a dedicated method of automatic image analysis." In: *Journal of Microscopy* 250, pp. 130–141. DOI: 10.1111/jmi.12029.

Binder, Tobias. *Ice Microstructure Analyzer*. http://www.ice-image.org/. Accessed: 2019-01-10.

Binder, Tobias (2014). "Measurements of grain boundary networks in deep polar ice cores - A digital image processing approach." PhD thesis. Naturwissenschaftlich-Mathematischen Gesamtfakultät der Ruprecht-Karls-Universität Heidelberg. URL: http://hci.iwr.uni-heidelberg.de/Staff/tobinder/BinderDissertation_final.pdf.

Bindschadler, Robert A., Sophie Nowicki, Ayako Abe-Ouchi, Andy Aschwanden, Hyeungu Choi, Jim Fastook, Glen Granzow, Ralf Greve, Gail Gutowski, Ute Herzfeld, Charles Jackson, Jesse Johnson, Constantine Khroulev, Anders Levermann, William H. Lipscomb, Maria A. Martin, Mathieu Morlighem, Byron R. Parizek, David Pollard, Stephen F. Price, Diandong Ren, Fuyuki Saito, Tatsuru Sato, Hakime Seddik, Helene Seroussi, Kunio Takahashi, Ryan Walker, and Wei Li Wang (2013). "Ice-sheet model sensitivities to environmental forcing and their use in projecting future sea level (the SeaRISE project)." In: *Journal of Glaciology* 59.214, pp. 195–224. DOI: 10.3189/2013jog12j125.

Blackford, Jane R. (2007). "Sintering and microstructure of ice: a review." In: *J. Phys. D: Appl. Phys.* 40, R355–R385. DOI: 10.1088/0022-3727/40/21/R02.

Blunier, Thomas and Edward J. Brook (2001). "Timing of Millennial-Scale Climate Change in Antarctica and Greenland During the Last Glacial Period." In: *Science* 291.5501, pp. 109–112. DOI: 10.1126/science.291.5501.109.

Bohleber, Pascal, Dietmar Wagenbach, W. Schöner, and R. Böhm (2013). "To what extent do water isotope records from low accumulation Alpine ice cores reproduce instrumental temperature series?" In: *Tellus B* 65, pp. 1–17. DOI: 10.3402/tellusb.v65i0.20148.

Bohleber, Pascal, Tobias Erhardt, Nicole Spaulding, Helene Hoffmann, Hubertus Fischer, and Paul Mayewski (2018). "Temperature and mineral dust variability recorded in two low-accumulation Alpine ice cores over the last millennium." In: *Clim. Past* 14, 21–37. DOI: 10.5194/cp-14-21-2018. URL: https://doi.org/10.5194/cp-14-21-2018.

Bons, Paul D., Daniela Jansen, Felicitas Mundel, Catherine C. Bauer, Tobias Binder, Olaf Eisen, Mark W. Jessell, Maria-Gema Llorens, Florian Steinbach, Daniel Steinhage, and Ilka Weikusat (Apr. 2016). "Converging flow and anisotropy cause large-scale folding in Greenland's ice sheet." In: *Nat Commun* 7, p. 11427. DOI: 10.1038/ncomms11427.

Bons, Paul D., Thomas Kleiner, Maria-Gema Llorens, David J. Prior, Till Sachau, Ilka Weikusat, and Daniela Jansen (2018). "Greenland Ice Sheet - Higher non-linearity of ice flow significantly reduces estimated basal motion." In: *Geophysical Research Letters* 45.13, pp. 6542–6548. DOI: 10.1029/2018GL078356.

Bons, P.D., D. Koehn, and M.W. Jessell (2008). *Microdynamic Simulation*. Ed. by P.D. Bons, D. Köhn, and M.W. Jessell. Vol. Lecture Notes in Earth Sciences 106. 106. Springer, Berlin, p. 404.

Borthwick, V. E., S. Piazolo, L. Evans, A. Griera, and P. D. Bons (2013). "What happens to deformed rocks after deformation? A refined model for recovery based on numerical simulations." In: *Geological Society, London, Special Publications* 394.1, pp. 215–234. DOI: 10.1144/sp394.11.

Breton, Daniel J., Ian Baker, and David M. Cole (2016). "Microstructural evolution of polycrystalline ice during confined creep testing." In: *Cold Regions Science and Technology* 127, pp. 25–36. DOI: 10.1016/j.coldregions.2016.03.009.

Brovchenko, Ivan and Alla Oleinikova (2008). "Multiple Phases of Liquid Water." In: *ChemPhysChem* 9.18, pp. 2660–2675. DOI: 10.1002/cphc.200800639.

Budd, W. F. and T. H. Jacka (1989). "A review of ice rheology for ice sheet modelling." In: *Cold Reg. Sci. Technol.* 16, pp. 107–144.

Bueler, Ed and Jed Brown (2009). "Shallow shelf approximation as a "sliding law" in a thermomechanically coupled ice sheet model." In: *Journal of Geophysical Research* 114.F3. DOI: 10.1029/2008jf001179.

Bueler, Ed, Jed Brown, and Craig Lingle (July 2007). "Exact solutions to the thermomechanically coupled shallow-ice approximation: effective tools for verification." In: *Journal of Glaciology* 53, 499–516(18). DOI: doi:10.3189/002214307783258396. URL: http://www.ingentaconnect.com/content/igsoc/jog/2007/00000053/00000182/art00019.

Bunge, H. J. (Sept. 3, 2013). *Texture Analysis in Materials Science*. Elsevier Science. 614 pp. URL: https://www.ebook.de/de/product/23286873/h_j_bunge_texture_analysis_in_materials_science.html.

Calov, R., A. Sawin, R. Greve, I. Hansen, and K. Hutter (1998). "Simulation of the Antarctic ice sheet with a three-dimensional polythermal ice-sheet model, in support of the EPICA project." In: *Ann. Glac.* 27 (1), pp. 201–206. DOI: 10.3198/1998AoG27-1-201-206. URL: https://doi.org/10.3198/1998AoG27-1-201-206.

Castelnau, O., P. Duval, M. Montagnat, and R. Brenner (2008). "Elastoviscoplastic micromechanical modeling of the transient creep of ice." In: *Journal of Geophysical Research* 113.B11. DOI: 10.1029/2008jb005751.

Chaplin, Martin. *Water Structure and Science*. http://www1.lsbu.ac.uk/water/water_anomalies.html. Accessed: 2018-11-20.

Chauve, T., M. Montagnat, S. Piazolo, B. Journaux, J. Wheeler, F. Barou, D. Mainprice, and A. Tommasi (2017). "Non-basal dislocations should be accounted for

in simulating ice mass flow." In: *Earth and Planetary Science Letters* 473.Supplement C, pp. 247 –255. ISSN: 0012-821X. DOI: https://doi.org/10.1016/j.epsl.2017.06.020. URL: http://www.sciencedirect.com/science/article/pii/S0012821X17303308.

Colbeck, S. C. (1983). "Theory of metamorphism of dry snow." In: *Journal of Geophysical Research: Oceans* 88.C9, pp. 5475–5482. DOI: 10.1029/jc088ic09p05475.

Comiso, Josefino C. (2000). "Variability and Trends in Antarctic Surface Temperatures from In Situ and Satellite Infrared Measurements." In: *Journal of Climate* 13.10, pp. 1674–1696. DOI: 10.1175/1520-0442(2000)013<1674:vatias>2.0.co;2.

Cuffey, K. M. (2006). "Glacier Science and Environmental Change, Knight, P.G. (ed.)" In: ed. by P. G. Knight. Blackwell Publishing. Chap. Manifestation of ice microphysical processes at the scale of the whole ice sheet, pp. 290–300.

Cuffey, K. M., Th. Thorsteinsson, and E. D. Waddington (2000a). "A renewed argument for crystal size control of ice sheet strain rates." In: *J. Geophys. Res.* 105.B12, pp. 27,889–27,894.

Cuffey, K. M., H. Conway, A. Gades, B. Hallet, C. F. Raymond, and S. Whitlow (2000b). "Deformation properties of subfreezing glacier ice: Role of crystal size, chemical impurities, and rock particles inferred from in situ measurements." In: *J. Geophys. Res.* 105.B12, pp. 27,895–27,916.

Cuffey, K.M. and W.S.B. Paterson (2010). *The Physics of Glaciers*. Elsevier Science. ISBN: 9780080919126.

Cullen, D. and I. Baker (2001). "Observation of Impurities in Ice." In: *Microsc. Res. Techn.* 55, pp. 198–207.

Dahl-Jensen, D. and N. S. Gundestrup (1987). "Constitutive properties of ice at Dye3, Greenland." In: *The physical basis of ice sheet modelling*. Ed. by E. D. Waddington and J. S. Walder. IAHS Publication 170, pp. 31–43.

Dahl-Jensen, D., T. Thorsteinsson, R. Alley, and H. Shoji (1997). "Flow properties of the ice from the Greenland Ice Core Project ice core: The reason for folds?" In: *Journal of Geophysical Research: Oceans* 102.C12, pp. 26831–26840. ISSN: 2156-2202. DOI: 10.1029/97JC01266. URL: http://dx.doi.org/10.1029/97JC01266.

Dansgaard, W. (1953). "The Abundance of O18 in Atmospheric Water and Water Vapour." In: *Tellus* 5.4, pp. 461–469. DOI: 10.1111/j.2153-3490.1953.tb01076.x.

Dansgaard, W. (1964). "Stable isotopes in precipitation." In: *Tellus* 16.4, pp. 436–468. DOI: 10.1111/j.2153-3490.1964.tb00181.x.

Dansgaard, W. and S. J. Johnsen (1969). "A Flow Model and a Time Scale for the Ice Core from Camp Century, Greenland." In: *Journal of Glaciology* 8.53, 215–223. DOI: 10.3189/S0022143000031208.

Dansgaard, W., S. J. Johnsen, J. Møller, and C. C. Langway (1969). "One Thousand Centuries of Climatic Record from Camp Century on the Greenland Ice Sheet." In: *Science* 166.3903, pp. 377–380. ISSN: 0036-8075. DOI: 10.1126/science.166.3903.377. eprint: http://science.sciencemag.org/content/166/3903/377.full.pdf. URL: http://science.sciencemag.org/content/166/3903/377.

Dansgaard, W., H. B. Clausen, N. Gundestrup, C. U. Hammer, S. F. Johnsen, P. M. Kristinsdottir, and N. Reeh (1982). "A New Greenland Deep Ice Core." In: *Science* 218.4579, pp. 1273–1277. ISSN: 0036-8075. DOI: 10.1126/science.218.4579.1273. eprint: http://science.sciencemag.org/content/218/4579/1273.full.pdf. URL: http://science.sciencemag.org/content/218/4579/1273.

Dash, J. G., A. W. Rempel, and J. S. Wettlaufer (2006). "The physics of premelted ice and its geophysical consequences." In: *Reviews of Modern Physics* 78.3, pp. 695–741. DOI: 10.1103/revmodphys.78.695.

De La Chapelle, S., O. Castelnau, V. Lipenkov, and P. Duval (1998). "Dynamic recrystallization and texture development in ice as revealed by the study of deep ice cores in Antarctica and Greenland." In: *J. Geophys. Res.* 103.B3, pp. 5.091–5,106.

Della Lunga, D., W. Müller, S. O. Rasmussen, A. Svensson, and P. Vallelonga (2017). "Calibrated cryo-cell UV-LA-ICPMS elemental concentrations from the NGRIP ice core reveal abrupt, sub-annual variability in dust across the GI-21.2 interstadial period." In: *The Cryosphere* 11.3, pp. 1297–1309. DOI: 10.5194/tc-11-1297-2017.

Della Lunga, Damiano, Wolfgang Müller, Sune Olander Rasmussen, and Anders Svensson (2014). "Location of cation impurities in NGRIP deep ice revealed by cryo-cell UV-laser-ablation ICPMS." In: *Journal of Glaciology* 60.223, pp. 970–988. ISSN: 0022-1430. DOI: 10.3189/2014JoG13J199.

Diez, A. and O. Eisen (2015). "Seismic wave propagation in anisotropic ice – Part 1: Elasticity tensor and derived quantities from ice-core properties." In: *The Cryosphere* 9.1, pp. 367–384. DOI: 10.5194/tc-9-367-2015. URL: http://www.the-cryosphere.net/9/367/2015/.

Diez, A., O. Eisen, I. Weikusat, J. Eichler, C. Hofstede, P. Bohleber, T. Bohlen, and U. Polom (2014). "Influence of ice crystal anisotropy on seismic velocity analysis." In: *Ann. Glaciol.* 55.67, pp. 97–106. DOI: 10.3189/2014AoG67A002.

Diez, A., O. Eisen, C. Hofstede, A. Lambrecht, C. Mayer, H. Miller, D. Steinhage, T. Binder, and I. Weikusat (2015). "Seismic wave propagation in anisotropic ice – Part 2: Effects of crystal anisotropy in geophysical data." In: *The Cryosphere* 9.1, pp. 385–398. DOI: 10.5194/tc-9-385-2015. URL: https://www.the-cryosphere.net/9/385/2015/.

DiPrinzio, C. L., L. A. Wilen, Richard B. Alley, J. J. Fitzpatrick, M. K. Spencer, and A. J. Gow (2005). "Fabric and texture at Siple Dome, Antarctica." In: *J. Glaciol.* 51.173, pp. 281–290.

Dominé, F. and P. B. Shepson (Aug. 2002). "Air-Snow Interactions and Atmospheric Chemistry." In: *Science* 297, pp. 1506–1510. DOI: 10.1126/science.1074610.

Drews, R., O. Eisen, I. Weikusat, S. Kipfstuhl, A. Lambrecht, D. Steinhage, F. Wilhelms, and H. Miller (2009). "Layer disturbances and the radio-echo free zone in ice sheets." In: *The Cryosphere* 3, pp. 195–203. URL: www.the-cryosphere.net/3/195/2009/.

Drews, R., O. Eisen, D. Steinhage, I. Weikusat, S. Kipfstuhl, and F. Wilhelms (2012). "Potential mechanisms for anisotropy in ice-penetrating radar data." In: *J. Glaciol.* 58, p. 12. DOI: 10.3189/2012JoG11J114.

Drury, M. R. and J. L. Urai (1990). "Deformation-related recrystallization processes." In: *Tectonophysics* 172, pp. 235–253.

Drury, M.R. and G.M. Pennock (2007). "Subgrain Rotation Recrystallization in Minerals." In: *Materials Science Forum* 550, pp. 95–104. URL: http://www.scientific.net.

Durand, G., J. Weiss, V. Lipenkov, J. M. Barnola, G. Krinner, F. Parrenin, B. Delmonte, C. Ritz, P. Duval, R. Röthlisberger, and M. Bigler (2006a). "Effect of impurities on grain growth in cold ice sheets." In: *J. Geophys. Res.* 111.F1.

Durand, G., O. Gagliardini, Th. Thorsteinsson, A. Svensson, S. Kipfstuhl, and D. Dahl-Jensen (2006b). "Ice microstructure and fabric: an up-to-date approach for measuring textures." In: *J. Glaciol.* 52.179, pp. 619–630. DOI: 10.3189/172756506781828377.

Durand, G., F. Gillet-Chaulet, A. Svensson, O. Gagliardini, S. Kipfstuhl, J. Meyssonnier, F. Parrenin, P. Duval, and D. Dahl-Jensen (2007). "Change in ice rheology during climate variations - implications for ice flow modelling and dating of the EPICA Dome C core." In: *Clim. Past* 3, pp. 155–167.

Durand, G., A. Persson, D. Samyn, and A. Svensson (2008). "Relation between neighbouring grains in the upper part of the NorthGRIP ice core - Implications for rotation recrystallization." In: *Earth Planet. Sci. Lett.* 265, pp. 666–671.

Durand, G., A. Svensson, S. Kipfstuhl, A. Persson, O. Gagliardini, F. Gillet, J. Sjolte, M. Montagnat, and D. Dahl-Jensen (2009). "Evolution of the texture along the EPICA dome C ice core." In: *Low Temperature Science Supplement Issue*. Vol. 68. Nepal: Institute of Low Temperature Science, Hokkaido University, Sapporo Japan, pp. 91–106.

Duval, P. (1985). "Grain growth and mechanical behaviour of polar ice." In: *Ann. Glaciol.* 6, pp. 79–82.

Duval, P. and O. Castelnau (1995). "Dynamic recrystallisation of ice in polar ice sheets." In: *Journal de Physique* 5, pp. 197–205.

Duval, P., M. F. Ashby, and I. Anderman (1983). "Rate-Contolling Processes in the Creep of Polycrystalline Ice." In: *J. Phys. Chem.* 87, pp. 4066–4074.

Duval, Paul (1979). "Creep and recrystallization of polycrystalline ice." In: *Bulletin de Minéralogie* 102.2, pp. 80–85. DOI: 10.3406/bulmi.1979.7258.

Duval, Paul, Maurine Montagnat, Fanny Grennerat, Jerome Weiss, Jacques Meyssonnier, and Armelle Philip (2010). "Creep and plasticity of glacier ice: a material science perspective." In: *Journal of Glaciology* 56.200, pp. 1059–1068. DOI: doi:10.3189/002214311796406185. URL: http://www.ingentaconnect.com/content/igsoc/jog/2010/00000056/00000200/art00010.

Ebner, P. P., H. C. Steen-Larsen, B. Stenni, M. Schneebeli, and A. Steinfeld (2017). "Experimental observation of transient δ^{18}O interaction between snow and advective airflow under various temperature gradient conditions." In: *The Cryosphere* 11.4, pp. 1733–1743. DOI: 10.5194/tc-11-1733-2017. URL: https://www.the-cryosphere.net/11/1733/2017/.

Eichler, Jan (2013). "C-Axis Analysis of the NEEM Ice Core – An Approach based on Digital Image Processing." MA thesis. Fachbereich Physik, Freie Universität Berlin *Alfred-Wegener-Institut Helmholtz-Zentrum für Polar- und Meeresforschung. URL: http://epic.awi.de/33070/.

Eichler, Jan, Ilka Weikusat, and Sepp Kipfstuhl (2013). *C-axis fabric analysis of ice samples collected from the NEEM ice core*. data set. DOI: 10.1594/PANGAEA.838063.

Eichler, Jan, Ina Kleitz, Maddalena Bayer-Giraldi, Daniela Jansen, Sepp Kipfstuhl, Wataru Shigeyama, Christian Weikusat, and Ilka Weikusat (2017). "Location and distribution of micro-inclusions in the EDML and NEEM ice cores using optical microscopy and in situ Raman spectroscopy." In: *The Cryosphere* 11.3, pp. 1075–1090. DOI: 10.5194/tc-11-1075-2017. URL: https://www.the-cryosphere.net/11/1075/2017/tc-11-1075-2017.pdf.

Eichler, Jan, Christian Weikusat, Anna Wegner, Birthe Twarloh, Melanie Behrens, Hubertus Fischer, Maria Hörhold, Daniela Jansen, Sepp Kipfstuhl, Urs Ruth, Frank Wilhelms, and Ilka Weikusat (2019). "Impurity Analysis and Microstructure Along the Climatic Transition From MIS 6 Into 5e in the EDML Ice Core Using Cryo-Raman Microscopy." In: *Frontiers in Earth Science* 7. DOI: 10.3389/feart.2019.00020.

Eisen, O., I. Hamann, S. Kipfstuhl, D. Steinhage, and F. Wilhelms (2007). "Direct evidence for radar reflector originating from changes in crystal-orientation fabric."

In: *The Cryosphere* 1, pp. 1–10. URL: http://www.the-cryosphere.net/recent_papers.html.

EPICA community members (2004). "Eight glacial cycles from an Antarctic ice core." In: *Nature* 429, pp. 623–628.

EPICA community members (2006). "One-to-one coupling of glacial climate variability in Greenland and Antarctica." In: *Nature* 444, pp. 195–198. DOI: doi:10.1038/nature05301.

EPICA Community Members (2010). *Stable oxygen isotopes of ice core EDML*. data set. DOI: 10.1594/PANGAEA.754444. URL: https://doi.org/10.1594/PANGAEA.754444.

Etheridge, D. M., L. P. Steele, R. L. Langenfelds, R. J. Francey, J.-M. Barnola, and V. I. Morgan (1996). "Natural and anthropogenic changes in atmospheric CO2 over the last 1000 years from air in Antarctic ice and firn." In: *Journal of Geophysical Research: Atmospheres* 101.D2, pp. 4115–4128. DOI: 10.1029/95JD03410. URL: https://agupubs.onlinelibrary.wiley.com/doi/abs/10.1029/95JD03410.

Faria, S. H. (2006). "Creep and recrystallization of large polycrystalline masses. III. Continuum theory of ice sheets." In: *Proceedings of the Royal Society A: Mathematical, Physical and Engineering Science* A462, pp. 2797–2816. DOI: doi:10.1098/rspa.2006.1698.

Faria, S. H. and S. Kipfstuhl (2005). "Comment on "Deformation of grain boundaries in polar ice" by G. Durand et al." In: *Europhys. Lett.* 71, pp. 873–874.

Faria, S. H., I. Hamann, S. Kipfstuhl, and H. Miller (2006). "Is Antarctica like a birthday cake? MPI für Mathematik in den Naturwissenschaften. Leipzig. Communication Preprint No. 33/06." MPI für Mathematik in den Naturwissenschaften. Leipzig. Communication Preprint No. 33/06. URL: $www.mis.mpg.de/preprints/2006/preprint2006_33.pdf$.

Faria, S. H., J. Freitag, and S. Kipfstuhl (2010). "Polar ice structure and the integrity of ice-core paleoclimate records." In: *Quat. Sci. Rev.* 29.1, pp. 338–351.

Faria, Sérgio H., Dimitri Ktitarev, and Kolumban Hutter (2002). "Modelling evolution of anisotropy in fabric and texture of polar ice." In: *Annals of Glaciology* 35, pp. 545–551. DOI: 10.3189/172756402781817040.

Faria, Sergio H., Sepp Kipfstuhl, Nobuhiko Azuma, Johannes Freitag, Ilka Weikusat, Mangir M. Murshed, and Werner F. Kuhs (2009). "Multiscale Structures in the Antarctic Ice Sheet Part I: Inland Ice." In: *Physics of Ice Core Records II*. Ed. by T. Hondoh. Vol. 2. PICR. Supplement Issue of Low Temperature Science, Vol. 68, pp. 39–59. DOI: 10013/epic.35759.

Faria, Sérgio H., Ilka Weikusat, and Nobuhiko Azuma (2014a). "The microstructure of polar ice. Part I: Highlights from ice core research." In: *Journal of Structural Geology* 61, pp. 2–20. DOI: 10.1016/j.jsg.2013.09.010. URL: http://www.sciencedirect.com/science/article/pii/S0191814113001740.

Faria, Sergio H., Ilka Weikusat, and Nobuhiko Azuma (2014b). "The microstructure of polar ice. Part I: Highlights from ice core research." In: *J. Struct. Geol.* 61. Microdynamics of Ice, pp. 2–20. ISSN: 0191-8141. DOI: 10.1016/j.jsg.2013.09.010.

Faria, Sérgio H., Ilka Weikusat, and Nobuhiko Azuma (2014c). "The microstructure of polar ice. Part II: State of the art." In: *Journal of Structural Geology* 61, pp. 21–49. DOI: 10.1016/j.jsg.2013.11.003. URL: http://www.sciencedirect.com/science/article/pii/S0191814113002009.

Faria, Sérgio Henrique, Sepp Kipfstuhl, and Anja Lambrecht (2018). *The EPICA-DML Deep Ice Core*. Springer-Verlag Berlin Heidelberg. DOI: 10.1007/978-3-662-55308-4.

Fierz, C., R.L. Armstrong, Y. Durand, P. Etchevers, E. Greene, D.M. McClung, K. Nishimura, P.K. Satyawali, and S.A. Sokratov (2009). "The International Classification for Seasonal Snow on the Ground." In: *IHP-VII Technical Documents in Hydrology (UNESCO-IHP, Paris)* 83, p. 90.

Fischer, H., J. Severinghaus, E. Brook, E. Wolff, M. Albert, O. Alemany, R. Arthern, C. Bentley, D. Blankenship, J. Chappellaz, T. Creyts, D. Dahl-Jensen, M. Dinn, M. Frezzotti, S. Fujita, H. Gallee, R. Hindmarsh, D. Hudspeth, G. Jugie, K. Kawamura, V. Lipenkov, H. Miller, R. Mulvaney, F. Parrenin, F. Pattyn, C. Ritz, J. Schwander, D. Steinhage, T. van Ommen, and F. Wilhelms (2013). "Where to find 1.5 million yr old ice for the IPICS "Oldest-Ice" ice core." In: *Climate of the Past* 9.6, pp. 2489–2505. DOI: 10.5194/cp-9-2489-2013. URL: https://www.clim-past.net/9/2489/2013/.

Fischer, Hubertus, Felix Fundel, Urs Ruth, Birthe Twarloh, Anna Wegner, Roberto Udisti, Silvia Becagli, Emiliano Castellano, Andrea Morganti, Mirko Severi, Eric Wolff, Genevieve Littot, Regine Röthlisberger, Rob Mulvaney, Manuel A. Hutterli, Patrik Kaufmann, Urs Federer, Fabrice Lambert, Matthias Bigler, Margareta Hansson, Ulf Jonsell, Martine de Angelis, Claude Boutron, Marie-Louise Siggaard-Andersen, Jorgen Peder Steffensen, Carlo Barbante, Vania Gaspari, Paolo Gabrielli, and Dietmar Wagenbach (2007). "Reconstruction of millennial changes in dust emission, transport and regional sea ice coverage using the deep EPICA ice cores from the Atlantic and Indian Ocean sector of Antarctica." In: *Earth Planet. Sci. Lett.* 260, pp. 340–354.

Fisher, D.A. and R.M. Koerner (1986). "On the Special Rheological Properties of Ancient Microparticle-Laden Northern Hemisphere Ice as Derived from Bore-Hole and Core Measurements." In: *Journal of Glaciology* 32.112, pp. 501–510. DOI: 10.1017/S0022143000012211.

Fitzpatrick, Joan J., Donald E. Voigt, John M. Fegyveresi, Nathan T. Stevens, Matthew K. Spencer, Jihong Cole-Dai, Richard B. Alley, Gabriella E. Jardine, Eric D. Cravens, Lawrence A. Wilen, T.J. Fudge, and Joseph R. Mcconnell (2014). "Physical properties of the WAIS Divide ice core." In: *Journal of Glaciology* 60.224, pp. 1181–1198. DOI: 10.3189/2014jog14j100.

Fliervoet, Timon F., Martyn R. Drury, and Prame N. Chopra (1999). "Crystallographic preferred orientations and misorientations in some olivine rocks deformed by diffusion or dislocation creep." In: *Tectonophysics* 303.1-4, pp. 1–27. ISSN: 0040-1951. DOI: DOI:10.1016/S0040-1951(98)00250-9. URL: http://www.sciencedirect.com/science/article/B6V72-3W06TVD-2/2/e297373d760005f704edd2c6b6a6617e.

Fortuin, J.P.F. and J. Oerlemans (1990). "Parameterization of the Annual Surface Temperature and Mass Balance of Antarctica." In: *Annals of Glaciology* 14, pp. 78–84. DOI: 10.3189/s0260305500008302.

Freitag, J., F. Wilhelms, and S. Kipfstuhl (2004). "Microstructure-dependent densification of polar firn derived from x-ray microtomography." In: *J. Glaciol.* 30, 243–250. DOI: hdl:10013/epic.19834.

Freitag, Johannes, Sepp Kipfstuhl, Thomas Laepple, and Frank Wilhelms (2013). "Impurity-controlled densification: a new model for stratified polar firn." In: *Journal of Glaciology* 59.218, pp. 1163–1169. DOI: 10.3189/2013JoG13J042. URL: http://www.igsoc.org/journal/59/218/j13J042.html.

Fretwell, P., H. D. Pritchard, D. G. Vaughan, J. L. Bamber, N. E. Barrand, R. Bell, C. Bianchi, R. G. Bingham, D. D. Blankenship, G. Casassa, G. Catania, D. Callens, H. Conway, A. J. Cook, H. F. J. Corr, D. Damaske, V. Damm, F. Ferraccioli, R. Forsberg, S. Fujita, Y. Gim, P. Gogineni, J. A. Griggs, R. C. A. Hindmarsh, P.

Holmlund, J. W. Holt, R. W. Jacobel, A. Jenkins, W. Jokat, T. Jordan, E. C. King, J. Kohler, W. Krabill, M. Riger-Kusk, K. A. Langley, G. Leitchenkov, C. Leuschen, B. P. Luyendyk, K. Matsuoka, J. Mouginot, F. O. Nitsche, Y. Nogi, O. A. Nost, S. V. Popov, E. Rignot, D. M. Rippin, A. Rivera, J. Roberts, N. Ross, M. J. Siegert, A. M. Smith, D. Steinhage, M. Studinger, B. Sun, B. K. Tinto, B. C. Welch, D. Wilson, D. A. Young, C. Xiangbin, and A. Zirizzotti (2013). "Bedmap2: improved ice bed, surface and thickness datasets for Antarctica." In: *The Cryosphere* 7.1, pp. 375–393. DOI: 10.5194/tc-7-375-2013. URL: http://www.the-cryosphere.net/7/375/2013/.

Frost, H. J. and M. F. Ashby (1982). *Deformation mechanism maps - The plasticity and creep of Metals and Ceramics*. Pergamon Press.

Fuentes-Landete, V., Christian Mitterdorfer, P. H. Handle, Guadalupe Ruiz, J. Bernard, Anatoli Bogdan, M. Seidl, Katrin Amann-Winkel, J. Stern, S. Fuhrmann, and Thomas Loerting (2015). "Crystalline and amorphous ices." In: *Proceedings of the International School of Physics "Enrico Fermi"*. Vol. 187. Water: Fundamentals as the Basis for Understanding the Environment and Promoting Technology, pp. 173–208.

Fujita, Shuji, Hideo Maeno, and Kenichi Matsuoka (2006). "Radio-wave depolarization and scattering within ice sheets: a matrix-based model to link radar and ice-core measurements and its application." In: *J. Glaciol.* 52.178, pp. 407–424. DOI: 10.3189/172756506781828548.

Fujita, Shuji, Motohiro Hirabayashi, Kumiko Goto-Azuma, Remi Dallmayr, Kazuhide Satow, Jiancheng Zheng, and Dorthe Dahl-Jensen (2014). "Densification of layered firn of the ice sheet at NEEM, Greenland." In: *Journal of Glaciology* 60.223, pp. 905–921. DOI: 10.3189/2014JoG14J006.

Fukazawa, H., K. Sugiyama, S. Mae, H. Narita, and T. Hondoh (1998a). "Acid ions at triple junction of Antarctic ice observed by Raman scattering." In: *Geophysical Research Letters* 25, pp. 2845–2848.

Fukazawa, Hiroshi, Ken Sugiyama, Shinji Mae, Hideki Narita, and Takeo Hondoh (1998b). "Acid ions at triple junction of Antarctic ice observed by Raman scattering." In: *Geophysical Research Letters* 25.15, pp. 2845–2848. ISSN: 1944-8007. DOI: 10.1029/98GL02178. URL: http://dx.doi.org/10.1029/98GL02178.

Gagliardini, O., G. Durand, and Wang. Y. (2004). "Grain area as a statistical weight for polycrystal constituents." In: *J. Glaciol.*

Galewsky, Joseph, Hans Christian Steen-Larsen, Robert D. Field, John Worden, Camille Risi, and Matthias Schneider (2016). "Stable isotopes in atmospheric water vapor and applications to the hydrologic cycle." In: *Reviews of Geophysics* 54.4, pp. 809–865. DOI: 10.1002/2015RG000512.

Gao, H. (1999). "Mechanism-based strain gradient plasticity? I. Theory." In: *Journal of the Mechanics and Physics of Solids* 47.6, pp. 1239–1263. DOI: 10.1016/s0022-5096(98)00103-3.

Gao, X. Q. and T. H. Jacka (1987). "The approach to similar tertiary creep rates for Antarctic core ice and laboratory prepared ice." In: *Le Journal de Physique Colloques* 48.C1, pp. 289–296. DOI: 10.1051/jphyscol:1987141.

Gerbi, Christopher C., Stephanie G. Mills, Steven Bernsen, Ian R. Lee, David Clemens-Sewall, Kate Hruby, Seth W. Campbell, Robert L. Hawley, Renee Clavette, Jacquelyn Bellefontaine, and Karl J. Kreutz (2018). "Crystallographic Orientations in the Lateral Margin of Jarvis Glacier, Eastern Alaska Range." In: AGU Fall Meeting, Washington D.C., 10 - 14 December 2018.

Gillet-Chaulet, Fabien, Richard C. A. Hindmarsh, Hugh F. J. Corr, Edward C. King, and Adrian Jenkins (2011). "In-situquantification of ice rheology and direct measurement of the Raymond Effect at Summit, Greenland using a phase-sensitive radar." In: *Geophysical Research Letters* 38.24. DOI: 10.1029/2011gl049843.

Glen, J. W. (1952). "Experiments on the Deformation of Ice." In: *Journal of Glaciology* 2.12, pp. 111–114. DOI: 10.3189/s0022143000034067.

Glen, J. W. (1955). "The creep of polycrystalline ice." In: *Proc. Roy. Soc. London* A228, pp. 519–538.

Glen, J.W. (1968). "The effect of hydrogen disorder on dislocation movement and plastic deformation of ice." English. In: *Physik der kondensierten Materie* 7.1, pp. 43–51. ISSN: 0031-9236. DOI: 10.1007/BF02422799. URL: http://dx.doi.org/10.1007/BF02422799.

Gödert, Günter and K. Hutter (1998). "Induced anisotropy in large ice shields: theory and its homogenization." In: *Continuum mechanics and thermodynamics* 10, pp. 293–318. URL: http://tubiblio.ulb.tu-darmstadt.de/14247/.

Golding, N., E.M. Schulson, and C.E. Renshaw (2012). "Shear localization in ice: Mechanical response and microstructural evolution of P-faulting." In: *Acta Materialia* 60.8, pp. 3616–3631. DOI: 10.1016/j.actamat.2012.02.051.

Goldsby, D. L. (2006). "Glacier Science and Environmental Change, Knight, P.G. (ed.)" In: ed. by P. G. Knight. Blackwell Publishing. Chap. Superplastic flow of ice relevant to glacier and ice-sheet mechanics, pp. 308–314.

Goldsby, D. L. and D. L. Kohlstedt (1997a). "Flow of Ice I by Dislocation, Grain Boundary Sliding, and Diffusion Processes." In: *28th Annual Lunar and Planetary Science Conference*. 28th Annual Lunar and Planetary Science Conference, March 17-21, 1997. Houston, TX, p. 429.

Goldsby, D. L. and D. L. Kohlstedt (1997b). "Grain boundary sliding in fine-grained Ice I." In: *Scr. Mater.* 37.9, 1399–1406 (8). DOI: 10.1016/S1359-6462(97)00246-7.

Goldsby, D. L. and D. L. Kohlstedt (2001). "Superplastic deformation of ice: experimental observations." In: *J. Geophys. Res. (Solid Earth)* 106.B6, pp. 11,017–11,030.

Goldsby, D.L., D.L. Kohlstedt, and R. Pappalardo (2001). "A composite flow law for water ice for use in modelling of glaciers, polar caps and icy planetary interiors." In: *Abstracts of the Lunar and Planetary Science Conference XXXII*.

Gow, A. J. (1969). "On the rates of growth of grains and crystals in south polar firn." In: *J. Glaciol.* 8.53, pp. 241–252.

Gow, A. J. and T. Williamson (1976). "Rheological implications of the internal structure and crystal fabrics of the West Antarctic ice sheet as revealed by deep core drilling at Byrd Station." In: *CRREL Rep.* 76.35, pp. 1665–1677.

Gow, A. J., D. A. Meese, R. B. Alley, J. J. Fitzpatrick, S. Anandakrishnan, G. A. Woods, and B. C. Elder (1997). "Physical and structural properties of the Greenland Ice Sheet Project 2 ice core: A review." In: *Journal of Geophysical Research: Oceans* 102.C12, pp. 26559–26575. DOI: 10.1029/97JC00165.

Gow, Anthony J. (1971). "Relaxation of Ice in Deep Drill Cores from Antarctica." In: *Journal of Geophysical Research* 76 (11), pp. 2533–2541.

Gow, Anthony J. and Debra A. Meese (2007). "The distribution and timing of tephra deposition at Siple Dome, Antarctica: possible climatic and rheologic implications." In: *Journal of Glaciology* 53.183, pp. 585–596. ISSN: 0022-1430. DOI: 10.3189/002214307784409270.

Graham, F. S., M. Morlighem, R. C. Warner, and A. Treverrow (2018). "Implementing an empirical scalar constitutive relation for ice with flow-induced polycrystalline anisotropy in large-scale ice sheet models." In: *The Cryosphere* 12.3, pp. 1047–1067. DOI: 10.5194/tc-12-1047-2018.

Greve, R. and H. Blatter (2009). *Dynamics of Ice Sheets and Glaciers*. Ed. by Kolumban Hutter. Advances in Geophysical and Environmental Mechanics and Mathematics. Springer-Verlag Berlin Heidelberg, p. 287. DOI: DOI10.1007/978-3-642-03415-2_10.

Greve, Ralf (1997). "Application of a Polythermal Three-Dimensional Ice Sheet Model to the Greenland Ice Sheet: Response to Steady-State and Transient Climate Scenarios." In: *Journal of Climate* 10.5, pp. 901–918. DOI: 10.1175/1520-0442(1997)010<0901:AOAPTD>2.0.CO;2. eprint: https://doi.org/10.1175/1520-0442(1997)010<0901:AOAPTD>2.0.CO;2. URL: https://doi.org/10.1175/1520-0442(1997)010<0901:AOAPTD>2.0.CO;2.

Griera, Albert, Maria-Gema Llorens, Enrique Gomez-Rivas, Paul D. Bons, Mark W. Jessell, Lynn A. Evans, and Ricardo Lebensohn (2013). "Numerical modelling of porphyroclast and porphyroblast rotation in anisotropic rocks." In: *Tectonophysics* 587. Deformation, Pophyroblasts and Mountain Building: A Special Issue in Honor of the Career Contributions of T.H. Bell, pp. 4 –29. ISSN: 0040-1951. DOI: http://dx.doi.org/10.1016/j.tecto.2012.10.008. URL: http://www.sciencedirect.com/science/article/pii/S0040195112006427.

Grinsted, Aslak, J. Moore, and S. Jevrejeva (2010). "Reconstructing sea level from paleo and projected temperatures 200 to 2100 AD." In: *Climate Dynamics* 34 (4). 10.1007/s00382-008-0507-2, pp. 461–472. ISSN: 0930-7575. URL: http://dx.doi.org/10.1007/s00382-008-0507-2.

GRIP Project Members (1993). "Climate instability during the last interglacial period recorded in the GRIP ice core." In: *Nature* 364. Corresponding author: David Peel, British Antarctic Survey, High Cross, Madingley Road, Cambridge CB3 0ET, UK Please be aware that these conclusions have been modified in the light of later findings. Please see later papers for more details., pp. 203–207.

Gundestrup, Niels S., Henrik B. Clausen, and B. Lyle Hansen (1994). "The UCPH borehole logger." In: *Memoirs of National Institute of Polar Research. Special issue* 49, pp. 224–233. ISSN: 03860744. URL: http://ci.nii.ac.jp/naid/110000010330/en/.

Gusmeroli, Alessio, Erin C. Pettit, Joseph H. Kennedy, and Catherine Ritz (2012). "The crystal fabric of ice from full-waveform borehole sonic logging." In: *J. Geophys. Res.* 117, F03021. DOI: 10.1029/2012JF002343.

Haasen, Peter (1994). *Physikalische Metallkunde*. Springer.

Hamann, I., Ch. Weikusat, N. Azuma, and S. Kipfstuhl (2007). "Evolution of ice crystal microstructures during creep experiments." In: *J. Glaciol.* 53.182, pp. 479–489.

Hamann, I., S. Kipfstuhl, A. Lambrecht, and N. Azuma (2008). "Deformation modes and geometries in the EPICA-DML ice core, Antarctica." In: *EPICA Open Science Conference, Venice, Italy, 10-13 November 2008*. DOI: 10013/epic.32065.d001.

Heilbronner, R. and S. Barrett (2014). *Image Analysis in Earth Sciences: Microstructures and Textures of Earth Materials*. Lecture notes in earth system sciences. Springer. ISBN: 9783642103438. URL: https://books.google.de/books?id=IeE_AAAAQBAJ.

Hellmann, Sebastian, Johanna Kerch, Andreas Bauder, and Hansruedi Maurer (2018). "Crystal orientation fabric analysis on ice core samples from a temperate Alpine glacier." In: 16th Swiss Geoscience Meeting, Bern, 1 Dec 2018.

Herron, S. L. and C. C. Langway (1982). "A comparison of ice fabrics and textures at Camp Century, Greenland and Byrd Station, Antarctica." In: *Ann. Glaciol.* 3, pp. 118–124.

Herwegh, M. and M.R. Handy (1998). "The origin of shape preferred orientations in mylonite: inferences from in-situ experiments on polycrystalline norcamphor."

In: *Journal of Structural Geology* 20.6, pp. 681 –694. ISSN: 0191-8141. DOI: http://dx.doi.org/10.1016/S0191-8141(98)00011-X. URL: http://www.sciencedirect.com/science/article/pii/S019181419800011X.

Herwegh, Marco, Mark R. Handy, and Renée Heilbronner (1997). "Temperature- and strain-rate-dependent microfabric evolution in monomineralic mylonite: evidence from in situ deformation of norcamphor." In: *Tectonophysics* 280.1-2, pp. 83–106. DOI: 10.1016/s0040-1951(97)00139-x.

Hidas, Károly, Andréa Tommasi, David Mainprice, Thomas Chauve, Fabrice Barou, and Maurine Montagnat (2017). "Microstructural evolution during thermal annealing of ice-I h." In: *Journal of Structural Geology* 99, pp. 31–44. DOI: 10.1016/j.jsg.2017.05.001.

Higashi, Akira (1967). "Ice crystal growth in a temperate glacier in Alaska." In: *Physics of Snow and Ice: Proceedings* 1.1, pp. 409–430.

Hirth, Greg and Jan Tullis (1992). "Dislocation creep regimes in quartz aggregates." In: *Journal of Structural Geology* 14.2, pp. 145 –159. ISSN: 0191-8141. DOI: http://dx.doi.org/10.1016/0191-8141(92)90053-Y. URL: http://www.sciencedirect.com/science/article/pii/019181419290053Y.

Hirth, John Price and Jens Lothe (1982). *Theory of Dislocations*. Second Edition. Malabar, Florida: Krieger Publishing Company, p. 857.

Hobbs, P. V. (1974). *Ice Physics*. Oxford University Press.

Hoelzle, Martin, G Darms, MP Lüthi, and S Suter (2011). "Evidence of accelerated englacial warming in the Monte Rosa area, Switzerland/Italy." In: *The Cryosphere* 5.1, pp. 231–243. DOI: 10.5194/tc-5-231-2011.

Hoffman, P. F. (1998). "A Neoproterozoic Snowball Earth." In: *Science* 281.5381, pp. 1342–1346. DOI: 10.1126/science.281.5381.1342.

Hoffmann, Helene, Susanne Preunkert, Michel Legrand, David Leinfelder, Pascal Bohleber, Ronny Friedrich, and Dietmar Wagenbach (2017). "A New Sample Preparation System for Micro-14C Dating of Glacier Ice with a First Application to a High Alpine Ice Core from Colle Gnifetti (Switzerland)." In: *Radiocarbon*, 1–17. DOI: 10.1017/RDC.2017.99.

Hofstede, Coen, Anja Diez, Olaf Eisen, D. Jansen, and Y. Kristoffersen (2012). "A combined Vibroseis-Explosive survey at Halvfarryggen, a local ice dome in East Antarctica." In: AGU Fall Meeting, San Francisco, 2 - 7 December 2012. URL: http://epic.awi.de/31890/.

Hondoh, T. (2010). "An Overview of Microphysical Processes in Ice Sheets: Toward Nanoglaciology." In: *Physics of Ice Core Records II*. Ed. by T. Hondoh. Vol. 68. Supplement Issue of Low Temperature Science 1-23.

Hooke, R. LeB. (1973). "Structure and flow in the margin of the Barnes Ice Cap, Baffin Island, N.W.T., Canada." In: *J. Glaciol.* 12.64, pp. 423–438.

Hooke, Roger LeB. (1981). "Flow law for polycrystalline ice in glaciers: Comparison of theoretical predictions, laboratory data, and field measurements." In: *Reviews of Geophysics* 19.4, p. 664. DOI: 10.1029/rg019i004p00664.

Horgan, H.J., S. Anandakrishnan, R.B. Alley, L.E. Peters, G.P. Tsoflias, D.E. Voigt, and J.P. Winberry (2008). "Complex fabric development revealed by englacial seismic reflectivity - Jakobshavn Isbrae, Greenland - DRAFT." In: *GRL*.

Hörhold, Maria, Thomas Laepple, Johannes Freitag, Matthias Bigler, Hubertus Fischer, and Sepp Kipfstuhl (2012). "On the impact of impurities on the densification of polar firn." In: *Earth and Planetary Science Letters* 325-32, pp. 93–99. DOI: 10.1016/j.epsl.2011.12.022.

Hudleston, Peter J (1980). "The progressive development of inhomogeneous shear and crystallographic fabric in glacial ice." In: *J. Struct. Geol.* 2.1-2, pp. 189–196. DOI: 10.1016/0191-8141(80)90049-8.

Hudleston, Peter J. (2015). "Structures and fabrics in glacial ice: A review." In: *Journal of Structural Geology* 81, pp. 1 –27. ISSN: 0191-8141. DOI: http://dx.doi.org/10.1016/j.jsg.2015.09.003. URL: http://www.sciencedirect.com/science/article/pii/S0191814115300365.

Humphreys, F. J. and M. Hatherly (2004). *Recrystallization and Related Annealing Phenomena*. Elsevier.

Hutter, Kolumban (1983). *Theoretical Glaciology*. Springer Netherlands. DOI: 10.1007/978-94-015-1167-4.

Huybrechts, P. (2007). "Ice Sheet Modeling." In: ed. by B. Riffenburgh. Routledge, New York and London. Chap. Encyclopedia of the Antarctic, pp. 514–517.

Huybrechts, P., O. Rybak, F. Pattyn, U. Ruth, and D. Steinhage (2007). "Ice thinning, upstream advection, and non-climatic biases for the upper 89% of the EDML ice core from a nested model of the Antarctic ice sheet." In: *Clim. Past* 3, pp. 577–589. URL: www.clim-past.net/3/577/2007/.

Hvidberg, Christine Schøtt, Jørgen Peder Steffensen, Henrik B. Clausen, Hitoshi Shoji, and Joseph Kipfstuhl (2002). "The NorthGRIP ice-core logging procedure: description and evaluation." In: *Annals of Glaciology* 35, pp. 5–8. DOI: 10.3189/172756402781817293.

Iizuka, Yoshinori, Shinichiro Horikawa, Toshimitsu Sakurai, Sigfus Johnson, Dorthe Dahl-Jensen, Jørgen Peder Steffensen, and Takeo Hondoh (2008). "A relationship between ion balance and the chemical compounds of salt inclusions found in the Greenland Ice Core Project and Dome Fuji ice cores." In: *Journal of Geophysical Research: Atmospheres* 113.D7. DOI: 10.1029/2007JD009018. eprint: https://agupubs.onlinelibrary.wiley.com/doi/pdf/10.1029/2007JD009018. URL: https://agupubs.onlinelibrary.wiley.com/doi/abs/10.1029/2007JD009018.

Iliescu, D. and I. Baker (2008). "Effects of impurities and their redistribution during recrystallization of ice crystals." In: *J. Glaciol.* 54.185, pp. 362–370.

IPCC (2013). "Climate Change 2013: The Physical Science Basis. Contribution of Working Group I to the Fifth Assessment Report of the Intergovernmental Panel on Climate Change." In: *[Stocker, T.F., D. Qin, G.-K. Plattner, M. Tignor, S.K. Allen, J. Boschung, A. Nauels, Y. Xia, V. Bex and P.M. Midgley (eds.)]. Cambridge University Press, Cambridge, United Kingdom and New York, NY, USA*, 1535 pp. DOI: 10.1017/CBO9781107415324. URL: http://www.climatechange2013.org/report/full-report/.

Jacka, T. H. (1984). "The time and strain required for development of minimum strain rates in ice." In: *Cold Reg. Sci. Technol.* 8.3, pp. 261–268.

Jacka, T. H. (1994). "Investigations of discrepancies between laboratory studies of the flow of ice: density, sample shape and size, and grain-size." In: *Ann. Glaciol.* 19, pp. 146–154.

Jacka, T. H. and L. Jun (1994). "The steady-state crystal size of deforming ice." In: *Ann. Glaciol.* 20, pp. 13–18.

Jacka, T. H. and M. Maccagnan (1984). "Ice crystallographic and strain rate changes with strain in compression and extension." In: *Cold Reg. Sci. Technol.* 269-286.3, p. 8.

Jansen, Daniela, Maria Gema Llorens, Julien Westhoff, Florian Steinbach, Sepp Kipfstuhl, Paul D. Bons, Albert Griera, and Ilka Weikusat (2016). "Small-scale disturbances in the stratigraphy of the NEEM ice core: observations and numerical

model simulations." In: *The Cryosphere* 10, pp. 359–370. DOI: 10.5194/tc-10-359-2016.

Jansen, Daniela, Ilka Weikusat, Thomas Kleiner, Frank Wilhelms, D. Dahl-Jensen, Andreas Frenzel, Tobias Binder, Jan Eichler, S. H. Faria, S. Sheldon, C. Panton, Sepp Kipfstuhl, and Heinrich Miller (2017). "In situ-measurement of ice deformation from repeated borehole logging of the EPICA Dronning Maud Land (EDML) ice core, East Antarctica." In: *EGU General Assembly*.

Jessell, M., P. Bons, L. Evans, T. Barr, and K. Stüwe (2001). "Elle: the numerical simulation of metamorphic and deformation microstructures." In:

Jessell, M.W. (1986). "Grain boundary migration and fabric development in experimentally deformed octachloropropane." In: *Journal of Structural Geology* 8.5, pp. 527–542. DOI: 10.1016/0191-8141(86)90003-9.

Johnsen, S. J., D. Dahl-Jensen, N. Gundestrup, J. P. Steffensen, H. B. Clausen, Heinrich Miller, V. Masson-Delmotte, A. E. Sveinbjörnsdottir, and J. White (2001). "Oxygen isotope and palaeotemperature records from six Greenland ice-core stations: Camp Century, Dye-3, GRIP, GISP2, Renland and NorthGRIP." In: *Journal of Quaternary Science* 16.4, pp. 299–307.

Jones, S. J. and J. W. Glen (1969). "The effect of dissolved impurities on the mechanical properties of ice crystals." In: *Philosophical Magazine* 19.157, pp. 13–24. DOI: 10.1080/14786436908217758. eprint: http://dx.doi.org/10.1080/14786436908217758. URL: http://dx.doi.org/10.1080/14786436908217758.

Jones, S.J. (1967). "Softening of ice crystals by dissolved fluoride ions." In: *Physics Letters A* 25.5, pp. 366 –367. ISSN: 0375-9601. DOI: http://dx.doi.org/10.1016/0375-9601(67)90702-5. URL: http://www.sciencedirect.com/science/article/pii/0375960167907025.

Jonsson, Stig (1970). "Structural studies of subpolar glacier ice." In: *Geografiska Annaler: Series A, Physical Geography* 52.2, pp. 129–145. DOI: 10.2307/520606.

Journaux, Baptiste, Thomas Chauve, Maurine Montagnat, Andrea Tommasi, Fabrice Barou, David Mainprice, and Léa Gest (2018). "Microstructure and texture evolution in polycrystalline ice during hot torsion. Impact of intragranular strain and recrystallization processes." In: *The Cryosphere Discussions*, pp. 1–25. DOI: 10.5194/tc-2018-213.

Jun, Li, T. H. Jacka, and Vin Morgan (1998). "Crystal-size and microparticle record in the ice core from Dome Summit South, Law Dome, East Antarctica." In: *Annals of Glaciology* 27, 343—348. DOI: 10.3189/1998AoG27-1-343-348.

Jun, Li, T. H. Jacka, and W. F. Budd (2000). "Strong single maximum crystal fabrics developed in ice undergoing shear with unconstrained normal deformation." In: *Ann. Glac.* 30, pp. 88–92.

Kamb, W. B. (1959). "Ice petrofabric observations from Blue Glacier, Washington, in relation to theory and experiment." In: *J. Geophys. Res.* 64(11), 1891–1909. DOI: 10.1029/JZ064i011p01891.. URL: http://www.agu.org/journals/jz/v064/i011/JZ064i011p01891/.

Karato, Shun-Ichiro (2008). *Deformation of Earth Materials - An Introduction to the Rheology of Solid Earth*. Cambridge University Press. ISBN: 9781139469562. URL: http://books.google.de/books?id=rZC7osgnyyYC.

Karlsson, N. B., T. Binder, G. Eagles, V. Helm, F. Pattyn, B. Van Liefferinge, and O. Eisen (2018). "Glaciological characteristics in the Dome Fuji region and new assessment for "Oldest Ice"." In: *The Cryosphere* 12.7, pp. 2413–2424. DOI: 10.5194/tc-12-2413-2018. URL: https://www.the-cryosphere.net/12/2413/2018/.

Kaufmann, P., Felix Fundel, Hubertus Fischer, M. Bigler, Urs Ruth, R. Udisti, M. Hansson, M. de Angelis, C. Barbante, E. W. Wolff, M. Hutterli, and D. Wagenbach

(2010). "Ammonium and non-sea-salt sulfate in the EPICA ice cores as indicator of biological activity in the Southern Ocean." In: *Quaternary Science Reviews* 29, pp. 313–323. DOI: 10.1016/j.quascirev.2009.11.009. URL: http://dx.doi.org/10.1016/j.quascirev.2009.11.009.

Kaufmann, Patrik R., Urs Federer, Manuel A. Hutterli, Matthias Bigler, Simon Schüpbach, Urs Ruth, Jochen Schmitt, and Thomas F. Stocker (2008). "An Improved Continuous Flow Analysis System for High-Resolution Field Measurements on Ice Cores." In: *Environmental Science & Technology* 42.21. PMID: 19031900, pp. 8044–8050. DOI: 10.1021/es8007722. eprint: http://dx.doi.org/10.1021/es8007722. URL: http://dx.doi.org/10.1021/es8007722.

Kennedy, Joseph H., Erin C. Pettit, and Carlos L. Di Prinzio (2013). "The evolution of crystal fabric in ice sheets and its link to climate history." In: *Journal of Glaciology* 59 (214), pp. 357–373. DOI: 10.3189/2013JoG12J159.

Kerch, J., O. Eisen, J. Eichler, T. Binder, P. Bohleber, J. Freitag, P. Bons, and I. Weikusat (2018a). DOI: 10.1594/PANGAEA.887838.

Kerch, J., A. Diez, I. Weikusat, and O. Eisen (2018b). "Deriving seismic velocities on the micro-scale from c-axis orientations in ice cores." In: *The Cryosphere Discuss.* Pp. 1–27. DOI: 10.5194/tc-2017-281.

Kerch, Johanna (2016). "Crystal-orientation fabric variations on the cm-scale in cold Alpine ice: Interaction with paleo-climate proxies under deformation and implications for the interpretation of seismic velocities." PhD thesis. Combined Faculties for the Natural Sciences and for Mathematics of the Ruperto-Carola University of Heidelberg, Germany. URL: http://archiv.ub.uni-heidelberg.de/volltextserver/22326/.

Ketcham, W. M. and P. V. Hobbs (1969). "An experimental determination of the surface energies of ice." In: *Phil. Mag.* 19, pp. 1161–73.

Kipfstuhl, S., I. Hamann, A. Lambrecht, J. Freitag, S.H. Faria, D. Grigoriev, and N. Azuma (2006). "Microstructure mapping: a new method for imaging deformation induced microstructural features of ice on the grain scale." In: *J. Glaciol.* 52.178, pp. 398–406.

Kipfstuhl, S., S. H. Faria, N. Azuma, J. Freitag, I. Hamann, P. Kaufmann, H. Miller, K. Weiler, and F. Wilhelms (2009). "Evidence of dynamic recrystallization in polar firn." In: *J. Geophys. Res.* 114, B05204. DOI: doi:10.1029/2008JB005583.

Kipfstuhl, Sepp (2010). *Large area scan macroscope images from the NEEM ice core*. unpublished dataset. DOI: 10.1594/PANGAEA.743296. URL: https://doi.pangaea.de/10.1594/PANGAEA.743296.

Kleitz, Ina (2015). "Analysis of physical properties and impurities in Greenland ice using optical and Raman microscopy." MA thesis. Martin-Luther Universität Halle-Wittenberg. URL: http://epic.awi.de/39465/.

Krischke, Anja, Ulrich Oechsner, and Sepp Kipfstuhl (2015). "Rapid Microstructure Analysis of Polar Ice Cores." In: *Optik & Photonik* 10.2, pp. 32–35. DOI: 10.1002/opph.201500016. URL: https://onlinelibrary.wiley.com/doi/abs/10.1002/opph.201500016.

Kuramoto, Takayuki, Kumiko Goto-Azuma, Motohiro Hirabayashi, Takayuki Miyake, Hideaki Motoyama, Dorthe Dahl-Jensen, and Jørgen Peder Steffensen (2011). "Seasonal variations of snow chemistry at NEEM, Greenland." In: *Annals of Glaciology*, pp. 193–200. DOI: 10.3189/172756411797252365.

Lambert, F., B. Delmonte, J. R. Petit, M. Bigler, P. R. Kaufmann, M. A. Hutterli, T. F. Stocker, Urs Ruth, J. P. Steffensen, and V. Maggi (2007). "Dust-climate couplings over the past 800,000 years from the EPICA Dome C ice core." In: *Nature* 452,

pp. 616–619. DOI: 10.1038/nature06763. URL: http://dx.doi.org/10.1038/nature06763.

Lambrecht, Anja, Josef Kipfstuhl, Frank Wilhelms, and Heinz Miller (2004). "Visual stratigraphy of the EDML ice core with a linescanner." Unpublished dataset No.208005. URL: http://doi.pangaea.de/10.1594/PANGAEA.208005.

Lebensohn, R. A. (2001). "N-site modeling of a 3D viscoplastic polycrystal using Fast Fourier Transform." In: *Acta Materialia* 49, pp. 2723–2737. DOI: 10.1016/S1359-6454(01)00172-0. URL: http://www.sciencedirect.com/science/article/pii/S1359645401001720.

Lebensohn, R. A., M. Montagnat, P. Mansuy, P. Duval, J. Meysonnier, and A. Philip (2009). "Modeling viscoplastic behavior and heterogeneous intracrystalline deformation of columnar ice polycrystals." English. In: *ACTA MATERIALIA* 57.5, 1405–1415. ISSN: 1359-6454. DOI: {10.1016/j.actamat.2008.10.057}.

Legrand, Michel and Paul Mayewski (1997a). "Glaciochemistry of polar ice cores: A review." In: *Reviews of Geophysics* 35.3, pp. 219–243. ISSN: 1944-9208. DOI: 10.1029/96RG03527. URL: http://dx.doi.org/10.1029/96RG03527.

Legrand, Michel and Paul Mayewski (1997b). "Glaciochemistry of polar ice cores: A review." In: *Reviews of Geophysics* 35.3, pp. 219–243. ISSN: 1944-9208. DOI: 10.1029/96RG03527. URL: http://dx.doi.org/10.1029/96RG03527.

Li, J., J. A. Vélez González, C. Leuschen, A. Harish, P. Gogineni, M. Montagnat, I. Weikusat, F. Rodriguez-Morales, and J. Paden (2018). "Multi-channel and multi-polarization radar measurements around the NEEM site." In: *The Cryosphere* 12.8, pp. 2689–2705. DOI: 10.5194/tc-12-2689-2018. URL: https://www.the-cryosphere.net/12/2689/2018/.

Li, Yuan, Sepp Kipfstuhl, and Moahuan Huang (2017). "Ice Microstructure and Fabric of Guliya Ice Cap in Tibetan Plateau, and Comparisons with Vostok3G-1, EPICA DML, and North GRIP." In: *Crystals* 7.4. DOI: 10.3390/cryst7040097.

Licciulli, Carlo (2018). "Full Stokes ice-flow modeling of the high-Alpine glacier saddle Colle Gnifetti, Monte Rosa: Flow
field characterization for an improved interpretation of the ice-core records." PhD thesis. Combined Faculties for the Natural Sciences and for Mathematics of the Ruperto-Carola University of Heidelberg, Germany. URL: http://archiv.ub.uni-heidelberg.de/volltextserver/23981/.

Liefferinge, Brice Van, Frank Pattyn, Marie G. P. Cavitte, Nanna B. Karlsson, Duncan A. Young, Johannes Sutter, and Olaf Eisen (2018). "Promising Oldest Ice sites in East Antarctica based on thermodynamical modelling." In: *The Cryosphere* 12.8, pp. 2773–2787. DOI: 10.5194/tc-12-2773-2018.

Lipenkov, V. Y., N. I. Barkov, P. Duval, and P. Pimienta (1989). "Crystalline texture of the 2083 m ice core at vostok station, Antarctica." In: *J. Glaciol.* 35.121, pp. 392–398.

Lliboutry, L. and P. Duval (1985). "Various isotropic and anisotropic ices found in glaciers and polar ice caps and their corresponding rheologies." In: *Annales Geophysicae* 3(2), pp. 207–224.

Llorens, Maria Gema, Albert Griera, Paul D. Bons, Jens Roessiger, Ricardo Lebensohn, Lynn Evans, and Ilka Weikusat (2016a). "Dynamic recrystallisation of ice aggregates during co-axial viscoplastic deformation: a numerical approach." In: *Journal of Glaciology* 62.232, pp. 359–377. DOI: 10.1017/jog.2016.28. URL: http://journals.cambridge.org/action/displayAbstract?fromPage=online&aid=10354953&fileId=S0022143016000289.

Llorens, Maria Gema, Albert Griera, Paul D. Bons, Ricardo A. Lebensohn, Lynn A. Evans, Daniela Jansen, and Ilka Weikusat (2016b). "Full-field predictions of ice

dynamic recrystallisation under simple shear conditions." In: *Earth and Planetary Science Letters* 450, pp. 233–242. DOI: 10.1016/j.epsl.2016.06.045. URL: http://www.sciencedirect.com/science/article/pii/S0012821X16303326.

Llorens, Maria-Gema, Albert Griera, Florian Steinbach, Paul D. Bons, Enrique Gomez-Rivas, Daniela Jansen, Jens Roessiger, Ricardo A. Lebensohn, and Ilka Weikusat (2017). "Dynamic recrystallization during deformation of polycrystalline ice: insights from numerical simulations." In: *Philosophical Transactions of the Royal Society of London A: Mathematical, Physical and Engineering Sciences* 375.2086, 20150346 (1–24). ISSN: 1364-503X. DOI: 10.1098/rsta.2015.0346. eprint: http://rsta.royalsocietypublishing.org/content/375/2086/20150346.full.pdf. URL: http://rsta.royalsocietypublishing.org/content/375/2086/20150346.

Lorius, C., Merlivat, J. Jouzel, and Pourchet (1979). "A 30,000-yr isotope climatic record from Antarctic ice." In: *Nature* 280, pp. 644–648.

Loulergue, Laetitia, Adrian Schilt, Renato Spahni, Valérie Masson-Delmotte, Thomas Blunier, Bénédicte Lemieux, Jean-Marc Barnola, Dominique Raynaud, Thomas F. Stocker, and Jérôme Chappellaz (2008). "Orbital and millennial-scale features of atmospheric CH4 over the past 800,000 years." In: *Nature* 453.7193, pp. 383–386. DOI: 10.1038/nature06950.

Mangeney, Anne, Francesco Califano, and Kolumban Hutter (1997). "A numerical study of anisotropic, low Reynolds number, free surface flow for ice sheet modeling." In: *Journal of Geophysical Research: Solid Earth* 102.B10, pp. 22749–22764. DOI: 10.1029/97jb01697.

Martin, C. and G. H. Gudmundsson (2012). "Effects of nonlinear rheology, temperature and anisotropy on the relationship between age and depth at ice divides." In: *The Cryosphere* 6.5, pp. 1221–1229. DOI: 10.5194/tc-6-1221-2012. URL: http://www.the-cryosphere.net/6/1221/2012/.

Martin, Carlos, G. Hilmar Gudmundsson, Hamish D. Pritchard, and Olivier Gagliardini (2009). "On the effects of anisotropic rheology on ice flow, internal structure, and the age-depth relationship at ice divides." In: *J. Geophys. Res. Lett.* 114, F04001. DOI: 10.1029/2008JF001204.

Martin, M. A., R. Winkelmann, M. Haseloff, T. Albrecht, E. Bueler, C. Khroulev, and A. Levermann (2011). "The Potsdam Parallel Ice Sheet Model (PISM-PIK) â€“ Part 2: Dynamic equilibrium simulation of the Antarctic ice sheet." In: *The Cryosphere* 5.3, pp. 727–740. DOI: 10.5194/tc-5-727-2011. URL: http://www.the-cryosphere.net/5/727/2011/.

Mathiesen, J., J. Ferkinghoff-Borg, M. H. Jensen, M. Levinsen, P. Olesen, D. Dahl-Jensen, and A. Svensson (2004). "Dynamics of crystal formation in the Greenland NorthGRIP Ice Core." In: *J. Glaciol.* 50.170, pp. 325–328.

Matsuoka, Kenichi, Teruo Furukawa, Shuji Fujita, Hideo Maeno, Seiho Uratsuka, Renji Naruse, and Okitsugu Watanabe (2003). "Crystal orientation fabrics within the Antarctic ice sheet revealed by a multipolarization plane and dual-frequency radar survey." In: *J. Geophys. Res.* 108.B10. DOI: 10.1029/2003JB002425.

Maule, Cathrine Fox, Michael E. Purucker, Nils Olsen, and Klaus Mosegaard (2005). "Heat Flux Anomalies in Antarctica Revealed by Satellite Magnetic Data." In: *Science* 309.5733, pp. 464–467. ISSN: 0036-8075. DOI: 10.1126/science.1106888. eprint: http://science.sciencemag.org/content/309/5733/464.full.pdf. URL: http://science.sciencemag.org/content/309/5733/464.

Mayewski, P. A., M. P. Meredith, C. P. Summerhayes, J. Turner, A. Worby, P. J. Barrett, G. Casassa, N. A. N. Bertler, T. Bracegirdle, A. C. Naveira Garabato, D. Bromwich, H. Campbell, G. S. Hamilton, W. B. Lyons, K. A. Maasch, S. Aoki,

C. Xiao, and T. van Ommen (2009). "State of the Antarctic and Southern Ocean climate system." In: *Rev. Geophys.* 47.RG1003. URL: http://dx.doi.org/10.1029/2007RG000231.

McConnell, Joseph R., Ross Edwards, Gregory L. Kok, Mark G. Flanner, Charles S. Zender, Eric S. Saltzman, J. Ryan Banta, Daniel R. Pasteris, Megan M. Carter, and Jonathan D. W. Kahl (2007). "20th-Century Industrial Black Carbon Emissions Altered Arctic Climate Forcing." In: *Science* 317.5843, pp. 1381–1384. ISSN: 0036-8075. DOI: 10.1126/science.1144856. eprint: http://science.sciencemag.org/content/317/5843/1381.full.pdf. URL: http://science.sciencemag.org/content/317/5843/1381.

Means, W. D. (1983). "Microstructure and micromotion in recrystallization flow of octachloropropane: A first look." In: *Geologische Rundschau* 72.2, pp. 511–528. DOI: 10.1007/bf01822080.

Means, W.D. (1981). "The concept of steady-state foliation." In: *Tectonophysics* 78.1-4, pp. 179–199. DOI: 10.1016/0040-1951(81)90013-5.

Means, W.D. (1989). "Synkinematic microscopy of transparent polycrystals." In: *Journal of Structural Geology* 11.1–2, pp. 163 –174. ISSN: 0191-8141. DOI: 10.1016/0191-8141(89)90041-2. URL: http://www.sciencedirect.com/science/article/pii/0191814189900412.

Meer, S. De, M. R. Drury, J. H. P. De Bresser, and G. M. Pennock (2002). "Current issues and new developments in deformation mechanisms, rheology and tectonics." In: *Geological Society, London, Special Publications* 200.1, pp. 1–27. DOI: 10.1144/gsl.sp.2001.200.01.01.

Meier, Mark F, George P Rigsby, and Robert P Sharp (1954). "Preliminary data from Saskatchewan Glacier, Alberta, Canada." In: *Arctic* 7.1, pp. 3–26.

Mellor, Malcolm and Richard Testa (1969). "Effect of Temperature on the Creep of Ice." In: *Journal of Glaciology* 8.52, pp. 131–145. DOI: 10.3189/S0022143000020803.

Michalski, J. R. and P. B. Niles (Mar. 2011). "Formation of Jarosite in the Mawrth Vallis Region of Mars by Weathering Within Paleo-Ice Deposits." In: *Lunar and Planetary Science Conference*. Vol. 42. Lunar and Planetary Science Conference, p. 1926.

Mikesell, Thomas Dylan, Kasper van Wijk, Larry Thomas Otheim, Hans-Peter Marshall, and Andrei Kurbatov (2017). "Laser Ultrasound Observations of Mechanical Property Variations in Ice Cores." In: *Geosciences* 7.3. ISSN: 2076-3263. DOI: 10.3390/geosciences7030047.

Miyamoto, A., H. Shoji, A. Hori, T. Hondoh, H.B. Clausen, and O. Watanabe (2005). "Ice fabric evolution process understood from anisotropic distribution of a-axis orientation on the GRIP (Greenland) ice core." In: *Ann. Glaciol.* 42, pp. 47–52.

Moldovan, D., D. Wolf, and S.R. Phillpot (2001). "Theory of diffusion-accommodated grain rotation in columnar polycrystalline microstructures." In: *Acta Materialia* 49.17, pp. 3521–3532. DOI: 10.1016/s1359-6454(01)00240-3.

Montagnat, M., P. Duval, P. Bastie, B. Hamelin, and V. Y. Lipenkov (2003). "Lattice distortion in ice crystals from the Vostok core (Antarctica) revealed by hard X-ray diffraction; implication in the deformation of ice at low stresses." In: *Earth Planet. Sci. Lett.* 214, pp. 369–378. DOI: 10.1016/S0012-821X(03)00364-9.

Montagnat, M., D. Buiron, L. Arnaud, A. Broquet, P. Schlitz, R. Jacob, and S. Kipfstuhl (2012). "Measurements and numerical simulation of fabric evolution along the Talos Dome ice core, Antarctica." In: *Earth and Planetary Science Letters* 357-358, pp. 168–178. DOI: 10.1016/j.epsl.2012.09.025.

Montagnat, M., O. Castelnau, P.D. Bons, S.H. Faria, O. Gagliardini, F. Gillet-Chaulet, F. Grennerat, A. Griera, R.A. Lebensohn, H. Moulinec, J. Roessiger, and P. Suquet

(2013). "Multiscale modeling of ice deformation behavior." In: *J. Struct. Geol.* 61, pp. 78–108. DOI: 10.1016/j.jsg.2013.05.002.

Montagnat, M., N. Azuma, D. Dahl-Jensen, Jan Eichler, S. Fujita, F. Gillet-Chaulet, Sepp Kipfstuhl, D. Samyn, A. Svensson, and Ilka Weikusat (2014). "Fabric along the NEEM ice core, Greenland, and its comparison with GRIP and NGRIP ice cores." In: *The Cryosphere* 8.4, pp. 1129–1138. DOI: 10.5194/tc-8-1129-2014. URL: http://www.the-cryosphere.net/8/1129/2014/tc-8-1129-2014.html.

Montagnat, Maurine and Paul Duval (2000). "Rate controlling processes in the creep of polar ice, influence of grain boundary migration associated with recrystallization." In: *Earth and Planetary Science Letters* 183.1-2, pp. 179 –186. ISSN: 0012-821X. DOI: 10.1016/S0012-821X(00)00262-4.

Montagnat, Maurine, Thomas Chauve, Fabrice Barou, Andrea Tommasi, Benoît Beausir, and Claude Fressengeas (2015). "Analysis of dynamic recrystallization of ice from EBSD orientation mapping." In: *Frontiers in Earth Science* 3.81. ISSN: 2296-6463. DOI: 10.3389/feart.2015.00081. URL: http://www.frontiersin.org/cryospheric_sciences/10.3389/feart.2015.00081/abstract.

Monz, Morgan and Peter Hudleston (2018). "Microfabric and structures in glacial ice: A case study of Storglaciären, Sweden." In: *EGU General Assembly Conference Abstracts*. Vol. 20, p. 10077.

Moore, John C., Hideki Narita, and Norikazu Maeno (1991). "A continuous 770-year record of volcanic activity from east Antarctica." In: *Journal of Geophysical Research: Atmospheres* 96.D9, pp. 17353–17359. DOI: 10.1029/91JD01283. eprint: https://agupubs.onlinelibrary.wiley.com/doi/pdf/10.1029/91JD01283. URL: https://agupubs.onlinelibrary.wiley.com/doi/abs/10.1029/91JD01283.

Moore, John C., Eric W. Wolff, Henrik B. Clausen, and Claus U. Hammer (1992). "The chemical basis for the electrical stratigraphy of ice." In: *Journal of Geophysical Research: Solid Earth* 97.B2, pp. 1887–1896. DOI: 10.1029/91JB02750. eprint: https://agupubs.onlinelibrary.wiley.com/doi/pdf/10.1029/91JB02750. URL: https://agupubs.onlinelibrary.wiley.com/doi/abs/10.1029/91JB02750.

Morland, L. W. (1987). "Unconfined Ice-Shelf Flow." In: *Dynamics of the West Antarctic Ice Sheet*. Springer Netherlands, pp. 99–116. DOI: 10.1007/978-94-009-3745-1_6.

Mudelsee, Manfred (2003). "Estimating Pearson's Correlation Coefficient with Bootstrap Confidence Interval from Serially Dependent Time Series." In: *Mathematical Geology* 35.6, pp. 651–665. ISSN: 1573-8868. DOI: 10.1023/B:MATG.0000002982.52104.02.

Mullins, W. W. (1957). "Theory of thermal grooving." In: *J. Appl. Phys.* 28.3, pp. 333–339.

Mulvaney, R., E.W. Wolff, and K. Oates (1988). "Sulphuric acid at grain boundaries in Antarctic ice." In: *Nature* 331, p. 247. DOI: 10.1038/331247a0.

Nakaya, U. (1958). "Mechanical properties of single crystal of ice. Part I. Geometry of deformation." In: *US Army Snow Ice and Permafrost Research Establishment, Research Report* 28.

Nasello, O.B., C.L. Di Prinzio, and P.G. Guzmán (2005). "Temperature dependence of "pure" ice grain boundary mobility." In: *Acta Materialia* 53.18, pp. 4863–4869. DOI: 10.1016/j.actamat.2005.06.022.

Nedelcu, Aneta F., Sergio H. Faria, and Werner F. Kuhs (2009). "Raman spectra of plate-like inclusions in the EPICA-DML (Antarctica) ice core." In: *J. Glaciol.* 55.189, pp. 183–184.

NEEM community members (2013). "Eemian interglacial reconstructed from a Greenland folded ice cores." In: *Nature* 493, pp. 489–494. DOI: 10.1038/nature11789. URL: http://www.nature.com/nature/journal/v493/n7433/full/nature11789.html.

Ng, Felix and T.H. Jacka (2014). "A model of crystal-size evolution in polar ice masses." In: *Journal of Glaciology* 60.221, pp. 463–477. DOI: 10.3189/2014jog13j173.

Nishida, K. and H. Narita (1996). "Three-dimensional observations of ice crystal characteristics in polar ice sheets." In: *J. Geophys. Res.* 101.D16, pp. 21,311–21,317. DOI: 10.1029/96JA02313,1996.

Nowicki, Sophie, Robert A. Bindschadler, Ayako Abe-Ouchi, Andy Aschwanden, Ed Bueler, Hyeungu Choi, Jim Fastook, Glen Granzow, Ralf Greve, Gail Gutowski, Ute Herzfeld, Charles Jackson, Jesse Johnson, Constantine Khroulev, Eric Larour, Anders Levermann, William H. Lipscomb, Maria A. Martin, Mathieu Morlighem, Byron R. Parizek, David Pollard, Stephen F. Price, Diandong Ren, Eric Rignot, Fuyuki Saito, Tatsuru Sato, Hakime Seddik, Helene Seroussi, Kunio Takahashi, Ryan Walker, and Wei Li Wang (2013). "Insights into spatial sensitivities of ice mass response to environmental change from the SeaRISE ice sheet modeling project I: Antarctica." In: *Journal of Geophysical Research: Earth Surface* 118.2, pp. 1002–1024. DOI: 10.1002/jgrf.20081.

Nowicki, Sophie M. J., Tony Payne, Eric Larour, Helene Seroussi, Heiko Goelzer, William Lipscomb, Jonathan Gregory, Ayako Abe-Ouchi, and Andrew Shepherd (2016). "Ice Sheet Model Intercomparison Project (ISMIP6) contribution to CMIP6." In: *Geoscientific Model Development Discussions*, pp. 1–42. DOI: 10.5194/gmd-2016-105.

Nye, J.F. (1957). "The distribution of stress and velocity in glaciers and ice-sheets." In: *Proc. R. Soc. London, Ser. A* 239 (1216), pp. 113–133. DOI: 10.1098/rspa.1957.0026.

Obbard, Rachel, Ian Baker, and Daniel. Iliescu (2006). "Grain boundary grooving in ice in a scanning electron microscope. Correspondence." In: *J. Glaciol.* 52.176, 169–172(4).

Oerter, H., W. Graf, H. Meyer, and F. Wilhelms (2004). "The EPICA ice core from Dronning Maud Land: first results from stable-isotope measurements." In: *Ann. Glaciol.* 39, pp. 307–312.

Oerter, H., C. Drücker, S. Kipfstuhl, and F. Wilhelms (2009). "Kohnen Station - the Drilling Camp for the EPICA Deep Ice Core in Dronning Maud Land." In: *Polarforschung* 78.1/2, pp. 1–23. DOI: hdl:10013/epic.32552.d001.

Oerter, Hans (2009). "Klimaschwankungen: Daten aus Eisbohrkernen in der Antarktis und ihre Interpretation." In: *AK Polarlehrer in der DGfP, 4. Meeting, Karlsruhe. November 2009.* Vol. 14.

Ohno, H., M. Igarashi, and T. Hondoh (2005). "Salt inclusions in polar ice core: Location and chemical form of water-soluble impurities." In: *Earth Planet. Sci. Lett.* 232, pp. 171–178.

Ohno, H., M. Igarashi, and T. Hondoh (2006). "Characteristics of salt inclusions in polar ice from Dome Fuji, East Antarctica." In: *Geophysical Research Letters* 33.8. DOI: 10.1029/2006GL025774.

Parrenin, F., J.-M. Barnola, J. Beer, T. Blunier, E. Castellano, J. Chappellaz, G. Dreyfus, H. Fischer, S. Fujita, J. Jouzel, K. Kawamura, B. Lemieux-Dudon, L. Loulergue, V. Masson-Delmotte, B. Narcisi, J.-R. Petit, G. Raisbeck, D. Raynaud, U. Ruth, J. Schwander, M. Severi, R. Spahni, J. P. Steffensen, A. Svensson, R. Udisti, C.

Waelbroeck, and E.Wolff (2007). "The EDC3 chronology for the EPICA Dome C ice core." In: *Clim. Past* 3, pp. 485–497. URL: www.clim-past.net/3/485/2007/.

Parrenin, Frédéric, Marie G. P. Cavitte, Donald D. Blankenship, Jérôme Chappellaz, Hubertus Fischer, Olivier Gagliardini, Valérie Masson-Delmotte, Olivier Passalacqua, Catherine Ritz, Jason Roberts, Martin J. Siegert, and Duncan A. Young (2017). "Is there 1.5-million-year-old ice near Dome C, Antarctica?" In: *The Cryosphere* 11.6, pp. 2427–2437. DOI: 10.5194/tc-11-2427-2017.

Passchier, C. W. and R. A. J. Trouw (2005). *Microtectonics*. geo 326 7(2). Springer Verlag.

Paterson, W. S. B. (1977). "Secondary and tertiary creep of glacier ice as measured by borehole closure rates." In: *Reviews of Geophysics* 15.1, pp. 47–55. ISSN: 1944-9208. DOI: 10.1029/RG015i001p00047. URL: http://dx.doi.org/10.1029/RG015i001p00047.

Paterson, W. S. B. (1991). "Why ice-age ice is sometimes "soft"." In: *Cold Reg. Sci. Technol.* 20.1, pp. 75–98.

Paterson, W.S.B. (1983). "Deformation within polar ice sheets: An analysis of the Byrd station and Camp Century borehole-tilting measurements." In: *Cold Reg. Sci. Technol.* 8.2, pp. 165–179.

Paterson, W.S.B. and W.F. Budd (1982). "Flow parameters for ice sheet modelling." In: *Cold Reg. Sci. Technol.* 6.2, pp. 175–177.

Pattyn, F., L. Perichon, A. Aschwanden, B. Breuer, B. de Smedt, O. Gagliardini, G. H. Gudmundsson, R. C. A. Hindmarsh, A. Hubbard, J. V. Johnson, T. Kleiner, Y. Konovalov, C. Martin, A. J. Payne, D. Pollard, S. Price, M. Rückamp, F. Saito, O. Souček, S. Sugiyama, and T. Zwinger (2008). "Benchmark experiments for higher-order and full-Stokes ice sheet models (ISMIP–HOM)." In: *The Cryosphere* 2.2, pp. 95–108. DOI: 10.5194/tc-2-95-2008.

Pauling, Linus (1935). "The Structure and Entropy of Ice and of Other Crystals with Some Randomness of Atomic Arrangement." In: *Journal of the American Chemical Society* 57.12, pp. 2680–2684. DOI: 10.1021/ja01315a102.

Peternell, Mark, Fabian Kohlmann, Christopher J.L. Wilson, Christian Seiler, and Andrew J.W. Gleadow (2009). "A new approach to crystallographic orientation measurement for apatite fission track analysis: Effects of crystal morphology and implications for automation." In: *Chemical Geology* 265.3-4, pp. 527–539. ISSN: 0009-2541. DOI: DOI:10.1016/j.chemgeo.2009.05.021. URL: http://www.sciencedirect.com/science/article/B6V5Y-4WD7B79-1/2/6bd6283dcb2936f3eecdf961a070d9e4.

Peternell, Mark, David S. Russel-Head, and Chris J.L. Wilson (2010). "A technique for recording polycrystalline structure and orientation during in situ deformation cycles of rock analogues using an automated fabric analyser." In: *Journal of Microscopy*. DOI: 10.1111/j.1365-2818.2010.03456.x.

Petrenko, V. F. and R. W. Whitworth (1999). *Physics of ice*. ISBN 0-19-851894-3. Oxford University Press.

Pettit, E.C., Th. Thorsteinsson, H.P. Jacobson, and E.D. Waddington (2007). "The role of crystal fabric in flow near an ice divide." In: *J. Glaciol.* 53.181, pp. 277–288.

Pettit, Erin C. and Edwin D. Waddington (2003). "Ice flow at low deviatoric stress." In: *Journal of Glaciology* 49.166, pp. 359–369. DOI: 10.3189/172756503781830584.

Piazolo, S., M. W. Jessell, P. D. Bons, L. Evans, and J. K. Becker (2010). "Numerical simulations of microstructures using the Elle platform: A modern research and teaching tool." In: *Journal of the Geological Society of India* 75.1, pp. 110–127. DOI: 10.1007/s12594-010-0028-6.

Pimienta, P. and P. Duval (1987). "Rate controlling processes in the creep of polar glacier ice." In: *Journal de Physique* C1.3, pp. 243 –248.

Placidi, Luca, Ralf Greve, Hakime Seddik, and Sérgio H. Faria (2010). "Continuum-mechanical, Anisotropic Flow model for polar ice masses, based on an anisotropic Flow Enhancement factor." In: *Continuum Mechanics and Thermodynamics* 22.3, pp. 221–237. ISSN: 1432-0959. DOI: 10.1007/s00161-009-0126-0. URL: https://doi.org/10.1007/s00161-009-0126-0.

Preunkert, Susanne, Dietmar Wagenbach, Michel Legrand, and Christian Vincent (2000). "Col du Dôme (Mt Blanc Massif, French Alps) suitability for ice-core studies in relation with past atmospheric chemistry over Europe." In: *Tellus B: Chemical and Physical Meteorology* 52.3, pp. 993–1012. DOI: 10.3402/tellusb.v52i3.17081.

Purucker, M. (2012). *Geothermal heat flux data set based on low resolution observations collected by the CHAMP satellite between 2000 and 2010, and produced from the MF-6 model following the technique described in Maule et al. (2005)*. http://websrv.cs.umt.edu/isis/images/c/c8/Antarctica_heat_flux_5km.nc. Accessed: 2016-09-22.

Qi, C., D. J. Prior, L. Craw, S. Fan, M.-G. Llorens, A. Griera, M. Negrini, P. D. Bons, and D. L. Goldsby (2019, in press). "Crystallographic preferred orientations of ice deformed in direct-shear experiments at low temperatures." In: *The Cryosphere* 2018, pp. 1–35. DOI: 10.5194/tc-2018-140.

Qi, Chao, David J. Prior, Lisa Craw, Sheng Fan, Maria-Gema Llorens, Albert Griera, Marianne Negrini, Paul D. Bons, and David L. Goldsby (2018). "Crystallographic preferred orientations of ice deformed in direct-shear experiments at low temperatures." In: *The Cryosphere Discussions*, pp. 1–35. DOI: 10.5194/tc-2018-140.

Raj, R. and M. F. Ashby (1972). "Grain boundary sliding, and the effects of particles on its rate." In: *Metallurgical and Materials Transactions B* 3.7, pp. 1937–1942. DOI: 10.1007/bf02642582.

Raman, C. V. and K. S. Krishnan (1928). "A New Type of Secondary Radiation." In: *Nature* 121, pp. 501 –502. URL: http://dx.doi.org/10.1038/121501c0.

Ran, Hao, Tamara de Riese, Maria-Gema Llorens, Melanie A. Finch, Lynn A. Evans, Enrique Gomez-Rivas, Albert Griera, Mark W. Jessell, Ricardo A. Lebensohn, Sandra Piazolo, and Paul D. Bons (2018). "Time for anisotropy: The significance of mechanical anisotropy for the development of deformation structures." In: *Journal of Structural Geology*. DOI: 10.1016/j.jsg.2018.04.019.

Rasmussen, S. O., P. M. Abbott, T. Blunier, A. J. Bourne, E. Brook, S. L. Buchardt, C. Buizert, J. Chappellaz, H. B. Clausen, E. Cook, D. Dahl-Jensen, S. M. Davies, M. Guillevic, Sepp Kipfstuhl, Thomas Laepple, I. K. Seierstad, J. P. Severinghaus, J. P. Steffensen, C. Stowasser, A. Svensson, P. Vallelonga, B. M. Vinther, Frank Wilhelms, and M. Winstrup (2013). "A first chronology for the North Greenland Eemian Ice Drilling (NEEM) ice core." In: *Climate of the Past* 9.6, pp. 2713–2730. DOI: 10.5194/cp-9-2713-2013.

Read, W. T. (1953). *Dislocations in Crystals*. McGraw-Hill, p. 228.

Redenbach, Claudia, Aila Särkkä, Johannes Freitag, and Katja Schladitz (2009). "Anisotropy analysis of pressed point processes." English. In: *AStA Advances in Statistical Analysis* 93.3, pp. 237–261. ISSN: 1863-8171. DOI: 10.1007/s10182-009-0106-5. URL: http://dx.doi.org/10.1007/s10182-009-0106-5.

Reinhardt, H and 6 others (2001). "Laser ablation inductively coupled plasma mass spectrometry: a new tool for trace element analysis in ice cores." In: *Fresenius' J. Anal. Chem.*, 370(5), 629–636. DOI: 10.1007/s002160100853.

Rempel, A. W., E. D. Waddington, J. S. Wettlaufer, and M. G. Worster (2001). "Possible displacement of the climate signal in ancient ice by premelting and anomalous diffusion." In: *Nature* 411, pp. 568 –571. DOI: http://dx.doi.org/10.1038/35079043.

Riese, Tamara de, Lynn A Evans, Enrique Gomez-Rivas, Albert Griera, Ricardo A Lebensohn, M. G. Llorens, Hao Ran, T. Sachau, I. Weikusat, and P. D. Bons (2019, in review). "Shear localisation in anisotropic, non-linear viscous materials that develop a CPO: a numerical study." In: *J. Struct. Geol.*

Rignot, E., J. Mouginot, and B. Scheuchl (2011). "Ice Flow of the Antarctic Ice Sheet." In: *Science* 333.6048, pp. 1427–1430. ISSN: 0036-8075. DOI: 10.1126/science.1208336. eprint: http://science.sciencemag.org/content/333/6048/1427.full.pdf. URL: http://science.sciencemag.org/content/333/6048/1427.

Rigsby, G. P. (1951). "Crystal fabric studies on Emmons Glacier, Mount Rainier, Washington." In: *J. Geol.* 49, pp. 590–598.

Rigsby, George P (1960). "Crystal orientation in glacier and in experimentally deformed ice." In: *J. Glaciol.* 3.27, pp. 589–606.

Roessiger, Jens, Paul D. Bons, and Sérgio H. Faria (2014). "Influence of bubbles on grain growth in ice." In: *Journal of Structural Geology* 61.0. Microdynamics of Ice - MicroDICE, pp. 123 –132. ISSN: 0191-8141. DOI: http://dx.doi.org/10.1016/j.jsg.2012.11.003. URL: http://www.sciencedirect.com/science/article/pii/S0191814112002532.

Rössiger, J., P. D. Bons, A. Griera, M. W. Jessell, L. Evans, M. Montagnat, S. Kipfstuhl, S. H. Faria, and I. Weikusat (2011). "Competition between grain growth and grain-size reduction in polar ice." In: *J. Glaciol.* 57.205, pp. 942–948.

Röthlisberger, Regine, Manuel A. Hutterli, Stefan Sommer, Eric W. Wolff, and Robert Mulvaney (2000a). "Factors controlling nitrate in ice cores: Evidence from the Dome C deep ice core." In: *Journal of Geophysical Research: Atmospheres* 105.D16, pp. 20565–20572. DOI: 10.1029/2000JD900264. eprint: https://agupubs.onlinelibrary.wiley.com/doi/pdf/10.1029/2000JD900264. URL: https://agupubs.onlinelibrary.wiley.com/doi/abs/10.1029/2000JD900264.

Röthlisberger, Regine, Matthias Bigler, Manuel Hutterli, Stefan Sommer, Bernhard Stauffer, Hans G. Junghans, and Dietmar Wagenbach (2000b). "Technique for Continuous High-Resolution Analysis of Trace Substances in Firn and Ice Cores." In: *Environmental Science & Technology* 34.2, pp. 338–342. DOI: 10.1021/es9907055. eprint: https://doi.org/10.1021/es9907055. URL: https://doi.org/10.1021/es9907055.

Ruth, U., J. M. Barnola, J. Beer, M. Bigler, T. Blunier, E. Castellano, H. Fischer, F. Fundel, P. Huybrechts, P. Kaufmann, S. Kipfstuhl, A. Lambrecht, A. Morganti, H. Oerter, F. Parrenin, O. Rybak, M. Severi, R. Udisti, F. Wilhelms, and E. Wolff (2007). "EDML1: A chronology for the EPICA deep ice core from Dronning Maud Land, Antarctica, over the last 150 000 years." In: *Clim. Past* 3, pp. 475–484. URL: www.clim-past.net/3/475/2007/.

Ruth, Urs, Carlo Barbante, Matthias Bigler, Barbara Delmonte, Hubertus Fischer, Paolo Gabrielli, Vania Gaspari, Patrik Kaufmann, Fabrice Lambert, Valter Maggi, Federica Marino, Jean-Robert Petit, Roberto Udisti, Dietmar Wagenbach, Anna Wegner, and Eric W. Wolff (2008). "Proxies and Measurement Techniques for Mineral Dust in Antarctic Ice Cores." In: *Environmental Science & Technology* 42.15. PMID: 18754492, pp. 5675–5681. DOI: 10.1021/es703078z. eprint: https://doi.org/10.1021/es703078z. URL: https://doi.org/10.1021/es703078z.

Sakurai, Toshimitsu, Hiroshi Ohno, Shinichiro Horikawa, Yoshinori Iizuka, Tsutomu Uchida, Kazuomi Hirakawa, and Takeo Hondoh (2011). "The chemical forms of

water-soluble microparticles preserved in the Antarctic ice sheet during Termination I." In: *Journal of Glaciology* 57.206, pp. 1027–1032. ISSN: 0022-1430. DOI: 10.3189/002214311798843403. URL: http://www.ingentaconnect.com/content/igsoc/jog/2011/00000057/00000206/art00004.

Samyn, D., A. Svensson, and S. J. Fitzsimons (2008). "Dynamic implications of discontinuous recrystallization in cold basal ice: Taylor Glacier, Antarctica." In: *J. Geophys. Res.* 113. DOI: 10.1029/2006JF000600.

Savvin, A., R. Greve, R. Calov, B. Mügge, and K. Hutter (2000). "Simulation of the Antarctic ice sheet with a three-dimensional polythermal ice-sheet model, in support of the EPICA project. II. Nested high-resolution treatment of Dronning Maud Land, Antarctica." In: *Annals of Glaciology* 30, pp. 69–75. DOI: 10.3189/172756400781820831.

Schaller, C. F., J. Freitag, S. Kipfstuhl, T. Laepple, H. C. Steen-Larsen, and O. Eisen (2016). "A representative density profile of the North Greenland snowpack." In: *The Cryosphere* 10.5, pp. 1991–2002. DOI: 10.5194/tc-10-1991-2016.

Schaller, Christoph Florian, Johannes Freitag, and Olaf Eisen (2017). "Critical porosity of gas enclosure in polar firn independent of climate." In: *Climate of the Past* 13.11, pp. 1685–1693. DOI: 10.5194/cp-13-1685-2017.

Schulson, Erland M. and Paul Duval (2009). *Creep and Fracture of Ice*. Cambridge University Press, p. 401.

Schüpbach, S., U. Federer, P. R. Kaufmann, S. Albani, C. Barbante, T. F. Stocker, and H. Fischer (2013). "High-resolution mineral dust and sea ice proxy records from the Talos Dome ice core." In: *Clim. Past* 9, pp. 2789–2807. DOI: 10.5194/cp-9-2789-2013. URL: www.clim-past.net/9/2789/2013/.

Schwander, J. and B. Stauffer (1984). "Age difference between polar ice and the air trapped in its bubbles." In: *Nature* 311.5981, pp. 45–47. DOI: 10.1038/311045a0.

Schwikowski, M, S Brütsch, HW Gäggeler, and U Schotterer (1999). "A high-resolution air chemistry record from an Alpine ice core: Fiescherhorn glacier, Swiss Alps." In: *J. Geophys. Res.* 104.D11, pp. 13709–13719. DOI: 10.1029/1998JD100112.

Seddik, Hakime, Ralf Greve, Luca Placidi, Ilka Hamann, and Olivier Gagliardini (2008). "Application of a continuum-mechanical model for the flow of anisotropic polar ice to the EDML core, Antarctica." In: *J. Glaciol.* 54.187, pp. 631–642.

Shapiro, N (2004). "Inferring surface heat flux distributions guided by a global seismic model: particular application to Antarctica." In: *Earth and Planetary Science Letters* 223.1-2, pp. 213–224. DOI: 10.1016/j.epsl.2004.04.011.

Shiklomanov, Igor A. (2000). "Appraisal and Assessment of World Water Resources." In: *Water International* 25.1, pp. 11–32. DOI: 10.1080/02508060008686794. eprint: https://doi.org/10.1080/02508060008686794. URL: https://doi.org/10.1080/02508060008686794.

Shoji, H. and A. Higashi (1978). "A deformation mechanism map of ice." In: *J. Glaciol.* 21.85, pp. 419–427.

Sigl, M., M. Winstrup, J. R. McConnell, K. C. Welten, G. Plunkett, F. Ludlow, U. Buntgen, M. Caffee, N. Chellman, D. Dahl-Jensen, H. Fischer, S. Kipfstuhl, C. Kostick, O. J. Maselli, F. Mekhaldi, R. Mulvaney, R. Muscheler, D. R. Pasteris, J. R. Pilcher, M. Salzer, S. Schupbach, J. P. Steffensen, B. M. Vinther, and T. E. Woodruff (July 2015). "Timing and climate forcing of volcanic eruptions for the past 2,500 years." In: *Nature* 523, pp. 543–549. DOI: 10.1038/nature14565.

Smith, C. S. (1948). "Grains, Phases, and Interfaces: An Interpretation of Microstructure." In: *AIME Trans.* 175, pp. 15–51.

Smith, Cyril Stanley (1964). "SOME ELEMENTARY PRINCIPLES OF POLYCRYSTALLINE MICROSTRUCTURE." In: *Metallurgical Reviews* 9.1, pp. 1–48. DOI: 10.1179/mtlr.1964.9.1.1.

Spaulding, Nicole E, Sharon B Sneed, Michael J Handley, Pascal Bohleber, Andrei V Kurbatov, Nicholas J Pearce, Tobias Erhardt, and Paul A Mayewski (2017). "A New Multielement Method for LA-ICP-MS Data Acquisition from Glacier Ice Cores." In: *Environ. Sci. Technol.* 51.22, pp. 13282–13287. DOI: 10.1021/acs.est.7b03950.

Stauffer, B., J. Schwander, and H. Oeschger (1985). "Enclosure of Air During Metamorphosis of Dry Firn to Ice." In: *Annals of Glaciology* 6, pp. 108–112. DOI: 10.3189/1985aog6-1-108-112.

Steinbach, F., P. D. Bons, A. Griera, D. Jansen, M.-G. Llorens, J. Roessiger, and I. Weikusat (2016). "Strain localisation and dynamic recrystallisation in the ice-air aggregate: A numerical study." In: *The Cryosphere Discussions* 2016, pp. 1–30. DOI: 10.5194/tc-2016-167. URL: http://www.the-cryosphere-discuss.net/tc-2016-167/.

Steinbach, Florian, Ernst-Jan N. Kuiper, Jan Eichler, Paul D. Bons, Martyn R. Drury, Albert Griera, Gill M. Pennock, and Ilka Weikusat (2017). "The Relevance of Grain Dissection for Grain Size Reduction in Polar Ice: Insights from Numerical Models and Ice Core Microstructure Analysis." In: *Frontiers in Earth Science* 5, p. 66. ISSN: 2296-6463. DOI: 10.3389/feart.2017.00066. URL: https://www.frontiersin.org/article/10.3389/feart.2017.00066.

Steinemann, Samuel (1954). "Results of Preliminary Experiments on the Plasticity of Ice Crystals." In: *Journal of Glaciology* 2.16, pp. 404–416. DOI: 10.3189/002214354793702533.

Stillman, David E., Joseph A. MacGregor, and Robert E. Grimm (2013). "The role of acids in electrical conduction through ice." In: *Journal of Geophysical Research: Earth Surface* 118.1, pp. 1–16. ISSN: 2169-9011. DOI: 10.1029/2012JF002603. URL: http://dx.doi.org/10.1029/2012JF002603.

Summerhayes, Colin P. (Oct. 16, 2015). *Earth's Climate Evolution*. John Wiley & Sons Inc. 410 pp. ISBN: 1118897390. URL: https://www.ebook.de/de/product/23546317/colin_p_summerhayes_earth_s_climate_evolution.html.

Svensson, A., S. W. Nielsen, S. Kipfstuhl, S. J. Johnsen, J. P. Steffensen, M. Bigler, U. Ruth, and R. Röthlisberger (2005). "Visual stratigraphy of North Greenland Ice Core Project (NorthGRIP) ice core during the last glacial period." In: *Journal of Geophysical Research: Atmospheres* 110.D2. DOI: 10.1029/2004JD005134.

Svensson, A., M. Bigler, E. Kettner, D. Dahl-Jensen, S. Johnsen, S. Kipfstuhl, M. Nielsen, and J. P. Steffensen (2011). "Annual layering in the NGRIP ice core during the Eemian." In: *Climate of the Past* 7.4, pp. 1427–1437. DOI: 10.5194/cp-7-1427-2011.

Svensson, Anders, Pauli Baadsager, Asbjørn Persson, Christine Schøtt Hvidberg, and Marie-Louise Siggaard-Andersen (2003). "Seasonal variability in ice crystal properties at NorthGRIP: a case study around 301 m depth." In: *Ann. Glaciol.* 37.1, pp. 119–122.

Talalay, P.G. and Roger LeB. Hooke (2007). "Closure of deep boreholes in ice sheets: a discussion." In: *Annals of Glaciology* 47.1, pp. 125–133. DOI: doi:10.3189/172756407786857794.

Taylor, K. C., C. U. Hammer, R. B. Alley, H. B. Clausen, D. Dahl-Jensen, A. J. Gow, N. S. Gundestrup, J. C. Kipfstuhl J. andMoore, and E. D. Waddington (1993). "Electrical conductivity measurements from the GISP2 and GRIP Greenland ice cores." In: *Nature* 366, pp. 549–552.

Taylor, Lawrence D (1963). "Structure and fabric on the Burroughs Glacier, southeast Alaska." In: *J. Glaciol.* 4.36, pp. 731–752. DOI: 10.3189/S0022143000028331.

Thibert, Emmanuel and Florent Dominé (1997). "Thermodynamics and Kinetics of the Solid Solution of HCl in Ice." In: *The Journal of Physical Chemistry B* 101.18, pp. 3554–3565. DOI: 10.1021/jp962115o. eprint: http://dx.doi.org/10.1021/jp962115o. URL: http://dx.doi.org/10.1021/jp962115o.

Thibert, Emmanuel and Florent Dominé (1998). "Thermodynamics and Kinetics of the Solid Solution of HNO_3 in Ice." In: *The Journal of Physical Chemistry B* 102.22, pp. 4432–4439. DOI: 10.1021/jp980569a. eprint: http://dx.doi.org/10.1021/jp980569a. URL: http://dx.doi.org/10.1021/jp980569a.

Thompson, Lonnie G, E Mosley-Thompson, ME Davis, PN Lin, J Dai, JF Bolzan, and T Yao (1995). "A 1000 year climate ice-core record from the Guliya ice cap, China: its relationship to global climate variability." In: *Ann. Glaciol.* 21, pp. 175–181. DOI: 10.3189/S0260305500015780.

Thompson, Lonnie G, Ellen Mosley-Thompson, Henry Brecher, Mary Davis, Blanca León, Don Les, Ping-Nan Lin, Tracy Mashiotta, and Keith Mountain (2006). "Abrupt tropical climate change: Past and present." In: *PNAS* 103.28, pp. 10536–10543. DOI: 10.1073/pnas.0603900103.

Thorsteinsson, Th. (2002). "Fabric development with nearest-neighbor interaction and dynamic recrystallisation." In: *J. Geophys. Res.* B107.1, p. 2014.

Thorsteinsson, Th., J. Kipfstuhl, H. Eicken, S. J. Johnsen, and K. Fuhrer (1995). "Crystal size variations in Eemian-age ice from the GRIP ice core, Central Greenland." In: *Earth Planet. Sci. Lett.* 131, pp. 381–394.

Thorsteinsson, Th., J. Kipfstuhl, and H. Miller (1997). "Textures and fabrics in the GRIP ice core." In: *J. Geophys. Res.* 102.C12, pp. 26,583–26,599.

Tison, J.-L. and B. Hubbard (2000). "Deformation of Glacial Materials." In: ed. by A. J. Maltman, B. Hubbard, and M. J. Hambrey. Vol. 176. London: Geological Society, Special Publications. Chap. Ice crystallographic evolution at a temperate glacier: Glacier de Tsanfleuron, Switzerland, pp. 23–38.

Treverrow, A., J. Li, and T.H. Jacka (2016). "Ice crystal c-axis orientation and mean grain size measurements from the Dome Summit South ice core, Law Dome, East Antarctica." In: *Earth Syst. Sci. Data Discuss.* DOI: 10.5194/essd-2015-45.

Treverrow, Adam, William F. Budd, Tim H. Jacka, and Roland C. Warner (2012). "The tertiary creep of polycrystalline ice: experimental evidence for stress-dependent levels of strain-rate enhancement." In: *Journal of Glaciology* 58.208. DOI: 10.3189/2012JoG11J149.

Trimby, Patrick W, David J Prior, and John Wheeler (1998). "Grain boundary hierarchy development in a quartz mylonite." In: *Journal of Structural Geology* 20.7, pp. 917–935. DOI: 10.1016/s0191-8141(98)00026-1.

Trimby, Patrick W., Martyn R. Drury, and Christopher J. Spiers (2000). "Misorientations across etched boundaries in deformed rocksalt: a study using electron backscatter diffraction." In: *Journal of Structural Geology* 22.1, pp. 81–89. DOI: 10.1016/s0191-8141(99)00126-1.

Tullis, Jan, Lisa Dell'Angelo, and Richard A. Yund (1990). "Ductile shear zones from brittle precursors in feldspathic rocks: The role of dynamic recrystallization." In: *The Brittle-Ductile Transition in Rocks*. American Geophysical Union, pp. 67–81. DOI: 10.1029/gm056p0067.

Twiss, R.J. and E.M. Moores (2007). *Structural Geology*. W. H. Freeman. ISBN: 9780716749516. URL: http://www.whfreeman.com/catalog/Product/structuralgeology-secondedition-twiss.

Uchida, Tsutomu, Keita Yasuda, Yuya Oto, Renkai Shen, and Ryo Ohmura (2014). "Natural supersaturation conditions needed for nucleation of air-clathrate hydrates in deep ice sheets." In: *Journal of Glaciology* 60 (224), pp. 1111–1116. DOI: doi:10.3189/2014JoG13J232.

Urai, J. and J. Humphreys (2000). "A collection of time-lapse movies from transmitted light deformation experiments." In: *Journal of the Virtual Explorer* 02. DOI: 10.3809/jvirtex.2000.00020.

Urai, Janos L. (1983). "Water assisted dynamic recrystallization and weakening in polycrystalline bischofite." In: *Tectonophysics* 96.1-2, pp. 125–157. DOI: 10.1016/0040-1951(83)90247-0.

Urai, Janos L. (1987). "Development of microstructure during deformation of carnallite and bischofite in transmitted light." In: *Tectonophysics* 135.1-3, pp. 251–263. DOI: 10.1016/0040-1951(87)90166-1.

Urai, Janos L and Mark Jessell (2001). "Recrystallization and grain growth in minerals: recent developments." In: *Recrystallization and Grain Growth, Proceedings of the first joint international conference*.

Urai, JL, WD Means, and GS Lister (1986). "Dynamic recrystallization of minerals." In: *Mineral and Rock Deformation: Laboratory Studies: The Paterson Volume* DOI: 10.1029/GM036p0161, pp. 161–199.

Vallelonga, P., G. Bertagna, T. Blunier, H. A. Kjær, T. J. Popp, S. O. Rasmussen, J. P. Steffensen, C. Stowasser, A. S. Svensson, E. Warming, M. Winstrup, M. Bigler, and Sepp Kipfstuhl (2012). "Duration of Greenland Stadial 22 and ice-gas Δage from counting of annual layers in Greenland NGRIP ice core." In: *Climate of the Past* 8.6, pp. 1839–1847. DOI: 10.5194/cp-8-1839-2012.

Vallon, M., J.R. Petit, and B. Fabre (1976). "Study of an ice core to the bedrock in the accumulation zone of an alpine glacier." In: *J. Glaciol.* 17, pp. 13–28.

Vaughan, M. J., K. van Wijk, D. J. Prior, and M. H. Bowman (2016). "Monitoring the temperature-dependent elastic and anelastic properties in isotropic polycrystalline ice using resonant ultrasound spectroscopy." In: *The Cryosphere* 10.6, pp. 2821–2829. DOI: 10.5194/tc-10-2821-2016.

Veen, C.J. van der and I.M. Whillans (1994). "Development of fabric in ice." In: *Cold Regions Science and Technology* 22.2, pp. 171–195. DOI: 10.1016/0165-232x(94)90027-2.

Veen, C.J. Van Der and I.M. Whillans (1990). "Flow Laws For Glacier Ice: Comparison Of Numerical Predictions And Field Measurements." In: *Journal of Glaciology* 36.124, pp. 324–339. DOI: 10.3189/002214390793701372.

Veres, D., L. Bazin, A. Landais, H. Toyé Mahamadou Kele, B. Lemieux-Dudon, F. Parrenin, P. Martinerie, E. Blayo, T. Blunier, E. Capron, J. Chappellaz, S. O. Rasmussen, M. Severi, A. Svensson, B. Vinther, and E. W. Wolff (2013). "The Antarctic ice core chronology (AICC2012): an optimized multi-parameter and multi-site dating approach for the last 120 thousand years." In: *Climate of the Past* 9.4, pp. 1733–1748. DOI: 10.5194/cp-9-1733-2013. URL: https://www.clim-past.net/9/1733/2013/.

Vinther, B. M., S. L. Buchardt, H. B. Clausen, D. Dahl-Jensen, S. J. Johnsen, D. A. Fisher, R. M. Koerner, D. Raynaud, V. Lipenkov, K. K. Andersen, T. Blunier, S. O. Rasmussen, J. P. Steffensen, and A. M. Svensson (2009). "Holocene thinning of the Greenland ice sheets." In: *Nature* 461, pp. 385–388. DOI: 10.1038/nature08355.

Wagenbach, D, KO Münnich, U Schotterer, and H Oeschger (1988). "The anthropogenic impact on snow chemistry at Colle Gnifetti, Swiss Alps." In: *Ann. Glaciol* 10.183, pp. 183–187.

Wagenbach, Dietmar and Klaus Geis (1989). "The Mineral Dust Record in a High Altitude Alpine Glacier (Colle Gnifetti, Swiss Alps)." In: *Paleoclimatology and Paleometeorology: Modern and Past Patterns of Global Atmospheric Transport*. Ed. by Margaret Leinen and Michael Sarnthein. Springer Netherlands, pp. 543–564. ISBN: 978-94-010-6937-3. DOI: 10.1007/978-94-009-0995-3_23.

Wagenbach, Dietmar, Pascal Bohleber, and Susanne Preunkert (2012). "Cold, Alpine ice bodies revisited: What may we learn from their impurity and isotope content?" In: *Geografiska Annaler: Series A, Physical Geography* 94.2, pp. 245–263. DOI: 10.1111/j.1468-0459.2012.00461.x.

Wallbrecher, E. (1979). "Methoden zum quantitativen Vergleich der Regelungsgrade und -formen von strukturgeologischen Datenmengen mit Hilfe der Vektorstatistik und Eigenwert-Analyse." In: *Neues Jahrbuch für Geologie und Paläontologie Abhandlungen* 159, pp. 113–149.

Wallbrecher, E. (1986). *Tektonische und gefügeanalytische Arbeitsweisen*. geo 326 19. Ferdinand Enke Verlag Stuttgart.

Wang, Mo, Baiqing Xu, Susan D. Kaspari, Gerd Gleixner, Valérie F. Schwab, Huabiao Zhao, Hailong Wang, and Ping Yao (2015). "Century-long record of black carbon in an ice core from the Eastern Pamirs: Estimated contributions from biomass burning." In: *Atmospheric Environment* 115, pp. 79 –88. ISSN: 1352-2310. DOI: https://doi.org/10.1016/j.atmosenv.2015.05.034. URL: http://www.sciencedirect.com/science/article/pii/S1352231015301072.

Wang, Y. and N. Azuma (1999). "A new automatic ice-fabric analyzer which uses image-analysis techniques." In: *Ann. Glaciol.* 29, pp. 155–162. DOI: 10.3189/172756499781821021.

Wang, Y., Th. Thorsteinsson, S. Kipfstuhl, H. Miller, D. Dahl-Jensen, and H. Shoji (2002). "A vertical girdle fabric in the NorthGRIP deep ice core, North Greenland." In: *Ann. Glaciol.* 35, pp. 515–520.

Wang, Y., S. Kipfstuhl, N. Azuma, Th. Thorsteinsson, and H. Miller (2003). "Ice-fabrics study in the upper 1500 m of Dome C (East Antarctica) deep ice core." In: *Ann. Glaciol.* 37, pp. 97–104.

Warneck, Peter (1988). *Chemistry of the Natural Atmosphere*. International Geophysics. Elsevier Science. ISBN: 9780080954684.

WCRP Global Sea Level Budget Group (2018). "Global sea-level budget 1993–present." In: *Earth System Science Data* 10.3, pp. 1551–1590. DOI: 10.5194/essd-10-1551-2018. URL: https://www.earth-syst-sci-data.net/10/1551/2018/.

Weaire, D. and N. Rivier (1984). "Soap, cells and statistics—random patterns in two dimensions." In: *Contemporary Physics* 25.1, pp. 59–99. DOI: 10.1080/00107518408210979.

Weertman, J. (1973). "Creep of Ice." In: *Physics and Chemistry of Ice*, pp. 320–337.

Weertman, J. (1983). "Creep Deformation of Ice." In: *Annu. Rev. Earth Planet. Sci.* 11, p. 215.

Weertman, J. and J. R. Weertman (1992). *Elementary Dislocation Theory*. Oxford University Press.

Wegner, Anna, Hubertus Fischer, Barbara Delmonte, Jean Robert Petit, Tobias Erhardt, Urs Ruth, Anders Svensson, Bo M. Vinther, and Heinrich Miller (2015). "The role of seasonality of mineral dust concentration and size on glacial/interglacial dust changes in the EPICA Dronning Maud Land ice core." In: *Journal of Geophysical Research-Atmospheres* 120, pp. 9916–9931. DOI: 10.1002/2015JD023608. URL: http://onlinelibrary.wiley.com/doi/10.1002/2015JD023608/full.

Weikusat, Christian, Johannes Freitag, and Sepp Kipfstuhl (2012). "Raman spectroscopy of gaseous inclusions in EDML ice core: First results - microbubbles." In: *Journal of Glaciology* 58, pp. 761–766.

Weikusat, Christian, Sepp Kipfstuhl, and Ilka Weikusat (2015). "Raman tomography of natural air hydrates." In: *Journal of Glaciology* 61.229, pp. 923–930. DOI: 10.3189/2015JoG15J009.

Weikusat, I., S. Kipfstuhl, N. Azuma, S. H. Faria, and A. Miyamoto (2009a). "Deformation Microstructures in an Antarctic Ice Core (EDML) and in Experimentally Deformed Artificial Ice." In: *Physics of Ice Core Records II*. Ed. by T. Hondoh. Vol. 2. Supplement Issue of Low Temperature Science, Vol. 68, pp. 115–123. DOI: 10013/epic.35758.

Weikusat, I., S. Kipfstuhl, S. H. Faria, N. Azuma, and A. Miyamoto (2009b). "Subgrain boundaries and related microstructural features in EPICA-Dronning Maud Land (EDML) deep ice core." In: *J. Glaciol.* 55.191, pp. 461–472. DOI: 10.3189/002214309788816614.

Weikusat, I., D. A. M. de Winter, G. M. Pennock, M. Hayles, C. T. W. M. Schneijdenberg, and M. R. Drury (2010). "Cryogenic EBSD on ice: preserving a stable surface in a low pressure SEM." In: *J. Microsc.* 242.3, pp. 295–310. DOI: 10.1111/j.1365-2818.2010.03471.x.

Weikusat, I., A. Miyamoto, S. H. Faria, S. Kipfstuhl, N. Azuma, and T. Hondoh (2011). "Subgrain boundaries in Antarctic ice quantified by X-ray Laue diffraction." In: *J. Glaciol.* 57.201, pp. 85–94. DOI: 10013/epic.36402.

Weikusat, I., E.-J. N. Kuiper, G. M. Pennock, S. Kipfstuhl, and M. R. Drury (2017a). "EBSD analysis of subgrain boundaries and dislocation slip systems in Antarctic and Greenland ice." In: *Solid Earth* 8, 883–898. DOI: 10.5194/se-8-883-2017. URL: https://www.solid-earth.net/8/883/2017/.

Weikusat, Ilka and Sepp Kipfstuhl (2010). *Crystal c-axes (fabric) of ice core samples collected from the NEEM ice core*. unpublished dataset. DOI: 10.1594/PANGAEA.744004. URL: https://doi.pangaea.de/10.1594/PANGAEA.744004.

Weikusat, Ilka, Sepp Kipfstuhl, and Anja Lambrecht (2013a). *Crystal c-axes (fabric G20) of ice core samples collected from the EDML ice core with links to raw data files*. data set. Alfred Wegener Institute, Helmholtz Center for Polar and Marine Research, Bremerhaven. DOI: 10.1594/PANGAEA.807207. URL: https://doi.org/10.1594/PANGAEA.807207.

Weikusat, Ilka, Sepp Kipfstuhl, and Anja Lambrecht (2013b). *Crystal c-axes (fabric G50) of ice core samples collected from the EDML ice core with links to raw data files*. data set. Alfred Wegener Institute, Helmholtz Center for Polar and Marine Research, Bremerhaven. DOI: 10.1594/PANGAEA.807206. URL: https://doi.org/10.1594/PANGAEA.807206.

Weikusat, Ilka, Anja Lambrecht, and Sepp Kipfstuhl (2013c). *Eigenvalues of crystal orientation tensors for c-axes distributions of horizontal thin sections from the EDML ice core*. data set. DOI: 10.1594/PANGAEA.807141. URL: https://doi.org/10.1594/PANGAEA.807141.

Weikusat, Ilka, Anja Lambrecht, and Sepp Kipfstuhl (2013d). *Eigenvalues of crystal orientation tensors for c-axes distributions of vertical thin sections from the EDML ice core*. data set. DOI: 10.1594/PANGAEA.807142. URL: https://doi.org/10.1594/PANGAEA.807142.

Weikusat, Ilka, Daniela Jansen, Tobias Binder, Jan Eichler, Sérgio H. Faria, Frank Wilhelms, Sepp Kipfstuhl, Simon Sheldon, Heinrich Miller, Dorthe Dahl-Jensen, and Thomas Kleiner (2017b). "Physical analysis of an Antarctic ice core–towards an integration of micro- and macrodynamics of polar ice." In: *Philosophical*

Transactions of the Royal Society A: Mathematical, Physical and Engineering Sciences 375.2086, p. 20150347. DOI: 10.1098/rsta.2015.0347. URL: http://doi.org/10.1098/rsta.2015.0347.

Weller, R., F. Traufetter, H. Fischer, H. Oerter, C. Piel, and H. Miller (2004). "Postdepositional losses of methane sulfonate, nitrate, and chloride at the European Project for Ice Coring in Antarctica deep-drilling site in Dronning Maud Land, Antarctica." In: *Journal of Geophysical Research: Atmospheres* 109.D7. D07301, n/a–n/a. ISSN: 2156-2202. DOI: 10.1029/2003JD004189. URL: http://dx.doi.org/10.1029/2003JD004189.

Wesche, C., O. Eisen, H. Oerter, D. Schulte, and D. Steinhage (2007). "Surface topography and ice flow in the vicinity of the EDML deep-drilling site, Antarctica." In: *J. Glaciol.* 53.182, pp. 442–448.

Wessem, J. M. van, C. H. Reijmer, J. T. M. Lenaerts, W. J. van de Berg, M. R. van den Broeke, and E. van Meijgaard (2014). "Updated cloud physics in a regional atmospheric climate model improves the modelled surface energy balance of Antarctica." In: *The Cryosphere* 8.1, pp. 125–135. DOI: 10.5194/tc-8-125-2014.

White, S. (1977). "Geological significance of recovery and recrystallization processes in quartz." In: *Tectonophysics* 39.1-3, pp. 143–170. DOI: 10.1016/0040-1951(77)90093-2.

Whitworth, R. W., J. G. Paren, and J. W. Glen (1976). "The velocity of dislocations in ice, - a theory based on proton disorder." In: *Philosophical Magazine* 33.3, pp. 409–426. DOI: 10.1080/14786437608221110. eprint: http://www.tandfonline.com/doi/pdf/10.1080/14786437608221110. URL: http://www.tandfonline.com/doi/abs/10.1080/14786437608221110.

Wilen, L. A., C. L. Diprinzio, R. B. Alley, and N. Azuma (2003). "Development, Principles and Applications of Automated Ice Fabric Analyzers." In: *Microsc. Res. Techn.* 62, pp. 2–18.

Wilhelms, F., S. G. Sheldon, I. Hamann, and S. Kipfstuhl (2007). "Implications for and findings from deep ice core drillings - An example: The ultimate tensile strength of ice at high strain rates." In: *Physics and Chemistry of Ice (The proceedings of the International Conference on the Physics and Chemistry of Ice held at Bremerhaven, Germany on 23-28 July 2006)*. Ed. by W. F. Kuhs. The Royal Society of Chemistry Special Publication 311, pp. 635–639.

Wilhelms, Frank (2005). "Explaining the dielectric properties of firn as a density-and-conductivity mixed permittivity (DECOMP)." In: *Geophysical Research Letters* 32.16. DOI: 10.1029/2005GL022808.

Wilhelms, Frank, J. Kipfstuhl, Heinrich Miller, K. Heinloth, and J. Firestone (1998). "Precise dielectric profiling of ice cores: A new device with improved guarding and its theory." In: *Journal of Glaciology* 44.146, pp. 171–174.

Wilhelms, Frank, Heinrich Miller, Michael D. Gerasimoff, Cord Drücker, Andreas Frenzel, Diedrich Fritzsche, Hannes Grobe, Steffen Bo Hansen, Sverrir Æ. Hilmarsson, Georg Hoffmann, and et al. (2014). "The EPICA Dronning Maud Land deep drilling operation." In: *Annals of Glaciology* 55.68, 355–366. DOI: 10.3189/2014AoG68A189.

Wilkinson, D.S and M.F Ashby (1975). "Pressure sintering by power law creep." In: *Acta Metallurgica* 23.11, pp. 1277–1285. DOI: 10.1016/0001-6160(75)90136-4.

Wilson, C. J. L. and Y. Zhang (1994). "Comparison between experiment and computer modelling of plane-strain simple-shear ice deformation." In: *J. Glaciol.* 40.134, pp. 46–55.

Wilson, C. J. L., D. S. Russell-Head, and H. M. Sim (2003). "The application of an automated fabric analyzer system to the textural evolution of folded ice layers in shear zones." In: *Ann. Glaciol.* 37, pp. 7–17.

Winkelmann, R., M. A. Martin, M. Haseloff, T. Albrecht, E. Bueler, C. Khroulev, and A. Levermann (2011). "The Potsdam Parallel Ice Sheet Model (PISM-PIK) â€“ Part 1: Model description." In: *The Cryosphere* 5.3, pp. 715–726. DOI: 10.5194/tc-5-715-2011. URL: http://www.the-cryosphere.net/5/715/2011/.

Wolff, E. W. and J. G. Paren (1984). "A two-phase model of electrical conduction in polar ice sheets." In: *Journal of Geophysical Research: Solid Earth* 89.B11, pp. 9433–9438. ISSN: 2156-2202. DOI: 10.1029/JB089iB11p09433. URL: http://dx.doi.org/10.1029/JB089iB11p09433.

Wolff, E. W., H. Fischer, F. Fundel, U. Ruth, B. Twarloh, G. C. Littot, R. Mulvaney, R. Röthlisberger, M. de Angelis, C. F. Boutron, M. Hansson, U. Jonsell, M. A. Hutterli, F. Lambert, P. Kaufmann, B. Stauffer, T. F. Stocker, J. P. Steffensen, M. Bigler, M. L. Siggaard-Andersen, R. Udisti, S. Becagli, E. Castellano, M. Severi, D. Wagenbach, C. Barbante, P. Gabrielli, and V. Gaspari (2006). "Southern Ocean sea-ice extent, productivity and iron flux over the past eight glacial cycles." In: *Nature* 440. Article, 491 EP –. URL: http://dx.doi.org/10.1038/nature04614.

Wolff, Eric W. (1995). "Nitrate in Polar Ice." In: *Ice Core Studies of Global Biogeochemical Cycles*. Ed. by Robert J. Delmas. Berlin, Heidelberg: Springer Berlin Heidelberg, pp. 195–224. ISBN: 978-3-642-51172-1.

Wolff, Eric W. (2011). "Greenhouse gases in the Earth system: a palaeoclimate perspective." In: *Philosophical Transactions of the Royal Society of London A: Mathematical, Physical and Engineering Sciences* 369.1943, pp. 2133–2147. ISSN: 1364-503X. DOI: 10.1098/rsta.2010.0225. eprint: http://rsta.royalsocietypublishing.org/content/369/1943/2133.full.pdf. URL: http://rsta.royalsocietypublishing.org/content/369/1943/2133.

Wolff, Eric W., William D. Miners, John C. Moore, and Julian G. Paren (1997). "Factors Controlling the Electrical Conductivity of Ice from the Polar Regions – A Summary." In: *The Journal of Physical Chemistry B* 101.32, pp. 6090–6094. DOI: 10.1021/jp9631543.

Woodcock, N. H. (1977). "Specification of fabric shapes using an eigenvalue method." In: *Geological Society of America Bulletin* 88.9, pp. 1231–1236. DOI: 10.1130/0016-7606(1977)88<1231:SOFSUA>2.0.CO;2. eprint: http://gsabulletin.gsapubs.org/content/88/9/1231.full.pdf+html. URL: http://gsabulletin.gsapubs.org/content/88/9/1231.abstract.

Young, D. A., J. L. Roberts, C. Ritz, M. Frezzotti, E. Quartini, M. G. P. Cavitte, C. R. Tozer, D. Steinhage, S. Urbini, H. F. J. Corr, T. van Ommen, and D. D. Blankenship (2017). "High-resolution boundary conditions of an old ice target near Dome C, Antarctica." In: *The Cryosphere* 11.4, pp. 1897–1911. DOI: 10.5194/tc-11-1897-2017. URL: https://www.the-cryosphere.net/11/1897/2017/.

Zwally, H. J., M. B. Giovinetto, Beckley M. A., and Saba J. L. (2012). *Antarctic and Greenland Drainage Systems*. GSFC Cryospheric Sciences Laboratory. URL: http://icesat4.gsfc.nasa.gov/cryo_data/ant_grn_drainage_systems.php (visited on 04/08/2016).

Acknowledgements

I want to express my greatest appreciation to my supervisors Ilka Weikusat, Paul D. Bons and Frank Wilhelms. Thanks to Ilka for all the support and guidance she gave me and for her expertise and soft skills which both were very important for me to bring this work to an end. Thanks to Paul for receiving me in Tübingen so many times and for all the helpful consultations.

Many thanks to Christian Weikusat for being my Raman guru inside the lab and a close friend outside of it.

My deep gratitude to Sepp Kipfstuhl for his support, expertise and enthusiasm.

Many thanks to Daniela Jansen for constructive discussions and a great time in the rehearsal room.

I appreciated very much being part of the network of people brought together by Ilka. Thanks to Tobias Binder, Johanna Kerch, Florian Steinbach, Ernst-Jan Kuiper, Ina Kleitz, Gema Llorens and others for fruitful exchange and discussions.

Thanks to Coen Hofstede for teaching me to stand the cold.

Many thanks to all the colleagues and friends at AWI for creating such a friendly and inspiring environment.

Thanks to the colleagues in Tübingen for their hospitality during my stays there.

My gratitude to the colleagues in Utrecht, especially Gill Pennock and Martyn Drury.

I am deeply grateful to my whole family who never gave up trusting in me and supporting me in all my intentions.

Special thanks to my friends Anna and Matti, who helped me to bring the writing of this thesis to a finish.

Many thanks to my house mates Antje and Andres, it was a pleasure.

Thanks to *Innenlebenscheiß* and *Chef Speck*.

Thanks to my friends in Bremerhaven and elsewhere who were there for me during the last years, especially Antje & Lars, Andres, Fabio, Anna, Jan & Luisa, Marnie, Mauro, Lara & Samuel, Matti & Franz, Martin & Lena, Felix & Isa, Axel & Ulrike, Quique & Iolanda and others.

I am very grateful to Pjönghwa for his conjuring art.

And many thanks to Sara for her patience and love.